

ulm university universität
uulm

The Thermal Instability of Nanocrystalline Materials – An Experimental Case Study of Microstructural Evolution in Ball-Milled Iron

DISSERTATION

zur Erlangung des akademischen Grades eines

DOKTOR-INGENIEURS

(DR.-ING.)

der Fakultät für Ingenieurwissenschaften
und Informatik der Universität Ulm

von

Heiko Paul

aus Mutlangen

Gutachter:	Prof. Carl E. Krill III, Ph.D.
	Prof. Dr. Rainer Birringer
Amtierender Dekan:	Prof. Dr.-Ing. Klaus Dietmayer

Ulm, 27.07.2012

Heiko Paul

The Thermal Instability of Nanocrystalline Materials

— An Experimental Case Study of Microstructural Evolution in Ball-Milled Iron

Meinen Eltern

„Wer immer tut, was er schon kann,
bleibt immer das, was er schon ist.“

Henry Ford (1863 – 1947)

Abstract

Manifesting superior properties compared to their coarser-grained conventional counterparts, nanocrystalline materials are attracting growing attention in the areas of basic research and industrial application. However, the advantages of these materials — which relate to their exceptionally high number density of grain boundaries — come at the cost of an inherent instability with respect to grain growth. In order to develop strategies for retaining grain-size-related property enhancements, the nature and mechanisms of grain growth occurring in nanocrystalline materials must be understood thoroughly. This thesis represents an effort to carry out a comprehensive experimental investigation of thermally induced microstructural evolution in nanocrystalline α-Fe prepared by mechanical attrition.

Recent theoretical and experimental studies suggest that, below a certain characteristic grain size in the submicrometer range, the rate-controlling mechanism for boundary migration is expected to change, when the lower mobility of microstructural elements that are defined by the intersection of grain boundaries (i.e. triple lines or quadruple points) may become the critical parameter determining the kinetics of coarsening. Although previous investigations of this issue have indeed found evidence for deviations from the ideal parabolic kinetics of boundary-curvature-controlled growth at small grain sizes, no conclusive evidence has been presented so far that these observations are characteristic for the nanocrystalline state itself — i.e. that parabolic growth of the average grain size is a phenomenon that is restricted to grain sizes above a certain threshold. Nevertheless, since the presumably slower migration of triple lines could exert a powerfully stabilizing influence on nanometer-sized grains, it is important to assess the potential impact of this phenomenon on the overall rate of grain growth in nanocrystalline materials.

In view of this issue, the present study was focused on the non-destructive *in-situ* recording of microstructural evolution in nanocrystalline Fe, with the primary objective being the search for a possible transition in the rate-controlling mechanism for grain growth as a function of grain size. Through an analysis of a variety of experimental results, it was concluded that the occurrence of a grain-size-dependent transition could not be confirmed in α-Fe, at least in the investigated range of grain sizes ($D \gtrsim 15$ nm). Nevertheless, both *in-situ* measurements and electron micrographs indicated that the microstructure of α-Fe evolves quite differently in the nanocrystalline state than during the normal grain growth observed in coarse-grained samples of the same material. The experimental findings reported in this thesis demonstrate that the ensemble of nano-scaled grains undergoes a non-uniform evolution, involving the interaction of two grain subpopulations that show significantly different kinetics of boundary migration. Comparison to a numerical model for abnormal grain growth (AGG) revealed that the measured microstructural evolution could be explained quantitatively by a minority population of grains having fast kinetics growing at the expense of a majority population of nearly stagnant matrix grains. Gradual annihilation of the matrix species by the rapidly growing "abnormal" grains leads to the development of a quasi-bimodal grain-size distribution with its centroid shifting gradually to larger grain sizes and the volume fraction of abnormal grains increasing continuously.

A critical assessment of these findings determined that, out of the many possible causes for differences in the grain-boundary kinetics of the various grain subpopulations present in the as-prepared nanocrystalline state, the misorientation-dependent grain-boundary mobility — which is associated with the formation of low-angle grain boundaries by dislocation recovery — is the most likely explanation for the rapid growth of a subset of the starting grains. The fundamental characteristics of such misorientation-induced AGG are reflected in a numerical model proposed by Humphreys, which considers the growth advantage provided by an anisotropic grain-boundary mobility. Application of Humphreys' model to

the nanocrystalline Fe growth data led to the prediction that the measured range of misorientations of the stagnant matrix grains would entail only a moderate increase in the size of the abnormal grains relative to their matrix neighbors, which nicely accounts for the "weak" broadening and narrowing observed for the polycrystalline grain-size distribution; moreover, the moderate nature of the growth advantage of the abnormal grains facilitates a transient occurrence of AGG, rather than the more typical "secondary recrystallization" of the initial microstructure, which proceeds through an intermediate state of very large abnormal grains surrounded by much smaller matrix grains. A further consequence of the moderate nature of AGG in nanocrystalline Fe is the restriction that the misorientation distributions of the two grain subpopulations might be quite similar, rather than clearly distinct; this, in turn, explains why transient AGG was able to emerge from a single texture component of sufficient angular width. The excellent agreement of this model with experimental observations revealed further that only abnormal grains of a certain above-average size are candidates for abnormal *growth*, whereas smaller-than-average grains in the abnormal subpopulation would actually be expected to *shrink* at a rapid rate; this phenomenon appears to be responsible for the noticeable jump in average grain size that was always observed during the earliest stage of isothermal annealing of nanocrystalline Fe. Additional calorimetric measurements provided evidence for the occurrence of dislocation recovery in α-Fe, thus ruling out conventional recrystallization as a cause of the anomalous microstructural evolution.

Zusammenfassung

Die Möglichkeiten neuer und ausgezeichneter materialspezifischer Eigenschaften, welche in unmittelbarem Zusammenhang mit einer außergewöhnlich hohen Korngrenzendichte stehen, begründen das nachhaltige wissenschaftliche und anwendungsorientierte Interesse an nanokristallinen Werkstoffen. Jedoch liegt nicht nur die Ursache für die Veränderung der Materialeigenschaften in der nano-Strukturierung des Werkstoffes, so führt die enorme Korngrenzendichte in gleichem Maße zu einem signifikanten Anstieg der freien Energie, und somit zu einer verstärkten thermodynamischen Instabilität der Mikrostruktur. Aus diesem Grunde ist es nicht ungewöhnlich, dass insbesondere in nanostrukturierten Materialien eine substantielle und inhärente Tendenz zur Relaxation der exzessiven freien Energie durch Kornwachstum besteht, und somit der potenzielle Verlust ausgezeichneter und korngrößenabhängiger Eigenschaften ein systematisches Problem darstellt. Vor diesem Hintergrund ist es deshalb zwingend notwendig, die Mechanismen, welche den Prozess des nanokristallinen Kornwachstums kontrollieren, experimentell zu untersuchen und im Detail zu verstehen, um darauf aufbauend geeignete Maßnahmen zur Stabilisierung der Nanostruktur entwickeln zu können. In einer experimentellen Fallstudie am Beispiel von nanokristallinem α-Fe untersucht die vorliegende Arbeit die Mechanismen des temperaturabhängigen Kornwachstum und diskutiert die Ergebnisse im Kontext aktueller Modelle.

Im Gegensatz zu konventionellen polykristallinen Materialien, in denen typischerweise die Diffusionsgeschwindigkeit der Korngrenze selbst die bestimmende Größe für die Kornwachstumskinetik darstellt, zeigen neuere theoretische und experimentelle Arbeiten die Möglichkeit, dass bei unterschreiten einer kritischen Korngröße der ratenbegrenzende Prozess wechselt, und fortan die Migration von null- oder eindimensionalen topologischen Strukturen (die durch das Zusammentreffen von drei oder mehr Korngrenzen definiert werden — auch als Tripellinien (TL) und Quadrupelpunkte (QP) bezeichnet) die Bewegungskinetik der Korngrenzen bestimmt. Obwohl frühere experimentelle Untersuchungen tatsächlich eine Abweichung nanokristallinen Kornwachstums vom parabolischen Wachstumsverhalten konventioneller Materialien festgestellt haben, so gibt es bislang keine zuverlässige Erkenntnis über den systematischen Einfluß solcher topologiebedingter Strukturen. Da aufgrund ihrer vermeintlich geringeren Mobilität diese Mechamismen aber zu einer natürlichen Stabilisierung von nanostrukturieten Werkstoffen beitragen können, war ihr Einfluß auf die Migrationskinetik von Korngrenzen eine der zentralen Fragestellungen in der vorliegenden Untersuchung.

Zur Bewertung eines möglichen Einflusses von TL oder QP wurde die Wachstumskinetik von nanokristallinem α-Fe bei niedrigen Anlasstemperaturen in isothermen Experimenten mittels zerstörungsfreier Röntgenbeugung untersucht. Aus den experimentellen Resultaten konnte geschlossen werden, dass sich im untersuchten Korngrößenbereich ($D \gtrsim 15$ nm) ein derartiger Wechsel des ratenbegrenzenden Prozesses mit Unterschreiten einer kritischen Korngröße nicht bestätigen lässt. Da das beobachtete Wachstumsverhalten der Proben, welches sich insbesonders durch eine instationäre, nicht selbstähnliche Korngrößenverteilung (KGV) und eine vermeintliche zeitweise Zunahme der Kinetik auszeichnet, sich jedoch signifikant von Ergebnissen grobkristalliner Proben unterscheidet (d.h. einer selbstähnlichen Entwicklung der KGV und einer monoton abnehmende Wachstumskinetik), wurde die Möglichkeit anormalen Kornwachstums (AKW) eingehend untersucht. Im Rahmen der Diskussion wurde zur quantitativen Untersuchung von AKW ein numerisches Modell entwickelt, welches die inhomogene Entwicklung einer binären Mikrostruktur betrachtet. Basierend auf der Annahme, dass die Gesamtheit der Mikrostruktur durch Körner zweier Populationen definiert wird (einer geringeren Anzahl spezieller Körner hoher Korngrenzenkinetik, die sich in einer Umgebung gehemmter Matrixkörnern befinden) konnte gezeigt werden, dass die beobachteten Eigenschaften des Kornwachs-

tums in nanokristallinem Fe — insbesondere die Entstehung einer „quasi-bimodalen“ KGV und eine zwischenzeitliche Zunahme der gemessenen Kinetik, hervorgerufen durch eine kontinuierliche Verschiebung des Schwerpunktes der integralen KGV — durch AKW erklärt werden können, und die inhomogene Entwicklung der Mikrostruktur durch die deutlich unterschiedliche Kinetik der beiden Spezies verursacht wird.

Die Bewertung möglicher Mechanismen, welche zu einer derartigen Anisotropie der Korngrenzeneigenschaften führen können verdeutlichte, dass lediglich die Abhängigkeit der Korngrenzenmobilität von der tatsächlichen Fehlorientierung von Kleinwinkelkorngrenzen (hervorgegangen aus der Relaxation von Kristallversetzungen infolge mechanischer Deformation während der Probenpräparation) eine plausible Erklärung für AKW liefert. Bestätigt wurde diese Betrachtung durch ein quantitatives Modell für AKW, welches für die vorliegende Fehlorientierung der gehemmten Matrixkörner nur eine mäßige Vergrößerung der anormalen Körner, und somit eine moderate Verbreiterung der KGV durch eine transiente anormale Entwicklung der Mikrostruktur, ergab. Die Untersuchung des Modells zeigte, dass unter den gegebenen Bedingungen Matrixkörner und anormale Körner prinzipiell einer Texturkomponente entstammen können, und somit ähnliche Korngrenzeneigenschaften erwarten lassen. Das Modell verdeutlichte weiter, dass das Ergebnis anormaler Korngrenzenkinetik sehr wohl auf dem Bestehen einer Verteilung von Fehlorientierungen basiert, in gleicher Weise jedoch auch die relative Größe eines spezifischen Korns im Vergleich zu seiner Umgebung wesentlich für die Entwicklung anormalen Wachstums in positiver oder negativer Richtung ist. Dies bedeutet, dass Körner mit bevorzugter Mobilität sowohl mit hoher Kinetik wachsen als auch schrumpfen können, und sich somit aus zeitlicher Sicht zwei aufeinander folgende Bereiche anormalen Wachstums definieren, jeweils geprägt durch die Spezies rasch schrumpfender bzw. rasch wachsender spezifischer Körner.

Contents

Abstract III

Zusammenfassung V

1 Introduction 1
- 1.1 The Current State of Knowledge: A Concise Review . . . 3
- 1.2 Open Questions . . . 7
- 1.3 Outline . . . 7

2 Grain Growth in Polycrystalline Structures 9
- 2.1 Grain-Boundary Energy: The Thermodynamic Driving Force . . . 9
- 2.2 The Energy and Mobility of Grain Boundaries . . . 12
- 2.3 Curvature-Driven Boundary Migration . . . 18
- 2.4 Grain Growth in the Mean-Field Approach . . . 20
  - 2.4.1 The Classical Mean-Field Model . . . 21
  - 2.4.2 Size-Correlation Effects of the Topology . . . 24
- 2.5 Impact of Structural Entities on Grain-Growth Kinetics . . . 27
  - 2.5.1 The Kinetics of Triple Lines and Quadruple Points . . . 27
  - 2.5.2 The Grain-Boundary Excess Volume . . . 33
- 2.6 The Role of Impurities in Grain-Boundary Migration . . . 35

3 Experimental Characterization of Grain Growth 41
- 3.1 X-Ray Diffraction . . . 41
  - 3.1.1 Experimental Setup for XRD . . . 41
  - 3.1.2 Quantitative Analysis of X-Ray-Diffraction Experiments . . . 43
  - 3.1.3 Statistical Aspects of X-ray Diffraction: The Grain-Size Distribution and the Average Grain Size of Polycrystals . . . 50
  - 3.1.4 Peak Broadening due to real Microstructures: Size and Strain Broadening . . . 56
  - 3.1.5 Instrumental Peak Broadening and Peak Correction . . . 65
- 3.2 Calorimetric Analysis . . . 71
  - 3.2.1 Differential Scanning Calorimetry . . . 72
  - 3.2.2 Analysis of DSC Experiments . . . 73
  - 3.2.3 Experimental Procedure of DSC Experiments . . . 80
- 3.3 Electron Microscopy . . . 81
  - 3.3.1 Transmission Electron Microscopy . . . 81
  - 3.3.2 Orientation Imaging Microscopy . . . 84

4 Experimental Investigation of Grain-Growth Kinetics 87
4.1 Synthesis of Nanocrystalline Iron . . . 87
4.1.1 Overview . . . 87
4.1.2 Sample Preparation: Experimental Procedure . . . 89
4.1.3 Post-Preparational Treatment of Nanocrystalline Fe . . . 92
4.2 Isothermal Annealing: *In-situ* XRD . . . 94
4.2.1 Measuring the True Temperature . . . 97
4.2.2 Thermally-Induced Grain Growth . . . 99
4.2.3 Evolution of the Grain-Size Distribution . . . 107
4.2.4 Relaxation of Microstrain . . . 110
4.3 Calorimetric Analyses on Nanocrystalline Fe . . . 113
4.4 Electron Micrographs and Orientation Imaging . . . 119
4.4.1 TEM Imaging . . . 119
4.4.2 Orientation Imaging . . . 122

5 Discussion and Conclusions 129
5.1 Review of Experimental Results . . . 129
5.2 Evaluation of the Experimental Results in the Context of Grain-Growth Theory . . . 130
5.3 A Phenomenological Model for Abnormal Grain Growth . . . 133
5.4 Analysis of the Root Cause for Abnormal Grain Growth in Nanocrystalline α-Fe . . . 142
5.4.1 Assessment of the Potential Candidates for Anisotropic Boundary Properties . . . 143
5.4.2 Processes Related to the Refinement of the Microstructure . . . 144
5.5 Abnormal Grain Growth Induced by Grain-Boundary Misorientation . . . 150

6 Summary & Prospective Questions 159
6.1 Resumé . . . 167
6.2 Outlook — Prospective Questions . . . 168

Bibliography 171

Curriculum Vitae 181

List of Publications 182

Chapter 1

Introduction

Depending on the requirements and the aspired performance of a specific application or technological solution, the involved materials are selected according to their physical and chemical properties. Those properties are usually determined by the actual short-range interaction of the atoms building-up the material, and therefore dependent on the atomic density and the coordination of the nearest-neighbor atoms [1]. For conventional crystalline materials it is therefore consequent that the periodic arrangement of atoms on defined lattice positions and the interaction of valence electrons will define the optical, mechanical, chemical and other properties of the material. The properties of a material with the same chemical composition may change however, if by appropriate treatment the crystallization is suppressed during fabrication, and the material remains in an amorphous (disordered) atomic structure. A widely known example for such amorphous materials are bulk metallic glasses (BMG), which entered the stage of broad interest only in the last two or three decades. It is usually observed that the properties of metallic glasses significantly deviate from their crystalline counterparts, reflecting for example in a higher hardness and yield limit, or an improved corrosion resistance. Comparing the amorphous and crystalline state of a material it is obvious, that the physical and chemical properties are strongly influenced by the actual atomic configuration, and the two states of ordering — crystalline and amorphous — are defining the limits of material behavior. In between of those two extremes the nanocrystalline state of a material defines an intermediate "hybrid phase", combining the structural characteristics and the material behavior of both limit cases — depending on the actual size of the aggregated crystallites in the nano-structured material.

H. Gleiter suggested that nanocrystalline materials are a composite of a crystalline phase (grains) and a disordered phase (grain boundaries), the latter separating the individual grains of different orientation and compensating the orientation mismatch between them [1,2]. As the number density of grain boundaries scales inversely proportional with grain size, it is obvious that the number of grain boundaries per unit volume will continuously increase as the grain size reduces. Gleiter estimated that for grains of $5 \ldots 10$ nm in size about 50% of the atoms belong to the grain boundaries, i.e. there are as many atoms in the disordered state of the grain boundaries as there are atoms inside the crystalline volume of the grains. Compared to that, polycrystalline materials with grains in the micron range have a fraction of interface atoms that is basically negligible. Thus, if the grain size in a polycrystalline material enters the regime of nano-scaled crystallinity, the influence of grain boundaries on the microstructure increases and both the microscopic and the macroscopic features of a material will no longer be defined by the crystalline state only. As a rule of thumb it is usually quoted that the alteration of physical or chemical

properties in nanocrystalline materials becomes substantial at grain sizes $D \lesssim 100$ nm. Comparing the characteristics of nanocrystalline and coarse-grained materials, it is found that the influence of grain boundaries in nanocrystalline materials can modify material properties in a favorable way to open up new fields of application for conventional materials, or may even provide the kick-off to approach solutions of currently open problems. Some examples for new or enhanced material properties that are related to the nano-structuring of crystalline materials are [1, 3, 4]:

- ◇ Higher diffusion rates along the grain boundaries, which can be used for example to improve the loading and unloading kinetics for hydrogen storage in metal hydrides, or creating membranes with higher permeability.
- ◇ Increased strength and hardness according to the empirical Hall-Petch relationship.
- ◇ Higher ductility of brittle materials and superplasticity of metals and alloys due to grain gliding.
- ◇ Lowering of the Curie temperature or super-paramagnetic behavior of ferromagnetic materials, which might be used in data-storage devices or magnets with reduced magnetic losses.
- ◇ Enhanced activity of catalytic materials.

This short overview, which addresses of course only a few of the possible grain-size-dependent properties in nanocrystalline materials, explains the increasing industrial and scientific interest in this new class of materials. However, in spite of all their advantages and superior features, nanocrystalline materials are fraught with the problem that they represent a highly non-equilibrium and therefore unstable state of the material, since the reason for the improved properties is also their major handicap: the high number density of grain boundaries. As will be discussed in Chapter 2, the excess energy, which is associated to the area of grain boundaries per unit volume in a nanocrystalline material, induces a sustaining driving force for the material to undergo a gradual coarsening of the microstructure. Of course, if such a coarsening leads to a notable increase of the grain size (equal to a decrease of the number density of grain boundaries), the dedicated physical and chemical properties of the nano-scaled microstructure will be irretrievably lost. Thus, it is not only of interest to investigate the potential applications of nanocrystalline materials, but it is equally important to understand the underlying coarsening processes and find strategies to prevent the loss of the nanocrystalline features caused by microstructural coarsening via "grain growth". The inherent instability of nano-structured materials, which has been for their coarse-grained counterparts in the focus of materials science for many decades, is the motivation for the present thesis, as the success of unraveling the microstructural stability and grain-growth characteristics of nanocrystalline materials is up to now only of very limited advance. A review of the experimental efforts to investigate nanocrystalline grain growth is given in Ref. [5].

Although it seems quite likely that the grain-growth properties of a particular material will depend on a number of parameters, like for example the actual chemical composition, contamination and other material-specific parameters, it is reasonable for fundamental research to study nanocrystalline grain growth on simple model systems, since this reduces the number of free parameters considerably, and therefore may allow to attribute experimental observations to particular properties of the grain assembly. The experimental analyses of this study should therefore concentrate on the structural instability of single-phase microstructures in the nano-scaled regime.

1.1 The Current State of Knowledge: A Concise Review

Beginning with Burke and Turnbull, who proposed more then 50 years ago empirically a parabolic time dependence of the average grain size [6], the models for structural coarsening of polycrystalline materials became more and more sophisticated over time, and included also aspects of grain growth, which have not been considered by Burke and Turnbull — for example, the fact that the coarsening process must be compatible to a physically reasonable evolution of the grain-size and grain-topology distribution, or the required conservation of mass. Especially Hillert's idea of considering a common "mean-field" environment for all grains of a polycrystal, which defines together with the grain-boundary curvature the growth kinetics of a particular grain, was an important milestone on the way to a realistic grain-growth theory. Nevertheless, it is the common feature of basically all curvature-based models that were developed after Burke and Turnbull to predict the same parabolic coarsening of the average grain size, as it was already found more than 50 years ago [5],

$$\langle D\rangle^m(t) - \langle D\rangle^m(t_0) = k\cdot(t-t_0)\,, \tag{1.1}$$

with k and m being a temperature-sensitive rate constant and the growth exponent, respectively (for parabolic growth, the exponent m will be equal to 2). With the attempt to find a representative and physically reasonable theory for grain growth it became clear that the coarsening of a microstructure may occur in two quite different ways, either if the grain-size distribution follows a self-scaling evolution (which was found to require that the coarsening kinetics of all grains is determined by an unique grain-size-scaled growth law that is defined by the grain-boundary curvature, and yielding a growth characteristic with $m = 2$), or the grain-size distribution evolves in an unpredictable way; while the first case is known as *normal* grain growth, the latter one is usually denoted as *abnormal* grain growth [7]. The case of normal grain growth is particularly interesting, since it allows to predict the state of the microstructure at any point in time (determined by a power law like Eq. (1.1) — ideally with $m = 2$ — and the self-scaling evolution of the grain assembly).

A preeminent example for normal grain growth are the isothermal annealing experiments by H. Hu conducted on coarse-grained iron [8, 9]. Fig. 1.1 shows three isothermal annealing series at 700°C, 750°C and 800°C of Hu's experiments, all revealing a power-law growth characteristic equal to Eq. (1.1). However, different to ideal curvature-driven coarsening the growth exponent of the plotted temperatures seems to be larger than $m = 2$ (only at temperatures higher than ~60% of the melting point Hu found exponents close to 2). Although Hu treated the investigated samples prior to the anneal in a zone-melting process, the obviously large grain size and the therewith connected small curvature-induced driving force may allow that even low residual impurity concentration cause a measurable degradation of the grain-boundary kinetics (usually known as solute drag), and thus a degradation of the growth rate with $m > 2$. Additionally, Fig. 1.1 presents for the 800°C anneal the rescaled grain-size distribution after 2.5, 5 and 12 min. The concurrence of the three curves evinces that the samples investigated by Hu undergo a self-scaling coarsening (with a size distribution similar to a lognormal function), which indicates together with the power-law growth of the mean grain size that homogeneous grain growth and a size-scaled growth kinetics apparently hold in Hu's experiments on coarse-grained iron.

One of the major drawbacks of the established grain growth theories on normal grain growth is the

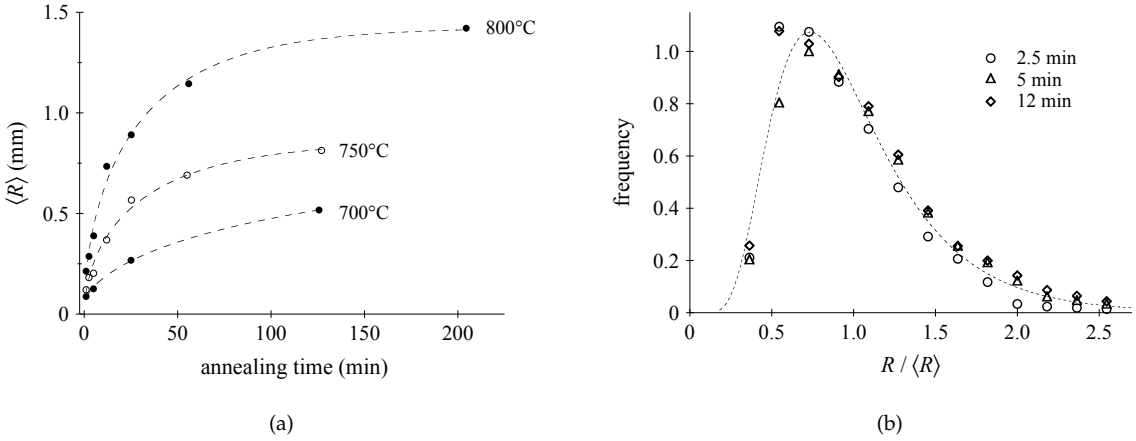

Figure 1.1: (a) Experimental results of isothermal grain growth at 700, 750 and 800°C in coarse-grained polycrystalline Fe, taken from Ref. [8]. The results indicate that the microstructure evolves in a power-law characteristic, as given by Eq. (1.1). The Arrhenius analysis of the isothermal curves yielded an activation enthalpy of 249 kJ/mol for the rate-limiting step, which is apparently close to lattice self-diffuison in Fe (rather than grain-boundary diffusion, as normally expected to be the rate-controlling step) [8, 9]. (b) Plot of the grain-size frequency as a function of the normalized grain size $R/\langle R\rangle$. The three data sets relate to an annealing time of 2.5, 5 and 12 min of the 800°C anneal. The concurrence of the the individual data sets indicates a self-similar evolution of the coarse-grained microstructure.

predicted grain-size distribution that was found to be clearly different to basically any experimental observation (as for example the lognormal-like characteristic of Hu's data in Fig. 1.1). It was therefore for a long time under discussion whether the proposed models are a suitable description of microstructural coarsening or not. Only recently it has been demonstrated that a Rayleigh function (which resembles a lognormal shape fairly well) can be a self-similar solution for the grain-size distribution, yielding also an ideally parabolic evolution of the average grain size — however, the Rayleigh function holds only, if the idea of a general mean field is discarded and an appropriate size correlation between a particular grain and his adjoining neighbors is obeyed (see Chapter 2).

Isothermal annealing experiments like the ones in Fig. 1.1 provided evidence that a power law constitutes an adequate description of curvature-driven coarsening kinetics. Of course, this finding was an important result, since now the growth curves could be fitted with a function like Eq. (1.1), which allows to analyze the rate parameter $k(T)$ in an Arrhenius plot (this requires to repeat the same experiment at different isothermal conditions). As will turn out in Chapter 2, the rate parameter is determined by the product of the grain-boundary energy γ^{GB} and the grain-boundary mobility M^{GB}, which are both in principal changing with temperature. However, as the temperture has a much lower effect on γ^{GB} than on M^{GB}, the temperature-sensitivity of $k(T)$ is mainly driven by the grain-boundary mobility and hence, the Arrhenius analysis will provide the activation enthalpy of the rate-controlling microscopic mechanism of grain-boundary migration. It is usually observed that in highly pure coarse-grained materials this activation enthalpy is close to the one for grain-boundary self-diffusion [10] (with respect to this, α-Fe could be an exception because R.A. Vandermeer deduced from Hu's experiments an activation enthalpy

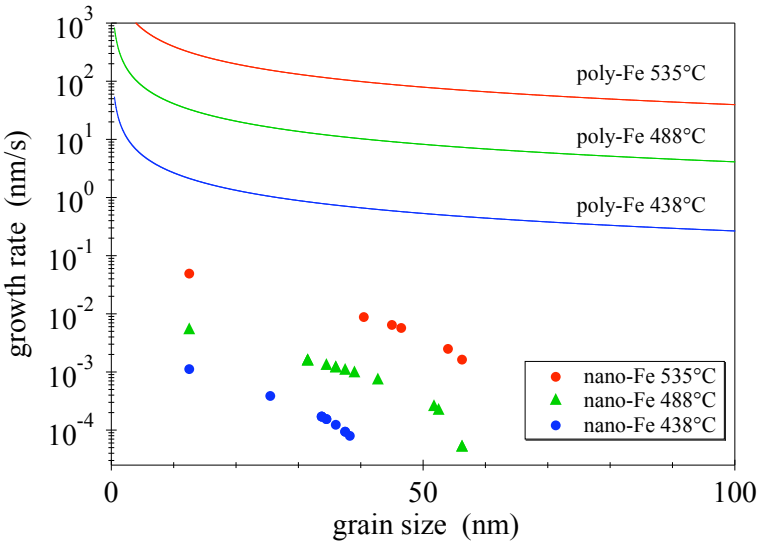

Figure 1.2: Comparison of measured growth rates on nanocrystalline Fe [11] and the growth rates of Hu's polycrystalline data [8], which have been extrapolated to the nano-scaled regime by using Eq. (1.2).

of 249 kJ/mol, which is very similar to the characteristic activation enthalpy of lattice self-diffuison in α-Fe [9]). The analysis of the activation enthalpy is often used to identify the critical process in grain growth, which may deviate from grain-boundary diffusion, if growth-inhibiting obstacles are involved in the samples under investigation, or the grain boundaries migrate by another process than the diffusion of atoms across the interface.

As most of todays models on the curvature-induced coarsening of polycrystalline materials have been developed at a time where nanocrystalline materials were not in the focus of scientific research, the validity of grain-growth theories were tested only on the available experimental annealing data of conventional coarse-grained microstructures in the size regime of microns and above. At a first glance, this circumstance does not appear as a major problem, since the average grain size of nanocrystalline materials is much smaller than conventional polycrystals (which entails a much larger curvature of the grain boundaries in nano-structured materials) and thus, it would be tempting to assume that due to the high driving force for boundary migration the coarsening of the nanocrystalline state should perfectly agree with a curvature-driven grain-growth model. On the other hand however, the very high driving force, and thus the high grain-boundary kinetics of nanocrystalline materials, may involve that other — up to now unknown or not considered — effects come into play, which might take over the position of the rate-controlling step in grain growth. To answer the question whether grain-boundary diffusion is also the key parameter for the growth of nanocrystalline materials, A. Michels and colleagues compared the growth rates of Hu's data with growth rates of nanocrystalline iron samples [11]. By taking the time derivative of Eq. (1.1), the growth rate for parabolic grain growth ($m = 2$) can be expressed by,

$$\frac{\mathrm{d}\langle D\rangle}{\mathrm{d}t} = \frac{k(T)}{2\langle D\rangle}. \tag{1.2}$$

Eq. (1.2) involves that in an isothermal experiment the growth rate is inversely proportional to the grain size, while all other parameters are constant. Thus, a fit of Hu's data with the power law of Eq. (1.1) will yield for each isothermal anneal the rate parameter $k(T)$, which can then be inserted into the rate equation (1.2) and extrapolated to the nano-scaled regime. Fig. 1.2 compares for three isothermal experiments the respective growth rates of poly and nanocrystalline samples. Obviously, despite the higher growth kinetics predicted by Eq. (1.2) for small grain sizes, the growth rate of the nanocrystalline iron is obviously 3...4 orders of magnitude *slower* compared to Hu's polycrystalline data.

The finding of a lower growth kinetics as expected is not unusual and is in the most cases ascribed to impeding obstacles like impurities, second phases or pores. Since those are well known to influence the growth dynamics substantially, Michels *et al.* assessed their likeliness and concluded that basically none of them has the needed impact to restrain the kinetics of the investigated nanocrystalline iron samples in Fig. 1.2 [11]. However, if this means that a lower growth rate is an inherent feature of nanocrystalline materials (and not attributed to inadvertent effects), it should be asked what could cause such a deviation? As the nanocrystalline kinetics is compared with the extrapolation of polycrystalline data, the answer to this question might be found in the assumptions on which Eq. (1.2) is based. The conventional model for curvature-induced grain growth relates the grain-boundary kinetics and the thermodynamic driving force via the mobility of the grain interface, i.e. other constraints than the transport of atoms across the interface are not considered for the migration of a grain boundary. This assumption might be justified for grains of certain size, however it might be an oversimplification, if the grain size reaches a limit, below which additional constraints for boundary migration can no longer be neglected. In such a situation it is in principal possible that those "new" constraints take over the rate-controlling position from simple grain-boundary diffusion, which means that now another microscopic process defines (or at least affects) the overall growth kinetics. Since this new rate-controlling process must be obviously slower than intrinsic grain-boundary migration to be effective, it is consequent that the measured kinetics should also be slower than for a conventional polycrystal. In fact, recent theoretical and experimental work suggests that structural obstacles defined by grain-boundary intersections and the dissolution of grain-boundary excess volume during grain growth may become relevant in coarsening of nano-scaled grains, and could lead below a certain threshold grain size to a change of the rate-controlling process (see Chapter 2).

In the light of this premise, C.E. Krill and colleagues analyzed the isothermal growth kinetics of nanocrystalline iron [12]. It was observed that the evolution of the average grain size is apparently described by an initially constant growth rate (i.e. a growth rate that is independent of the grain size), which turns over into the well-known power law evolution after a specific transition grain size has been reached. For the initial linear stage of growth the related activation enthalpy has been determined as 330 kJ/mol, which is clearly larger than the activation enthalpy of comparable coarse-grained iron (~250 kJ/mol [8,9]), and would support the idea of different rate-controlling mechanisms during the linear stage and the subsequent power-law growth. Although both observations, the apparently linear growth and the higher activation enthalpy, suggest that the early coarsening of the nanocrystalline state does not agree with grain-boundary-diffusion controlled interface migration (and would therefore adequately explain a lower growth rate of the nanocrystalline material in Fig. 1.2), particularly the conclusion of linear growth is a difficult-to-establish interpretation of the experimental data, since the ability to distinguish linear growth from the early stage of a power-law curve is a complicated task for short annealing intervals [12].

In spite of this uncertainty, the review of experimental analyses on the microstructural coarsening of nanocrystalline materials connotes that the evolution of the grain assembly apparently deviates from the experiences made on coarse-grained samples. Although considerable effort has been devoted to approach this topic, the experimental data basis does not yet allow to find a conclusive explanation for the physics controlling the evolution of a nano-structured material. Starting from that, the present experimental study will focus on this open question and will contribute to unveil the coarsening mechanisms of nanocrystalline materials. To compare the results with available literature data of experiments on both the poly and nanocrystalline state, a model system should be selected, which provides a sound basis of reference experiments. For this reason, single-phase nanocrystalline iron was selected as the model system for the present experimental study.

1.2 Open Questions

From both the existing literature data on nanocrystalline grain growth and the recently proposed theoretical models addressing the influence of topological constraints on the migration of grain boundaries in nano-structured materials, the following three "Questions" might be formulated and used as guidelines for this thesis. It will be the challenge of the here presented experimental investigations in combination with a concluding comprehensive discussion of all related aspects, to provide adequate answers to these questions in the summary part at the end of this thesis.

◇ Question 1: Can evidence be found that a process other than grain-boundary diffusion can become rate-controlling in naocrystalline materials, i.e. is there a transition grain size below which the rate-controlling step changes and thus, a slower growth kinetics is introduced?

◇ Question 2: Can nanocrystalline materials fulfill the prerequisites for self-similar normal grain growth, or are they growing irregularly via abnormal grain growth? This means, is grain growth in nano-scaled microstructures predictable?

◇ Question 3: To what extent can the microstructural evolution observed in the model system ball-milled Fe be generalized to other nanocrystalline materials?

1.3 Outline

The following chapter will present an overview over the most relevant models that have been developed on grain growth up to today (Chapter 2). It is also the intention of this Chapter to present the recently proposed mechanism, which are assumed to modify the growth behavior of nano-scaled grains compared to conventional polycrystals. The experimental techniques used in the present study will then

be introduced in Chapter 3, where particularly the evaluation of *in-situ* x-ray diffraction is addressed, as this will be the major investigation tool for the assessment of nanocrystalline growth kinetics. The experimental results of the various analysis techniques and their evaluation are presented in Chapter 4. A comprehensive discussion of the experimental results in relation to existing models and with respect to a new developed model within this study are included in Chapter 5. The thesis concludes with a summary of the key results found from the experimental investigations, and will provide answers to the "working questions" defined before in this introductory chapter.

Chapter 2

Grain Growth in Polycrystalline Structures

2.1 Grain-Boundary Energy: The Thermodynamic Driving Force

In polycrystalline materials, typically a large number of arbitrarily oriented grains (coherent crystalline volumes) are aggregated to establish a space-filling unit, which can be orders of magnitude larger than the size of the individual crystallites. The crystallographic misorientation between adjacent grains causes at the interfaces (grain boundaries) a discontinuity of the periodic arrangement of atoms, as it is found in the crystalline interior of the grains [13]. Obviously, the smaller the grains are, the larger will be the density of grain boundaries per unit volume (A^{GB}/V) and thus, in polycrystalline materials the properties and the behavior are likely to be defined by both the grains and the grain boundaries. A schematic representation of a grain-boundary interface is illustrated in Fig. 2.1, showing the disordered grain boundary and the adjacent misoriented grains.

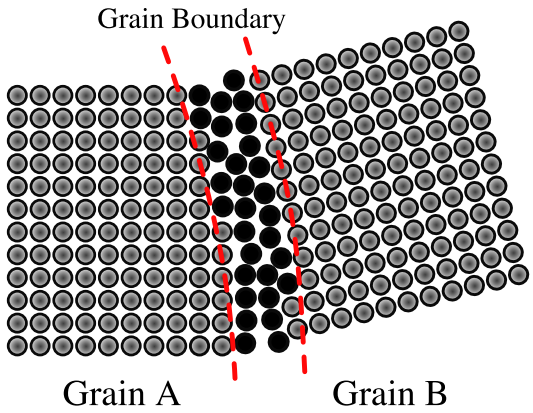

Figure 2.1: Sketch of two grains of a polycrystalline material, which are misaligned by a defined angle. The schematic illustrates the highly organized crystallinity of the grains, and the lower atomic coordination and lower atomic density of the grain boundary that is compensating the mismatch between the two grains.

At the structurally disordered grain boundaries, a lower atomic coordination and unfavorable bonding of valence electrons induces that the potential energy of the boundary atoms is typically higher than the one of atoms incorporated in the bulk crystal. Thus, grain boundaries can become a substantial quantity in the thermodynamic evaluation of the microstructure. If the excess energy of the boundary atoms is express in terms of a specific grain-boundary energy γ^{GB} (energy per unit grain-boundary area), the change of the total free energy in a polycrystalline microstructure can be equated as the summation of the boundary-free bulk term and the specific grain-boundary excess [14],

$$\mathrm{d}G = \left[-S \cdot \mathrm{d}T + V \cdot \mathrm{d}p + \sum_{i=1}^{n} \mu_i \, \mathrm{d}N_i\right]^{\mathrm{bulk}} + \left[\gamma^{\mathrm{GB}} \cdot \mathrm{d}A^{\mathrm{GB}}\right]^{\mathrm{excess}}, \tag{2.1}$$

with the intensive thermodynamic variables T, p and μ_i, i.e the absolute temperature, pressure and the chemical potential respectively, and the extensive variables V, S, N_i and A^{GB}, which are the volume, the entropy, the mole fraction of species i and the grain-boundary area. For a closed system that is also restrictive to the exchange of energy with the environment, i.e. $\mathrm{d}N = 0$, $\mathrm{d}T = 0$ and $\mathrm{d}p = 0$, the change in free energy is solely dependent on the variation of the grain-boundary area. Thus, the specific grain-boundary energy can be defined as [14],

$$\gamma^{\mathrm{GB}} \equiv \left.\frac{\partial G}{\partial A^{\mathrm{GB}}}\right|_{N,T,p=\mathrm{const.}} \geqslant 0. \tag{2.2}$$

Obviously, Eq. (2.2) yields that for a polycrystalline material the system's free energy will be increased compared to the boundary-free state, if $A^{\mathrm{GB}} > 0$. However, the thermodynamic stability of any system is determined by the lowest energy configuration possible, which compels the system to move along the free-energy gradient to a state of minimum configuration energy. For the case of polycrystalline materials this imposes that the excess term in Eq. (2.1) converges to a minimum, i.e. $(\gamma^{\mathrm{GB}} \cdot A^{\mathrm{GB}}) \to 0$. Since γ^{GB} is an inherent feature of the grain boundary, only $A^{\mathrm{GB}} \to 0$ can provide a way to approach a more stabel configuration.

Fig. 2.2 illustrates schematically an infinitesimal segment of a grain boundary (for simplicity the boundary segment is curved only in one dimension). Starting from a flat segment (this is indiacted in Fig. 2.2 by the dashed lines), the energy of the segment increases due to a larger surface A^{GB}, if it is virtually bended to a certain curvature. Since the increase of the energy requires the application of mechanical work equal to $\gamma^{\mathrm{GB}} \cdot \Delta A^{\mathrm{GB}}$, it is evident that γ^{GB} is related to the resistance of the interface to increase its surface area — or in other words, the surface tension γ^{GB} tries to shrink the respective grain-boundary area, since this will reduce the grain-boundary energy. Correspondingly, along the edges of an infinitesimal grain-boundary segment of length l (see Fig. 2.2), there will be a force $F = \gamma^{\mathrm{GB}} \cdot l$ acting on the edges of the segment that points to the center of the boundary. However, the atoms of a solid body are not free to move arbitrarily and thus, there should be a opposite force F_i that balances the interface tension. Considering the summation of all forces $\mathbf{F}_i$ that are acting on the edges of a spherical segment, the net force $\mathbf{F}_{\mathrm{res}} = \sum \mathbf{F}_i$ is directed from the curved boundary plane to the center of curvature.

Since $\mathbf{F}_{\mathrm{res}}$ is the direct consequence of the interface tension, it is evident that this force should be distributed

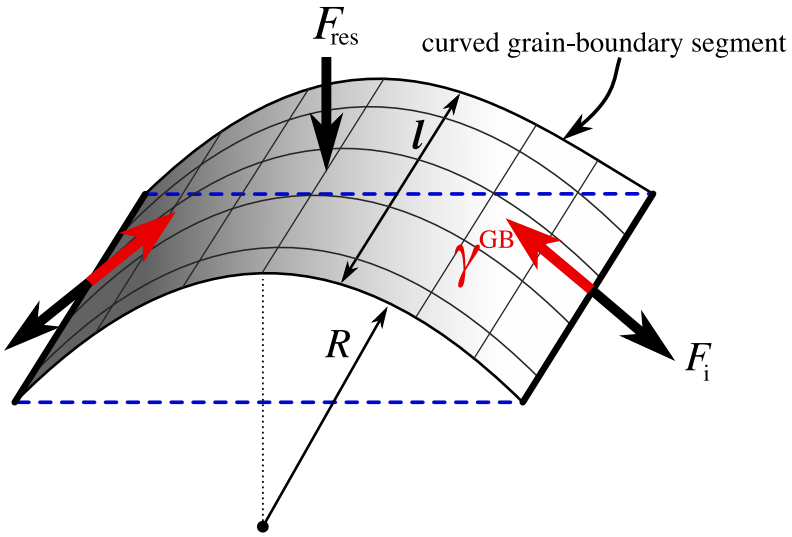

Figure 2.2: Curvature-induced pressure $p_{eff} = |\mathbf{F}_{res}|/A^{GB}$ on an infinitesimal grain-boundary segment, caused by the specific grain-boundary-excess energy γ^{GB}. For the sake of a simplified illustration, the grain-boundary segment of radius R is only curved in one dimension (the radius of the orthogonal direction is $R \to \infty$).

over the complete boundary area. It is therefore reasonable to consider an effective pressure p_{eff} that is acting on the curved boundary segment, rather than a singular force,

$$p_{eff} = \frac{|\mathbf{F}_{res}|}{A^{GB}}. \tag{2.3}$$

From Fig. 2.2 it is conceivable that there will be a pressure on the boundary only, if the curvature $\mathscr{K}$ of the segment is different from zero, i.e. if the grain boundary is not flat.[1] For flat boundary segments with $\mathscr{K} = 0$, the surface tension cancels out and the effective pressure will be zero.

The natural response of a grain boundary to an effective pressure, which intends to minimize the associated free energy, would be the migration of the curved boundary plane towards the center of curvature. Obviously, such a migration process correlates to the transportation of atoms across the interface in the opposite direction of boundary migration. Of course, boundary atoms will only move across the boundary, if the configurational energy for a particular atom is reduced thereby. This constraint is illustrated in the energy diagram in Fig. 2.3, which shows the energy states across the grain boundary (the labels "Grain A" and "Grain B" are according to Fig. 2.1).

It can be seen that the configurational energy of an atom is lower on the concave side of the boundary ("Grain B"), and higher on the convex side ("Grain A"). The difference in energy of both sides is given by ΔG, by which amount the total enthalpy of the polycrystalline system is reduced, if one atom is moved

[1] The curvature of a one-dimensional line can be defined as $\mathscr{K} = 1/R$, where R is the radius of the osculating circle to the line in a specific point. Analogously for two-dimensional planes, the curvatures along the main directions are determined by the principal radii $1/R_1$ and $1/R_2$, with a mean curvature $\mathscr{K} = 1/R_1 + 1/R_2$.

from Grain A to Grain B. Thus, if the grain boundary migrates over a distance dR towards the center of curvature, the total free energy of the system is reduced by,

$$\mathrm{d}G = -\Delta G \cdot \rho \cdot A^{\mathrm{GB}} \cdot \mathrm{d}R, \tag{2.4}$$

where ρ denotes the density of atoms at the interface.

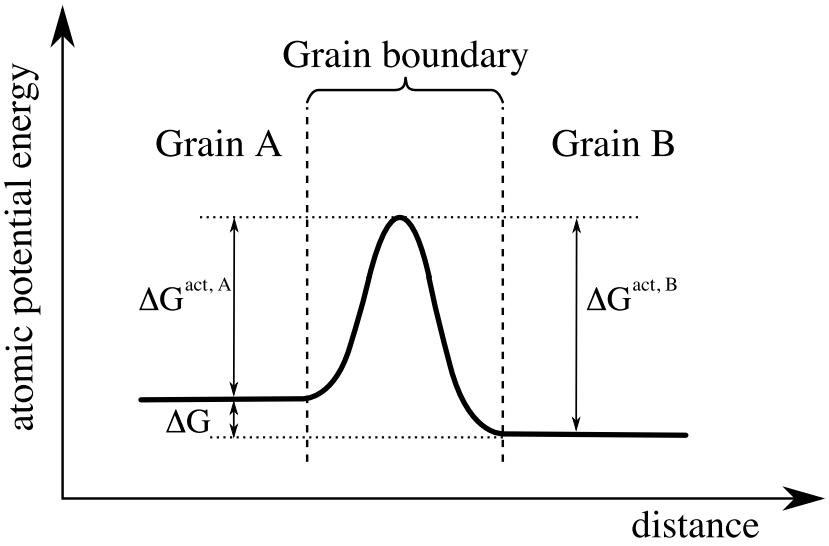

Figure 2.3: The diagram illustrates schematically the energy state of an atom in the crystalline areas of grain A and B, and shows the energy barrier that the atoms need to overcome in order to move across the interface during grain-boundary migration.

Hence, with the driving force for boundary migration, $F_{\mathrm{res}} = \mathrm{d}G/\mathrm{d}R$, the effective pressure can be equated as [14],

$$p_{\mathrm{eff}} = \frac{F_{\mathrm{res}}}{A^{\mathrm{GB}}} = \frac{1}{A^{\mathrm{GB}}}\frac{\mathrm{d}G}{\mathrm{d}R} = \Delta G \cdot \rho. \tag{2.5}$$

The above considerations show that the grain-boundary energy is the root cause for the inherent instability of polycrystalline structures. Particularly for very small grain sizes the number density of grain boundaries can reach a considerable level, which evokes a severe deviation from a thermodynamically stable configuration.

2.2 The Energy and Mobility of Grain Boundaries

Compared to a single crystal, which has naturally only one interface (the surface of the crystal body), polycrystalline materials are aggregates of individual crystallites (grains) that can be in principal of random orientation. Of course, similar to a single crystal, the polycrystalline material will also have an

outer surface to the external environment, but more important, the material will have internal interfaces between adjoining grains of different orientation. The misorientation of two adjoining grains at a grain boundary is determined by six degrees of freedom (DoF) that define the relative orientation of the two grains: three DoF for tilt and twist rotations, and three DoF for rigid body translations. It is conjecturable (and will be addressed below) that the grain boundaries will only have the same properties, if the misorientation — and therefore the grain-boundary structure — is the same. In addition to the misorientation of the grains, the orientation of the boundary plane (having two DoF) with respect to the crystallographic orientation of the grains will also have impact on the atomic structure of the boundary.[2]

Although inherent grain-boundary features like the excess energy γ^{GB} or, as will be shown shortly, the macroscopic mobility M^{GB} of a grain boundary are important parameters for both the actual instability of a microstructure and the modeling of grain growth, the extent of quantitative data reaching beyond fundamental concepts is surprisingly small [14,15]. The following paragraphs review the current understanding of grain-boundary characteristics that can be used for a quantitative assessment of the grain-boundary energy and mobility.

Depending on the degree of misorientation, grain boundaries are usually divided into two categories, low (LAB) and high-angle boundaries (HAB). The designation "low-angle" and "high-angle" refers to the misorientation angle Θ in terms of tilt or twist rotation, where LAB have a smaller misalignment than HAB. The transition between the two regimes is usually found to be arround $\Theta_0 \approx 15^\circ \ldots 20^\circ$ [13,15,16]. The reason for this classification of boundary types is given by the conception of grain boundaries. In a simple model, LAB are considered as an array of dislocations, which are compensating the mismatch between the grains. For those boundaries, γ^{GB} is determined by the energy of the involved dislocations, and a functional correlation between γ^{GB} and Θ can be established ($\Theta < \Theta_0$). However, in case of HAB the mismatch cannot be overcome by organized dislocations, and the structure of the boundary will be in general more complex. While at the beginning of grain-boundary investigations HAB have been assumed to have no distinct ordering, this means that the atoms in the boundary would be amorphously distributed, more recent investigations suggest that the structure of HAB consists of small atomic clusters with distinct short-range ordering [15]. A special case of high-anlge boundaries are misorientations at which the individual lattices of the adjoining grains have common lattice sites in the boundary (coincident site lattice, CSL), which define an ordered boundary structure and cause, compared to random HAB misorientation, a significantly lower excess energy and higher mobility [17]. The lower γ^{GB} of CSL orientations can be observed in Fig. 2.4 as "cusps" in the HAB regime. For random HAB, the energy is usually assumed to be approximately constant ($\Theta > \Theta_0$) [15].

For an ideal tilt boundary, the interface structure is determined by a defined arrangement of dislocations, which are spatially separated in the boundary plane by a distance x (this is basically the simplest possible configuration of a grain boundary and allows for an analytical treatment of $\gamma^{\mathrm{GB}}(\Theta)$). Thus, the misorientation can be expressed as $\Theta \approx |\mathbf{b}|/x$, if $\mathbf{b}$ denotes the Burgers vector of the dislocations [15]. Consequently, for increasing misorientation the dislocation density in the low-angle tilt boundary increases. For this

[2] It is in general difficult to measure the influence of boundary-plane position experimentally. As most orientation analyses are performed on 2-dimensional cross-sections, the boundary plane reduces to a 1-dimensional line, which means that only one DoF can be determined in this way. It is therefore usually not possible to include the question of boundary-plane orientation in the evaluation of experimental data, like the measurement of grain-boundary energy or mobility, and boundary-plane orientation is therefore mostly neglected.

particularly simple configuration the excess energy of the boundary is basically determined by the energy of the dislocations and according to this, Read and Shockley calculated the grain-boundary energy from the strain field of the interface dislocations [16],

$$\gamma^{\mathrm{GB}}_{\mathrm{LAB}}(\Theta) = \gamma_0 \cdot \Theta \cdot (A - \ln \Theta)\,, \tag{2.6}$$

with

$$\gamma_0 = \frac{G_\mathrm{s} \cdot |\mathbf{b}|}{4\pi(1-\nu)} \quad \text{and} \quad A = 1 + \ln\left(|\mathbf{b}|/2\pi r_0\right).$$

Thereby denotes G_s the shear modulus of the material, ν Poisson's ratio and r_0 the radius of the dislocation core. Eq. (2.6) shows that the energy gradually increases for larger misorientations and approaches asymptotically the maximum energy at the transition to the HAB regime. However, for general LAB (apart from the ideal tilt boundary), dislocations with different Burgers vectors may interact and form dislocation networks; the energy of LAB is then dependent on the actual dislocations involved [15].

D. Wolf calculated by computer simulation the grain-boundary energy in bcc Fe for different tilt and twist misorientations [18,19]. Fig. 2.4 presents the results of the computer simulations, which basically show — similar to Eq. (2.6) — a substantial increase of $\gamma^{\mathrm{GB}}(\Theta)$ in the LAB regime and an asymptotic approach to a certain limit. At the transition between LAB and HAB, the energy approaches the maximum value that obviously ranges between 0.7 and 1.6 $\mathrm{J/m^2}$ — especially the lower values of $0.7 \ldots 0.8\ \mathrm{J/m^2}$ are close to experimentally found grain-boundary energies in Fe [10,20]. Even though the absolute values may suffer from uncertainties in the simulation, the general trend clearly evinces that for any existing misorientation distribution in the low-angle regime, the grain-boudary energy γ^{GB} is likely to be anisotropic. Since γ^{GB} is the root cause for the instability of polycrystalline structures, it is likely that an equivalent anisotropy should be characteristic for the grain-boundary migration and thus, for the coarsening kinetics.

If anisotropic boundary conditions are analyzed, it is usually preferred to express $\gamma^{\mathrm{GB}}(\Theta)$ in the low-angle regime in a normalized form of the Read-Shockley equation. The grain-boundary energy of LAB is then given as a relative fraction of the ideally constant high-angle energy γ_{HAB} [15],

$$\frac{\gamma^{\mathrm{GB}}(\Theta)}{\gamma_{\mathrm{HAB}}} = \frac{\Theta}{\Theta_0} \cdot \left(1 - \ln \frac{\Theta}{\Theta_0}\right). \tag{2.7}$$

The advantage of Eq. (2.7) is the freedom to evaluate the effect of anisotropic boundary properties on grain-growth kinetics (by knowing or assuming the misorientation distribution of a microstructure), even without knowing the exact values of $\gamma^{\mathrm{GB}}(\Theta)$.

To initiate grain-boundary migration, the thermodynamic driving force is definitely an indispensable prerequisite, but it is not sufficient. It is also required that the interface can move in response to a curvature-induced pressure, which means that the grain boundary needs a macroscopic mobility. Of course, such a mobility depends on the microscopic ability of the interface atoms to diffuse across the grain boundary, i.e. the mobility depends on the ease of atoms to brake away from their parent grain, travel through the boundary, and finally join the more favorable neighbored grain. Although the mobility of grain boundaries is a key parameter in grain growth, the underlying mechanisms (in terms of accessory

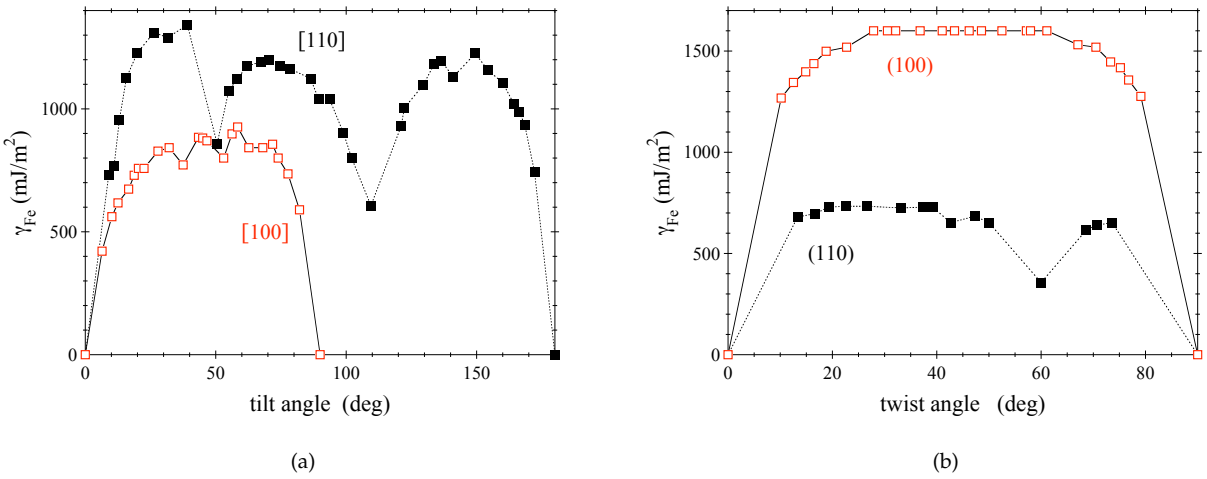

Figure 2.4: Numerical calculation of the grain-boundary energy γ_{GB} in bcc Fe for different grain misorientations of tilt (a) and twist (b) type. As the actual atomic structure of the interface, and therefore also the grain-boundary energy, depends also on the inclination of the boundary plane with respect to the crystallographic orientation of the lattices, the plots show the change of γ_{GB} for different alignments of the boundary plane, referenced to the cubic crystal structure. The data for both the tilt and twist dependence is taken from Refs. [18, 19].

rate-controlling processes) and their interaction are sometimes not fully understood. In spite of that, the concepts of intrinsic grain-boundary migration are mostly confirmed, and the apparent impact of grain-boundary structure can be assessed for LAB and HAB separately.

In the case of LAB, the grain boundary moves by the migration of the dislocation array, which defines the low-angle interface. This means, the involved processes for the migration of the grain boundary will be on the one hand the gliding of dislocations on slip planes and dislocation climb on the other, where in the latter case the rate-controlling process will be the diffusion of vacancies towards the edge of the climbing dislocations [17, 21]. Different to the cross-slip of dislocations, which is merely a switching of atomic bonding between neighboring lattice planes (something that is obviously not related to a process of large thermal activation), the diffusion of vacancies in order to allow for dislocation climb requires solid-state self-diffusion between the dislocation edge and the next-nearest vacancy source/sink. Thus, if a LAB contains dislocations, which require climb to move into the direction of grain-boundary migration, the characteristic activation enthalpy is usually found to be similar to the activation enthalpy for lattice self-diffusion [6, 17, 22]. Experimental results show that the interface mobility can increase by orders of magnitude in the low-angle regime, if the misorientation of the grains increases [17, 23, 24] — an ascertained explanation for this substantial increase is however difficult.

A completely different situation can be observed for random HAB, which may have a short-range ordering, but are in principle stochastically organized over a larger scale. The atomic structure at the interface is basically independent of the actual misorientation, and the HAB mobility is therefore in principal constant (i.e. independent of misorientation). The migration of the grain boundary occurs then no longer by the

defined migration of a dislocation array, but proceeds by stochastic jumps of atoms, i.e. the detaching of an atom from one grain and the reattaching to the neighboring grain. With the nomenclature given in the energy diagram of Fig. 2.3, the probability for such a thermally-activated jump event is determined by [6, 13],

$$\nu(T) = \nu_0 \cdot \exp\left\{-\frac{\Delta G^{\mathrm{act}}}{k_{\mathrm{B}} T}\right\}, \tag{2.8}$$

where ΔG^{act} denotes the activation enthalpy for detaching of an atom, and ν_0 and k_{B} are a temperature-independent pre-factor and Boltzmann's constant, respectively. Evidently, atoms will migrate in both direction, i.e. $A \rightleftarrows B$, but owing to the difference in potential energy $\Delta G = \Delta G^{\mathrm{act,\,A}} - \Delta G^{\mathrm{act,\,B}}$, there will be a net flux J_{net} of atoms from the convex to the concave side of the interface, i.e. $A \rightarrow B$. If there are n atoms per unit grain-boundary area, the net flux can be equated to [17],

$$J_{\mathrm{net}} = C \cdot n \cdot \exp\left\{-\frac{\Delta G^{\mathrm{act,A}}}{k_{\mathrm{B}} T}\right\} \cdot \left[1 - \exp\left\{-\frac{\Delta G}{k_{\mathrm{B}} T}\right\}\right], \tag{2.9}$$

where C is a constant. Thus, the grain boundary requires on average the time $t = n/J_{\mathrm{net}}$ to migrate over a distance of one atomic layer (approximately equal to the lattice spacing d_{hkl}). If the energy gradient is small, i.e. $\Delta G \ll k_{\mathrm{B}} T$, Eq. (2.9) can be expanded and the velocity of the boundary becomes [17],

$$v^{\mathrm{GB}} = J_{\mathrm{net}} \frac{d_{\mathrm{hkl}}}{n} \approx v_0 \cdot \frac{\Delta G}{k_{\mathrm{B}} T} \cdot \exp\left\{-\frac{\Delta G^{\mathrm{act,A}}}{k_{\mathrm{B}} T}\right\}. \tag{2.10}$$

If it is assumed that the mobility M^{GB} of a grain boundary does not depend on the driving force p_{eff} for boundary migration, the macroscopic velocity of the grain boundary is given from Eq. (2.5) and (2.10) by [13, 17],

$$v^{\mathrm{GB}} = p_{\mathrm{eff}} \cdot M^{\mathrm{GB}}. \tag{2.11}$$

Comparing Eqs. (2.11), (2.10) and (2.5) yields that the grain-boundary mobilty follows the Nernst-Einstein relation, i.e. $D = M^{\mathrm{GB}} \cdot k_{\mathrm{B}} T$ (note that D is the diffusion coefficient and not the grain size). Thus, the mobility of a high-angle boundary obeys the form [13, 17],

$$M^{\mathrm{GB}}(T) = \frac{M_0}{T} \cdot \exp\left\{-\frac{\Delta H^{\mathrm{act}}}{k_{\mathrm{B}} T}\right\}, \quad \text{with} \quad M_0 = \frac{v_0}{\rho\, k_{\mathrm{B}}} \cdot \exp\left\{\frac{\Delta S^{\mathrm{act}}}{k_{\mathrm{B}}}\right\} \tag{2.12}$$

where the relation for the Gibbs free energy $\Delta G^{\mathrm{act}} = \Delta H^{\mathrm{act}} - T \cdot \Delta S^{\mathrm{act}}$ has been applied, and M_0 represents a temperature-independent pre-factor. The common notation for the activation enthalpy in literature is usually Q^{GB} instead of ΔH^{act}, which should also be used within this study.

For random HAB, the activation enthalpy for migration is determined by the grain-boundary self-diffusion [17], which is for α-Fe $Q_{\mathrm{B}} = 60 \ldots 175$ kJ/mol (the large spread of the activation enthalpy is caused by

the paramagnetic transition at 770°C) [25,26]. Since Eq. (2.11) holds for LAB and HAB, a similar mobility term like Eq. (2.12) can also be applied for LAB migration — however, the rate-limiting process will not be the stochastic jump of atoms, but the climb of dislocations. Accordingly, the activation enthalpy for grain-boundary self-diffusion (HAB) is replaced by lattice self-diffusion (LAB), where in case of α-Fe values $Q_s = 250 \ldots 290$ kJ/mol are cited in literature [26]. For the experimental conditions of this study, the activation enthalpies are expected to be $Q_s \approx 250$ kJ/mol and $Q_B \approx 125 \ldots 175$ kJ/mol (all temperatures of this study are significantly below the Curie temperature of 770°C).[3]

Although the basic concepts for the migration of LAB and HAB are reasonable, an analytical relationship like the Read-Shockley equation for the increase of γ^{GB} in the low-angle regime is missing for the misorientation dependence of $M^{GB}(\Theta)$. This deficit is not surprising, since the experimental data on grain-boundary mobility is limited — and often inconsistent. A review of experimental efforts to measure grain-boundary mobilities is given in Ref. [17]. In spite of the non-availability of an established relationship for $M^{GB}(\Theta)$, there is the general observation that the mobility of LAB is significantly lower than for HAB, and the mobility increases in the low-angle regime by approximately 2...3 orders of magnitude [17,27]. The higher mobility of HAB is a reasonable consequence (at least at low annealing temperatures) of the different activation enthalpies for the rate-controlling processes in LAB and HAB, where $Q_s > Q_B$.

Since detailed knowledge of $M^{GB}(\Theta)$ is currently not available, most computer simulations on anisotropic boundary properties employ the following empirical relationship, which assumes a sigmoidal function to describe the misorientation dependence of the grain-boundary mobility in the low-angle regime [28–30],

$$M^{GB}(\Theta) = M_{HAB} \cdot \left[1 - \exp\left\{ -B \left(\frac{\Theta}{\Theta_0} \right)^N \right\} \right], \tag{2.13}$$

where M_{HAB} and Θ_0 are the mobility of high-angle boundaries and the upper limit of the LAB regime, respectively. Measurements on Aluminum, which are currently the only available data basis, yielded for the fitting parameters of Eq. (2.13) the empirical values $B = 5$ and $N = 4$ [28]. Fig. 2.5 illustrates the misorientation dependence of the sigmoidal mobility function of Eq. (2.13) and the quasi-logarithmic Read-Shockley function of Eq. (2.7), both in normalized form $M^{GB}(\Theta)/M_{HAB}$ and $\gamma^{GB}(\Theta)/\gamma_{HAB}$, respectively.

Compared to the grain-boundary energy for which experiments and computer simulations revealed $\gamma_{HAB}/\gamma^{GB}(\Theta) \lesssim 4$ [18,19,31], the range of the mobility ratio $M_{HAB}/M^{GB}(\Theta)$ can be 2...3 orders of magnitude [17,27]. This demonstrates that the impact of misorientation on the mobility is significantly more pronounced than on the excess energy. Thus, similar to the before mentioned energy-induced anisotropy of boundary kinetics due to the existence of a low-angle misorientation distribution, the same effect will occur due to $M^{GB}(\Theta)$ — but the anisotropy will be significantly stronger. It is obvious that in such a situation the analysis of grain growth and the modeling for analytical treatment or computer simulations must certainly consider the actual misorientation as an additional parameter.

[3] At this point it is worth to note that the measurement of activation enthalpies for grain-boundary migration is always a critical issue, since grain boundaries are preferred locations for the segregation of solute atoms, or may suffer from other mobility inhibitions, which then might become the rate-controlling step during grain-boundary migration. If this happens, the measured activation enthalpy changes from intrinsic diffusion processes to the one of the impeding mechanism (*cf.* Section 2.6).

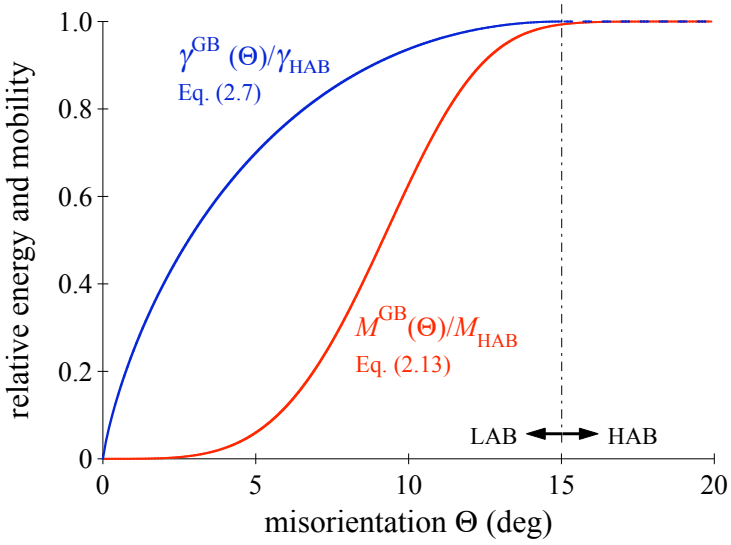

Figure 2.5: Plot of the relative grain-boundary energy and mobility, $\gamma^{GB}(\Theta)/\gamma_{HAB}$ and $M^{GB}(\Theta)/M_{HAB}$, in the low-angle regime (Eqs. (2.7) and (2.13)). The transition between the LAB and HAB is assumed for both curves to occur at $\Theta_0 = 15°$.

2.3 Curvature-Driven Boundary Migration

The excess energy $G^{excess} = A^{GB} \cdot \gamma^{GB}$ that is carried by the grain boundaries of the polycrystal involves that for increasing grain-boundary area the gap to a thermodynamically stable microstructure will increase. Particularly in nanocrystalline materials the small grain sizes cause a significant density of grain boundaries per unit volume (and therefore a significant excess-energy density), which shows that a substantial driving force must be imposed on the microstructure that will try to reduce G^{excess}, and bring the microstructure into a less unstable configuration. Since the grain-boundary excess is defined by the product of specific grain-boundary excess and grain-boundary area, the lowering of G^{excess} entails that either $A^{GB} \to 0$ or $\gamma^{GB} \to 0$. The latter case is particularly interesting, since it would allow to create stable microstructures of arbitrary grain size. In fact, experiments on the binary systems Fe-P and Pd-Zr have shown that the segregation of "impurity elements" can yield a significant reduction of γ^{GB}, e.g. by a factor of two for Fe, or a nearly stabilized nano-scaled grain structure in Pd at temperatures close to the melting point [20, 32]. In undoped single-phase materials such a thermodynamic stabilization of the microstructure is not possible and hence, physics requires A^{GB} to shrink.

To estimate the kinetics of grain-boundary-area shrinkage, a section of an infinitesimal grain-boundary segment with area $dA = (d\beta \cdot R)^2$ and mean curvature $\mathcal{K} = 2/R$ (the principal radii of the curved boundary segment are assumed to be equal, i.e. $R_1 = R_2$) is shown in Fig. 2.6. In response to the pressure p_{eff}, which acts as a consequence of γ^{GB} on the boundary (see Fig. 2.2), A^{GB} will be reduced and the boundary moves accordingly with the velocity $v^{GB} = M^{GB} \cdot p_{eff}$ towards the center of curvature — the grain is shrinking. After an infinitesimal time period dt, the grain size reduced to $R - dR$, and the area of

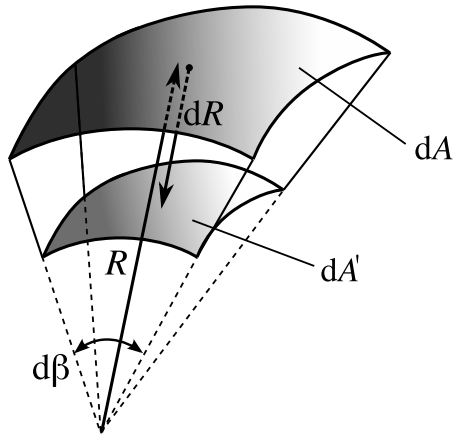

Figure 2.6: The figure illustrates an infinitesimal grain-boundary segment that shrinks in surface area due to the inherent excess energy $\mathrm{d}G = \mathrm{d}A \cdot \gamma^{\mathrm{GB}}$ from $\mathrm{d}A$ to $\mathrm{d}A'$, when the grain size reduces from R to $R - \mathrm{d}R$ (in this context the grain size is defined by the equivalent grain radius $R = D/2$).

the segment shrank to $\mathrm{d}A' = (\mathrm{d}\beta \cdot (R - \mathrm{d}R))^2$. Accordingly, the surface-excess energy of the segment has been reduced by,

$$\mathrm{d}G = -(\mathrm{d}A - \mathrm{d}A') \cdot \gamma^{\mathrm{GB}} \approx -\frac{2\,\gamma^{\mathrm{GB}}}{R}\,\mathrm{d}A\,\mathrm{d}R, \tag{2.14}$$

and therefore the effective pressure on the boundary is given by [33,34],

$$p_{\mathrm{eff}} = \frac{1}{\mathrm{d}A}\frac{\mathrm{d}G}{\mathrm{d}R} = -\frac{2\,\gamma^{\mathrm{GB}}}{R}. \tag{2.15}$$

For the spherical surface segment of Fig. 2.6 the identity $v^{\mathrm{GB}} = \mathrm{d}R/\mathrm{d}t$ holds and thus, the kinetics equation for grain-boundary migration in response to curvature pressure can be written as [6,33],

$$\frac{\mathrm{d}R}{\mathrm{d}t} = -\frac{2 \cdot M^{\mathrm{GB}}(T) \cdot \gamma^{\mathrm{GB}}}{R}. \tag{2.16}$$

Integration of the differential equation yields the parabolic relation for the shrinkage of the grain,

$$R^2(t) = R_0^2 - 4 \cdot M^{\mathrm{GB}} \cdot \gamma^{\mathrm{GB}} \cdot (t - t_0)\,, \tag{2.17}$$

where R_0 is the starting grain radius at time t_0. Obviously, the grain surface — and thus the grain itself — would shrink until $R = 0$, i.e until the grain disappeared. However, where are the atoms of the shrinking grain going? This problem demonstrates that due to mass conservation an individual grain cannot change its size, unless there are other grains, which receive the mass of a shrinking grain. This entails that, whenever a grain is shrinking, there must be at the same time at least one grain that is

growing, and vice versa. Since there is still the need to minimize the excess energy — although some grains are obviously growing —, it is clear that the total grain-boundary area of the entire polycrystal is the relevant parameter, and not the surface area of a particular grain. The system will therefore try to reduce the grain-boundary area per unit volume, A^{GB}/V, which is related to the mean grain size via the stereologic relation [35],

$$\frac{A^{\mathrm{GB}}}{V} = \frac{2}{\langle L \rangle}, \tag{2.18}$$

with $\langle L \rangle$ being the mean intercept length of the grains. Eq. (2.18) shows that for a constant sample volume the relaxation of grain-boundary-excess energy induces an increase of $\langle L \rangle$ — that is equal to a global coarsening of the microstructure (for details on the relation between $\langle L \rangle$ and the grain size please see Section 3.1.3.2). Since this is contradicting Eq. (2.17), where basically all grains are shrinking, Burke and Turnbull proposed the following empirically-based kinetics equation for the average grain size $\langle R \rangle$ [6],

$$\frac{\mathrm{d}\langle R \rangle}{\mathrm{d}t} = \frac{\overline{M}(T) \cdot \overline{\gamma}}{\langle R \rangle}, \tag{2.19}$$

where $\overline{M}$ and $\overline{\gamma}$ are the mobility and energy that applies for all grain boundaries of the aggregate. Integration of Eq. (2.19) yields the well-established parabolic growth law that holds in both 2- and 3-dimensional space (*cf.* Eq. (1.1)).

W.W. Mullins demonstrated in an analytical derivation that the parabolic coarsening according to Eq. (2.19) indeed yields the growth law for the mean grain size $\langle R \rangle (t)$, provided that the prerequisites for normal grain growth, which are uniform grain-boundary properties (i.e. all grain boundaries possess the same energy and mobility), scaling of the driving force holds ($v^{\mathrm{GB}} \propto 1/R$), and a self-similar grain-size distribution are obeyed [36,37].

Evidence for a parabolic coarsening can be attained from a number of annealing experiments on highly pure coarse-graind and nanocrystalline materials [8,10,34]. However, the experimental results are only in compliance with a parabolic characteristics, if the temperature during annealing is close to the melting point, i.e. $T/T_{\mathrm{m}} \gtrsim 0.7$. Although the grain-size evolution at lower temperatures usually shows a deviation from a parabolic curve, it still follows a power-law relation with growth exponent m,

$$\langle R \rangle^m (t) = \langle R_0 \rangle^m + K \cdot (t - t_0), \tag{2.20}$$

where K is a temperature-dependent rate constant, and m typically varies between 2 and 4 in high-purity metals [4].

2.4 Grain Growth in the Mean-Field Approach

During the coarsening of the microstructure the grain-boundary area per unit volume is continuously reduced, which involves the simultaneous growth and shrinkage of grains. From this understanding it

is straight to ask "What is the criterion for a grain to belong to the growing or the shrinking species?". If uniform-boundary conditions and a curvature-induced driving force for boundary migration are presupposed, the only remaining parameter to distinguish the grains is their size and topology. For 2-dimensional grain structures it was shown by von Neumann and Mullins that the area A_n of a n-sided grain changes as [38],

$$\frac{\mathrm{d}A_n(t)}{\mathrm{d}t} = 2\pi \cdot R \cdot \frac{\mathrm{d}R}{\mathrm{d}t} = k \cdot \frac{\pi}{3}(n-6), \tag{2.21}$$

where k specifies the temperature-sensitive rate constant for boundary migration. Thus, in 2-dimensional space the criterion whether a grain grows or finally disappears is determined by the topology, i.e. by the number of grain faces, but does not depend — at least not directly — on the actual size of a grain. The quite simple relation in Eq. (2.21) shows that grains with $n = 6$ faces are stable, whereas grains with $n < 6$ and $n > 6$ will shrink or grow, respectively. It is conceivable that n and R must be interrelated, since only larger grains can accommodate sufficient neighbors to enable growth. Thus, if a relation like $n(R_i)$ can be established (of course, such a relation can only be of average nature), it would be of interest to know the number of grains in the size class R_i (since this would tell how many grains are growing or shrinking according to $n(R_i)$) — or more generally, it would be interesting to know the grain-size-distribution function (GDF) $f(R,t)$. Since every grain out of the R_i subset has then the same (mean) topology, those grains will be embedded in a similar environment and therefore experience the same rate of growth or shrinkage. The treatment of grain growth in this way is usually called a "mean-field" approach, since it is based on an equivalent environment for all grains, that belong to the same grain-size class.

Provided that the GDF is known, then the product $f(R_i,t) \cdot \Delta R$ represents the number of grains that belong to the ith grain-size class in the size interval $[R_i, R_i + \Delta R]$. Upon growth or shrinkage the grains receive or lose atoms and shift accordingly to the next higher $(i+1)$ or lower $(i-1)$ grain-size class, respectively. Thus, microstructural coarsening of the polycrystalline material reduces to a flux $j(R,t)$ of grains in the grain-size/time space (R/t-space), which induces a continuous evolution of the GDF $f(R,t)$. Assuming that a positive $j(R,t)$ represents a net flux of growing grains, the following continuity equation relates $j(R,t)$ and $f(R,t)$ [39,40],

$$\left(\frac{\partial f(R,t)}{\partial t} \cdot \Delta t\right) \cdot \Delta R = \left(-\frac{\partial j(R,t)}{\partial R} \cdot \Delta R\right) \cdot \Delta t. \tag{2.22}$$

Obviously, given an appropriate expression for $j(R,t)$ can be established, Eq. (2.22) provides the opportunity to predict the evolution of the GDF and thus, the answer to the question on which grains are growing and which are dissolving with time. In the following, the approach to determine $j(R,t)$ for the classical mean-field model and for a size-correlated topology model will be briefly discussed.

2.4.1 The Classical Mean-Field Model

Based on a theory of Lifshitz and Slyozov on the coarsening of second-phase particles, M. Hillert suggested that there must be a critical grain size R_c, which divides the GDF into two parts — the one of growing

grains and the one of shrinking grains [33],

$$\frac{\mathrm{d}R}{\mathrm{d}t}\begin{cases} < 0 \;\; (\text{shrinking}) & \dots \text{if } \; R < R_\mathrm{c} \\ = 0 \;\; (\text{stable}) & \dots \text{if } \; R = R_\mathrm{c} \\ > 0 \;\; (\text{growing}) & \dots \text{if } \; R > R_\mathrm{c}. \end{cases} \tag{2.23}$$

To introduce such a cutoff for the evolution of a grain (i.e. whether a grain of size R is growing or shrinking), Hillert proposed the following size-dependent growth kinetics [33],

$$\frac{\mathrm{d}R}{\mathrm{d}t} \approx v^{\mathrm{GB}} = \alpha \cdot \overline{M} \cdot \overline{\gamma} \cdot \left(\frac{1}{R_\mathrm{c}(t)} - \frac{1}{R} \right), \tag{2.24}$$

with $\alpha = 1/2$ in two dimensions and $\alpha \approx 1.0$ for 3-dimensional structures. Comparing Eq. (2.21) and (2.24), the topological relation $n(R)$ for a 2-dimensional system can then be expressed by [33],

$$n(R) \approx 6 + 6 \cdot \left(\frac{R}{R_\mathrm{c}} - 1 \right). \tag{2.25}$$

Rios and Glicksman found in computer simulations on grain growth in 3-dimensional systems an equivalent relation $n(R)$ between the topology and the size of a grain, where the criterion for a grain to support growth was found in terms of number of faces to be $n > n_\mathrm{c} \approx 13.4$ [41]. Although the functional relationship of $n(R)$ in three dimensions is obviously more complex than the simple linear term in Eq. (2.25), the general statement that small grains shrink while large grains grow is evidently valid. Hillert showed that for the constraint of a stable GDF, i.e. non of the grains covered by $f(R,t)$ will lead to unlimited abnormal growth, the evolution of the critical grain size is given by,

$$\frac{\mathrm{d}R_\mathrm{c}^2}{\mathrm{d}t} = \frac{1}{2} \cdot \alpha \cdot \overline{M} \cdot \overline{\gamma}. \tag{2.26}$$

Integration of Eq. (2.26) yields that the critical size $R_\mathrm{c}(t)$ follows a parabolic time dependence, i.e. the cutoff is moving to larger grain sizes during grain growth. However, how does the average grain size $\langle R \rangle$ change during coarsening? To know this it is necessary to find an appropriate expression for $f(R,t)$. Provided that the changes in $f(R,t)$ with time are induced by grain-boundary migration only, the flux in R/t-space is given by the product [33, 42],

$$j(R,t) = v^{\mathrm{GB}} \cdot f(R,t) = \overline{M} \cdot \overline{\gamma} \cdot \left(\frac{1}{R_\mathrm{c}(t)} - \frac{1}{R} \right) \cdot f(R,t). \tag{2.27}$$

The continuity equation according to Eq. (2.22) of Hillert's model reads then,

$$\frac{\partial f(R,t)}{\partial t} = -\overline{M} \cdot \overline{\gamma} \cdot \frac{\partial}{\partial R} \left[\left(\frac{1}{R_\mathrm{c}(t)} - \frac{1}{R} \right) \cdot f(R,t) \right]. \tag{2.28}$$

With $R_c(t)$ from Eq. (2.26) and the constraint of mass conservation, Hillert proposed for 3-dimensional growth the following quasi-stationary GDF that solves for the respective boundary conditions the continuity equation (2.28),

$$f_{\text{Hillert}}(x) = (2e)^3 \cdot \frac{3x}{(2-x)^5} \cdot \exp\left(-\frac{6}{2-x}\right), \tag{2.29}$$

where $x = R/R_c$ denotes the relative grain size and e is Euler's constant. Taking $f_{\text{Hillert}}(x)$ and calculating the corresponding average grain size, it is possible to show that $\langle R \rangle = {}^8/_9 R_c$ and thus, to prove that parabolic growth holds also for the mean grain size of the microstructure, i.e. $\langle R \rangle^2 - \langle R \rangle_0^2 \propto t$.

Although Hillert's deterministic model predicts both a stable quasi-stationary GDF and a parabolic evolution of the average grain size, the derived GDF deviates significantly from frequent experimental observations of a lognormal-like distribution of grain sizes [8, 43, 44]. Fig. 2.7 shows a comparison of the lognormal distribution and Hillert's function, which has a required cutoff at $x_{\max} = 2.0$ to ensure the stability of the system against catastrophic growth [33].

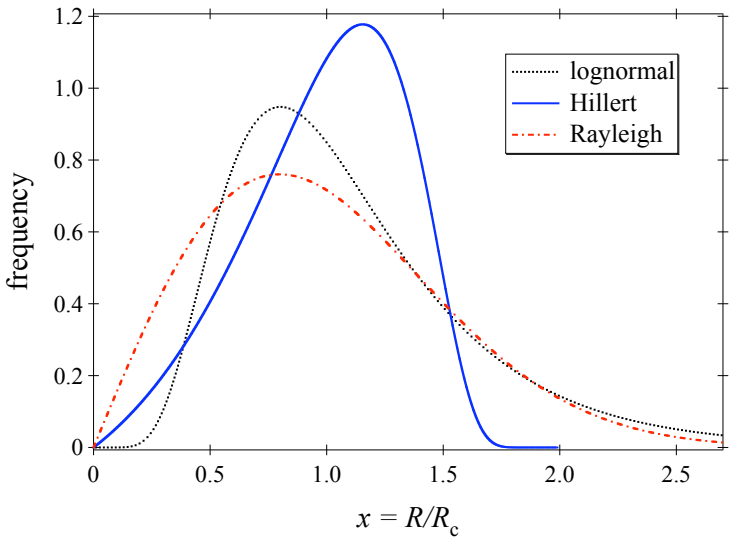

Figure 2.7: The graph shows Hillert's mean-field GDF, Eq. (2.29), together with a lognormal function. A comparison reveals that major differences between both curves exist, which can be seen in a shallower increase and a faster drawdown of Hillert's curve. However, a review of Figs. 1.1 and 3.7 shows that the lognormal function (and not Hillert's function) actually yields a sound description of measured grain-size distributions, which are clearly not showing the cutoff at $x_{\max} = 2.0$ of Hillert's function. The graph shows additionally a Rayleigh function, which has a strong similarity to the shape of the lognormal function and might therefore be used equivalently to the lognormal function to describe the distribution of grain sizes.

2.4.2 Size-Correlation Effects of the Topology

Although Hillert's strict mean field cutoff R_c agrees with the topology-sensitive relationship of Eq. (2.21), it is difficult to believe that only one reference grain size will be sufficient to assess the kinetics of all grains of different size in the polycrystal. This deficit is usually blamed to cause the failure of Hillert's GDF with respect to experimental observations. To rectify this flaw it is therefore essential to determine for a particular grain of size R_n the average size $\langle R_n|R\rangle$ of the surrounding grains, which will then be the crucial parameter for the evolution of the investigated grain. In terms of Hillert's mean field model this means that R_c will be a size-dependent parameter. If $\langle R_m\rangle$ denotes the mean size of all neighboring grains in the sample, Hillert's theory would require that $\langle R_n|R\rangle = \langle R_m\rangle$ in order to hold, because then all grains of arbitrary size will sit in the identical environment. Computer simulations on coarsening of polycrystalline microstructures disproved this conclusion, and revealed instead a correlation between the size of a grain and its environment [45–48]. It is the general trend that large grains are surrounded by small grains and vice versa, see Fig. 2.8(a). Compared to the universal R_c of Hillert's mean field, this "size-correlation" effect induces an accelerated growth of large grains and faster shrinkage of the small grains.

Marthinsen *et al.* proposed that it would be consequent to replace Hillert's universal mean-field cutoff R_c by the actual mean environment $\langle R_n|R\rangle$ of a specific grain [45],

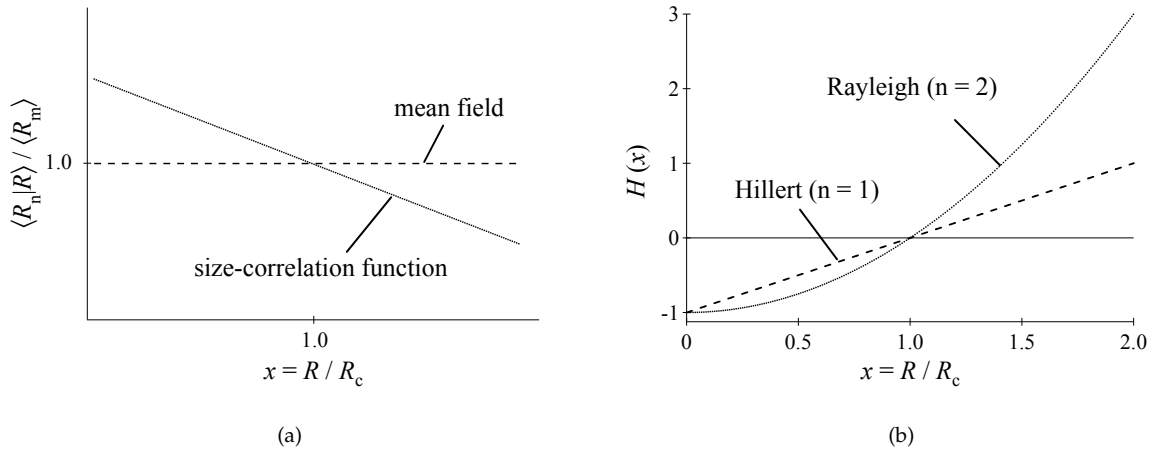

Figure 2.8: The failure of Hillert's GDF has drawn the attention to a size-dependent parameter $\langle R_n|R\rangle$ instead of an unique R_c. Figure (a) shows schematically the change of the cutoff parameter, if a size correlation is considered. Compared to Hillert's model are larger grains surrounded by smaller grains and vice versa. Figure (b) plots the function $H_n(x)$ of Eq. (2.37) for different strength of size correlation. The parameter $n = 1$ (i.e. $c_0 = 1$, $c_1 = 0$) represents the conventional mean field, i.e. there is no size correlation involved. For $n = 2$ (i.e. $c_0 = 0$, $c_1 = 1$) a size correlation similar to (a) is prevailing, for which the GDF attains the shape of a Rayleigh function.

$$\frac{\mathrm{d}R}{\mathrm{d}t} = K \cdot \left[\left\{ c_0 + c_1 \left(\frac{R}{R_\mathrm{c}} \right) + \cdots \right\} \cdot \frac{1}{R_\mathrm{c}} - \frac{1}{R} \right], \tag{2.30}$$

where the Taylor series,

$$\frac{R_\mathrm{c}}{\langle R_\mathrm{n} | R \rangle} \approx \left\{ c_0 + c_1 \left(\frac{R}{R_\mathrm{c}} \right) + \cdots \right\} \tag{2.31}$$

of the size-correlation function in Fig. 2.8(a) is used. Limiting the Taylor series to the linear part [45, 47], Eq. (2.30) arrives at the quadratic form,

$$R \cdot \frac{\mathrm{d}R}{\mathrm{d}t} = K \cdot H_\mathrm{corr}(x) = K \cdot \left(c_0 x + c_1 x^2 - 1 \right), \quad \text{with } x = \frac{R}{R_\mathrm{c}}. \tag{2.32}$$

On the other hand, the mean-field kinetics of Eq.(2.24) can be written in the same format to yield the linear relation,

$$R \cdot \frac{\mathrm{d}R}{\mathrm{d}t} = K \cdot H_\mathrm{mean}(x) = K \cdot (x - 1). \tag{2.33}$$

For the kinetics law of Eq. (2.32) and the continuity equation (2.22), the following stable and self-similar GDF function has been shown to hold for the proposed correlation function [45, 49],

$$f_\mathrm{corr}(x) = A \cdot \left(\frac{2e}{c_0} \right)^A \cdot \frac{x}{\left(\frac{2}{c_0} - x \right)^{A+2}} \cdot \exp\left\{ \frac{-2 \cdot A}{2 - c_0 \cdot x} \right\}, \quad \text{with } A = \frac{8\, c_1}{c_0^2} + 2. \tag{2.34}$$

For the mean-field assumption ($c_0 = 1$ and $c_1 = 0$), Eq. (2.34) merges to Hillert's GDF. Fig. 2.9 shows plots of Eq. (2.34) for different parameters c_0 and c_1, which emphasizes the sensitivity of the GDF on the size-dependent environment $\langle R_\mathrm{n} | R \rangle$. It shows that for a "stronger" correlation — i.e. increasing deviation from the mean field — the GDF gradually approaches the shape of a Rayleigh function, which represents a close approximation of a lognormal distribution — which would be appreciated from experimental experience.

If the Rayleigh function,

$$f_\mathrm{Rayleigh}(x, c(t)) = \frac{8}{\sqrt{6\pi}} \cdot c^3 \cdot x \cdot \exp\left\{ -\frac{3}{2} c^2 x^2 \right\}, \quad \text{with } x = \frac{R}{R_c}, \tag{2.35}$$

is assumed to be a valid solution for the GDF, where $c(t)$ is a time-dependent parameter, Jeppson *et al.* showed that then the associated kinetics equation, calculated from the continuity relationship for normal grain growth, is given by [50],

$$R \frac{\mathrm{d}R}{\mathrm{d}t} = \frac{1}{2} \frac{\mathrm{d}R_\mathrm{c}^2}{\mathrm{d}t} \cdot \left[\left(\frac{R}{R_\mathrm{c}} \right)^2 - 1 \right] = K_R \cdot \left(x^2 - 1 \right). \tag{2.36}$$

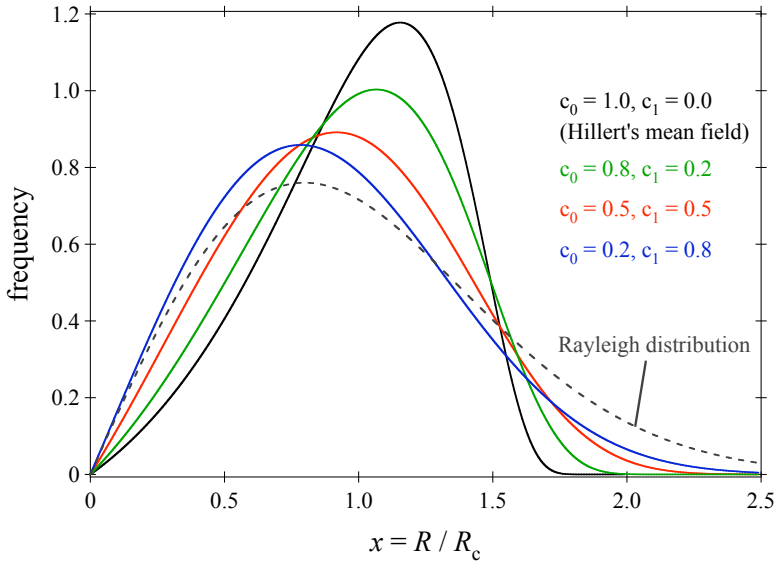

Figure 2.9: The graph shows plots of the GDF (2.34) for different parameters c_0 and c_1 of the size-correlation function employed in Eq. (2.30). The curves indicate that for increasing size correlation (i.e. $c_1 \to 1$), the GDF approaches gradually the shape of a Rayleigh function and a grain-size cutoff with $x_{\max} \to \infty$.

A thorough inspection of Hillert's kinetics law and the one found by Jeppsson for the Rayleigh function — Eqs. (2.33) and (2.36) — shows that both equations can be joined in one universal model with the free parameter n [50],

$$R\,\frac{\mathrm{d}R}{\mathrm{d}t} = K'\,H_n(x) = K'\cdot(x^n - 1) \quad , \tag{2.37}$$

where the kinetics constant K' must fulfill the needs of both, Hillert's mean-field theory, i.e. $K' = \frac{\alpha\cdot\overline{M}\cdot\overline{\gamma}}{\mu}$, and the Rayleigh distribution of the size-correlation model, $K' = \frac{1}{2}\frac{\mathrm{d}R_c^2}{\mathrm{d}t}$, which means that,

$$\frac{\alpha\cdot\overline{M}\cdot\overline{\gamma}}{\mu} = \frac{1}{2}\frac{\mathrm{d}R_c^2}{\mathrm{d}t}. \tag{2.38}$$

If the stability criterion (i.e. abnormal growth of grains is not allowed) used by Hillert in his pioneering work is also considered for the correlation theory [33,50], the parameter μ must satisfy,

$$\mu = \frac{2}{n}\cdot\left(\frac{2}{2-n}\right)^{(2-n)/n}. \tag{2.39}$$

Thus, the growth rate of the critical grain size for the universal model in Eq. (2.37) yields,

$$\frac{\mathrm{d}R_\mathrm{c}^2}{\mathrm{d}t} = \alpha \cdot \overline{M} \cdot \overline{\gamma} \cdot n \cdot \left(\frac{2}{2-n}\right)^{(n-2)/n}, \tag{2.40}$$

which proves that parabolic growth also holds for the Rayleigh distribution ($n = 2$). Of course, the Rayleigh distribution is only valid for $n = 2$, whereas a different GDF will be obtained for other values of n. For the universal kinetics law it can be shown that due to the constraint of a stable GDF, the maximum relative grains size will be $x_\mathrm{max} = \left(\frac{2}{2-n}\right)^{1/n}$ [50]. This obviously agrees with Hillert's GDF ($n = 1$), for which x_max will be equal to 2. For increasing values $1 < n \leqslant 2$ the universal model approachs the Rayleigh function, where for $n = 2$ no upper limit is found and $x_\mathrm{max} \to \infty$.

Fig. 2.8(b) shows the function $H_\mathrm{n}(x)$ of Eq. (2.37) for the two cases $n = 1$ (Hillert's uniform mean field) and $n = 2$ (size-correleation model with a Rayleigh GDF). Comparing the two curves shows that for a size-dependent environment both a faster growth and a faster shrinkage is induced compared to Hillert's universal mean field. Since the Rayleigh function is a clearly better approximation of real microstructures than Hillert's GDF, it is conjecturable that a size-dependent R_c is more appropriate than a general mean field to describe grain-growth kinetics analytically.

2.5 Impact of Structural Entities on Grain-Growth Kinetics

Conventional models on normal grain growth and their analytical prediction of the growth rate rely on the prerequisite of uniform grain-boundary properties, which means that the migration velocity of a grain boundary — and therefore the coarsening kinetics of the whole polycrystalline structure — is solely determined by grain-boundary curvature. However, a closer inspection of microstructures reveals that there are not only 2-dimensional grain boundaries, which separate individual grains, but there are also 1-dimensional or even 0-dimensional objects, which are defined by the intersection of grain boundaries. Since their migration is also required to allow for a long-range diffusion of grain boundaries, they could become a substantial issue for grain growth — particularly then, when their specific kinetics is slower than the intrinsic velocity of the grain boundaries. Under such circumstances, the kinetics of those structural objects could become a rate-controlling obstacle and coarsening of the microstructure will slow down (of course, this would be neat, as the microstructure would be self-stabilizing). Since there are indications that nanocrystalline materials are apparently growing at a slower rate than expected from extrapolated data of coarse-grained materials (see Fig. 1.2), it will be necessary to address the question of growth-impeding obstacles in detail.

In the following two paragraphs the mechanisms and the ability of structural obstacles (like triple lines and quadruple points) and impeding forces of vacancy supersaturation will be discussed.

2.5.1 The Kinetics of Triple Lines and Quadruple Points

Triple lines (TL) are defined by the intersection of three grain boundaries, which means that TL are 1-dimensional curved lines along the contour of grain boundaries. If the internal structure of grain

boundaries gives rise to the existence of an associated grain-boundary energy, it is straightforward to expected a similar excess energy also to be an inherent feature of TL. Due to the dimensionality of TL this excess energy γ^{TL} should be equal to a line tension that offers a driving force to reduce the TL length [51].

Fig. 2.2 shows that the grain-boundary energy γ^{GB} does not only provide the driving force for the decrease of grain-boundary area, but will also induce a force per unit length $\mathbf{F}_i/l = \gamma_i^{\mathrm{GB}} \cdot \mathbf{n}_i$ on a TL that borders a grain boundary, where $\mathbf{n}_i$ is a unit vector that is oriented perpendicular to both the line vector of the TL and the normal vector of the grain boundary near the TL. Thus, the total force on a TL segment of length l is determined by the vector sum of all three grain-boundary forces,

$$\mathbf{F} = l \cdot \sum_{i=1}^{3} \gamma_i^{\mathrm{GB}} \cdot \mathbf{n}_i. \tag{2.41}$$

For uniform grain boundaries the specific energies are equal $\gamma_i^{\mathrm{GB}} = \gamma^{\mathrm{GB}}$ and hence, the net force of Eq. (2.41) vanishes, if the interfaces meet at an equilibrium angle $\psi = \frac{2\pi}{3}$. Fig. 2.10 illustrates the equilibrium grain-boundary configuration at the TL. However, during the curvature-driven migration of a grain boundary the inclination of the boundary plane at the TL changes continuously and thus, there will be a net force $\mathbf{F}_{\mathrm{net}}$ induced that is acting on the TL in order to bring it back into an equilibrium configuration. The TL migrates then under the effect of the driving force with the velocity [17],

$$v^{\mathrm{TL}} = |\mathbf{F}_{\mathrm{net}}| \cdot M^{\mathrm{TL}}, \tag{2.42}$$

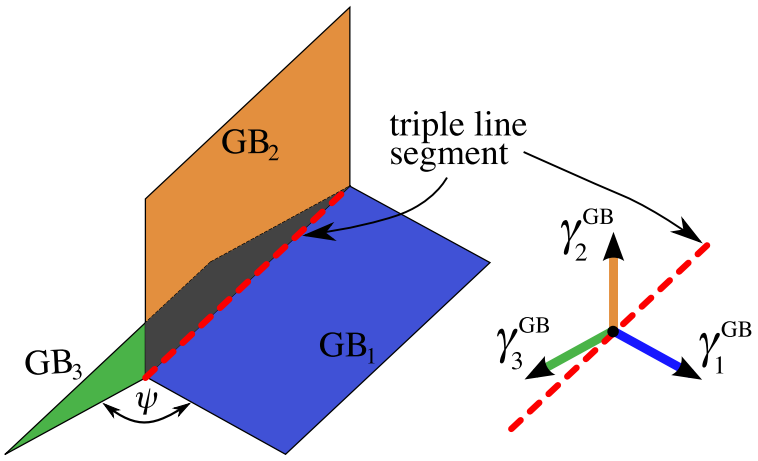

Figure 2.10: Triple-line segment with three adjoining grain boundaries. The involved grain-boundary energies γ^{GB} exert pulling forces that are acting on the triple line. In steady-state conditions the net force will be zero and the equilibrium angle between the boundary planes will attain a value of 120° if all three γ^{GB} are equal. If the grain boundaries carry different γ^{GB}, the equilibrium angle between the boundary planes will deviate from 120° in order to provide a vanishing net force.

provided that the mobility of the TL, which is given by,

$$M^{\mathrm{TL}}(T) = \frac{M_0^{\mathrm{TL}}}{T} \exp\left(-\frac{Q^{\mathrm{TL}}}{k_{\mathrm{B}}T}\right) \tag{2.43}$$

is sufficient (similar to the activation enthalpy for grain-boundary migration denotes Q^{TL} the activation enthalpy of the diffusion mechanism that is needed to allow for TL migration). The changing configuration of grain-boundary alignment during curvature-induced growth is schematically illustrated in Fig. 2.11(a) where the migration of GB_1 induced a deviation from the equilibrium configuration before. Fig. 2.11(a) further shows that an immobile TL will cause a flattening of the grain boundary ($\mathscr{K} \rightarrow 0$) and thus, a disruption of grain growth.

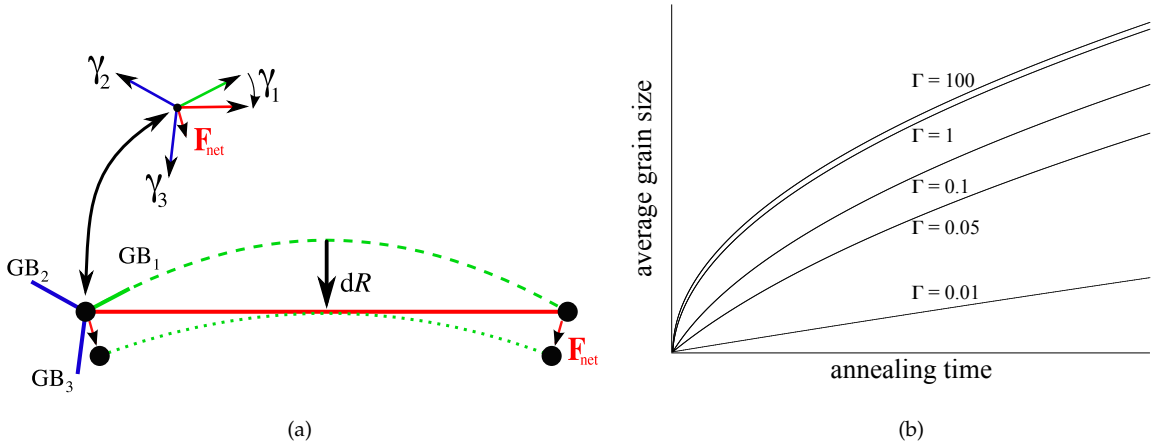

Figure 2.11: (a) Change of the boundary inclination at a triple line during grain-boundary migration. Starting from an equilibrium alignment of the boundaries, the curvature-induced boundary migration induces a net force that will pull the triple line towards the new equilibrium configuration. From the schematic it is evident that this process is indispensable for long-range grain-boundary migration. An immobility of triple lines will cause a flattening of the grain boundaries and a termination of grain growth. (b) Grain-size/time plots of Eq. (2.47) for different mobility ratios $\Gamma = M^{\mathrm{TJ}}/M^{\mathrm{GB}}$. The curves evince that for $M^{\mathrm{TJ}} \ll M^{\mathrm{GB}}$ the kinetics will be controlled by triple lines, and a quasi-linear growth law (with a growth rate independent of the actual grain size) is established.

It would be reasonable to assume that the migration of a TL is more difficult than boundary migration, since TL motion involves the atomic diffusion between three adjoining grains, whereas grain-boundary migration only has the exchange of atoms between two grains. In fact, a number of theoretical and experimental work suggests that TL possess a distinct mobility, which seems to be less than the one of grain boundaries [52–59]. Since it is always the slowest of the involved processes that is limiting the overall kinetics, it seems possible that TL could become the rate-controlling mechanism for grain-boundary migration, and the characteristic activation enthalpy would change from grain-boundary or lattice self-diffusion (depending on the boundary misorientation) to the one for TL migration.

The TL inhibition of grain-boundary migration is usually treated as a drag force f_{TL} that is exerted by the TL on the boundary. Considering TL drag, G. Gottstein and colleagues proposed therefore to extend Eq. (2.15) as [54, 60, 61],

$$p_{\mathrm{eff}} = \frac{2\,\gamma^{\mathrm{GB}}}{R} - \frac{f_{\mathrm{TL}}}{a}, \tag{2.44}$$

in which a is the spatial distance between next-nearest TL. Since the inter-TL spacing is basically determined by the actual size and topology of the grain, the exact form of $a(R)$ is not known. However, if it is assumed that $a \propto R$, the TL spacing might be approximated by $a \approx \eta \cdot R$, and Eq. (2.44) yields [61],

$$p_{\mathrm{eff}} \approx \frac{2\,\gamma^{\mathrm{GB}}}{R} - \frac{f_{\mathrm{TL}}}{\eta \cdot R}. \tag{2.45}$$

In the worst case, the TL will have vanishing mobility and the boundary will finally become flat (the inherent driving force due to grain-boundary curvature will then be zero). In that case, the further movement of the grain boundary is solely determined by the TL migration, i.e. $v^{\mathrm{GB}} = f_{\mathrm{TL}} \cdot M^{\mathrm{TL}}$. Thus, replacing f_{TL} in Eq. (2.45), the kinetics equation arrives at [60, 61],

$$v^{\mathrm{GB}} = \frac{2 \cdot M^{\mathrm{GB}} \cdot \gamma^{\mathrm{GB}}}{R} \cdot \left(\frac{1}{1 + \frac{1}{\Gamma \cdot R}} \right) = \frac{2 \cdot \gamma^{\mathrm{GB}}}{R} \cdot M^{*}(R), \quad \text{with } \Gamma = \frac{M^{\mathrm{TL}} \cdot \eta}{M^{\mathrm{GB}}}. \tag{2.46}$$

Apparently, TL drag induces a size-dependent rescaling of the grain-boundary mobility $M^{*}(R)$, which clearly discards uniform boundary conditions and thus, should disallow a self-similar coarsening of a polycrystal with grains of different size (and therefore different mobility). Integration of Eq. (2.46) yields with the rate constant K the growth law for curvature-driven grain growth under TL drag [61],[4]

$$\langle R \rangle^2 + \frac{2\,\langle R \rangle}{\langle \Gamma \rangle} = \frac{2\,K}{\langle \Gamma \rangle} \cdot (t - t_0) + \langle R_0 \rangle^2 + \frac{2\,\langle R_0 \rangle}{\langle \Gamma \rangle}. \tag{2.47}$$

Fig 2.11(b) includes plots of Eq. (2.47), where the mobility ration varies between $\Gamma = 0.01 \ldots 100$. The curves show that already $\Gamma = 1$ would in principle induce a deviation from intrinsic boundary migration, but this drag effect is still negligible. The influence of TL becomes more pronounced, if Γ approaches very small values. For small values of Γ the initial slope of the curve appears linear, and merges at larger grain sizes into the normal parabolic form. At $\Gamma \to 0$ the characteristics of the complete curve takes on a linear time dependence, which implies that TL migration is the dominating process over the full annealing time. Contrary to the uniform mobility of a mean-field growth law, which predicts the evolution of the microstructure in terms of the mean grain size, TL drag and the thereby induced size-dependent effective mobility $M^{*}(R)$ outlaws the prerequisites for a simple conclusion on the kinetics of the mean grain size. Nevertheless, a justification for the applicability of Eq. (2.47) might be inferred from computer simulations on 2-dimenssional grain growth (the simulation rests on the local configuration of grains, and is therefore governed by the local migration kinetics of Eq. (2.46)), which yielded for a limited TL mobility a growth

[4] Note that Eq. (2.47) expresses the evolution of the average grain size of the ensemble although the calculation of a mean value might be ambiguous, since it is likely that the microstructure will not grow uniformly.

kinetics similar to the curves in Fig. 2.11(b) [61]. The simulation showed further that for small values of Γ the ratio of $\langle R \rangle / R_{\max}$ increases at the beginning and diminishes after a maximum has been passed ($R_{\max}$ denotes the size of largest grains in the polycrystal). This characteristic indicates that the size dependence of the rescaled mobility causes obviously an inhomogeneous grain-size evolution, and initiates thereby abnormal grain growth.

If TL drag is strong ($\Gamma \to 0$), the grain-boundary velocity can be written according to Eq. (2.46) as $v^{\mathrm{GB}} = M^{\mathrm{TL}} \cdot \gamma^{\mathrm{GB}} \cdot g$, where g is a geometric constant on the order of unity. If this expression is compared with Eq. (2.16), the transition between TL and grain-boundary controlled growth can be estimated to occur at,

$$R_{\mathrm{t}} = \frac{M^{\mathrm{GB}}}{M^{\mathrm{TL}}\, g} = \frac{1}{\Gamma \cdot g}. \tag{2.48}$$

This means that for a grain size $R < R_{\mathrm{t}}$ TL drag is strong, and the curve tends to be linear, while for $R > R_{\mathrm{t}}$ TL drag diminishes and the curve attains parabolic shape. The existence of linear growth has been experimentally observed in special tricrystal geometries — however, evidence for TL drag in 3-dimensional polycrystals is up to now missing. Nevertheless, the information obtained from tricrystal experiments indicates that at lower annealing temperatures the inequality $M^{\mathrm{TL}} < M^{\mathrm{GB}}$ applies, i.e. $\Gamma < 1$ [61]. The lower mobility of TL is usually attributed to a higher activation enthalpy for TL motion, $Q^{\mathrm{GB}} < Q^{\mathrm{TL}}$ [52, 54, 56]. If both activation enthalpies Q^{TL} and Q^{GB} in Eq. (2.48) are known, the transition grain size can be calculated as a function of temperature,

$$R_{\mathrm{t}}(T) \approx \frac{M_0^{\mathrm{GB}}}{M_0^{\mathrm{TL}}} \cdot \exp\left\{\frac{Q^{\mathrm{TL}} - Q^{\mathrm{GB}}}{k_{\mathrm{B}} T}\right\}. \tag{2.49}$$

TL drag is therefore only expected at low annealing temperatures and at grain sizes $R < R_{\mathrm{t}}$. Thus, if TL drag plays a role for grain growth, nanocrystalline materials should be particularly susceptible to it. Fig. 2.12 shows schematically the transition between the two regimes, where TL and grain-boundary migration are the respective rate-controlling processes.

If the intersections of grain boundaries establishe 1-dimensional structures (triple lines) that are supposed to impact on boundary kinetics, it is straight forward to ask: What happens if TL intersect? Of course, the structures defined by the intersection of TL would be 0-dimensional points, which are frequently named "quadruple points" (QP) because four TL meet there. Only in the last years QP have become an issue for debate. This, and the complicated situation for clarifying experiments, is basically the reason why there are not more than conceptional ideas about QP and their features. It was suggested by G. Gottstein and L.S. Shvindlerman that QP have a similar impact on boundary kinetics as TL do [51, 62]. Because of the distinct grain-size-dependent density of QP, they may only play a role for sufficiently small grains, that is if $M^{\mathrm{QP}} \cdot a'^2 \ll M^{\mathrm{GB}}$, where M^{QP} denotes the mobility of QP and a' is the spatial distance between neighbored QP [63]. To account for QP drag, Eq. (2.44) might be further extended by an additional retarding force related to the presence of QP drag [63],

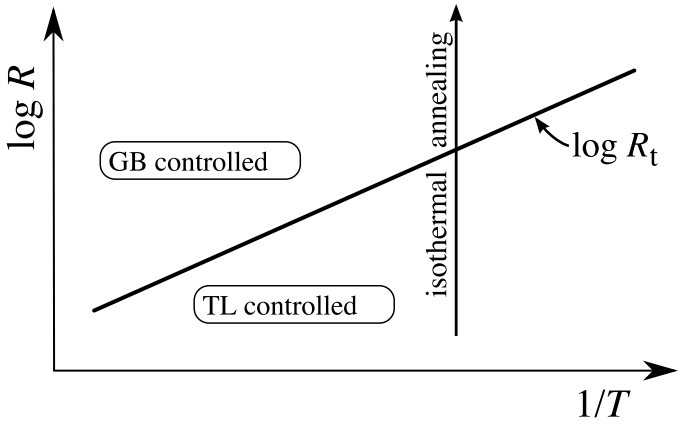

Figure 2.12: Plot of the transition grain size R_t between triple-line and curvature-controlled grain growth. As the drag effect of triple lines on boundary migration depends on both, the grain size and the mobility parameter Γ, R_t will decrease according to Eq. (2.49) with increasing temperature.

$$p_{\text{eff}} = \frac{2\,\gamma^{\text{GB}}}{R} - \frac{f_{\text{TL}}}{\eta \cdot R} - \frac{f_{\text{QP}}}{(\eta' \cdot R)^2}, \tag{2.50}$$

where $a' = \eta' \cdot R$ is assumed. Equally to TL drag before, the QP drag force might be expressed as $f_{\text{QP}} = v^{\text{GB}}/M^{\text{QP}}$. With $\Gamma' = (M^{\text{QP}}/M^{\text{GB}}) \cdot \eta'^2$, the velocity of a grain boundary with both TL and QP drag might therefore be written in the form,

$$v^{\text{GB}} = \frac{2 \cdot M^{\text{GB}} \cdot \gamma^{GB}}{R} \cdot \left(\frac{1}{1 + \frac{1}{\Gamma R} + \frac{1}{\Gamma' R^2}} \right). \tag{2.51}$$

In the limit of solely QP-controlled kinetics the entire grain boundary migrates then with the velocity $v^{\text{GB}} \approx 2 \cdot M^{\text{QP}} \cdot \gamma^{\text{GB}} \cdot R$. Thus, v^{GB} would increase with increasing grain size (i.e. with ongoing annealing) and the grain size evolves as,

$$R(t) \propto \exp(t)\,, \tag{2.52}$$

until $R(t)$ reached a level where the QP density per unit volume becomes insufficient and another mechanism turns over to be the rate-controlling process. It is important to note that currently there is basically no detailed knowledge on M^{QP} and the actual significance of QP. Nevertheless, assuming that QP and TL play the intended role in grain growth, the "integral" growth kinetics would be built-up of three subsequent stages:

$$
\begin{aligned}
R < R'_{\mathrm{t}}: \quad & R(t) = K_0 \cdot \exp\{t - t_0\} + R_0 && \text{(quadruple-point drag),} \\
R'_{\mathrm{t}} < R < R_{\mathrm{t}}: \quad & R(t) = K_1 \cdot (t - t_1) + R_1 && \text{(triple-line drag),} \\
R > R_{\mathrm{t}}: \quad & R(t)^2 = K_2 \cdot (t - t_2) + R_2^2 && \text{(grain-boundary curvature).}
\end{aligned}
$$

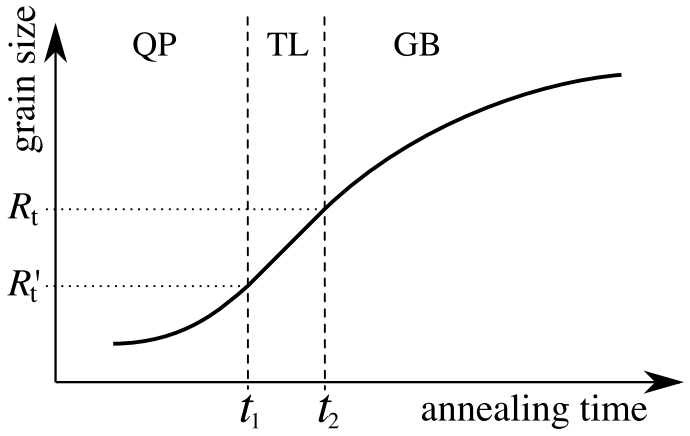

Figure 2.13: Grain-growth kinetics in a 3-stage sequence, if quadruple points, triple lines and grain-boundary curvature establish successively the rate-controlling step. The rate-controlling transition between QP (exponential growth) and TL (linear growth) occurs at R'_{t}, while the transition between TL and curvature-controlled growth (power-law growth) is found at R_{t}.

Fig. 2.13 summarizes qualitatively the different rate-controlling mechanisms and the respective growth kinetics.

2.5.2 The Grain-Boundary Excess Volume

The preceding Section revealed that drag forces, which are exerted by slower TL or QP migration, can reduce grain-boundary kinetics by lowering the effective mobility. However, a similar change of the growth rate would also be observed, if there is a size-dependent mechanism that lowers the overall thermodynamic driving force for boundary migration. Estrin *et al.* suggested that such a process could be the redistribution of the grain-boundary-excess volume, when the grain-boundary density A^{GB}/V is reduced during coarsening of a polycrystalline material [64].

The lower atomic density of grain boundaries — this deficit is often allocated to an fictive excess volume δV^{GB} within the grain boundary, or equivalently to a specific grain-boundary excess $\beta = \delta V^{\mathrm{GB}}/A^{\mathrm{GB}} \approx 0.01 \ldots 0.1$ nm [14] — requires that during grain growth the excess volume $\delta V^{\mathrm{GB}} = \beta \cdot \Delta A^{\mathrm{GB}}$, which is connected to the annihilated grain-boundary area ΔA^{GB}, has to be redistributed. This is possible either by transport of atoms to the shrinking grain boundary or by the accomodation of vacancies in the adjacent grains. Estrin and colleagues argued that the first case is unlikely due to mass conservation in

a closed system, and only the latter one would be available in order to compensate the released excess volume [65–67]. However, this entails that the vacancy density in the crystal lattice will be increased above the equilibrium concentration, which will in turn raise the system's free energy. Grain growth will therefore continue only until the effective release of energy becomes zero,

$$\mathrm{d}G^{\mathrm{tot}} = -\mathrm{d}G^{\mathrm{GB}} + \mathrm{d}G^{\mathrm{Vac}} = 0, \tag{2.53}$$

where $\mathrm{d}G^{\mathrm{GB}}$ and $\mathrm{d}G^{\mathrm{Vac}}$ denote the decrease of energy due to grain growth and the increase of energy due to vacancy generation in the lattice, respectively.

Parallel to the emission of vacancies from the shrinking boundary into the lattice, the excess-vacancy concentration might be compensated by the diffusion and annihilation of vacancies in dislocations and grain boundaries. Since this annihilation process needs the diffusion of vacancies along a distance l to the next-nearest vacancy sink, the characteristic time τ for a vacancy to be removed is determined by [64],

$$\tau = \frac{l^2}{D_{\mathrm{V}}}, \tag{2.54}$$

where D_{V} is the vacancy diffusivity in the lattice. Thus, $\mathrm{d}G^{\mathrm{Vac}}/\mathrm{d}t$ can become positive and negative — however, it is likely that the generation of new vacancies is faster than their annihilation, particularly if τ is large. In this case G^{Vac} increases until after a time t^* the condition of Eq. (2.53) is reached, and the effective driving force for boundary motion is zero; accordingly, the migration of the grain boundary, and thereby the emission of new vacancies, is stopped. At the same time the annihilation of the vacancy excess continues, and the vacancy concentration gradually reduces. At the moment the condition $\mathrm{d}G^{\mathrm{tot}} > 0$ is reached, grain growth will be enabled again. The boundary will then migrate and emit vacancies until the driving force is again zero and grain-boundary motion will be "locked" one more time [65]. If the relaxation time τ is on the order of t^*, the jerky migration of the grain boundary becomes continuous, but is now controlled by the diffusion of vacancies with [64, 65],

$$v^{\mathrm{GB}} = \frac{\gamma^{\mathrm{GB}} \cdot D_{\mathrm{s}}}{24 \cdot N \cdot k_{\mathrm{B}} T \cdot Z \cdot \beta^2} \cdot \left(\frac{R}{l}\right)^2, \tag{2.55}$$

where D_{s} is the lattice self-diffusion coefficient, N the number of atoms per unit volume and Z the atomic coordination number.

Vacancies can be annihilated by dislocations in the grain interior or by grain boundaries. However, for nanocrystalline materials it is unlikely to find dislocations in the grains, since there would be an image force $F \propto x^{-1}$ (x denotes the distance between the grain boundary and the dislocation, which will be obviously small in nanocrystalline materials) that tries to pull the dislocation out of the crystallite (provided that the mobility of the dislocation is sufficient) [65, 68]. This means that in nanocrystalline materials only grain boundaries are available as vacancy sinks, and the approximation $l \approx R$ should hold. Thus, if the redistribution of excess volume is the rate-limitting process, the kinetics of grain-boundary migration can be equated as [64, 65],

$$v^{\mathrm{GB}} = \frac{\gamma^{\mathrm{GB}} \cdot D_{\mathrm{s}}}{24 \cdot N \cdot k_{\mathrm{B}} T \cdot Z \cdot \beta^2}, \tag{2.56}$$

in which the grain-boundary velocity is apparently independent of the grain size — similar to the linear evolution of the grain size according to TL-induced rescaling of the mobility. Comparing Eq. (2.56) with the kinetics of Eq. (2.19) for conventional curvature-driven growth yields the transition grain size R_{v}, where the rate-controlling process shifts from the redistribution of excess volume to grain-boundary curvature [64],

$$R_{\mathrm{v}} = 24 \cdot N \cdot k_{\mathrm{B}} T \cdot Z \cdot \beta^2 \cdot \frac{M^{\mathrm{GB}}}{D_{\mathrm{s}}}. \tag{2.57}$$

In parallel to the change of growth kinetics from linear to parabolic at $R = R_{\mathrm{v}}$, a decrease of the activation enthalpy from lattice self-diffusion to grain-boundary diffusion should be observed ($Q_{\mathrm{s}} > Q_{\mathrm{B}}$ [26]). Particularly the change of the activation enthalpy should allow to distinguish whether linear growth — if actually found — occurs from TL drag or the redistribution of grain-boundary excess volume.

Although Estrin's suggestion of vacancy emission during grain growth is of course a possible scenario, the model does not take into consideration that a vacancy excess might also relax by diffusion along the boundaries to an appropriate vacancy sink, as the diffusivity in the atomically less dense grain boundaries should be larger than the diffusivity through the lattice. However, if vacancy diffusion in grain boundaries is dominating (in which case of course an activation enthalpy different to the one for lattice self-diffusion should be expected), the generation of vacancy excess, and therefore the prediction of a grain-size-independent growth rate, becomes unreliable. The application of Estrin's model should therefore be handled with care.

2.6 The Role of Impurities in Grain-Boundary Migration

In dealing with grain-boundary migration it is unavoidable to consider impeding effects due to solute atoms, either from intentional doping or by inadvertent contamination. At impurity concentrations below the solubility limit, the two species of atoms will form a solid solution with matrix concentration C_β and a much lower solute concentration C_α. In the presence of solute atoms, the lattice of the matrix atoms will be subjected to compressive or tensile deformation, if the solutes are either smaller or larger compared to the size of the matrix atoms. In particular when the atoms differ in size by more than ~15% a distinct elastic strain energy ΔH^{el} emerges in the host lattice [14,69]. In addition to the elastic strain, the difference in the electron-orbital and valance structure may prevent solute and lattice atoms from attaining a relaxed chemical state, and provokes thereby an additional increase of the free energy by ΔH^{chem} [69]. The electron (or chemical) contribution ΔH^{chem} can vary significantly for various combinations of matrix and solute elements, and can be positive or negative for transition metals, whereas the elastic energy ΔH^{el} will always be positive [69].

The free energy of a polycrystalline solid solution is determined by the bulk and grain-boundary quantities involved in Eq. (2.1), and additionally by the interaction energy of the host lattice and the solutes,

$$G = \sum_i \mu_{i,0}\, N_i + \Delta G_{\text{mix}} + \gamma^{\text{GB}} \cdot A^{\text{GB}}, \tag{2.58}$$

where $\mu_{i,0}$ is the chemical potential of the pure species i, N_i the number of moles of species i and $\Delta G_{\text{mix}} = \Delta H_{\text{mix}} - T \cdot \Delta S_{\text{mix}}$ the change in energy of the system when the solid solution is formed. The enthalpy of mixing follows from the summation of the elastic and chemical interaction enthalpies [70],

$$\Delta H_{\text{mix}} = \Delta H^{\text{el}} + \Delta H^{\text{chem}}. \tag{2.59}$$

Since ΔH^{el} and ΔH^{chem} are caused by the interaction of solutes with the host lattice, it is likely that they will depend on the actual configuration of the lattice. It is conceivable that particularly grain boundaries, which have a lower atomic density than the crystalline parts of a polycrystal, offer an attractive environment for solute atoms. This anisotropy of solute-atom excess energy is reflected in a lower enthalpy of mixing of the solid solution in the grain boundary than in the bulk, i.e. $\Delta H^{\text{GB}}_{\text{mix}} \leqslant \Delta H^{\text{bulk}}_{\text{mix}}$. The lower excess enthalpy at the interface establishes therefore a driving force for the segregation of solutes (by lowering the free energy of the system), and leads to an increase of C_α at the grain boundary — the consequence will be an excess concentration of solute atoms at the interface [71–73].

Fig. 2.14(a) shows schematically the ideal symmetric enrichment of solute atoms at a grain boundary that

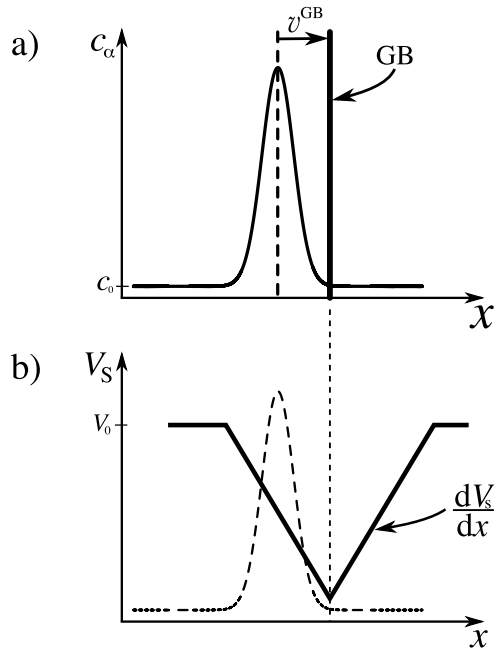

Figure 2.14: (a) Excess concentration of solute atoms at a grain boundary. (b) Influence of a solute pile-up at a migrating boundary. The energy of the system is increased, if the solute excess falls behind the migrating boundary. According to the gradient $\vec{\nabla} V_S$ of the potential energy of the solutes an attractive force between the solute atmosphere and the boundary is established.

is not moving (the grain boundary position is indicated by the dashed vertical line). If the boundary migrates with a velocity v^{GB}, the solute atmosphere may fall behind the grain boundary, depending on the ability of the solute atoms to follow (the position of the moving grain boundary is indicated by the solid vertical line in Fig. 2.14(a)). In this case, the excess pile-up of solute atoms will experience an attractive force [72,73],

$$f_{\mathrm{s.d.}} = N \cdot \int_{-\infty}^{\infty} c_\alpha(x)\, \vec{\nabla} V_{\mathrm{s}}(x)\, \mathrm{d}x, \tag{2.60}$$

according to the gradient $\vec{\nabla} V_{\mathrm{s}}$ of the solute's potential energy (see Fig. 2.14(b)), which tries to pull the solute atmosphere along with the grain boundary. The parameters N and $c_\alpha(x)$ in Eq. (2.60) specify the number of impurity-atom sites per unit area of the grain boundary and the impurity concentration, respectively. The equivalent, but opposite force $-f_{\mathrm{s.d.}}$ will be exerted by the solute atoms on the boundary, which in turn will slow down the grain-boundary velocity due to [73,74],

$$v^{\mathrm{GB}} = M^{\mathrm{GB}} \cdot \left(\frac{2\,\gamma^{\mathrm{GB}}}{R} - f_{\mathrm{s.d.}} \right), \tag{2.61}$$

where $f_{\mathrm{s.d.}}$ denotes the retarding force due to the lagging solute atmosphere (solute drag). In response to the attractive interaction between solutes and boundary, the impurity pile-up diffuses according to the Nernst-Einstein relation with a velocity [74],

$$v^{\mathrm{s}} = \frac{D_{\mathrm{sol}}}{k_{\mathrm{B}} T}\, f_{\mathrm{s.d.}} = M_{\mathrm{s}} \cdot f_{\mathrm{s.d.}}, \tag{2.62}$$

in which D_{sol} denotes the solute diffusivity and M_{s} the mobility of the solute atmosphere.

The ability of a certain species of impurity atoms to inhibit grain-boundary migration depends strongly on the relation between v^{s} and v^{GB}, and in the limits $v^{\mathrm{GB}} \gg v^{\mathrm{s}}$ and $v^{\mathrm{GB}} \ll v^{\mathrm{s}}$ the drag effect disappears. In the first case, the boundary will simply break away from the solutes and behave like in an impurity-free polycrystal, whereas in the second case the high solute velocity always keeps the pile-up along with the boundary. In both cases is $f_{\mathrm{s.d.}} \approx 0$ [73,75]. In the intermediate regime, the grain-boundary migration is controlled by the solute diffusivity, which has in general a significantly higher activation enthalpy than grain-boundary self-diffusion [26] and thus, at low and intermediate temperatures impurity kinetics controls grain-boundary migration, $v^{\mathrm{GB}} = v^{\mathrm{s}} = M_{\mathrm{s}} \cdot f_{\mathrm{s.d.}}$. This is basically the reason, why impurity concentrations always need to be critically discussed in the frame of experimental grain-growth investigation, and explains the observation of growth exponents $m > 2$.

Of course, the increased impurity concentration at the grain boundary may not only change the rate-controlling mechanism from boundary migration to solute diffusion, but it also brings up another question: Do the thermodynamic properties of the grain boundary change in the presence of an excess concentration? To find an answer to this question it is useful to consider the free energy of both the grain boundary and the crystallite separately (which is possible, as extensive thermodynamic variables can be treated additively). If the indices α and β denote the solute and the matrix atoms respectively, the

differential free energies of the boundary ($\mathrm{d}G^{\mathrm{B}}$) and the grain ($\mathrm{d}G^{\mathrm{X}}$) are given for $\mathrm{d}T = 0$ and $\mathrm{d}p = 0$ according to Eq. (2.1) by [76,77],

$$\mathrm{d}G^{\mathrm{X}} = \mu_\alpha \,\mathrm{d}N_\alpha^{\mathrm{X}} + \mu_\beta \,\mathrm{d}N_\beta^{\mathrm{X}} \tag{2.63a}$$

$$\mathrm{d}G^{\mathrm{B}} = \mu_\alpha \,\mathrm{d}N_\alpha^{\mathrm{B}} + \mu_\beta \,\mathrm{d}N_\beta^{\mathrm{B}} + \gamma^{\mathrm{GB}} \,\mathrm{d}A^{\mathrm{GB}}. \tag{2.63b}$$

Further, the Gibbs-Duhem equation, i.e. $\sum_i (n_i \mathrm{d}\mu_i) = -S\,\mathrm{d}T + V\,\mathrm{d}p$, can also be defined for the two domains separately, which yields,

$$N_\alpha^{\mathrm{X}} \,\mathrm{d}\mu_\alpha + N_\beta^{\mathrm{X}} \,\mathrm{d}\mu_\beta = 0 \tag{2.64a}$$

$$N_\alpha^{\mathrm{B}} \,\mathrm{d}\mu_\alpha + N_\beta^{\mathrm{B}} \,\mathrm{d}\mu_\beta + A^{\mathrm{GB}} \,\mathrm{d}\gamma^{\mathrm{GB}} = 0, \tag{2.64b}$$

where the same conditions for T and p apply as for Eq. (2.63). Solving Eq. (2.64a) for $\mathrm{d}\mu_\beta$ and substituting in Eq. (2.64b) gives,

$$\mathrm{d}\gamma^{\mathrm{GB}} = -\Gamma_\alpha \,\mathrm{d}\mu_\alpha \quad \text{with} \quad \Gamma_\alpha = \frac{1}{A^{\mathrm{GB}}} \left(N_\alpha^{\mathrm{B}} - N_\beta^{\mathrm{B}} \cdot \frac{N_\alpha^{\mathrm{X}}}{N_\beta^{\mathrm{X}}} \right), \tag{2.65}$$

which is the Gibbs' interface equation [77]. The parameter Γ_α describes the specific excess of solute atoms at the grain boundary with respect to the bulk solute concentration. The chemical potential μ_α of the solute atoms can be equated for an ideal solid solution with low solute concentration C_α as,

$$\mu_\alpha^{\mathrm{B}} = \mu_\alpha^{\mathrm{X}} = \mu_\alpha = \mu_0 + RT \cdot \ln C_\alpha, \tag{2.66}$$

where μ_0 specifies a reference level (the left-hand side of Eq. (2.66), i.e. $\mu_\alpha^{\mathrm{B}} = \mu_\alpha^{\mathrm{X}}$, holds only for thermodynamic equilibrium). Thus, Eq. (2.65) can be expressed in the form [77,78],

$$\left. \frac{\mathrm{d}\gamma^{\mathrm{GB}}}{\mathrm{d}\ln C_\alpha} \right|_{T,p} = -RT \cdot \Gamma_\alpha, \tag{2.67}$$

which is known as the Gibbs adsorption isotherm. Eq. (2.67) states that γ^{GB} decreases for increasing solute concentration, as long as $\Gamma_\alpha > 0$, i.e. if there is an accumulation (adsorption) of solute atoms at the grain boundary [77]. Since $\gamma^{\mathrm{GB}} > 0$ is the root cause for the inherent instability of polycrystalline microstructures, solute segregation can provide a thermodynamic stabilization against grain growth. For the maximum solute adsorption possible, the grain-boundary excess of solute atoms approaches the saturation level, $\Gamma_\alpha \to \Gamma_\alpha^{\mathrm{sat}}$. For this situation, grain growth — i.e. the decrease of A^{GB} — involves the emission of solutes from the grain boundary into the grain (similar to the redistribution of excess volume,

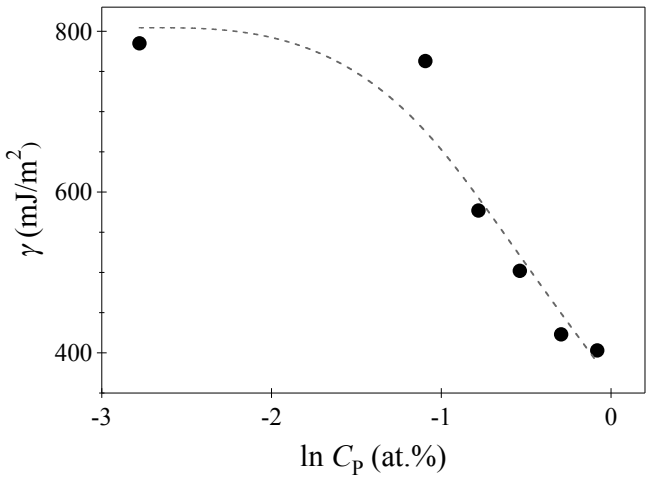

Figure 2.15: Lowering of γ^{GB} by segregation of solute atoms, Eq. (2.67), shown on the example of the Fe-P system. The graph shows that the grain-boundary energy of Fe can be reduced at least by a factor of two, if phosphorus atoms are segregating to the grain boundaries of the Fe host lattice. The data has been taken from Ref. [20].

see Section 2.5.2). However, since this process requires the expense of the segregation enthalpy, the effective driving force for grain-boundary migration is lowered thereby, and grain growth is additionally impeded.

A prominent example for solute-induced lowering of the grain-boundary energy is the binary system Fe-P, which was investigated by Hondros and Seah [20]. Fig. 2.15 shows the relationship between γ^{GB} and the phosphorous concentration, which demonstrates a significant decrease of γ^{GB} from 0.8 J/m^2 for pure Fe to 0.4 J/m^2 at a phosphorous concentration of $C_P \approx 1$ at.%.

The effectivity of solute-stabilized nanostructures has been demonstrated by C.E. Krill *et al.* on the Pd-Zr system, where a decrease of the grain-boundary energy by a factor of four has been achieved for zirconium concentrations of up to 20 at.%. The stability of nanocrystallie Pd against grain growth has been shown to extend for the highest zirconium concentrations investigated to temperatures very close to the melting temperature of Pd [79, 80].

Obviously, impurity atoms can have tremendous impact on the type and the kinetics of grain-growth, either by dragging the grain boundaries or by lowering the thermodynamic parameter γ^{GB}. Particularly interesting is the situation, if an inhomogeneous solute distribution induces anisotropic boundary properties, which may then set the stage for abnormal grain growth.

Chapter 3

Experimental Characterization of Grain Growth

The investigation of grain-growth kinetics in nanocrystalline materials and the question, whether grain-boundary curvature is superseded by a different rate-controlling mechanism when the grain size of a polycrystal falls below a certain critical limit, is in the focus of this study. This chapter will introduce the experimental investigation tools and techniques that have been deployed to elucidate these questions. Beside a brief presentation of basic principles of calorimetric analysis and electron microscopy, the quantitative investigation of isothermal grain growth by x-ray diffraction will be in the focus of this chapter.

3.1 X-Ray Diffraction

Beside its classical applications in crystallography, x-ray diffraction (XRD) offers two exceptional features, which makes it an outstanding characterization method for grain growth in nanocrystalline materials: firstly, it is a non-destructive method for fast *in-situ* tracking of grain coarsening and secondly, XRD provides — in contrast to cross-sectional micrographs — information of a significantly broader statistical basis. Thus, XRD can be used to investigate time-resolved grain growth continuously over extended time scales and on a large number of grains.

The following sections present the experimental setup for the XRD experiments, and discuss different quantitative analysis methods of the diffraction profile.

3.1.1 Experimental Setup for XRD

The investigations of isothermal grain growth under non-ambient conditions have been performed in a "Panalytical X'Pert Pro" powder-diffraction system that was equipped with a dedicated high-temperature heating stage. Fig. 3.1 illustrates the setup of the XRD facility.

The configuration of the incident-beam side included a Cobalt (Co) x-ray tube with the typical emission wavelengths at $K\alpha_1 = 1.78901$ Å, $K\alpha_2 = 1.79290$ Å and $K\beta = 1.62083$ Å that was followed by a Soller slit with a 0.02 rad divergence for axial confinement of the beam. Compared to other target materials, Co radiation was selected because it offers several advantages regrading signal-to-noise level, sample

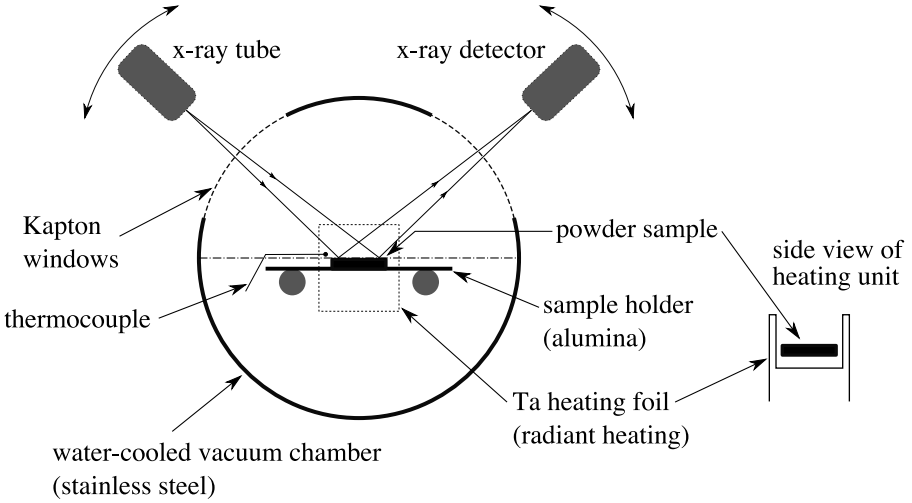

Figure 3.1: Experimental setup of the used x-ray diffractometer in Bragg-Brentano geometry. The system was equipped with a Co x-ray tube, a divergence filter on the incident side and a position-sensitive multi-channel detector on the diffracted side. To support annealing experiments at non-ambient conditions, the diffraction system included a high-temperature hot stage that allowed also for annealing under high-vacuum conditions.

penetration and peak profile. A short explanation of these three issues is given in the following:

- A critical issue in time-resolved grain-growth experiments is the quality of the diffraction pattern. In general, the counting statistics is determined by the product of the intrinsic diffraction intensity and the integration time, where the envisaged time-resolved analysis constraints the latter one. In the following sections it will be shown that the accurate evaluation of grain size (and also of microstrain), either from the width of the diffraction peaks (see Section. 3.1.2.2) or from the peak profile (see Section 3.1.4.2), strongly depends on a reliable measurement of the respective peak-shape-related quantity. Different to a standard Copper (Cu) x-ray source, Co radiation does practically not excite x-ray fluorescence (XRF) in Fe. Thus, a x-ray monochromator on the diffracted-beam side can be omitted, and a significant gain in diffraction intensity — and therefore an improved signal-to-noise ratio — is obtained.
- Trace impurities and oxidation are well known to have the potential of affecting the kinetics of grain growth tremendously. Particularly oxidation of the specimens during annealing can be a critical point in an *in-situ* experiment (since oxidation may further proceed by residual oxygen in the experiment chamber) and may influence growth kinetics detrimentally. Hence, x-ray radiation with a lower absorption coefficient, and therefore larger penetration depth, would be preferred in order to be less sensitive for a possible oxide layer at the surface. Additionally, the larger penetration depth increases the number of measured grains, which allows for a broader statistical basis, see Section 3.1.3.[1]

[1] X-ray absorption coefficients in Fe [81]: $\alpha_{Co} = 440\ \mathrm{cm}^{-1}$ and $\alpha_{Cu} = 2333\ \mathrm{cm}^{-1}$. The smaller absorption coefficient of Co radiation provides a penetration depth of ~5 μm and ~10 μm for the (110) and (220) peak in Fe, respectively.

- The larger wavelength of Co radiation compared to Cu entails a broadening of the diffraction peaks. If the inevitable apperative broadening of the diffraction system (*cf.* Section 3.1.5) is independent of the wavelength, the upper limit (resolution limit) of the grain size that can be measured by XRD can be extended to larger values.

The signal on the diffracted-beam side was detected by a combination of a position-sensitive multi-channel detector and a 0.02 rad Soller slit. The detection unit of the diffracted-beam side and the chosen scan parameters allowed for nearly real-time tracking of the microstructural evolution during annealing (the first and second order of the Fe (110) reflection could be accurately measured within approximately 4 min).

For the *in-situ* annealing experiments a high-temperature hot stage with a radiant heater was directly mounted inside the diffractometer. The heater was connected to an "Eurotherm 2216" PID controller, which used the input of a contact-free thermocouple for temperature feedback (see Fig. 3.1). The exact sample temperature was calculated in a second step from the lattice parameters that were determined by Cohen's method from the measured diffraction data, and being compared with the precise temperature-dependent thermal-expansion coefficient of α-Fe [82, 83]. The setpoint of the PID controller for each isothermal anneal was selected according to a before recorded calibration curve, where the true temperature was determined for a number of given readings of the thermocouple. In order to minimize oxidation of the sample during the anneal, the hot stage was connected to a turbo-molecular pump that maintained high-vacuum conditions throughout the annealing experiment (the dynamic pressure during the anneals was typically $p \lesssim 10^{-5}$ mbar).

3.1.2 Quantitative Analysis of X-Ray-Diffraction Experiments

At the beginning of the 20th century, von Laue and Bragg showed that a periodic crystal lattice can cause the diffraction of an incident x-ray beam, with an intensity distribution that is equal to the Fourier transformation of the real-space lattice [84]. Bragg showed that this phenomenon must be caused by the interference of scattered x-ray beams (electromagnetic waves), and concluded that the criterion to observe an intensity signal at a diffraction angle 2θ is given by [84, 85],

$$\sin\theta_{\text{hkl}} = \frac{\lambda}{2 \cdot d_{\text{hkl}}} \quad , \tag{3.1}$$

where λ is the wavelength of the x-ray radiation and d_{hkl} is the interplanar spacing of the diffracting lattice planes. Bragg's concept for the diffraction of an incident plane wave by the crystal lattice is illustrated in Fig. 3.2, which shows for the scattered x-rays the relationship between d_{hkl} and the coherency of diffracted waves. It is obvious that the condition to find a diffraction signal by constructive interference depends basically on the different path lengths, which the beams have to travel between the x-ray source and the point of observation (the difference in path length will define the phase differences between the scattered x-ray beams), and is therefore a measure for the atomic configuration of the crystal lattice, see Fig. 3.2.

Bragg's equation (3.1) allows for a particular spacing d_{hkl} of planes to calculate at which diffraction angle $2\theta_{\text{hkl}}$ a diffraction signal is expected (usually called a "Bragg angle"). Thus, under ideal conditions the

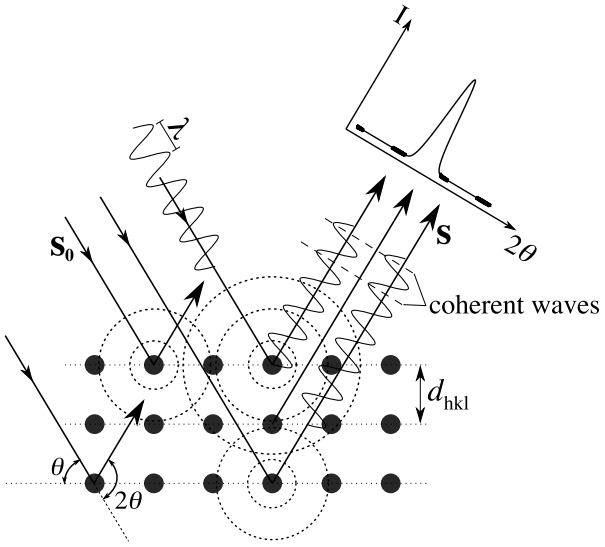

Figure 3.2: X-ray diffraction in crystalline materials. An incident x-ray beam (incident plane electromagnetic wave $\mathbf{s}_0$) is scattered by the atoms of a crystal. Depending on the spatial positions of the atoms, the phase relation of the scattered beams can be coherent or not. Only for coherent phases a constructive interference occurs and an intensity signal $I(2\theta)$ can be measured.

diffracted intensity in the plane of observation will be zero for any 2θ value, unless a Bragg angle $2\theta_{hkl}$ is measured (this reflects the discrete nature of d_{hkl}). However, the experience from diffraction experiments teaches that only the most perfect single crystals come close to this prediction of a δ-function intensity. Unlike Bragg's conception, any real sample — and for those in particular the nanocrystalline materials —- causes a broadening of the diffraction profile on the 2θ axis (either by size effects or lattice strain), and therefore an intensity distribution $I(2\theta)$ around the Bragg angle.

The following sections describe XRD by non-ideal crystalline specimens, and will show the high potential of XRD as an analyzing method in the course of nanocrystalline grain growth.

3.1.2.1 Wide-Angle X-ray Diffraction on Nanocrystalline Materials

Diffraction spectra measured on nanocrystalline materials are mostly designated by peaks that are significantly broader than the spot intensity according to Bragg's equation (3.1). However, why does Bragg's equation fail to describe the actual diffraction profile? The answer to this question is rather simple: The intensity $I(2\theta)$ will only be zero at 2θ positions different from the Bragg angles, if for each non-coherent beam a counterpart is found, for which the field vectors cancel out by interference. This constraint might only be met, if there is an infinite number of scattered beams, which means however that the diffracting grain or crystallite should also be of infinite size. To evaluate the diffraction profile for a crystallite of finite size it is necessary to inspect the process of interference. If E_k is the (complex) electric field vector of the scattered wave k,

$$E_k = E_{k,0} \cdot \exp\{i(2\pi\nu t - (2\pi/\lambda) \cdot x_k)\}, \tag{3.2}$$

with $\nu = c_0/\lambda$ being the frequency of the x-ray radiation (c_0 denotes the speed of light in vacuum), t the time and $(2\pi/\lambda) \cdot x_k$ the phase relation according to the travelled distance x_k, the observed intensity is determined by the summation of all scattered x-rays E_k, $I(2\theta) = |E|^2 = \left|\sum_k E_k\right|^2$. Since the incident plane wave is scattered by each atom of the crystallite independently, the summation of the electric field components is equal to a summation over all unit cells of the lattice. Since it is the crystallography that is defining the phase relation of the various scattered beams, it is needed to identify the spatial position of each unit cell — and therefore the path length x_k of the various waves. Fig. 3.3 illustrates schematically a crystallite with the spatial dimensions $x = (N_1 \cdot a_1)$, $y = (N_2 \cdot a_2)$ and $z = (N_3 \cdot a_3)$, and a vector $\mathbf{R}_{m_1 m_2 m_3} = m_1\mathbf{a}_1 + m_2\mathbf{a}_2 + m_3\mathbf{a}_3$ that identifies each unit cell according to the unique indices m_1, m_2 and m_3. The vectors $\mathbf{a_1}$, $\mathbf{a_2}$ and $\mathbf{a_3}$ are the basis vectors of the unit cells, with an individual length equal to the lattice parameter in the specific direction.

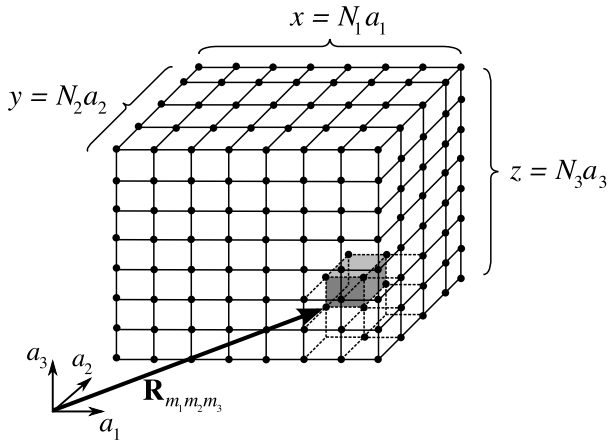

Figure 3.3: Crystallite of size $x = (N_1 \cdot a_1)$, $y = (N_2 \cdot a_2)$ and $z = (N_3 \cdot a_3)$. Each unit cell of the crystallite is identified by the unique indices m_1, m_2 and m_3, and is referenced by a vector $\mathbf{R}_{m_1 m_2 m_3}$ that is defining the spatial location of each unit cell according to its unique indices.

With the descriptions of Fig. 3.3 the intensity signal can then be calculated from the threefold summation over all scattered beams,

$$I(2\theta) = \left| \sum_{m_1=1}^{N_1} \sum_{m_2=1}^{N_2} \sum_{m_3=1}^{N_3} E_{m_1 m_2 m_3} \right|^2, \tag{3.3}$$

where $E_{m_1 m_2 m_3}$ defines the complex electric field component of the beam scattered by the unit cell with the indices m_1, m_2 and m_3. In terms of the diffraction vector $(\mathbf{s} - \mathbf{s}_0)$ — for which the identity $|\mathbf{s} - \mathbf{s}_0| = 2 \cdot \sin(\theta)$ can be quoted — the intensity $I(\mathbf{s} - \mathbf{s}_0)$ can then be evaluated to yield [84],

$$I(\mathbf{s}-\mathbf{s}_0) = I_0 \cdot \frac{\sin^2\left(\frac{\pi}{\lambda}(\mathbf{s}-\mathbf{s}_0)\, N_1 \cdot \mathbf{a}_1\right)}{\sin^2\left(\frac{\pi}{\lambda}(\mathbf{s}-\mathbf{s}_0)\, \mathbf{a}_1\right)} \cdot \frac{\sin^2\left(\frac{\pi}{\lambda}(\mathbf{s}-\mathbf{s}_0)\, N_2 \cdot \mathbf{a}_2\right)}{\sin^2\left(\frac{\pi}{\lambda}(\mathbf{s}-\mathbf{s}_0)\, \mathbf{a}_2\right)} \cdot \frac{\sin^2\left(\frac{\pi}{\lambda}(\mathbf{s}-\mathbf{s}_0)\, N_3 \cdot \mathbf{a}_3\right)}{\sin^2\left(\frac{\pi}{\lambda}(\mathbf{s}-\mathbf{s}_0)\, \mathbf{a}_3\right)}, \tag{3.4}$$

where $\mathbf{s_0}$ and $\mathbf{s}$ are unit vectors ($|\mathbf{s}| = |\mathbf{s_0}| = 1$) that describe the direction of the incident and the diffracted waves, respectively (see Fig. 3.2). The parameters N_1, N_2 and N_3 denote the highest index of the unit cells in one of the three crystal axis, wherefore those parameters are a quantitative measure for the dimension of the coherently-scattering crystallite volume.

To explore the characteristics of Eq. (3.4) it is useful to consider a situation where only one crystal axis is parallel to the diffraction vector (in the following this will be the $\mathbf{a}_3$ direction), while the other two directions ($\mathbf{a}_1$ and $\mathbf{a}_2$) are perpendicularly aligned with the diffraction vector. Such a situation might be found for example, if an arbitrary crystallite is rotated in a way that one set of (hkl) lattice planes is perpendicular to the diffraction vector, which might then be considered as $(00l)$ planes in a customized coordinate system. Then, Eq. (3.4) will reduce to,

$$I(2\theta) = I_0 \cdot \frac{\sin^2\left(\frac{2\pi}{\lambda}\sin(\theta)\, N_3 a_3\right)}{\sin^2\left(\frac{2\pi}{\lambda}\sin(\theta)\, a_3\right)}, \tag{3.5}$$

where the vector product $(\mathbf{s}-\mathbf{s}_0)\cdot\mathbf{a}_3 = 2\,a_3\sin(\theta)$ has been applied. Fig. 3.4 illustrates the alignment of $(00l)$ lattice planes with the diffraction vector $(\mathbf{s}-\mathbf{s_0})$, where $(\mathbf{s}-\mathbf{s_0})$ is assumed to be parallel to the $\mathbf{a}_3$ crystal axis.

Since the quantity $z = N_3 \cdot a_3$ is equal to the intercept length L of the crystallite in the direction of the diffraction vector, Eq. (3.5) has the quality to relate the uniaxial size L of a crystallite to the shape of the measured diffraction profile $I(2\theta)$. The effect of crystallite size on the peak profile is illustrated in Fig. 3.5

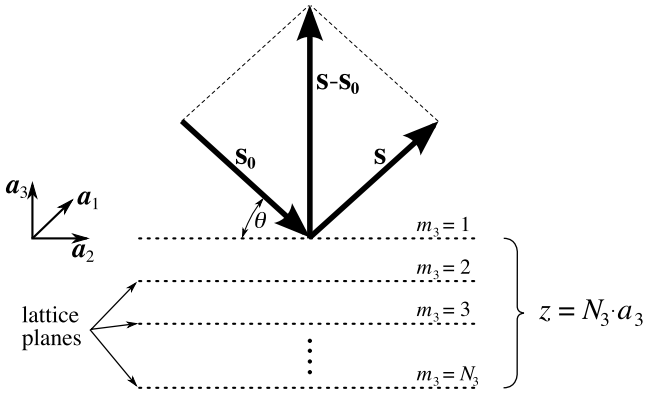

Figure 3.4: Alignment of a crystallite with respect to the diffraction vector $(\mathbf{s}-\mathbf{s_0})$. Only the $\mathbf{a}_3$ direction has a parallel orientation with the diffraction vector, whereas the other two directions are perpendicular. The vector products of Eq. (3.4) will therefore only be different from zero for the $\mathbf{a}_3$ direction, while the other two will be zero. The diffraction profile $I(2\theta)$ of this configuration is then given by Eq. (3.5).

for two different parameters $N_3 = 20$ and $N_3 = 80$. The peak maximum is found for both curves, if the denominator in Eq. (3.5) is equal to zero, i.e. if the condition $(2\pi/\lambda)\sin(\theta)a_3 = n\pi$ is satisfied, which is obviously equal to Bragg's equation (n denotes the different orders of the periodic $\sin^2()$ function in the denominator of Eq. (3.5)). Fig. 3.5 clearly shows that there is a tremendous impact of the crystallite size on the shape of the diffraction profile: Diffracting crystallites of small size obviously cause a substantial broadening of the intensity profile.

The correlation between crystallite size and the width of a measured diffraction peak offers the appealing opportunity to use XRD for the non-destructive *in-situ* investigation of the microstructural evolution in the course of grain growth — and due to the obvious sensitivity on very small grain sizes, XRD is particularly convenient to track the coarsening of nanocrystalline materials. The quantitative evaluation of the peak width with respect to the crystallite size was first proposed by Scherrer in 1918 [86]. The basic concepts of the Scherrer method and its limitations will be discussed in the following section.

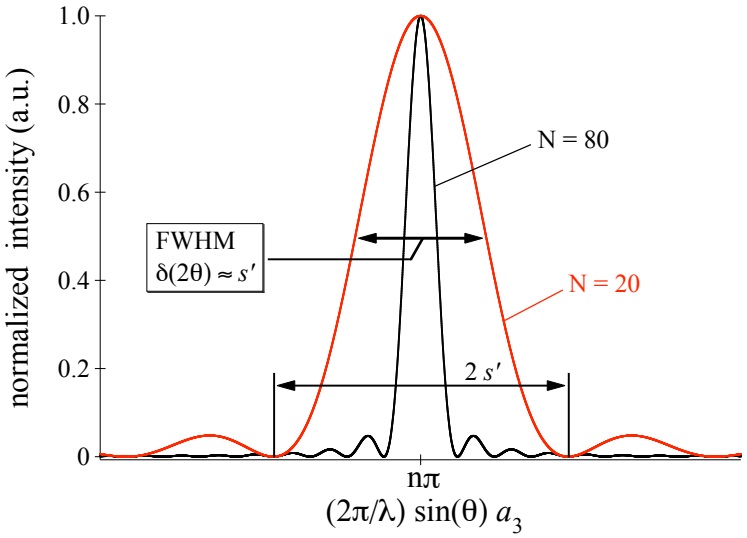

Figure 3.5: Plot of Eq. (3.5) for two different parameters $N_3 = 20$ and $N_3 = 80$. The graph illustrates that the crystallite size will have a substantial impact on the peak profile, which makes XRD to a convenient and powerful tool for the investigation of microstructural evolution.

3.1.2.2 The Scherrer Method and the Resolution Limit of Size-Broadening

Scherrer's approach to analyze diffraction peaks provides an exemplification on how a peak profile depends on the spatial dimension of a coherent domain [86]. To derive the Scherrer formula, the variable s with,

$$s \equiv \frac{2 \cdot \sin(\theta)}{\lambda}, \tag{3.6}$$

and the corresponding derivative $\delta s/\delta\theta$,

$$\delta s = \frac{\cos(\theta)}{\lambda}\,\delta(2\theta), \tag{3.7}$$

should be defined, in which $\delta(2\theta)$ will specify the full width at half maximum (FWHM) of the peak on the 2θ axis. The intensity profile of the diffraction peak according to Eq. (3.5) can then be expressed in terms of the new variable s,

$$I(s) = I_0 \cdot \frac{\sin^2\left(s \cdot \pi \cdot N_3 a_3\right)}{\sin^2\left(s \cdot \pi \cdot a_3\right)}. \tag{3.8}$$

Scherrer approximated the width δs of the peak (in s-space) by the distance between the peak maximum and the first zero $I\left(s'\right) = 0$ of Eq. (3.8) (this definition is shown in Fig. 3.5). Since this occurs for $\left(s' \cdot \pi \cdot N_3 a_3\right) = \pi$, the peak width (in terms of FWHM) can be equated as,

$$\delta s \approx s' = \frac{1}{L}, \text{ with } L = N_3 \cdot a_3. \tag{3.9}$$

Eq. (3.9) shows that the width of a diffraction peak is inversely proportional to the crystallite size, and with Eq. (3.7) the functional correlation between measured peak width $\delta(2\theta)$ and the crystallite size can be equated as [84, 86],

$$L = k \cdot \frac{\lambda}{\delta(2\theta)\cos(\theta)} \quad , \tag{3.10}$$

in which the numerical constant k was additionally introduced by Scherrer [86]. The constant ranges usually between $k = 0.84 \ldots 1.2$ [87] and depends mainly on the shape of the crystallites and on the kind of peak-width definition used in Eq. (3.10) — either in terms of the FWHM $\delta(2\theta)$ or alternatively in terms of the integral breadth β, which is defined by [84],

$$\beta = \frac{1}{I_{\max}} \cdot \int_0^\infty I(2\theta)\,\mathrm{d}(2\theta). \tag{3.11}$$

Fig. 3.6 shows the relationship between crystallite size L and peak width $\delta(2\theta)$ according to Eq. (3.10). The graph shows that the smaller the grains become, the broader the diffraction peak will be. Since the evaluation of the width of an experimentally measured peak is always connected to some uncertainty, it is obvious from Fig. 3.6 that the error in size will increase for larger grains. For example, assuming an uncertainty $\Delta\delta(2\theta) = 0.01°$, the relative error at 20 nm will be about 2%, but at 150 nm the error will be already 12%. Since multi-channel x-ray detectors have in general a lower angular resolution than point detectors, the real-time scanning of the samples is achieved at the expense of resolution and thus, there should be an upper limit of the measurable crystallite size (at least with respect to a tolerable error).

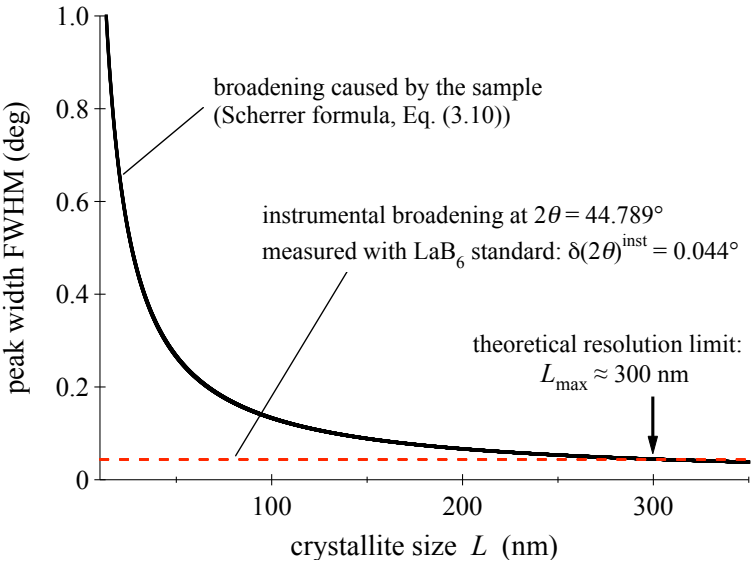

Figure 3.6: Plot of the size-dependent peak width (FWHM) according to Eq. 3.10, calculated for the (110) peak position $2\theta = 44.789°$ of Fe. The curve shows that particularly bellow ~100 nm the peak profile becomes significantly broadened due to the small grain size. The graph shows further for the used diffraction system the measured instrumental peak broadening $\delta(2\theta)^{\text{inst}} = 0.044°$ at the (110) diffraction angle of Fe (the system-related peak broadening has been measured with a standard LaB_6 powder sample). Comparing both curves, the intrinsic size broadening according to Eq. 3.10 and the size-independent instrumental broadening, reveals that the two curves intersect at a grain sizes of $L \approx 300$ nm, which obviously defines the largest measurable grain size, and therefore the size-resolution limit of the used diffraction system.

The problem of angular resolution seems not to apply to very small grains, however, some other problem can introduce a lower limit in the measurable grain size. This is, the diffracted intensity is strongly dependent on the volume of the grain and thus, the diffraction peak from very small grains might be lost in the background signal of the detector [84].

Apart from the low diffracted intensity by small grains and the increasing uncertainty at larger grain sizes, there is a further limitation in the applicability of grain-size measurements using wide-angle x-ray diffraction. Assuming an ideal δ-function intensity distribution $I(2\theta) = \delta(2\theta - 2\theta_0)$ that is recorded by a detector of finite angular resolution, the detector will start to measure the diffracted intensity as soon as the diffraction angle $2\theta_0 - \Delta_D/2$ is reached (Δ_D denotes the full angular aperture of the detection system). The detector signal will then gradually increase to attain a peak value at $2\theta = 2\theta_0$, which means that the δ-function intensity is mapped to a peak of finite width (the appropriate mathematical description of the measured peak profile is given by the convolution of a detector function and the intrinsic diffraction function [84]).

The unmeant instrumental peak broadening $\delta(2\theta)^{\text{inst}}$ that is caused by the involved equipment introduces a rigorous upper limit in the measurable crystallite size, see Fig. 3.6. At crystallite sizes above $L \approx 300$ nm the size broadening $\delta(2\theta)^{\text{size}}$ becomes smaller than $\delta(2\theta)^{\text{inst}}$, which defines the theoretical resolution limit

of the employed x-ray diffractometer. The required correction of the measured peak profile with respect to instrumental broadening — particularly at larger grain sizes — will be addressed in Section 3.1.5.

3.1.3 Statistical Aspects of X-ray Diffraction: The Grain-Size Distribution and the Average Grain Size of Polycrystals

The previous section revealed that XRD can be a powerful method to determine the size of an individual crystallite by evaluating the width of a diffraction peak. However, in polycrystalline materials, which are defined by a specific GDF and perhaps also by a distribution of grain shapes, there is of course a certain probability that out of the GDF a number of grains with similar orientation can be found that agree with the Bragg criterion of Eq. (3.1). It is conceivable that in a situation where more than one crystallite fulfills the condition for diffraction, the measured intensity peak will contain contributions from each of the diffracting crystallites. It is therefore consequent to ask what will be the meaning of L (evaluated from the width of the measured integral peak), if diffraction does not occur from a single crystallite, but is caused by an ensemble of grains?

Of course, it would be tempting to assume that the analysis of the peak width will yield some kind of average that is related to the different dimensions of the diffracting grains. To survey this problem (and to figure out how such an average could be interpreted) it is useful to start from the polycrystal itself and evaluate for a particular grain-size distribution of the microstructure the different averages of the grain size. Although the exact form of the GDF is often not known for a particular sample, empirically it is a lognormal function,[2]

$$g(D) = \frac{1}{\sqrt{2\pi}\; D\; \ln\sigma} \cdot \exp\left\{-\frac{1}{2}\cdot\left[\frac{\ln\left(D/D_0\right)}{\ln\sigma}\right]^2\right\}, \tag{3.12}$$

which was found in several cases to yield a sound compliance with the evaluated GDF, see for example the experiments on polycrystalline Fe in Fig. 1.1. The parameters D_0 and σ in Eq. (3.12) denote the median and the standard deviation of the distribution, respectively, and the pre-exponential factor normalizes the distribution in a way that $\int_0^\infty g(D)\,\mathrm{d}D = 1$. The question whether the nanocrystalline samples of the present study do also follow a lognormal size distribution was examined on a series of electron micrographs. The grain sizes of each micrograph have been evaluated by linear interception and are shown in the grain-size/frequency histogram of Fig. 3.7. The solid curve in Fig. 3.7 represents a least-square fit of Eq. (3.12), which demonstrates that a lognormal distribution yields obviously a decent description for the GDF of the studied nanocrystalline Fe samples.

If a lognormal function (or in principal any other mathematical function) can be used to approximate the GDF, it is possible to define a number of weighted averages of the GDF by using the nth moment $\langle D^n\rangle$ of

[2] It is very clear that in polycrystalline materials with non-uniform grain shape the set up of a GDF requires the definition of a virtual measure for the grain size. The two most frequently used parameters in this respect are the diameter D of a sphere with equivalent volume, and the mean intercept length L. The latter is particularly appealing, since, as will be shown in Section 3.1.3.1, it is the physical measure that is actually detected by XRD. Nevertheless, the application of standard growth theory requests the usage of the diameter D, or equivalently the grain radius $R = D/2$.

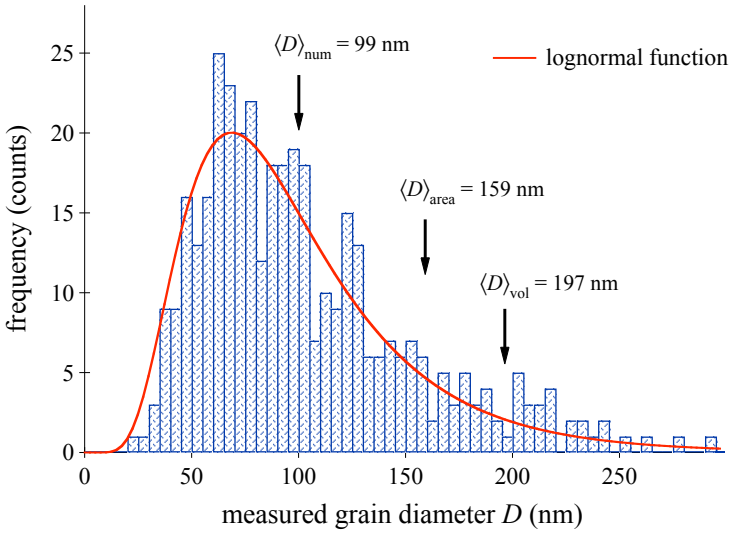

Figure 3.7: Histogram of grain sizes measured by the linear-intercept method on electron micrographs (the intercepting lines were aligned with the short and the long axis of each grain and both values have been averaged afterwards; thus, the frequency is plotted as a function of the "measured" diameter D, instead of the literal intercept length L). The nanocrystalline Fe sample of this histogram was annealed for 45 h at 452°C before sectioning. The solid line represents a least-square fit of Eq. (3.12), which obviously yields a remarkable compliance with the data and therefore supports the same GDF to hold for nanocrystalline Fe as has been found for polycrystalline (see Fig. 1.1). The three average grain sizes $\langle D\rangle_{\text{num}}$, $\langle D\rangle_{\text{area}}$ and $\langle D\rangle_{\text{vol}}$ that are included in the plot have been calculated for the lognormal fit via Eqs. (3.14) – (3.16).

$g(D)$,

$$\langle D^n\rangle = \frac{\int_0^\infty D^n\, g(D)\,\mathrm{d}D}{\int_0^\infty g(D)\,\mathrm{d}D}. \tag{3.13}$$

Eq. (3.13) shows that in principal there should be an endless number of moments and weighted averages that can be defined for the GDF, but for practical purpose only the three most important ones — those are the number-weighted, the area-weighted and the volume-weighted average grain size — are included in the following. Those three weighted grain-size averages can be defined by the respective moments of $g(D)$ as,

$$\langle D\rangle_{\text{num}} = \frac{\int_0^\infty D\cdot g(D)\,\mathrm{d}D}{\int_0^\infty g(D)\,\mathrm{d}D} = \langle D\rangle\,, \tag{3.14}$$

$$\langle D\rangle_{\text{area}} = \frac{\int_0^\infty D\cdot\left[kD^2\cdot g(D)\right]\mathrm{d}D}{\int_0^\infty \left[kD^2\cdot g(D)\right]\,\mathrm{d}D} = \frac{\left\langle D^3\right\rangle}{\langle D^2\rangle}, \tag{3.15}$$

$$\langle D\rangle_{\mathrm{vol}} = \frac{\int_0^\infty D\cdot\left[kD^3\cdot g(D)\right]\,\mathrm{d}D}{\int_0^\infty \left[kD^3\cdot g(D)\right]\,\mathrm{d}D} = \frac{\left\langle D^4\right\rangle}{\left\langle D^3\right\rangle}, \tag{3.16}$$

where k is a geometric constant within the weighting factor. Eqs. (3.14) – (3.16) indicate that each weighted average is defined by a weighting factor that is apparently equal to the physical meaning of the respective average. For example, $\langle D\rangle_{\mathrm{vol}}$ is calculated by using a factor of (kD^3), which is for $k = \pi/6$ equal to the volume of a sphere. Obviously, depending on the weighting factor used, the sensitivity of the average grain size will shift to the upper end of the GDF (i.e. to the largest grains of the microstructure), if higher moments of the distribution function are involved. This means, higher-order averages like $\langle D\rangle_{\mathrm{vol}}$ will mainly measure the size (and the kinetics) of the largest grains.

Obviously, a large variety of weighted averages is related to the GDF of a polycrystal, where each weighted average entails a different dependency on the actual population of the grain-size distribution. Thus, does one of those numerical averages correspond to the grain size measured by XRD on a polycrystalline sample? — According to the principles of interference, the crystallites that are in Bragg condition will diffract the incident beam independently, which means that the measured peak profile is determined by the superposition of the individual diffraction peaks related to each crystallite of particular size and shape. For the sake of simplicity the diffraction profile according to Eq. (3.5) (for a $(00l)$ reflection) can be approximated by a Gaussian peak [84],

$$\frac{\sin^2(N_3\cdot x)}{\sin^2(x)} \Rightarrow N_3^2\cdot\exp\left\{-\frac{(N_3\cdot x)^2}{\pi}\right\},\ \text{with}\, x = s\cdot\pi\cdot a_3. \tag{3.17}$$

The peak height from an individual crystallite is then given by $I_{\max}\propto(L^2\cdot A)$ and the total peak intensity $I_{\mathrm{tot}} = \int_{-\infty}^{\infty} I(s)\,\mathrm{d}s \propto (L\cdot A)$ can be calculated from the error function $\mathrm{erf}(\infty) = 1$ (again, $L = N_3\cdot a_3$ defines the uniaxial size of the crystallite along the diffraction vector). The parameter $A\propto L^2$ is used to take the lateral extent of the ideally uniaxial crystallites into account. The peak profile of the superimposed diffracted intensity is now determined by both the individual peaks according to Eq. (3.17) and the actual size distribution of the diffracting grains (for a large number of diffracting grains it might be assumed that the normalized GDF of the polycrystal should be a reasonable estimate for the size distribution of the involved grains), and the integral breadth of the superimposed peak might therefore be written according to Eq. (3.11) as,

$$\beta = \frac{I_{\mathrm{tot}}}{I_{\max}} \propto \frac{\int_0^\infty L^3\cdot g(L)\,\mathrm{d}L}{\int_0^\infty L^4\cdot g(L)\,\mathrm{d}L} \tag{3.18}$$

Since the grain size defined by the Scherrer equation (3.10) is $L\propto 1/\beta$, the mean grain size measured by the width of the diffraction profile is apparently,

$$L \propto \frac{\int_0^\infty L^4\cdot g(L)\,\mathrm{d}L}{\int_0^\infty L^3\cdot g(L)\,\mathrm{d}L} = \frac{\left\langle L^4\right\rangle}{\left\langle L^3\right\rangle}, \tag{3.19}$$

which is according to Eq. (3.16) equal to the volume-weighted average of the grain size — i.e. a peak-width-based grain-size analysis yields $\langle L \rangle_{\mathrm{vol}}$ (or equivalently $\langle D \rangle_{\mathrm{vol}}$).

It is easily seen from the conception of a superimposed XRD signal that the full peak profile must include much more information than only a single average like $\langle L \rangle_{\mathrm{vol}}$ (it is of course evident that a single parameter like the peak width can provide only a single grain-size average). Section 3.1.4.2 will show that a more sophisticated analysis, which considers the shape of the entire peak profile $I(2\theta)$, can yield beside an volume-weighted average also the area-weighted average of the grain size. This has profound consequences, since the availability of two independent averages of the grain size allows for the unique description of a GDF that is defined by two parameters — as it is the case for the lognormal function of Eq. (3.12). The analysis of XRD data will therefore not only provide the ability of *in-situ* tracking of the grain size and grain-growth kinetics, but will also enable the investigation of the evolution of the GDF during grain growth. Together with the examination of growth kinetics, the accessibility of the GDF allows to investigate whether coarsening of the microstructure occurs under normal or abnormal growth conditions. Even if the type of the GDF is unknown, or the GDF is defined by a more complex function, the ratio $\langle L \rangle_{\mathrm{vol}} / \langle L \rangle_{\mathrm{area}}$ will allow to assess the validity of normal grain growth, since only a self-similar evolution of the microstructure will yield a constant value of the defined ratio.

If a lognormal function applies for the GDF of a polycrystalline material, the two parameters D_0 and σ of Eq. (3.12) can be calculated from the volume and the area-weighted average grain sizes that are extracted from the XRD data via [88],

$$\langle D \rangle_{\mathrm{area}} = D_0 \cdot \exp\left\{\frac{5}{2}\,(\ln \sigma)^2\right\}, \tag{3.20}$$

and

$$\langle D \rangle_{\mathrm{vol}} = D_0 \cdot \exp\left\{\frac{7}{2}\,(\ln \sigma)^2\right\}. \tag{3.21}$$

3.1.3.1 Column-Length Distribution

Both Fig. 3.4 and Eq. (3.10) demonstrate that the shape of a diffraction peak in terms of FWHM or integral breadth is only determined by the linear intercept length $L = N \cdot a$ of the grain or crystallite in the direction of the diffraction vector, whereas the lateral dimension perpendicular to the diffraction vector has no impact on peak shape. Thus, it is in principal sufficient to know the length L (or better to say the uniaxial length of stacked unit cells; in Fig. 3.4 this length is $N_3 \cdot a_3$) in order to predict the shape of the peak profile. This means however, that all information for diffraction is included in such "columns of unit cells" and hence, each crystallite might be considered as an ensemble of "unit-cell columns" with specific length (of course, a crystallite of arbitrary size and shape will have a distribution of unit-cell columns of different length L_i) that are causing an independent diffraction of the incident beam (i.e. each column of length L_i will create a particular diffraction peak $I_i(2\theta)$).

This approach to treat grains with respect to diffraction has been proposed in 1949 by E.F. Bertaut. He suggested that every crystalline volume is composed of individual columns of unit cells, which extent over the full length of the crystallite and are perpendicularly aligned to the diffracting planes [89–91]. Of course, those unit cells are not the crystallographic unit cells, but are related to the spacing d_{hkl} of

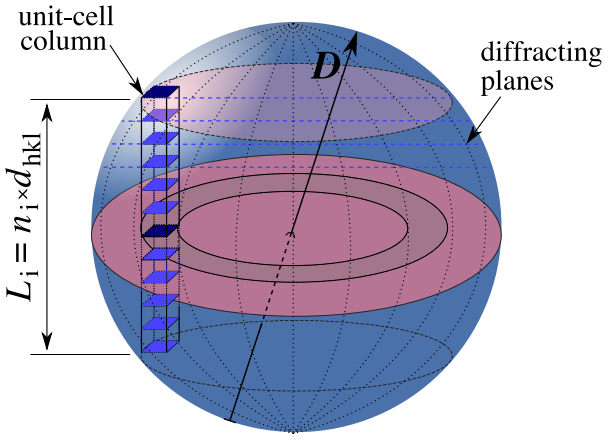

Figure 3.8: In Bertaut's treatment of diffraction, each grain is considered as an aggregate of unit-cell columns. Due to the different intercept lengths within a grain, each unit cell has a specific length of $L_i = n_i \cdot d_{\mathrm{hkl}}$. The columns are acting as independent entities in diffraction and thus, the length and the distribution of unit-cell columns are therefore the actually measured quantities by XRD.

the diffracting planes of the lattice. Bertaut's concept of columns is schematically illustrated in Fig. 3.8, showing a representative column of unit cells of length $L_i = n_i \cdot d_{\mathrm{hkl}}$ in a spherical grain, where n_i is the number of unit cells for this particular column. Evidently, the length L_i varies for an arbitrary grain size, and depends also on the position of the column inside the grain. For the spherical grain in Fig. 3.8, the length L_i ranges between a single unit cell at the perimeter of the sphere ($n_i = 1$) and $n_{\max} = D/d_{\mathrm{hkl}}$ along the diameter.

Bertaut concluded further that the total diffracted intensity $I(2\theta)$ is the summation of the intensities diffracted by individual columns, i.e. $I(2\theta) = \sum_i I_i(2\theta)$. This conclusion has an important consequence on the analytical treatment of diffraction data from polycrystalline materials: If a specific column of unit cells in the polycrystalline volume satisfies the Bragg condition and contributes thereby to the diffraction peak, it is irrelevant to which grain this column actually belongs, since diffraction will be independent from all other columns existing; or in other words, the whole polycrystalline sample can be treated as an ensemble of unit-cell columns — instead of an ensemble of grains. Hence, it is not the grain-size distribution $g(D)$ what is essentially determined by XRD, but rather the column-length distribution $p(L)$. Accordingly, the measured quantities by XRD (i.e. the volume and area-weighted averages of the grain size) are related to the intercept-length distribution $p(L)$, and are defined in analogy to Eqs. (3.14) - (3.16) as,

$$\langle L \rangle_{\mathrm{area}} = \frac{\int_0^\infty L \cdot [\delta a] \cdot p(L)\,\mathrm{d}L}{\int_0^\infty [\delta a] \cdot p(L)\,\mathrm{d}L} = \langle L \rangle_{\mathrm{num}} = \langle L \rangle \tag{3.22}$$

and

$$\langle L \rangle_{\mathrm{vol}} = \frac{\int_0^\infty L \cdot [\delta a \cdot L] \cdot p(L)\,\mathrm{d}L}{\int_0^\infty [\delta a \cdot L] \cdot p(L)\,\mathrm{d}L}, \tag{3.23}$$

where δa is the constant cross-section area of all columns, and $(\delta a \cdot L)$ is the column volume. Since δa is a constant, it is evident from Eq. (3.22) that with respect to the column length the weighted averages $\langle L \rangle_{\text{area}}$ and $\langle L \rangle$ are identical. With respect to Eq. (2.18) this entails that, if it is possible to determine the area-weighted average $\langle L \rangle_{\text{area}}$ as an experimental quantity, the results of XRD are instantaneously related to the grain-boundary density, and therefore to the driving force for microstructural coarsening.

3.1.3.2 Conversion between Column-Length and Grain-Size Distributions

The previous section showed that the XRD-measured quantities are not related to the GDF, but are defined on a lower level of the microstructure, namely the columns of unit cells. Thus, XRD experiments do not provide by themselves information about the size of grains, which is however need, if in an experiment curvature-based growth models like those of Section 2.3 are involved. It is therefore deemed necessary to establish a conversion rule between the measured quantities of $p(L)$ — i.e. $\langle L \rangle_{\text{vol}}$ and $\langle L \rangle_{\text{area}}$ — and the grain-growth parameters $\langle D \rangle_{\text{vol}}$ and $\langle D \rangle_{\text{area}}$ that are related to $g(D)$.

For a grain of both particular size D_0 and defined shape, the distribution of column length $p_0(L, D_0)$ can be evaluated. Thus, if all grains of the GDF are of the same particular shape considered for $p_0(L, D_0)$ and assuming further a self-similar scaling of $p(L, D)$ with respect to the size D of a grain, it is possible to calculate for a defined GDF the overall column-length distribution by [92],

$$p(L) = \int_0^\infty f(L, D) \cdot g(D) \, \mathrm{d}D. \tag{3.24}$$

The challenge to solve Eq. (3.24) is to find an appropriate description of $f(L, D)$. For some particular grain geometries (like cubic or spherical grains) this relationship can be established analytically, and W.L. Smith showed that for spherical grains of diameter D the function $f(L, D)$ is given by [92],

$$f(L, D) = \begin{cases} \dfrac{\pi}{2} \cdot L & \text{, if } L \leqslant D \\ 0 & \text{, if } L > D. \end{cases} \tag{3.25}$$

Based on this relationship C.E. Krill *et al.* showed for spherical grains that the following rather simple conversion rules between the measured values $\langle L \rangle_{\text{area}}$ and $\langle L \rangle_{\text{vol}}$ and the grain-size averages $\langle D \rangle_{\text{area}}$ and $\langle D \rangle_{\text{vol}}$ hold — basically independent of the detailed shape of $g(D)$ [88],

$$\langle L \rangle_{\text{area}} = \frac{2}{3} \cdot \langle D \rangle_{\text{area}} \tag{3.26}$$

$$\langle L \rangle_{\text{vol}} = \frac{3}{4} \cdot \langle D \rangle_{\text{vol}} \, . \tag{3.27}$$

3.1.4 Peak Broadening due to real Microstructures: Size and Strain Broadening

The preceding sections showed that the quantitative analysis of diffraction peaks is a powerful tool to evaluate both the (average) grain size and the GDF of nanostructured materials. However, since this ability relies on the correct interpretation of the peak width or the full peak profile, it is necessary to ensure that no other effects than the finite grain size are influencing the diffraction peak. However, a simple review of Bertaut's conception of column-induced diffraction shows that columns with slightly different lattice spacing $d_{\mathrm{hkl},i} = d_{\mathrm{hkl},0} \pm \delta d_{\mathrm{hkl},i}$ will result in diffraction peaks $I(2\theta_i)$, which are according to Bragg's equation slightly shifted by $\delta(2\theta)_i$ from the equilibrium diffraction angle $2\theta_0$. Consequently, a broadening of the measured peak profile should be expected, if there is a certain distribution of $\delta d_{\mathrm{hkl},i}$ [93,94] (this kind of broadening can even exist, when the grains are in a size range, where size broadening is negligible).

Since the lattice spacing d_{hkl} of cubic crystal structures is related to the crystallographic lattice parameter a_{bcc} via,

$$d_{\mathrm{hkl}} = \frac{a_{\mathrm{bcc}}}{\sqrt{h^2 + k^2 + l^2}}, \tag{3.28}$$

the variation $\delta d_{\mathrm{hkl},i}$ in lattice spacing is directly proportional to a shift of the lattice parameter, $a_i = a_0 \pm \delta a_i$. Such a deviation from the equilibrium lattice parameter a_0 can be caused for example by lattice defects like dislocations, vacancies or interstitial atoms, which induce a stress field $\sigma(r)$ in their environment. Depending on the strength of the material, the local stress causes a displacement $\delta a(r) \propto \sigma(r)$ of the atoms near the defect, which is equal to a local strain $\varepsilon(r) = \delta a(r)/a_0$. For dislocations for example, this strain will be proportional to $1/r$ and thus, there will be a distribution of δa_i [95] — and therefore a distribution of Bragg angles of one and the same reflection.

The nature of defect-induced strain entails both, it occurs on a microscopic scale and it is inhomogeneous, i.e. the strain is localized and bound to the causative defect structures. Due to that, such short-range strain is frequently termed as "microstrain" in literature. Different to microstrain, the homogeneous deformation of the lattice structure ($a_0 \rightarrow a_0^*$) leads to macroscopic strain, which however will result in a shift of the diffraction peak, but will not yield a change of the peak profile.

Beside the possibility of defect-induced microstrain, polycrystalline materials can also be susceptible to a completely different source for microscopic strain. In order to establish a space-filling assembly, the grains — defined by a size and topology distribution — have to be perfectly attached to each other. On the other hand, the grains are of discrete size (the length of a column of unit cells can only change by a multiple value of d_{hkl}), whereas the cavity to accommodated the grain can be in principal arbitrary in size and shape, depending on the topological needs. Considering unit-cell columns of length $L = n \cdot d_{\mathrm{hkl}}$, the possible misfit between a grain and the cavity can be at a maximum $\frac{1}{2} d_{\mathrm{hkl}}$ for every column, which must then be balanced by tensile or compressive deformation of the grain, see Fig. 3.9. If a unit-cell column of length L is stretched or compressed to fit the cavity, the actual strain in the column might be expressed as the elongation δL relative to the relaxed column length L, i.e. $\varepsilon(L) = \delta L/L$. Obviously, this type of strain cannot relax by the annihilation of defects and will only decrease during grain growth — either by an increasing grain size L or the change of topology (i.e. a reduced misfit δL).

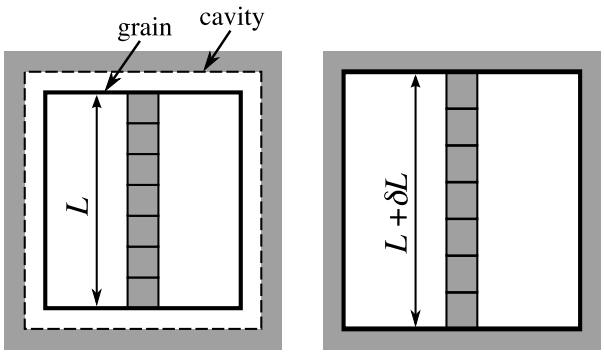

Figure 3.9: Microstrain induced by the need of grain contiguity in fully-dense polycrystalline materials. The misfit between the cavity size and the column length of the grain is overcome by the tensile or compressive deformation of the grain, yielding a size-dependent strain $\varepsilon(L) = \delta L/L$.

The consideration of microstrain shows that Scherrer's approach to analyze XRD data can give a reasonable estimate for low-strain materials, but in general it will yield an overestimation of size broadening if microstrain is present; this means that grain-size values of strained materials are in general smaller than the actual grain size. It is therefore an essential part of the evaluation of diffraction peaks to have a systematic and reliable technique to separate peak broadening due to grain-size and microstrain effects. The following two sections will discuss basic concepts on how the two effects might be discriminated.

3.1.4.1 The Williamson-Hall Analysis

The quantitative separation of size and strain broadening can be a challenging task, since the microstrain within the lattice is — similar to the grain size — defined by a particular distribution $\varepsilon(r, L)$. A decent approach to limit the complexity of this problem would be to consider only the limit strain $e = \delta d_{\max}/d_{\mathrm{hkl}}$ in a sample, i.e. to consider only the maximum value of the strain distribution $e = \max\{\varepsilon(r, L)\}$.

According to Bragg's law of Eq. (3.1), the diffraction peak from unit-cell columns with lattice spacing $d_{\max} = d_{\mathrm{hkl}} + \delta d_{\max}$ is determined by,

$$2 \cdot (d_{\mathrm{hkl}} \pm \delta d_{\max}) \cdot \sin(\theta_0 \mp \delta\theta) = \lambda. \tag{3.29}$$

Considering the distance $\delta\theta$ between this peak and the equilibrium peak position θ_0, Stokes and Wilson showed that the integral breadth of the measured strain-affected peak can be equated as [93],

$$\beta \approx 4 \cdot \frac{\delta d_{\max}}{d_{\mathrm{hkl}}} \cdot \tan(\theta), \tag{3.30}$$

or in terms of the variable $s = \frac{2 \cdot \sin(\theta)}{\lambda}$ and its derivative $\delta s = \frac{\delta(2\theta) \cdot \cos(\theta)}{\lambda} \approx \frac{\beta \cdot \cos(\theta)}{\lambda}$,

$$\delta s^{\text{strain}} = 2 \cdot s \cdot e. \tag{3.31}$$

To compare the strain-induced peak broadening δs^{strain} with peak broadening due to crystallite size, Scherrer's Equation (3.10) should also be converted into s-space to become then (with $k \approx 1$),

$$\delta s^{\text{size}} = \frac{1}{\langle L \rangle_{\text{vol}}}. \tag{3.32}$$

Comparing Eqs. (3.31) and (3.32) shows that in s-space the peak width due to size broadening will be the same for all (hkl) reflections (there is no influence of s on δs^{size}), while the peak width due to microstrain reveals a linear dependence on s — and will therefore be different for each (hkl) reflection. This difference in the dependence on s is the key for the separation of size and strain broadening, and hence to calculate a strain-corrected grain size — provided, more than one (hkl) reflection is measured [93, 96].

To perform such an analysis it is not sufficient to know the intrinsic broadening characteristics of grain size and microstrain according to Eqs. (3.32) and (3.31) only, it is also needed to know how these broadening mechanisms interact. In general, the measured peak profile $I(s)$ is given from the convolution of the size and strain-broadened intensity profiles [97],

$$I(s) = I^{\text{size}}(s) \ast I^{\text{strain}}(s). \tag{3.33}$$

Eq. (3.33) shows that the analysis of XRD data is not trivial, since it basically requires the convolution of the two intensity distributions $I^{\text{size}}(s)$ and $I^{\text{strain}}(s)$, and a least-square comparison of the convoluted peak with the experimental data. The exact evaluation of a diffraction profile requires therefore the detailed description of the intensity distributions $I^{\text{size}}(s)$ and $I^{\text{strain}}(s)$. Of course, this prerequisite would intricate the analysis, but fortunately the experience shows that a Gaussian or a Cauchy function (or a linear combination of both, which is usually known as a pseudo-Voigt function) can provide a sound approximation of $I^{\text{size}}(s)$ and $I^{\text{strain}}(s)$. Those functions have the advantage that the convolution of Eq. (3.33) simplifies to the following rather simple relationships [97],

$$\delta s = \left[\frac{k}{\langle L \rangle_{\text{vol}}}\right] + [2 \cdot e \cdot s] \quad \rightarrow \quad I^{\text{size}}_{\text{Cauchy}} \ast I^{\text{strain}}_{\text{Cauchy}} \tag{3.34}$$

$$[\delta s]^2 = \left[\frac{k}{\langle L \rangle_{\text{vol}}}\right]^2 + [2 \cdot e \cdot s]^2 \quad \rightarrow \quad I^{\text{size}}_{\text{Gauss}} \ast I^{\text{strain}}_{\text{Gauss}} \tag{3.35}$$

$$\delta s = \left[\frac{k}{\langle L \rangle_{\text{vol}}}\right] + \left[\frac{(2 \cdot e \cdot s)^2}{\delta s}\right] \quad \rightarrow \quad I^{\text{size}}_{\text{Cauchy}} \ast I^{\text{strain}}_{\text{Gauss}} \tag{3.36}$$

if the particular combinations of Gaussian and Cauchy peaks are assumed to represent the size and strain-broadened intensity profiles.[3]

[3] Scherrer's constant will be $k \approx 1$, if the integral breadth β is used instead of $\delta(2\theta)$ to define the measured peak width δs.

In materials of little microstrain, a Cauchy function usually provides a reasonable description of both $I^{\text{size}}(s)$ and $I^{\text{strain}}(s)$. In this case, Eq. (3.34) should allow for a reliable analysis of the diffraction data. For each (*hkl*) reflection, the peak width δs_{hkl} has to be evaluated by an appropriate fit of the diffraction profile. For the separation of grain size and microstrain, the values δs_{hkl} of all measured peaks are then plotted as a function of the respective peak position s_{hkl} in one graph. According to Eq. (3.34), a linear interpolation of the data points will then yield the actual microstrain (limit strain) $e = m/2$ (in which m is the slope of the linear fit) and the volume-weighted average grain size $\langle L \rangle_{\text{vol}}$ is determined by the intercept of the extrapolated linear fit with the ordinate of the graph at $s = 0$.

The Williamson-Hall approach is an important advancement of the original Scherrer equation to evaluate strain-corrected values of the grain size. However, as useful as this method is to extract a reliable grain-size parameter, the simplification of using the maximum strain e of the sample to assess the peak width δs^{strain} of the $I^{\text{strain}}(s)$ intensity distribution, will limit the significance of the strain results. Beyond this systematic problem, the interpretation of e is also difficult because basically all mechanism (like lattice defects or grain contiguity) that can create a microscopic perturbation of the lattice are concentrated in a single strain parameter. In spite of this difficulty, Révész *et al.* investigated the important case, where strain is solely driven by a dislocation density ϱ, and found that the strain-broadening term in Eq. (3.34) is then given by [98],

$$\delta s^{\text{strain}} = \left[\left(\frac{\pi b^2}{2 \cdot A} \cdot \overline{C}_{\text{hkl}} \cdot \varrho \right)^{1/2} \cdot s \right], \tag{3.37}$$

where A denotes a peak-shape-dependent constant, b the magnitude of the Burgers vector and $\overline{C}_{\text{hkl}}$ an averaged scaling factor that accounts for the relative orientation of the diffraction vector and the dislocation vectors (i.e. the Burgers vector and the line vector). Since the peak profile is not included in a peak-width-based XRD analysis, Révész *et al.* derived for nanocrystalline Fe a value of $A = 3.3$ from the Fourier analysis of the full-peak profile. For bcc Fe, the values of $\overline{C}_{\text{hkl}}$ are listed for the different (hkl) reflections in Table 3.1 [98].

Table 3.1: Scaling parameter $\overline{C}_{\text{hkl}}$ for the reflections of α-Fe, from Ref. [98].

(hkl) reflection	(110)	(200)	(211)	(220)
$\overline{C}_{\text{hkl}}$	0.061	0.285	0.118	0.061

Fig. 3.10 shows the Williamson-Hall plot of nanocrystalline Fe, measured in the as-prepared state after ball milling and after annealing to a final temperature of 315°C in a DSC scan (30 K/min). For both samples the plot includes the measured peak width δs as a function of the actual peak position s for the four (hkl) reflections that are within the accessible 2θ range of the diffractometer. The straight lines represent least-square fits of the data points according to Eqs. (3.34) in order to derive via Eq. (3.37) the dislocation density $\varrho = 4.0 \cdot 10^{15}\,\text{m}^{-2}$ (equals $e = 0.63\%$) and $1.5 \cdot 10^{15}\,\text{m}^{-2}$ ($e = 0.38\%$) for the as-prepared and the annealed state, respectively.

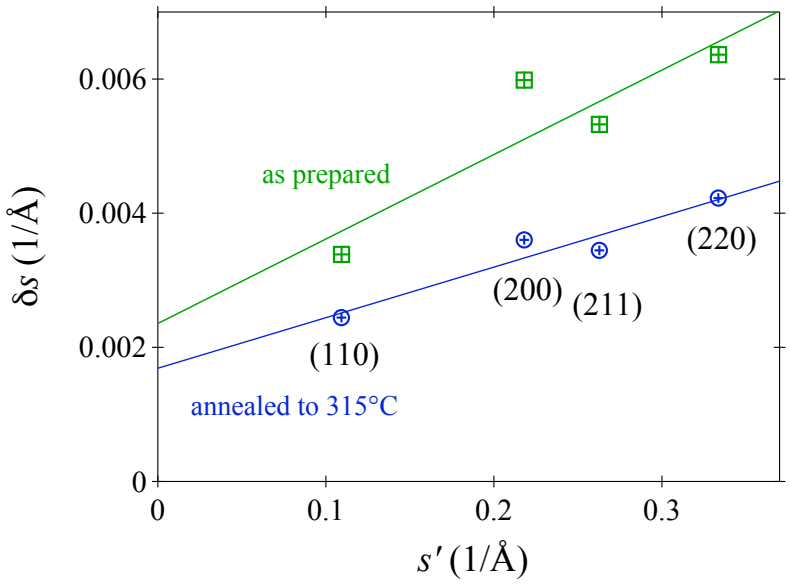

Figure 3.10: Williamson-Hall analysis on nanocrystalline Fe in the as-prepared state and after annealing to a maximum temperature of 315°C. The graph shows the measured peak width as a function of the rescaled peak position $s' = s \cdot \overline{C}_{hkl}^{1/2}$. The slope m_{WH} of a linear fit can then be used to calculated the dislocation density according to Révész *et al.* via $\varrho = 2 \cdot A \cdot m_{WH}/(\pi b^2)$.

Of course, from Eq. (3.34) it would be expected to find the data points in Fig. 3.10 on a straight line with linear δs versus s relationship. However, the data points obviously deviate from this linearity, caused by the anisotropic material strength. Only the (110), (211) and (220) orientation have an equal or similar elastic moduli (219 GPa), whereas the (200) orientation is softer (130 GPa) and features therefore a larger strain [10]. This problem might be overcome, if Eq. (3.34) is applied only to different orders of the same (*hkl*) reflection. In the case of Fe this could be the (110) and (220) peak.

3.1.4.2 The Warren-Averbach Analysis

The fundamental treatment of XRD that was introduced by von Laue reveals that the observed intensity profile $I(s)$ must be determined by the Fourier transformation of the real-space lattice into reciprocal space. Thus, it should be possible to express the diffraction profile of a $(00l)$ reflection in terms of a Fourier series with the reciprocal variable $h_3 = \frac{2\sin(\theta)}{\lambda} \cdot a_3$ [84], [4]

$$I(h_3) = I_0 \cdot \sum_{n=-\infty}^{+\infty} \{A_n \cdot \cos(2\pi n\, h_3) + B_n \cdot \sin(2\pi n\, h_3)\}, \tag{3.38}$$

[4] It was shown by Stokes and Wilson and by Warren that the limitation to a $(00l)$ reflection does not restrict the validity of the analysis [84, 99, 100].

where A_n and B_n are the cosine and sine Fourier coefficients, respectively, and n is the harmonic number of the Fourier series. The peak maximum of the diffraction signal $I(h_3)$ is then located at $h_3 = l$, and the interplanar distance of the diffracting planes becomes $d_{(00l)} = a_3/l \equiv a'_3$, with a_3 being the real-space lattice constant. The symmetry of the diffraction peaks requires the sine coefficients B_n to vanish and hence, the peak profile to be defined by the cosine coefficients A_n only.

As seen before in Section 3.1.3.1, it is the column-length distribution $p(L)$ of the sample that essentially determines the shape of the diffraction-peak profile. In addition to the entire length $L_i = n_i \cdot a'_3$ of the columns, all "sub-columns" of length $L_n = n \cdot a'_3$ (see Fig. 3.11) do also contribute to the column-length distribution $p(L)$, and therefore to the shape of the diffraction peak. Fig. 3.11 shows exemplarily columns of unit cells oriented along the $(00l)$ direction, where the unit cells are numerated $m = 1...N$, and the sub-columns are defined by $n = m - m' \leqslant N$.

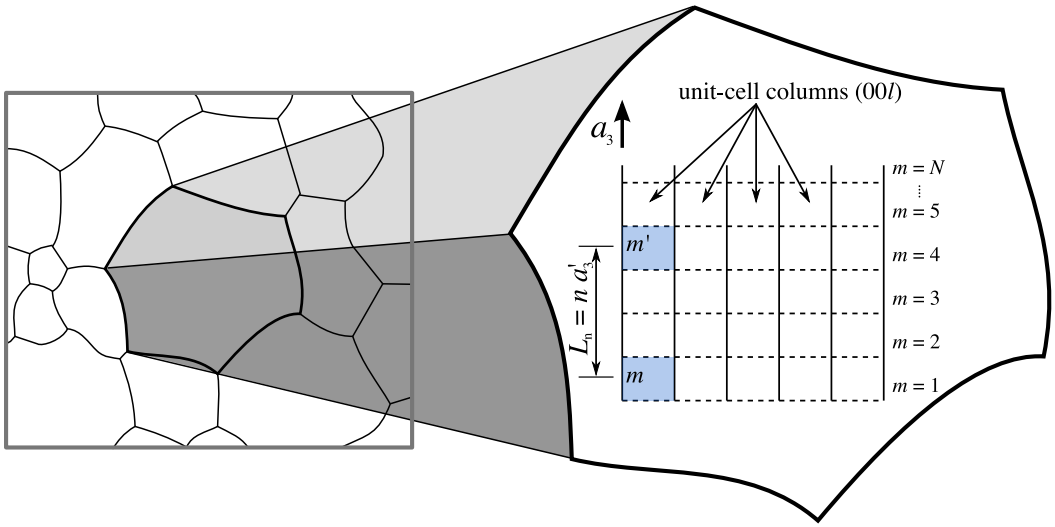

Figure 3.11: Unit-cell columns in (00l) direction. The position of each unit cell within a column of length L_i is identified by the parameter m, which ranges between $m = 1 \ldots N$. The schematic shows also the "sub-columns" of length L_n, which are defined as a subdivision of the unit-cells columns L_i ($1 \leqslant n \leqslant N$).

Warren and Averbach showed that, assuming a (00l) reflection, the cosine coefficients in Eq. (3.38) are given by [84],

$$A_n(l) = \left[\frac{N_n}{N_3}\right] \cdot \langle \cos\left(2\pi l\, \delta z_n\right) \rangle \,, \tag{3.39}$$

where N_n denotes the average number of unit-cell pairs per column that are separated by $L_n = n \cdot a'_3$, N_3 the average number of unit cells per column (which is proportional to the average column length $\langle L \rangle = N_3 \cdot a'_3$), l the order of diffraction and δz_n the displacement due to microstrain of two unit cells with index m and m' [84, 101–103]. Eq. (3.39) implicates that the cosine coefficients $A_n(l)$ can be split into a size-dependet term $A^{\mathrm{S}} = (N_n/N_3)$ and a strain-dependent term $A^{\mathrm{D}}(l) = \langle \cos\left(2\pi l \delta z_n\right) \rangle$, where the superscripts denote size and distortion respectively and hence, Eq. (3.39) can be written as the product,

$$A_n(l) = A_n^{\mathrm{S}} \cdot A_n^{\mathrm{D}}(l). \tag{3.40}$$

The relative displacement δz_n of the unit cells along the a_3 direction leads to a changed column length $L_n^* = L_n + \Delta L_n$, defining the strain $\varepsilon(L_n) = \Delta L_n / L_n = \delta z_n / n$ in the column, and $\left\langle \varepsilon^2 (L_n) \right\rangle^{1/2}$ yields the root-mean-square strain over all columns of length L_n. If $\delta z_n = n \cdot \varepsilon(L_n)$ is small (what is obviously true for low microstrain and/or small harmonic numbers n), so that $(2\pi l \delta z_n) \ll 1$, the averaged cosine term in Eq. (3.39) can be approximated by $\langle \cos(2\pi l \delta z_n) \rangle \Rightarrow \left[1 - 2\pi^2 l^2 \left\langle \delta z_n^2 \right\rangle\right]$ [104, 105].

By taking the logarithm on both sides of Eq. (3.40) one finally obtains [84],

$$\ln\left(A_n(l)\right) \cong \ln\left(\frac{N_n}{N_3}\right) - \left[2\pi^2 n^2 \left\langle \varepsilon^2(L) \right\rangle\right] \cdot l^2. \tag{3.41}$$

The different l-dependence of the two terms in Eq. (3.41) immediately highlights the procedure to separate size and strain broadening. For a fixed value of n, the logarithm of the cosine coefficients $\ln\left(A_n(l)\right)$ is plotted for different orders ($l = 1, 2, 3, ...$) of the same Bragg refection as a function of l^2. A linear fit to the data points is then extrapolated to $l = 0$, giving the strain-corrected size coefficient $A^{\mathrm{S}}(n) = N_n / N_3$ for each value of n [84].

The quantity N_3, which is a measure for the area-weighted average column length $\langle L \rangle_{\mathrm{area}} = N_3 \cdot a_3'$, *cf.* Eq. (3.22), can then be equated from the analysis of Eq. (3.41), if an appropriate expression for N_n can be established. For a sample with a column-length distribution $p(i)$, i.e. $p(i)$ gives the number of unit-cell columns that have a total length of $L_i = n_i \cdot a_3'$, the number of sub-columns with length L_n is determined by,

$$N_n = \sum_{i=|n|}^{\infty} (i - |n|) \cdot p(i). \tag{3.42}$$

If $p(i)$ is defined as a continuous distribution, the summation turns over into an integral and N_n can be written as,

$$N_n = \int_{i=|n|}^{\infty} i \cdot p(i)\, \mathrm{d}i - |n| \cdot \int_{i=|n|}^{\infty} p(i)\, \mathrm{d}i. \tag{3.43}$$

Since the integration variable is included in the lower integration limit, the treatment of Eq. (3.43) requires to use the theorem: $y = \int_n^{\infty} f(x)\, \mathrm{d}x \Leftrightarrow \mathrm{d}y/\mathrm{d}n = -f(n)$. For a normalized column-length distribution with $\int_0^{\infty} p(i)\, \mathrm{d}i = 1$ the derivative of the size coefficients $A_n^{\mathrm{S}} = N_n / N_3$ can therefore be equated as [84],

$$\left(\frac{\mathrm{d}A_n^{\mathrm{S}}}{\mathrm{d}n}\right)_{n \to 0} = -\frac{1}{N_3} \int_{n \to 0}^{\infty} p(i)\, \mathrm{d}i = -\frac{1}{N_3}. \tag{3.44}$$

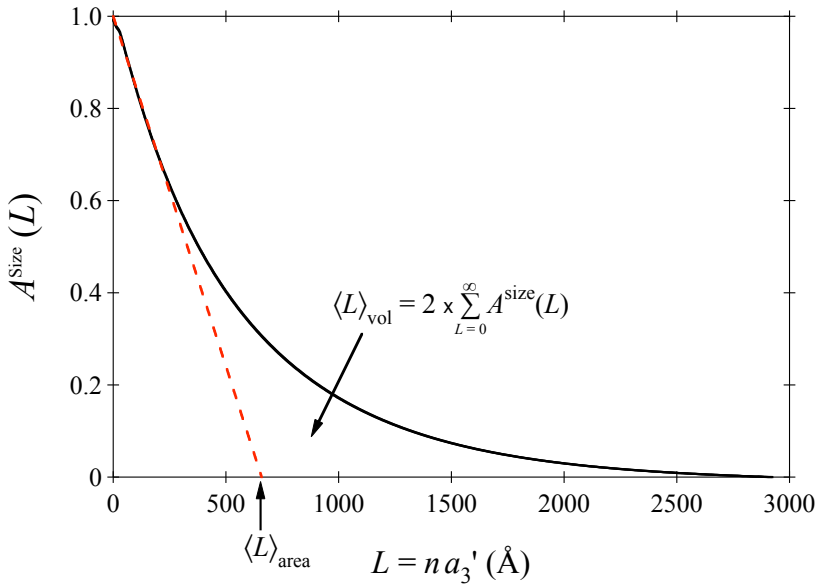

Figure 3.12: The graph shows for a nanocrystalline Fe sample the normalized Fourier size-coefficients $A^S(L)$ as a function of the column length $L = n \cdot a_3'$. The area-weighted average column length $\langle L\rangle_{\text{area}}$ is given by the intercept of the extrapolated slope at small L-values with the L-axis (dashed line). The volume-weighted average column length $\langle L\rangle_{\text{vol}}$ is defined by taking twice the area under the $A^S(L)$ curve.

If the coefficients are normalized in a way that $A^{\text{S}}_{n=0} = 1$, $\langle L\rangle_{\text{area}}$ is immediately found from the intercept of the tangent to $A^{\text{S}}_{n\to 0}$ with the L-axis ($A^{\text{S}}_n = 0$), as illustrated in Fig. 3.12.[5]

An interesting relation is found, if the second derivative of Eq. (3.44) is evaluated,

$$\frac{\mathrm{d}^2 A^{\text{S}}_n}{\mathrm{d}n^2} = -\frac{1}{N_3} \cdot \frac{\mathrm{d}}{\mathrm{d}n} \int_{i=|n|}^{\infty} p(i)\,\mathrm{d}i = \frac{p\,(|n|)}{N_3}. \tag{3.45}$$

Eq. (3.45) demonstrates that the second derivative of the size coefficients can in principle provide instantaneous access to the entire column-length distribution $p(n)$. Unfortunately, this relationship is of little practical relevance, since the second derivative of a measured quantity usually suffers from limited experimental accuracy. It should also be recognized that the performed separation of grain-size and microstrain broadening is not approved for larger numbers of n. Nevertheless, Eq. (3.45) shows that the Fourier analysis of XRD experiments is a powerful tool to investigate the nature of polycrystalline materials.

[5] A thorough inspection of the $A^{\text{S}}(L)$ cofficients in Fig. 3.12 reveals an unexpected "hook" in the curvature at $n \to 0$. The cause for this error is basically determined by the Fourier transformation of truncated fit functions, which can be pronounced if long-tailed Cauchy functions are involved in peak fitting. For practical purpose the size coefficients have been normalized for $A^{\text{S}}_{L=0} = 1$ by using a linear fit of $A^{\text{S}}(L)$ at small L-values, that is extrapolated to $L = 0$.

So far, the Fourier coefficients A_n have been defined with respect to the harmonic number n. For practical purpose it turned out to be more efficient to define the Fourier coefficients directly in terms of the physically meaningful column length, $A^{\mathrm{S}}(L)$ (see Fig. 3.12). Wagner *et al.* demonstrated that the integral breadth β_s of a diffraction peak in s-space is then given by,

$$\beta_s = \frac{\int_{-\infty}^{\infty} I(s)\,\mathrm{d}s}{I_{\max}} = \frac{1}{\sum\limits_{L=-\infty}^{+\infty} A^{\mathrm{S}}(L)}. \tag{3.46}$$

A comparison with Section 3.1.2.2 shows that $\langle L\rangle_{\mathrm{vol}} = 1/\beta_s$ and therefore,

$$\langle L\rangle_{\mathrm{vol}} = 2 \cdot \sum_{L=0}^{\infty} A_{\mathrm{L}}^{\mathrm{S}}, \tag{3.47}$$

where the summation is performed over the physically meaningful values of $L \geqslant 0$. Eq. (3.47) states that the volume-weighted average grain size $\langle L\rangle_{\mathrm{vol}}$ is given as twice the sum of all size coefficients, which is equal to twice the area under the curve in Fig. 3.12. Although the error in the strain-corrected size coefficients $A^{\mathrm{S}}(L)$ increases for larger values of L, the fast decline of $A^{\mathrm{S}}(L)$ averts a significant error in $\langle L\rangle_{\mathrm{vol}}$.

Eq. (3.44) and (3.47) demonstrate that the Fourier analysis of XRD data has the outstanding quality to yield two independent weighted averages of the polycrystalline distribution of grain sizes : $\langle L\rangle_{\mathrm{area}}$ and $\langle L\rangle_{\mathrm{vol}}$. Thus, according to Section 3.1.3 the WA method provides not only the ability to measure the kinetics of grain growth, but will also enable the qualitative assessment of the evolution of the GDF — or, in particular cases, will even allow the quantitative definition of the complete GDF.

The separation of size and strain-broadening according to Eq. (3.41) involves that the root-mean-square strain $\left\langle \varepsilon^2(n)\right\rangle^{1/2}$ is given by the slope of a linear fit of $\ln\left(A_n(l)\right)$ versus l^2 for each harmonic number n. Obviously, this entails that for every set of columns of length $L_n = n \cdot a_3'$ a corresponding mean strain $\left\langle \varepsilon^2(L_n)\right\rangle^{1/2}$ is obtained [105]. Since the prerequisite for the Taylor expansion to arrive at Eq. (3.41) requires the product $n \cdot \varepsilon_n$ to be small, the evaluation of microstrain should be restricted to small values of L (or n respectively), which is obviously the same constraint as for the determination of $\langle L\rangle_{\mathrm{area}}$ (from Fig. 3.12 the upper L-limit for the analysis of $\langle L\rangle_{\mathrm{area}}$ is approximately 20 nm). On the other hand, the evaluation of microstrain at $L \to 0$ may involve a higher uncertainty from the size/strain separation [97], which therefore defines a lower L-limit for the evaluation of microstrain. Fig. 3.13 depicts the result from the Warren-Averbach analysis with a plot of $\left\langle \varepsilon^2(L)\right\rangle^{1/2}$ as a function of L. As expected from $\left\langle \varepsilon^2(L)\right\rangle^{1/2} = \Delta L/L$, the level of microstrain increases significantly for small L, whereas at larger L-values the microstrain approaches asymptotically zero. For the sake of consistency, the root-mean-square microstrain will always be evaluated within this study at $L = 5$ nm.

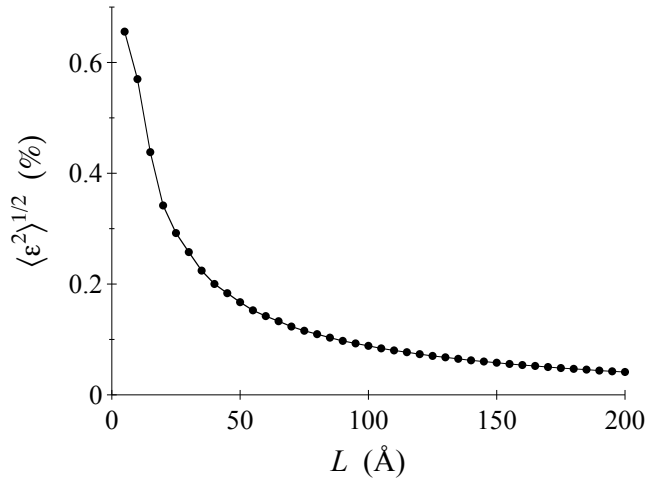

Figure 3.13: Plot of the root-mean-square strain $\left\langle \varepsilon^2 \right\rangle^{1/2}(L)$ in a nanocrystalline Fe sample as a function of L. The plot reveals that the "hook" effect of the size coefficients $A^{\text{size}}(L)$ at $L \to 0$ is similarly found for the microstrain, which suggests to limit the evaluation of the size-dependent microstrain to the unaffected regime. At larger L-values the strain approaches asymptotically zero and vanishes finally. This characteristic at large L-values relates to the definition of microstrain $\varepsilon(n) = \delta z_n / n$ in the WA analysis.

3.1.5 Instrumental Peak Broadening and Peak Correction

The broadening of diffraction peaks in micro and nanocrystalline specimens has been discussed in Section 3.1.4 in the light of small grain sizes and microstrain. However, inspection of XRD experiments on samples where broadening mechanisms due to the microstrucure are negligible reveals, that the diffraction peaks actually have a distinct width. This specimen-independent peak broadening is usually attributed to the experimental setup for XRD (called "instrumental peak broadening"), and can become an essential aspect in the quantitative evaluation of diffraction experiments — particularly, if the structural broadening by the sample becomes comparable to the instrumental one.

The reasons for instrumental peak broadening are in general diverse and of different significance. In the overview below only the most important aspects are briefly addressed.

A) Non-monochromatic radiation. X-ray photons are generated in a reversed photoelectric process when target atoms are excited by accelerated electrons. The corresponding wavelength of the emitted radiation is thereby determined by the energy difference of the initial and final state that are involved in the subsequent relaxation process. According to the selection rules for electronic transitions, there are only a few possible emission wavelengths, with $K\alpha_{1,2}$ ($L \to K$ transition) and $K\beta_1$ ($M \to K$ transition) being the most intense and experimentally observable ones [106]. However, the $K\alpha_{1,2}$ doublet and $K\beta_1$ do not occur as ideally narrow emission lines, but have a particular energy distribution, which is associated with a wavelength spread $\Delta\lambda$. This non-monochromatic characteristic leads to a broadening of diffraction signals [106]. Additionally, high-energy electrons undergo

inelastic scattering in the target and produce thereby a continuous spectrum of bremsstrahlung, which may also affect the peak profile.

B) Axial divergence. Divergent beam sources, i.e. non-parallel incident x-rays, are known to increase the width and asymmetry of diffraction peaks and have presumably the strongest impact on instrumental broadening [107, 108]. The divergence of the x-ray beams can be reduced by placing Soller slits (parallel metal plates with defined angular aperture angle) into the incident and/or diffracted optical path, which act as angular intensity filters. However, for divergent x-ray sources the Soller slits reduce the available intensity considerably.

C) Sample transparency. The problem of sample transparency is closely related to the precise determination of lattice constants. For geometrical reasons the measured position of a Bragg peak is only exact, if the sample is correctly aligned with respect to the reference plane of the diffractometer [82,94]. Every deviation of the sample position causes a shift of the Bragg peak to lower or higher 2θ angles. Thus, depending on the actual absorption characteristics, the penetration of x-rays into the specimen and the diffraction from lattice planes of subjacent grains leads to a superposition of shifted peaks and thus to both, a broadening of the diffraction peak and to an increased asymmetry of the peak profile.

D) Sample displacement and detector resolution. The height displacement of the specimen entails not only a shift of the diffraction peak from the nominal position, the shorter or longer optical path length of the incident and diffracted beam causes also in the Bragg-Brentano geometry (see Fig. 3.1) a defocusing of the intensity spot and thus, a broadened intensity profile on the goniometer circle [82, 94].

A further aspect for the broadening of diffraction peaks is related to the aperture Δ_D of the detector, which is a consequence of the finite receiving area of the scanning unit, see Section 3.1.2.2. Only for an ideal spot detector this additional broadening mechanism would disappear. For real detector setups, the aperture mostly increases with the sensitivity of the detector, because the intensity is integrated over a larger receiving area. Since highly sensitive detector units (like the position-sensitive detector used for the XRD scans of this study) are needed for low integration times in real-time tracking of grain growth, it is obvious that scan speed and instrumental peak broadening have to undergo a trade-off.

If instrumental peak broadening due to one or more of those effects is present, the measured diffraction profile $h(2\theta)$ is the result of the convolution of the intrinsic peak profile $f(2\theta)$ due to size and strain broadening and the instrumental profile $g(2\theta)$ [94, 109–112],

$$h(2\theta) = g(2\theta) * f(2\theta), \tag{3.48}$$

where the instrumental profile itself is a convolution of the different instrumental effects described in A) – D) before, i.e. $g(2\theta) = g_A(2\theta) * g_B(2\theta) * \ldots$ [94]. Especially in samples of larger crystallite sizes and moderate residual microstrain (which both obviously would yield a narrow diffraction peak) the convolution can cause a significant distortion and broadening of the intrinsic intensity signal. It will then be inevitable to perform a thorough evaluation of the instrumental broadening and develop a procedure to extract the intrinsic peak profile $f(2\theta)$.

Similar to the convolution of the size and strain-broadened peaks in Eq. (3.33), only the convolution of the two intensity distributions $g(2\theta)$ and $f(2\theta)$ yields an exact result for the measured signal. Since the instrumental broadening is sample independent, it should be possible to measure the two peak profiles $h(2\theta)$ and $g(2\theta)$ separately (of course, this requires the independent measurement of the sample and a reference material). To avoid the inconvenient convolution of Eq. (3.48) it is useful to transform both measured peak profiles $h(2\theta)$ and $g(2\theta)$ into Fourier space, which allows to replace the convolution by a simple multiplication [84, 113],

$$\mathscr{H}(n) = \mathscr{G}(n) \cdot \mathscr{F}(n), \tag{3.49}$$

where $h(2\theta) \circ\!\!-\!\!\bullet\, \mathscr{H}(n)$, $g(2\theta) \circ\!\!-\!\!\bullet\, \mathscr{G}(n)$ and $f(2\theta) \circ\!\!-\!\!\bullet\, \mathscr{F}(n)$ are the respective Fourier transforms. Thus, the peak profile $f(2\theta)$ due to size and strain broadening can then be calculated according to the Stokes correction from the inverse Fourier transformation [114],

$$\mathscr{F}(n) = \frac{\mathscr{H}(n)}{\mathscr{G}(n)} \bullet\!\!-\!\!\circ\, f(2\theta). \tag{3.50}$$

The deconvolution of $f(2\theta)$ is in principle the only exact method to determine the microstructure-broadened profile and is particularly expedient, if the subsequent analysis is based on the evaluation of the Fourier coefficients, e.g. by the Warren-Averbach analysis. A simplified approach to extract $f(2\theta)$ from the measured diffraction data is possible, if particular peak profiles are assumed for $f(2\theta)$ and $g(2\theta)$. Provided that a Gaussian or a Cauchy function is an appropriate description for both, $f(2\theta)$ and $g(2\theta)$, the width $\delta(2\theta)$ of the measured peak $h(2\theta)$ can be expressed by [97],

$$\begin{aligned} \delta(2\theta) &= \delta(2\theta)_{\text{inst.}} + \delta(2\theta)_{\text{microst.}} \quad \text{(both functions Cauchy)} \\ \delta(2\theta)^2 &= \delta(2\theta)^2_{\text{inst.}} + \delta(2\theta)^2_{\text{microst.}} \quad \text{(both functions Gaussian)}, \end{aligned} \tag{3.51}$$

where $\delta(2\theta)_{\text{inst.}}$ and $\delta(2\theta)_{\text{microst.}}$ are the peak width of $g(2\theta)$ and $f(2\theta)$, respectively (Eq. (3.51) will hold for both, the peak width in terms of the FWHM or the integral breadth). Not relying on a particular peak profile for $f(2\theta)$ and $g(2\theta)$, Wagner and Aqua proposed the following parabolic correction to yield a sample-broadened peak width that is more accurate than those of Eq. (3.51) [113, 114],

$$\delta(2\theta)_{\text{microst.}} = \delta(2\theta) \cdot \left[1 - \left(\frac{\delta(2\theta)_{\text{inst.}}}{\delta(2\theta)}\right)^2\right]. \tag{3.52}$$

Irrespective of which approach is used to account for instrumental peak broadening, it is always necessary to measure $g(2\theta)$. This is usually done by running a reference sample, which is not influencing the peak profile by itself, i.e. a sample material with sufficiently large grains and insignificant lattice distortions. This is possible, if either a coarse-grained sample of the investigated material is used, or an adequate standard sample. Within this study, all XRD experiments have been corrected for instrumental broadening

with a NIST SRM660a standard sample (LaB_6 powder sample).[6] The diffraction peaks of the LaB_6 sample (and also the *in-situ* XRD data of the isothermal anneals on nanocrystalline Fe) have been analyzed with a split-Pearson VII function,

$$I(x) = I_0 \cdot \begin{cases} \left[\left(2^{1/m_L} - 1\right) \cdot \left(\frac{x-x_0}{HW_L}\right)^2 + 1\right]^{-m_L}, & \text{for } x \leqslant x_0 \\ \left[\left(2^{1/m_R} - 1\right) \cdot \left(\frac{x-x_0}{HW_R}\right)^2 + 1\right]^{-m_R}, & \text{for } x > x_0, \end{cases} \tag{3.53}$$

with $m_{L,R}$ being shape factors (where $m = 1$ equals a Cauchy function and $m \to \infty$ approaches a Gaussian function) and $HW_{L,R}$ the half widths at half maximum, both independent for the left $(x \leqslant x_0)$ and right side $(x > x_0)$ of the peak (the indices "L" and "R" denote left and right, respectively) and x_0 defines the position of the peak maximum [116, 117].

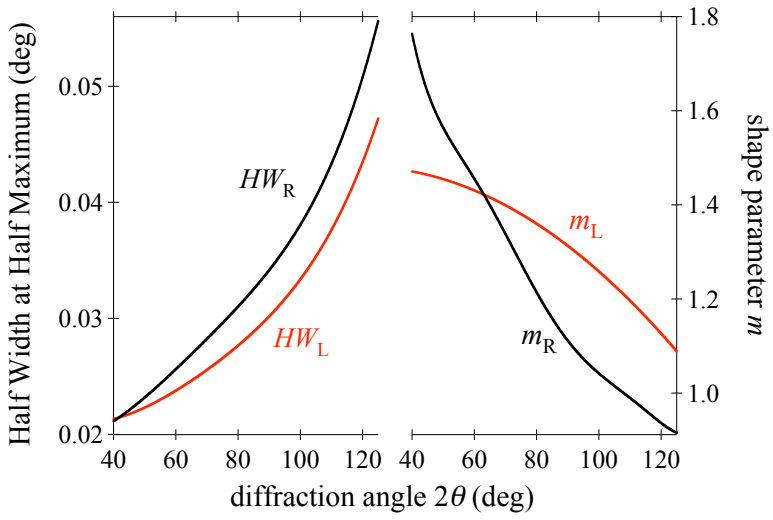

Figure 3.14: Plot of the parameters of a split-Pearson VII function as a function of diffraction angle to quantify instrumental peak broadening. The parameters $m_{L,R}(2\theta)$ and $HW_{L,R}(2\theta)$ have been deduced from a detailed XRD scan of a LaB_6 powder reference sample (NIST SRM660a) with the diffraction system in standard configuration for the *in-situ* experiments on nanocrystalline Fe. The data within this graph has been used for the correction of instrumental broadening.

Fig. 3.14 shows the interpolated polynomial functions for the split-Pearson-VII parameters $m_{L,R}(2\theta)$ and $HW_{L,R}(2\theta)$ that were measured on a LaB_6 reference sample and standard XRD settings for *in-situ* tracking of the investigated nanocrystalline Fe samples. The polynomial functions in Fig. 3.14 have been used to generate "numerical" reference peaks at the Bragg angles of the investigated samples, which were then used for the instrumental correction according to Eq. (3.50), see Figs. 3.16 and 3.17.

[6] Specific scattering and absorption properties of LaB_6 are given in Ref. [115].

Eqs. (3.51) and (3.52) show that the correction of instrumental broadening requires the precise evaluation of the two peak widths $\delta(2\theta)_{\text{inst.}}$ and $\delta(2\theta)$. However, if the radiation that is emitted by the x-ray tube contains photons of different energy, each (*hkl*) reflection is mapped according to Bragg's law to more than one diffraction peak. In principal this circumstance is not a bigger problem, since the (*hkl*) peaks from different wavelengths can be either physically separated by using an x-ray monochromator, or can be analytically cut-out by confining the 2θ range in a peak fit (both requires of course the peaks — or better to say the photon energies — to be sufficiently separated). Unfortunately, the two most intense emission lines $K\alpha_1$ and $K\alpha_2$ are so closely together that it is not possible to separated the peaks — thus, every (hkl) reflection will be reproduced at least by these two wavelengths. Particularly at small grain sizes the $K\alpha_1$ and $K\alpha_2$ peak will largely overlap due to the substantial size-broadened peak width, which means that the characteristics of the individual peaks are not immediately accessible. In case of a $K\alpha_{1,2}$ superposition the peak analysis requires therefore a least-square fit for both peaks at the same time. Fig. 3.15 shows the measured (110) and (220) peak of nanocrystalline Fe (annealed at 452°C for ~20 h) together with a least-square fit of the split-Pearson VII function of Eq. (3.53) (solid line). For the least-square fit, a superposition of two split-Pearson VII functions is used (one for $K\alpha_1$ and one for $K\alpha_2$), in which the parameters $m_{\text{L,R}}$ and $HW_{\text{L,R}}$ are taken to be the same for both peaks. Obviously, the chosen approach yields an excellent agreement between the measured peak profiles and the superimposed fit function.

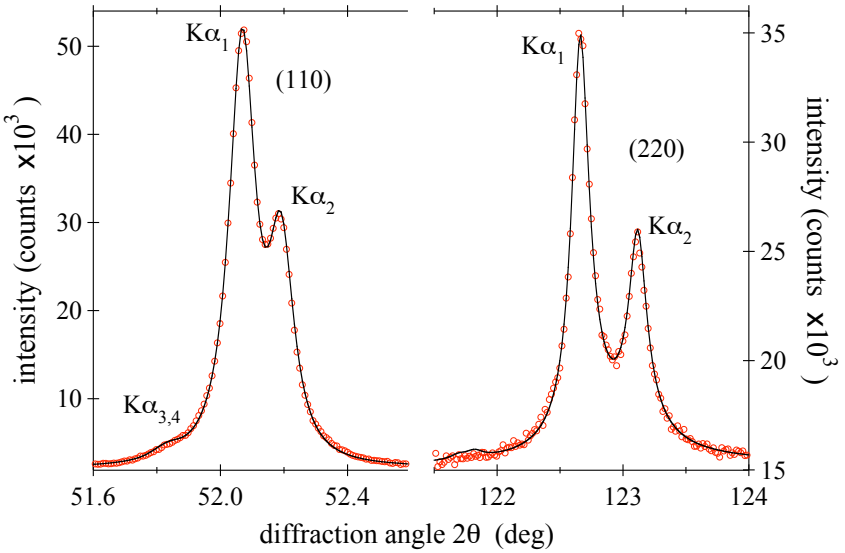

Figure 3.15: Raw data of the (110) and (220) diffraction profile of a nanocrystalline Fe sample that was annealed at 452°C for ~20 h. The plot indicates the four (110) Bragg peaks according to the $K\alpha_{1-4}$ x-ray lines. The solid lines are least-square fits with Eq. (3.53) to represent each of the $K\alpha_{1-4}$ peaks (the shape parameter $m_{\text{L,R}}(2\theta)$ and the peak width $HW_{\text{L,R}}(2\theta)$ were assumed to be the same for all four peaks of each reflection). The measured peaks are shifted from their nominal room-temperature position to lower 2θ values because of the elevated sample temperature during the *in-situ* scan.

Detailed inspection of the diffraction profile in Fig. 3.15 reveals a weak bump-like feature at the low-angel tail of the (110) peak, which cannot be assigned to one of the two main emission wavelengths. It seems likely that this feature is caused by so called "non-diagram" emission lines, which result from the electronic relaxation in multi-excited atoms [106, 118, 119]. Due to the relatively low intensity of those spectral components it is usually impossible to resolve them in the diffraction signal. Only for the most intense lines, which are for Co tubes $K\alpha_3$ (1.78180 Å) and $K\alpha_4$ (1.78071 Å), there is a chance to observe a weak signal, if a high-sensitive detector is used. From the LaB_6 diffraction pattern, a relative intensity of 1.7% and 1.1% (with respect to the $K\alpha_1$ intensity) was determined for $K\alpha_3$ and $K\alpha_4$, respectively. For the (220) peak the signal-to-noise ratio is too low and the peaks are obviously lost in the intensity background. Analysis of XRD data did not reveal any influence on grain size or microstrain, whether the $K\alpha_{3,4}$ peaks are considered during peak fitting of the (110) reflection or not. For this reason, $K\alpha_{3,4}$ was not considered in the further analysis of diffraction data.

If the experimental diffraction profile can be properly approximated by a suitable fit function, e.g. a split-Pearson VII function, the $K\alpha_1$ peak can be extracted without the influence of $K\alpha_2$ (the new peak will then be solely defined by the parameters of the fit function) and a noise-free replica can be generated. Fig. 3.16 illustrates the synthesized $K\alpha_1$ peak of the (110) and (220) reflection from Fig. 3.15. Using the parameters of Fig. 3.14, reference peaks can be calculated at the position of the Fe (110) and (220) peak. The reference peaks are additionally included in Fig. 3.16 and are shown as dashed lines (the reference peaks represent in principal the narrowest peak profile that can be measured with the current setup).

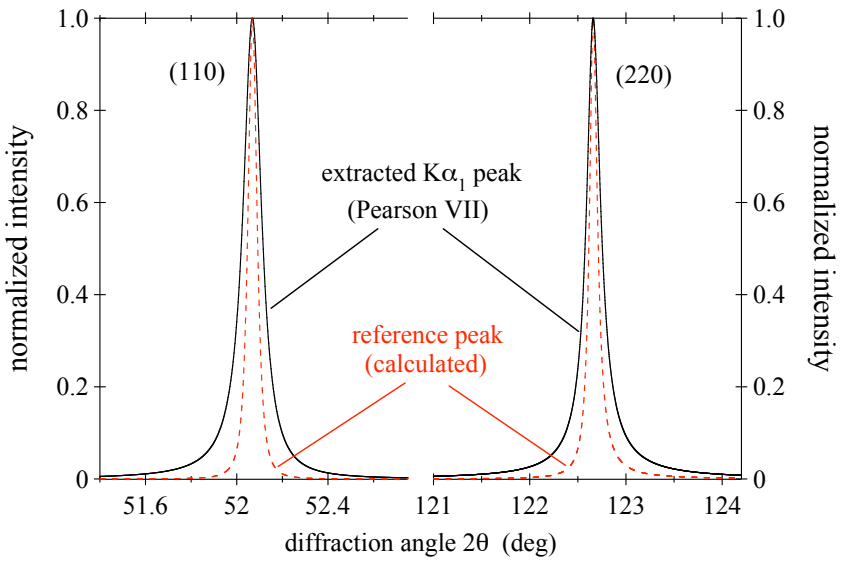

Figure 3.16: Plot of the synthesized $K\alpha_1$ peaks (solid lines) and the generated reference peaks at the same peak positions (dashed lines). The synthesized $K\alpha_1$ peak is calculated from the split-Pearson VII parameters that were found from the least-square fit on the (110) and (220) reflection in Fig. 3.15. The reference peak is generated by using the parameters measured on a LaB_6 reference sample (see Fig. 3.14).

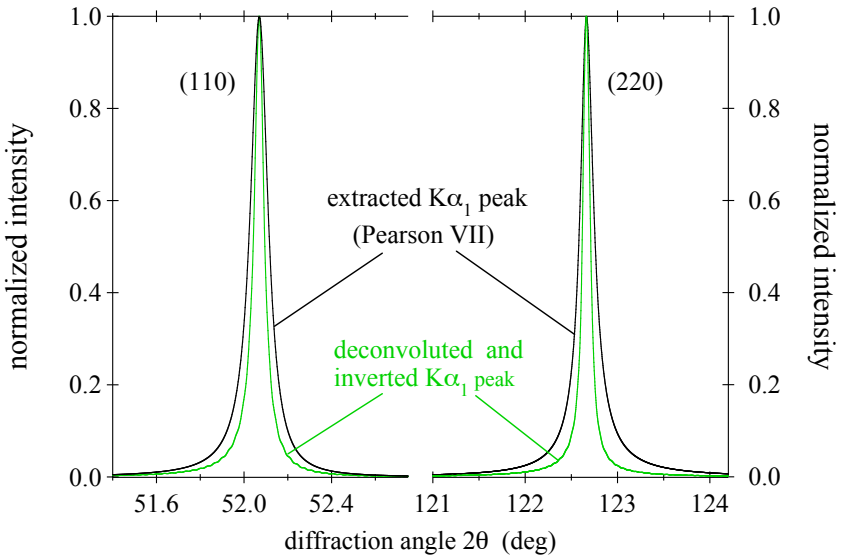

Figure 3.17: Comparison of the $K\alpha_1$ peak before and after correction for instrumental broadening. The correction of the peaks was performed via the Stokes correction according to Eq. (3.50) with the synthesized $K\alpha_1$ peaks and the reference peaks from Fig. 3.16.

Depending on the selected approach to correct for instrumental broadening — the need to perform this correction will increase with growing size of the grains in the investigated specimen — the generated peak profiles in Fig. 3.16 can then be used as an input to the Stokes deconvolution according to Eq. (3.50), or alternatively to the simplified techniques proposed by Eq. (3.51) or (3.52). Fig. 3.17 illustrates the corrected peak profiles after the Stokes correction and compares them with the synthesized (uncorrected) peak from the measured data. The peak profiles after instrumental correction can now be used to start the grain-size and microstrain analysis according to Section 3.1.4.1 or 3.1.4.2.

3.2 Calorimetric Analysis

The theory of thermodynamics describes the state and the stability of an arbitrary system — which could be for example a solid-state material of crytsalline or amorphous structure, but could also be a liquid or gaseous specimen — by the respective free energy. For single-phase polycrystalline materials the free energy (except for the excess enthalpies due to lattice defects) is basically given by Eq. (2.1).

The fundamental concept of thermodynamics postulates that a process, which reduces the free enthalpy of the system, will occur spontaneously, i.e. for an infinite period of time the probability of the process to take place will always be unity. Accordingly, for those processes there will be an equivalent flux of heat out of the system into the environment (exothermic reaction). Calorimetric analysis allows to investigate

the amount and the rate of exchanged heat Q between a specimen and a thermal reservoir as a function of time (for isothermal conditions) or temperature (for a defined temperature/time profile).

In solid-state materials the change of free energy can be connected to several processes, as for example phase transformations, diffusion or — for polycrystalline materials — to microstructural changes. Since the temperature interval of the investigated nanocrystalline Fe specimens does not cover the phase transformation at 910°C from α-Fe (bcc ferrite structure) to γ-Fe (fcc austenite structure), the heat release is mainly related to the decrease of microstructural excess energies: that is the grain-boundary excess energy and the excess energy of lattice defects (dislocations and point defects). While the first one is the stimulus for grain growth, the latter one enables recrystallization and recovery — but both will effect an exothermic heat release $Q < 0$.

3.2.1 Differential Scanning Calorimetry

The calorimetric experiments in the frame of this study have been performed in a "Perkin Elmer Pyris 1" calorimeter, which is operated in the differential scanning mode. In the Differential Scanning Calorimetry (DSC) the sample temperature is swept at a constant temperature gradient $RH = \mathrm{d}T/\mathrm{d}t$ (heating rate) through a defined temperature interval (the upper and lower bounds of the accessible temperature interval are defined by technical constraints and detrimental reactions between the sample and the equipment). During a temperature sweep the available thermal energy is increased, which means that the reaction kinetics, or equally the diffusion rate of a solid-state process, increases also (Arrhenius' law).

The quantity Q describes the amount of heat that is released by the specimen. Of course, during a DSC scan the measured quantity will be something like a heat $\mathrm{d}Q$ per unit time $\mathrm{d}t$, i.e. the DSC signal will be $\mathrm{d}Q/\mathrm{d}t = \dot{Q}$ with W (Watts) being the correct unit. Since $\mathrm{d}Q$ will be small compared to the heat capacity of the DSC setup, the precise measurement of an absolute quantity is very difficult, or maybe even impossible. To overcome this problem, the calorimetric analysis is usually performed in the differential mode. This means that simultaneously to the specimen (sample + sample holder) a reference scan (usually an empty sample holder) is run. The specimen and the reference sample are placed for this inside the DSC apparatus into separate measuring cells with high-precision thermometry and heater. Since the differential signal is calculated by the difference between the specimen and the reference signal, $\dot{Q}(t) = \dot{Q}_\mathrm{S}(t) - \dot{Q}_\mathrm{R}(t)$, it is important that the thermal properties of the measurement cells are identical. For a predefined heating rate the power of the reference cell $\dot{Q}_\mathrm{R}$ will be increased to follow the temperature set point, whereas the power of the specimen cell $\dot{Q}_\mathrm{S}$ will be adjusted according to the instantaneous exothermic or endothermic heat flow ("power-compensated DSC"). In this way only the intrinsic heat exchange by the sample is measured. The concept of a power-compensated DSC is schematically illustrated in Fig. 3.18.

The differential calorimetry allows to measure the exchange of heat between a specimen and a thermal reservoir, and thereby the change of free energy. However, during a temperature scan the enthalpy of a polycrystalline material will not only decrease due to grain growth or defect annihilation, it will also increase due to the heat capacity of the material, i.e. due to the increase of thermal energy. To correct for such systematic and reversible heat fluxes, two subsequent DSC scans of the unchanged configuration are performed. The corrected heat flow is then determined by the difference of the two

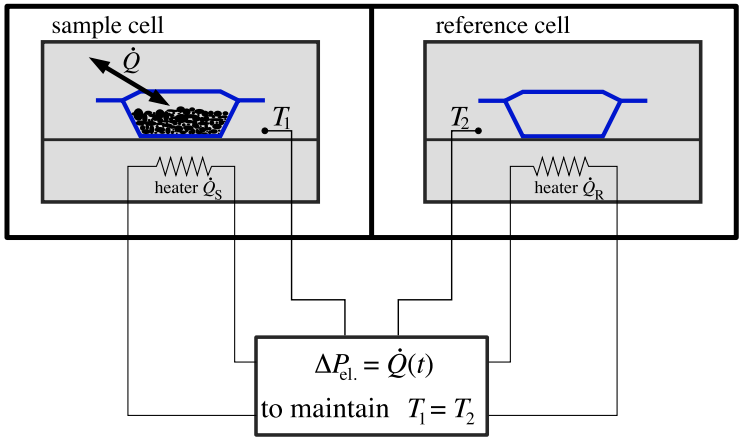

Figure 3.18: Schematic setup of a power-compensated DSC, showing the two separate cells for the specimen and the reference. Both measuring cells are individually equipped with high-precison thermometry and heater unit. For a given heating rate the electrical power of the reference cell is set nominally in order to keep up with the sweeping temperature set point, whereas the heating power of the sample cell considers additionally the exothermic or endothermic enthalpy release of the specimen.

scans, $\dot{Q}(t) = \dot{Q}_1(t) - \dot{Q}_2(t)$, see Fig. 3.19. Only the first scan includes the sought quantity, whereas the second scan (frequently denoted as "base-line measurement") solely contains the reversible effects. To ensure the prerequisite that the base-line scan involves only reversible effects (in particular to exclude grain growth during the second temperature sweep), the specimen must be thermodynamically "equilibrated" between the two scans.

The result of a DSC analysis on nanocrystalline Fe is shown in Fig. 3.19. The graph includes the two subsequent DSC scans $\dot{Q}_1$ and $\dot{Q}_2$ in the temperature interval $50 \ldots 580°C$, which has been passed through at a constant heating rate of 25 K/min. The graph includes additionally the intrinsic heat flow $\dot{Q}$ of the specimen that is calculated from the difference of the two measured curves, and relates to the evolution of the microstructure by grain growth and the annihilation of microstrain.

3.2.2 Analysis of DSC Experiments

3.2.2.1 Activation Enthalpy for Normal Grain Growth

A widely used quantitative analysis of DSC experiments has been proposed by H.E. Kissinger [120]. Kissinger suggested that the activation enthalpy Q_x of a reaction, where the component A reacts over time to the component B, i.e. $[A] \rightarrow [B(+A)]$, can be deduced from the observation of the maximum heat flow $\dot{Q}_{\max}(T)$ as a function of the selected heating rate,

$$Q_x = -k_B \cdot \frac{\mathrm{d}\,\ln\left(RH/T_{\max}^2\right)}{\mathrm{d}\left(1/T_{\max}\right)}, \tag{3.54}$$

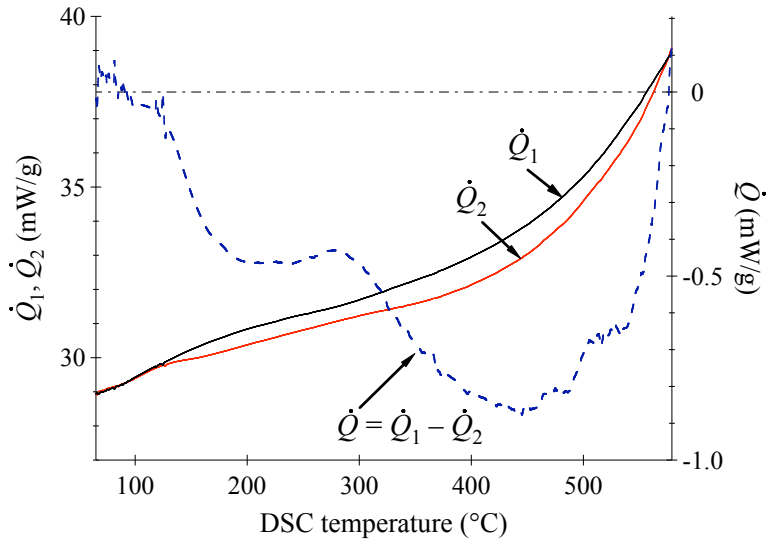

Figure 3.19: Example of a DSC analysis on nanocrystalline Fe, measured at a heating rate of 25 K/min. The DSC signals $\dot{Q}_1$ and $\dot{Q}_2$ (both normalized to the actual mass of the specimen) belong to the sample and the base-line measurement, respectively. The difference between both scans $\dot{Q} = \dot{Q}_1 - \dot{Q}_2$ represents the change of the specimen's free energy upon annealing.

where RH defines the heating rate of the temperature scan, and $T_{\max} = T\big|_{\mathrm{d}\dot{Q}/\mathrm{d}T=0}$ is the temperature of the maximum heat flux [120]. The reason to find a peak maximum of the heat transfer (this coincides with the maximum reaction rate) is the superposition of two effects. First, the kinetics of the reaction increases continuously with an increase of the temperature and second, the reaction rate depends on the amount of the remaining (unreacted) component A, and this quantity is monotonously decreasing. It is therefore evident that the maximum reaction rate will shift to higher temperatures, the higher the activation enthalpy Q_x of the reaction is.

However, the Kissinger method has been basically derived for first-order reactions only (although the order of the reaction is a free parameter in Kissinger's model), which does in general not include the microstructural evolution via grain coarsening.[7] Nevertheless, Fig. 3.19 reveals that there is a remarkable similarity between the DSC curves measured on nanocrystalline Fe and conventional DSC experiments on classical phase transformations. Although grain growth is not conform with Kissinger's derivation, L.C. Chen and F. Spaepen showed that the analysis of activation enthalpies according to Eq. (3.54) remains valid in the particular case of normal grain growth [121]. The free enthalpy H^{GB} of the specimen that is related to existence of grain boundaries equals,

$$H^{\mathrm{GB}} = \gamma^{\mathrm{GB}} \cdot A^{\mathrm{GB}}, \tag{3.55}$$

[7] Grain growth resembles according to Ehrenfest's classification of phase transformations a continuous phase-transformation process with respect to time and temperature, and is therefore not of first-order type.

with A^{GB} the total grain-boundary area. With Eq. (2.18) the energy per unit volume reads then,

$$\frac{H^{\mathrm{GB}}(t)}{V} = \frac{2 \cdot \gamma^{\mathrm{GB}}}{\langle L \rangle (t)} = H_0^{\mathrm{GB}} \frac{\langle L \rangle_0}{\langle L \rangle (t)}, \tag{3.56}$$

where H_0^{GB} and $\langle L \rangle_0$ denote the grain-boundary energy and the mean grain size prior to annealing respectively, and the exothermic flux of heat per unit volume becomes,

$$\dot{Q}(t) = \frac{1}{V} \frac{\mathrm{d}H^{GB}}{\mathrm{d}t} = -\frac{H_0^{\mathrm{GB}} \langle L \rangle_0}{\langle L \rangle^2 (t)} \cdot \frac{\mathrm{d} \langle L \rangle}{\mathrm{d}t}. \tag{3.57}$$

For a temperature-scanning experiment the average grain size can be expressed as [121],

$$\langle L \rangle (T) = \left[\langle L \rangle_0^2 + \int_0^T \frac{k(T)}{RH} \, \mathrm{d}T \right]^{1/2} = \left[\langle L \rangle_0^2 + \frac{I(T)}{RH} \right]^{1/2}, \tag{3.58}$$

where $k(T)$ is the temperature-dependent kinetics constant for grain growth, and the integration variable is substituted by $\mathrm{d}t = \mathrm{d}T/RH$. Thus, the heat flux due to normal grain growth (growth exponent $m = 2$) is then given by [121],

$$\dot{Q}(T) = -\frac{H_0^{\mathrm{GB}} \langle L \rangle_0}{2} \cdot \frac{k(T)}{\left(\langle L \rangle_0^2 + I(T)/RH \right)^{3/2}}, \tag{3.59}$$

with the approximated integral [121],

$$I(T) = \int_0^T k(T) \, \mathrm{d}T \approx \frac{k_B T^2}{Q_x} k(T). \tag{3.60}$$

With Kissinger's criterion to define the peak maximum of the heat output, i.e. $\mathrm{d}\dot{Q}(T)/\mathrm{d}T = 0$ (at $T = T_{\max}$), Chen and Speapen showed that for some simplifications the relationship,

$$\frac{Q^{\mathrm{GG}} \cdot \langle L \rangle_0^2}{k_{\mathrm{B}} T_{\max}^2} = \frac{k(T_{\max})}{2 \cdot RH} \tag{3.61}$$

can be derived, where Q^{GG} denotes now the activation enthalpy for grain growth [121]. If the rate constant is equated by the Nernst-Einstein relation,

$$k(T) = \frac{k_0}{T} \cdot \exp\left\{ -\frac{Q^{\mathrm{GG}}}{k_{\mathrm{B}} T} \right\}, \tag{3.62}$$

Eq. (3.61) yields,

$$\left(\frac{RH}{T_{\max}}\right) = \frac{1}{A} \cdot \exp\left\{-\frac{Q^{GG}}{k_B T_{\max}}\right\}, \tag{3.63}$$

where $A = \left(2Q^{GG}\langle L\rangle_0^2\right) / (k_B k_0)$ is an cumulative temperature-independent constant. Eq. (3.63) demonstrates that for the particular case of normal grain coarsening the activation enthalpy of the rate-limting mechanism can be found from the linear regression of a plot of $\ln(RH/T_{\max})$ versus $1/(k_B T_{\max})$. If the kinetics constant $k(T)$ is defined according to Eq. (4.6) in a slightly simplified way (which neglects the temperature dependence of the pre-exponential factor in Eq. (3.62)), the approach by Chen and Spaepen is obviously equal to Kissinger's method for first-order reactions.

At this point it should be emphasized that the here shown approach by Chen and Spaepen requires strictly normal grain growth, see Eq. (3.58), and fails, if this prerequisite is violated (e.g. if coarsening proceeds in an abnormal way).

3.2.2.2 The Grain-Boundary Energy

During grain growth, the decrease of grain-boundary area by ΔA^{GB} is associated with an amount of heat that is equal to $\Delta Q = \gamma^{GB} \cdot \Delta A^{GB}$. The instantaneous DSC signal during grain growth is therefore given by the time derivative of Eq. (3.55),

$$\dot{Q}(t) = \frac{\mathrm{d}H^{GB}}{\mathrm{d}t} = \frac{\mathrm{d}}{\mathrm{d}t}\left(\gamma^{GB} \cdot A^{GB}\right) = \gamma^{GB} \cdot \frac{\mathrm{d}A^{GB}}{\mathrm{d}t}, \tag{3.64}$$

provided that the specific grain-boundary energy γ^{GB} is not changing during grain growth. Of course, Eq. (3.64) will only be correct, if no other enthalpy-releasing processes are occurring in parallel to grain growth. This seems to be justified for the investigated nanocrystalline Fe samples, if no recovery or recrystallization takes place. If A^{GB} in Eq. (3.64) is related to the mean grain size via Eq. (2.18), i.e. $A^{GB}(t) = 2 \cdot V / \langle L\rangle(t)$, the heat flow per unit volume for isothermal or temperature-sweeping scans can be equated as,

$$\frac{\dot{Q}(t)}{V} = -\frac{2 \cdot \gamma^{GB}}{\langle L\rangle^2(t)} \cdot \frac{\mathrm{d}\langle L\rangle(t)}{\mathrm{d}t}. \tag{3.65}$$

Eq. (3.65) reveals that the DSC data contains information not only of the thermodynamic quantity γ^{GB}, but could in principle provide access to the kinetics of grain growth. Of course, the latter information will be only useful for isothermal analyses.

For the analysis of the specific grain-boundary energy, a time interval $[t_1; t_2]$ is selected in the DSC scan, in which other enthalpy sources than grain growth are either not present, or are negligible compared to the released grain-boundary-excess enthalpy. For the analysis of γ^{GB}, the mean grain sizes $\langle L\rangle_1(t_1)$ and $\langle L\rangle_2(t_2)$ of the microstructure at the beginning and the end of the interval have to be measured (this requires an additional grain-size analysis of the sample, e.g. via XRD). The grain-boundary-excess enthalpy that is stored at the time t_1 and t_2 inside the specimen can be evaluated according to Eq. (3.55),

and the difference ΔH^{GB} of both values will give the released enthalpy due to the coarsening of the microstructure within the specified time interval,

$$\Delta H^{\mathrm{GB}} = \gamma \cdot \Delta A^{\mathrm{GB}} = \int_{t_1}^{t_2} \dot{Q}(t)\,\mathrm{d}t. \tag{3.66}$$

With Eq. (2.18), the specific (mean) grain-boundary energy is then given from,

$$\left\langle \gamma^{\mathrm{GB}} \right\rangle = \frac{\Delta H^{\mathrm{GB}}}{2V} \cdot \left(\frac{\langle L \rangle_1 \cdot \langle L \rangle_2}{\langle L \rangle_2 - \langle L \rangle_1} \right), \tag{3.67}$$

where ΔH^{GB} is the result of the numerical integration of the measured DSC trace, as defined in Eq. (3.66).

Eq. (3.67) shows that the determination of the grain-boundary energy γ^{GB} requires two independent measurements: The calorimetric amount of released enthalpy and the measurement of the respective grain sizes at the beginning and the end of the DSC anneal.

3.2.2.3 The Enthalpy of Dislocations

During cold working of solid crystalline materials, dislocations are created within the crystal lattice. The approach of cold working is one of the established methods to prepare nanocrystalline materials in a top-down process, and it is the implemented synthesis process for the samples of this study. The observation of residual dislocations is therefore likely for the analyzed samples of nanocrystalline Fe. Depending on the characteristics of the material (mainly with respect to the mobility of dislocations), the created dislocations either migrate to lower the system's energy (this process is known as recovery), or for a low mobility the dislocations remain in the deformed material. In the latter case the excess-energy contribution of the dislocations may then initiate recrystallization, i.e. the nucleation and growth of a low-energy domain, where the immobile dislocations are swept up by the migrating boundary of the growing domain (recrystallization "nucleus").

During the annihilation of dislocations the enthalpy is lowered by $Q^{\mathrm{D}} = \sum Q_i^{\mathrm{D}}$, where Q_i^D is the enthalpy of a specific dislocation. If the energy of the dislocations is associated with the strain field in the surrounding lattice, the enthalpy per unit length can be estimated for isotropic elasticity by [122],

$$Q_i^{\mathrm{D}} = \frac{G \cdot b^2 \cdot f(\nu)}{4\,\pi} \cdot \ln\left(\frac{R}{R_0}\right), \tag{3.68}$$

where G is the shear modulus, b the magnitude of the Burgers vector, $f(\nu)$ a function of the Poisson ratio, and R and R_0 the outer and inner cutoff radius of the strain field. Eq. (3.68) provides a reasonable approximation of the dislocation excess energy, if the dislocation can be considered as an isolated defect. However, the actually high dislocation density in cold-worked materials causes an interaction of the dislocations and their strain fields, and the dislocation-associated enthalpy depends strongly on the actual environment of the defect.

Although detailed information for the exact enthalpy of a specific dislocation seems difficult to get, this level of knowledge is fortunately in practice not needed. The measured quantity of the calorimetric experiment will be the integral enthalpy Q^{D} of a large number of dislocations, and it is sufficient to have an adequate estimate for a mean dislocation enthalpy. If ϱ denotes the dislocation density in the material, the related excess enthalpy can be approximated by [122],

$$Q^{\mathrm{D}} = \int \dot{Q}\,\mathrm{d}t = \frac{1}{2}\cdot\varrho\cdot G\cdot b^2. \tag{3.69}$$

The numerical integration $\int \dot{Q}\,\mathrm{d}t$ of the DSC signal has to be limited to the dislocation-related part of the DSC curve.

3.2.2.4 Abnormal Grain Growth in DSC

Basically all models dealing with the temporal evolution of a polycrystalline microstructure describe the phenomenon as a homogeneous and size-scaled process. If this prerequisite holds, the evolution of the microstructure — for example represented by the average grain size — and the enthalpy output $H^{\mathrm{GB}}(t)$ upon grain growth is fully defined. However, if normal grain-growth theory is not valid and the microstructure grows irregularly, the evolution of the mean grain size and the released enthalpy are difficult to predict. Since the constraints to enable normal grain growth are quite restrictive, there is a substantial probability that abnormal grain growth occurs, i.e. only a sub-population of grains will perform significant growth, whereas the majority of grains (which will be called "matrix" in the following) are only of low kinetics, or are completely disengaged. The fact, that abnormal grain growth is of statistical nature requires to define an adequate numerical model to assess the associated heat release.

Fig. 3.20 illustrates a sphere model that was proposed by L.C. Chen and F. Spaepen to evaluate the enthalpy release when an abnormal grain is irregularly growing in the neighborhood of matrix grains [121]. The model assumes that an abnormal central grain of size D is embedded in a matrix of non-abnormal grains of mean size d (all grains are considered to be of spherical shape). While only the abnormal grain shares a high-velocity boundary with his neighbors, the boundaries between the matrix grains are "static". The reason for such a difference in kinetics can be quite diverse and will be discussed later. For the moment only the effect of different kinetics is considered.

The model examines the release of enthalpy when the abnormal grain grows into the matrix. For such a configuration the reduction of enthalpy is determined by the difference between the grain-boundary-excess enthalpy $\Delta H^{\mathrm{matrix}}$ of erased matrix boundaries, and the increased surface area of the abnormal grain $\Delta H^{\mathrm{abn.grain}}$ [28],

$$\Delta H^{\mathrm{AGG}} = \Delta H^{\mathrm{matrix}} - \Delta H^{\mathrm{abn.grain}}. \tag{3.70}$$

If the abnormal grain grows by an infinitesimal distance from initially D to $D + \Delta D$, the related lowering of matrix-excess enthalpy can be approximated by,

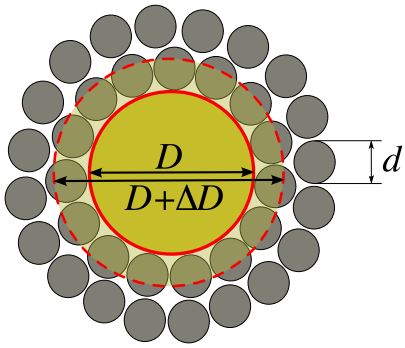

Figure 3.20: "Sphere model" to assess the enthalpy release during abnormal grain growth. The central abnormal grain of size D is embedded in a matrix of inhibited grains of size d. During abnormal grain growth the central grain is growing, and gradually annihilates the matrix grains together with the respective excess enthalpy of matrix-matrix grain boundaries.

$$\Delta H^{\text{matrix}} \approx \frac{\Delta V_\text{a}}{V_\text{m}} \cdot \frac{\gamma^{\text{GB}} \cdot A_\text{m}^{\text{GB}}}{2} = \frac{\pi D^2 \cdot \Delta D}{2\,(\pi/6)\,d^3} \cdot \frac{\gamma^{\text{GB}}}{2} \cdot \pi d^2, \tag{3.71}$$

where ΔV_a is the infinitesimal volume increase of the abnormal grain, and V_m and A_m^{GB} are the average volume and surface area of the matrix grains, respectively. On the other hand, the increasing excess-surface enthalpy of the abnormal grain is given by,

$$\Delta H^{\text{abn.grain}} \approx 2\pi \cdot D \cdot \Delta D \cdot \gamma^{\text{GB}}. \tag{3.72}$$

Using Eq. (3.71) and (3.72), the effective enthalpy release can then be equated as,

$$\Delta H^{\text{AGG}} = \left(\frac{3\,\gamma^{\text{GB}}}{d} - \frac{4\,\gamma^{\text{GB}}}{D} \right) \cdot \Delta V_\text{a}. \tag{3.73}$$

If the volume of the abnormal grain is expressed in terms of a volume fraction $x_\text{V} = V_\text{a}/V$, and $\mathrm{d}V_\text{a} = \mathrm{d}x_\text{V} \cdot V$, the specific heat flow per unit volume for abnormal grain growth is determined by,

$$\frac{1}{V} \cdot \frac{\mathrm{d}H^{\text{AGG}}}{\mathrm{d}t} = \frac{\mathrm{d}x_\text{V}}{\mathrm{d}t} \cdot \left(\frac{3\,\gamma^{\text{GB}}}{d} - \frac{4\,\gamma^{\text{GB}}}{D} \right) + \left(\frac{4\,\gamma^{\text{GB}}}{D^2} \cdot \frac{\mathrm{d}D}{\mathrm{d}t} \right) \cdot \mathrm{d}x_\text{V}, \tag{3.74}$$

where the conditions for a static matrix have been applied, i.e. $\mathrm{d}\,\langle d \rangle\,/\mathrm{d}t = 0$. Eq. (3.74) shows that even for such a simple model the expected DSC signal takes on a relatively complicated form.

Eq. (3.74) provides an appropriate description of the DSC signal as long as the abnormal growth occurs as illustrated in Fig. 3.20. It seems likely that in a DSC experiment only the beginning of AGG can be recorded, since the full scan will not last longer than ~50 min, and only at the higher temperatures at the end of the temperature sweep the kinetics is fast. Considering this, $\mathrm{d}V_\text{a}$ — and therefore also $\mathrm{d}x_\text{V}$ —

are assumed to be small. Further it might be argued that the two populations of abnormal and matrix grains are similar in size, which means that $\langle d \rangle \approx \langle D \rangle$ (this assumption should be justified for narrow size distributions in the initial state prior to annealing, as found for the here investigated samples).

Using these two assumptions, the specific heat flux due to abnormal grain growth is then approximately given by [121],

$$\frac{1}{V} \cdot \frac{\mathrm{d}H^{\mathrm{AGG}}}{\mathrm{d}t} \approx -\frac{\gamma^{\mathrm{GB}}}{D(t)} \cdot \frac{\mathrm{d}x_{\mathrm{V}}}{\mathrm{d}t}. \tag{3.75}$$

Eq. (3.75) shows an interesting detail: If the grain size $D(t)$ is known or could at least adequately be estimated, the measured DSC data would in principle allow to access the initial characteristics of x_{V}, and therefore may allow to draw inferences on the kinetics and eventually the nature of abnormal growth.

3.2.3 Experimental Procedure of DSC Experiments

To avoid inadvertent contamination of the DSC equipment, and to avoid oxidation of the nanocrystalline Fe specimens, the powder samples were hermetically sealed in suitable sample containers (aluminum cups) that where closed after loading with a mechanically crimped lid. Loading the powder and sealing the sample holders was done inside a glovebox under protective Argon atmosphere to prevent the inclusion of oxygen.

Since the released enthalpy of the specimen is an extensive quantity, it is important to determine the actual mass of sample material inside the cup, which allows afterwards to normalize the measured enthalpy in terms of Joule per mol. To determine the specimen's mass precisely, the empty cup including the lid was weighed by using a high-precision scale. After sealing the powder material in the sample holder, the weight was measured again, and the mass of the powder sample calculated accordingly from the difference (for the conducted DSC experiments the amount of sample material was typically ~50 mg). For the reference channel of the DSC an equivalent empty cup was prepared under identical conditions.

To perform a DSC experiment, the temperature was increased at a constant heating rate of 10, 15, 20 or 25 K/min from 50°C to the final temperature of 580°C . The upper limit of the DSC experiment is introduced by the properties of the sample-holder cups, and by chemical reactions between the specimen and the cup material. To guarantee identical conditions for each DSC run, the temperature was hold at the starting value of 50°C for 1 min to stabilize the system. When the final temperature of 580°C has been reached in the first scan (see $\dot{Q}_1$ in Fig. 3.19), this condition was maintained for additional 30 min before the sample was returned to ambient conditions. The intention of the holding time is an equilibration of the microstructure for the subsequent baseline measurement (it is important that the base-line measurement is performed without touching the sample in between the two scans).

3.3 Electron Microscopy

It is the main disadvantage of XRD and DSC that the evolution of the microstructure is not directly accessible. Both techniques require an appropriate interpretation of the experimental data to correlate the available information with the processes that are operative on the microstructural level. Different to those indirect investigation methods, the imaging of polycrystalline samples by microscopy can provide direct access to the microstructure. From this advantage of microscopy it would be tempting to assume that micrographs should be the preferred method to investigate the properties of microstructures. However, in reality there are basically three issues that are restraining microscopy:

- micrographic analysis provides only 2-dimensional information of the microstructure,
- the information of micrographs is always limited to small areas of the sample, and
- the influence of the surface normally disallows to observes the same *in-situ* kinetics as in the bulk.

For those reasons, microscopy can only be an auxiliary tool in the challenge of characterizing the evolution of nanocrystaline materials. The main application of microscopy within the present study will therefore be the assessment and validation of hypotheses and conclusions on nanocrystalline grain growth that have been drawn from bulk-analysis methods and numerical models.

3.3.1 Transmission Electron Microscopy

This section will briefly introduce the basic concepts of Transmission Electron Microscopy (TEM), to give a background for the interpretation of TEM micrographs. The imaging process in TEM is quite similar to optical systems, where the main difference is the usage of electromagnetic lenses to focus the electrons instead of optical lens systems. The advantage of TEM compared to optical microscopy is the outstanding resolution of the imaging process, which allows to examine structures on the scale of atoms. This high resolution is achieved by the extremely short wavelength λ_e of electrons, which is according to the de Broglie relation dependent on the actual velocity of the electrons,

$$\lambda_e = \frac{h}{p^*}, \tag{3.76}$$

where h and p^* denote Planck's constant and the relativistic momentum of the electron respectively [123]. For typical acceleration voltages of 200 kV the wavelength of the electrons becomes approximately $\lambda_e = 0.002$ nm, which is about five orders of magnitude smaller than visible light. Due to this advantage the possible resolution of modern TEM systems is approximately 1Å (= 10^{-10} m).

A TEM system is typically built up by four main components: the electron gun with condenser unit, the specimen, the object-lens unit and the imaging-lens unit. The electron source and the condenser are arranged above the specimen and are required to provide a high-energy collimated electron beam, whereas the object and the imaging-lens unit sit below the specimen and create the electron image. When electrons with wave vector $\mathbf{k}_0$ enter the sample, they will interact due to electrostatic Coulomb forces with the electrons and the atomic nuclei of the material, and will be scattered either elastically or

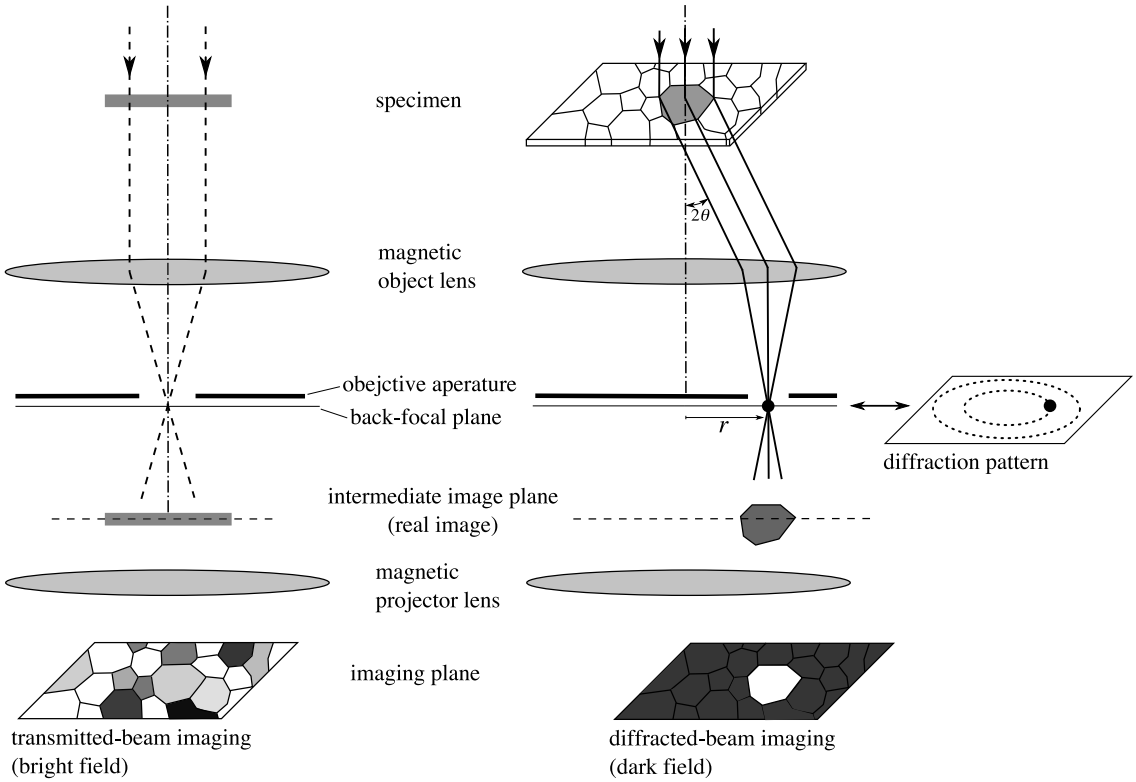

Figure 3.21: Schematic representation of the dark-field (right side) and the bright-field (left side) imaging process in a TEM.

inelastically. Accordingly, the wave vector $\mathbf{k}$ of an scattered electron will deviated from $\mathbf{k}_0$ [123]. The degree of scattering depends basically on material-specific parameters, like the atomic number and the density of the material, but depends also on the crystallographic orientation of the specimen.

Similar to the diffraction of light, the wave-like character of electrons may provoke the interference of coherently scattered electrons and hence, the occurrence of a diffraction-intensity distribution, which is likewise explained by the Bragg equation. Since λ_e is much smaller in the case of high-energy electrons than the wavelength of x-rays, it is obvious that the diffraction angle will be extremely small, which makes a lens system for a magnified projection necessary.

Depending on the operational mode of a TEM, two different imaging types are available: the bright-field and the dark-field image. Fig. 3.21 illustrates schematically these two types of imaging process.

Dark-Field (DF) Mode in TEM

The coherent scattering of electrons by crystalline materials will give rise to a measurable diffraction intensity, if the diffracted electrons fulfill the Bragg condition of Eq. (3.1). To allow for constructive interference at the point of observation, the diffraction vector $\Delta\mathbf{k} = \mathbf{k} - \mathbf{k}_0$ of the scattered electrons must be equal to a lattice vector $\mathbf{u}$ of the reciprocal lattice, i.e. $|\mathbf{u}| = |\mathbf{k} - \mathbf{k}_0| = n/d_{hkl}$ (n denotes the order of

diffraction) [123]. For polycrystalline materials it seems likely that at least some grains are oriented in a way that a set of (*hkl*) lattice planes satisfies the Bragg criterion. The electrons, which are scattered by those grains are then diffracted under an angle $2\theta_{\mathrm{hkl}}$ with respect to the incident direction, see Fig. 3.21 (right side). In a first step the diffracted electrons of each grain are focused by the object lens into points in the back-focal plane. If only a single grain is considered, the intensity distribution in the back-focal plane will then be equal to the mapped reciprocal lattice points n/d_{hkl} of the diffracting grain (individual spots of intensity). Since the number of grains in polycrystalline materials can be very large, it is likely that several grains satisfy the Bragg condition at the same time, which have the same orientation with respect to the incident beam, but can be rotated around the incident wave vector $\mathbf{k}_0$. In such a case the observed diffraction pattern would show rings of high intensity (Debye-Scherrer rings), rather than discrete spots. The radius of the diffraction rings (see Fig. 3.21) is determined by both the Bragg equation and the geometry of the TEM system, and can be calculated by,

$$r = \frac{\lambda \cdot L}{d_{\mathrm{hkl}}}. \tag{3.77}$$

The product $\lambda \cdot L$ is the camera constant of the used TEM, where L defines the projection length [123].

If in a further step the diffraction pattern in the back-focal plane is projected into the imaging plane by an appropriate excitation of the projector-lens unit, the electron-diffraction image can be observed on the screen. The DF image contains then all grains that fulfill the conditions for diffraction. For an efficient use of electron diffraction it is necessary to place an aperture close to the back-focal plane. If the aperture has the shape of a pinhole and is placed on an arbitrary position of a (*hkl*) diffraction ring, the orientation of grains that are visible in the observation plane, is uniquely defined. Only grains of this orientation can show up on the electron image, while diffraction from other grains is cut out by the aperture. At the position of non-diffracting grains, or diffracted electrons that are cut out by the aperture, the detector screen will be dark (i.e. the intensity is zero). Due to the finite size of the pinhole aperture the dark-field image of a polycrystalline sample will not be ideal, and contain grains that are aligned within a certain orientation spread.

The information from DF analysis can be particularly helpful, if the orientational relationship between neighboring grains or texture has to be investigated.

Bright-Field (BF) Mode in TEM

If the aperture in the back-focal plane is placed in the center of the optical axis (see left side of Fig. 3.21), diffracted and scattered electrons are mostly suppressed and only the transmitted electrons pass the aperture. In the BF mode it is therefore basically the thickness, the atomic weight and the crystallographic orientation of the specimen that determines the contrast of the observed electron image. This explains why in polycrystalline materials individual grains (of different crystallographic orientation) usually appear with different brightness. Since grain boundaries (but also dislocations) are regions of particularly disordered atomic structure, they will be reflected in the BF image as lines of different intensity. The BF micrographs yield therefore similar to optical imaging a direct picture of the microstructure. Especially for BF imaging the preparation of the specimen is particularly important, since the sample thickness will affect the measured signal directly. In particular, if the sample is thicker than one grain diameter, the

transmitted electron intensity can be subsequently influenced by several stacked grains, and a conclusive analysis of a BF image becomes very difficult.

3.3.2 Orientation Imaging Microscopy

The diffraction of high-energy electrons cannot only be used to create DF imaging in TEM, it establishes also the basis for Orientation Imaging Microscopy (OIM). If OIM is performed inside a Transmission or a Scanning-Electron Microscope (TEM or SEM), the position of the electron beam on the specimen surface allows to investigate the diffraction pattern of a defined spot — in principal, this feature enables a spatially resolved analysis of grain orientations. Similar to the DF and BF imaging by TEM provides the evaluation of OIM investigations information on grain size and grain topology, however it is the outstanding feature of OIM to support additionally the examination of spatial grain orientations and provides thereby information about the relative misorientation between adjoining grains, i.e. the misorientation of grain boundaries. This ability of OIM can be an important tool in the investigation of texture, or the assessment of misorientation-dependent grain-boundary properties.

OIM is based on the principles of the Electron-Back-Scattered Diffraction (EBSD), which means that this technique uses similar to TEM DF the interference of scattered electrons. Fig. 3.22 illustrates the principles of EBSD that is usually performed in laboratory TEM or SEM setups. The primary electron beam that is emitted by the high-voltage electron gun of the microscope enters the sample and undergoes inelastic scattering events with the material. The result of the inelastic scattering will be the generation of secondary electrons that are creating a divergent electron beam. Since the emission of secondary electrons occurs divergently, there is a certain probability that for a set of (hkl) lattice planes secondary electrons can be found, which fulfill the Bragg condition. The electrons will then be diffracted by elastic scattering at the lattice planes and leave the specimen under an diffraction angle θ relative to the lattice planes. Due to the divergence of the secondary electrons, diffraction can occur isotropically with respect to the lattice-plane normal, and therefore the diffracted intensity will form a cone (Kossel cone) with an opening angle $(180° - 2\theta)$, which has the central axis parallel to the normal of the diffracting planes (shown in Fig. 3.22). If at a certain distance from the specimen a fluorescence screen is located (to visualize the electron intensity), the intersection of the diffraction cone with the screen will define a "Kikuchi line".

Since the secondary electrons form a divergent beam, it is possible that different (*hkl*) planes of a grain can meet the conditions for diffraction. In this case the diffraction pattern on the fluorescence screen will show several Kikuchi lines, which have an angular orientation on the screen that reflects the orientation of the lattice planes. Thus, if the crystallographic structure of the specimen is known, the relative alignment of the Kikuchi lines can be used to calculate the orientation of the grain with respect to the Euler angles in laboratory coordinates.

For the present study on nanocrystalline Fe, OIM has been performed in a "Zeiss Leo 1540" SEM that is furnished with an EBSD system from Oxford Instruments. The normal operating condition of the SEM for EBSD was 20 kV acceleration voltage. Collecting the diffraction data from the fluorescence screen (via a CCD camera) and analyzing the Kikuchi diffraction pattern was automatically performed by the "INCA Microanalysis Suite". Since the spot position of the primary electron beam on the sample is controlled by the INCA software, the calculated crystallographic orientation can be related to a particular position

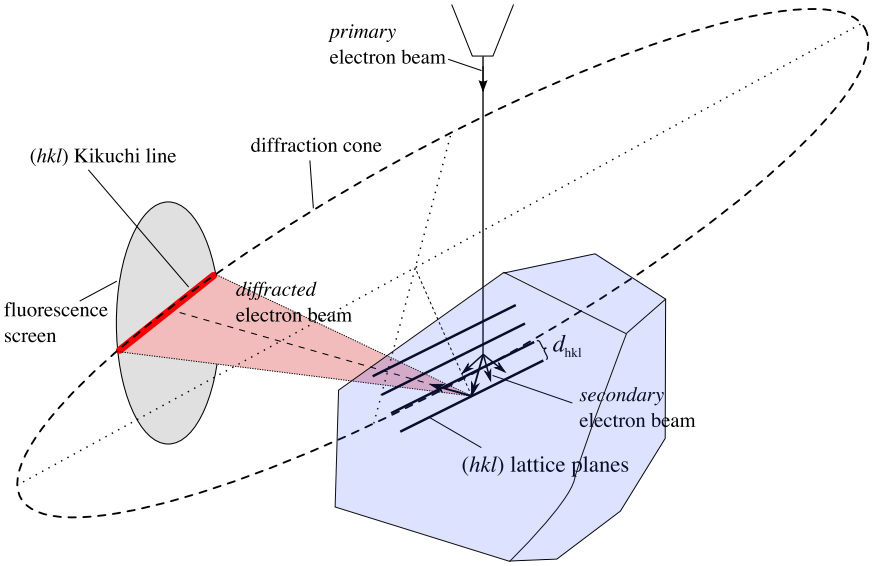

Figure 3.22: Functional principle of EBSD imaging. The secondary electrons are emerging from inelastic interaction of the primary electron beam with the material, and create a divergent electron beam. Lattice planes that are in Bragg condition with the secondary electrons will diffract and generate a Kikuchi-line pattern on the fluorescence screen.

of the sample. This allows to perform spatially-resolved mapping of grain orientation by line scans of the surface. Of course, for a scanning experiment on nanocrystalline materials the spatial resolution of OIM has to be adequate, which depends strongly on the minimum spot size of the focused electron beam and the surface quality of the specimen. This is aggravated by the fact that the sample is usually tilted for EBSD (typically by 70° from the horizontal plane), which requires particularly for large scanned areas an automatic adjustment of the beam focusing. The experience shows that with the used EBSD/SEM combination a grain-size resolution of ~20 nm can be achieved.

It is the nature of high-energy electrons that the mean-free-path length is small, and reaches values of 10 . . . 100 Å for electrons beyond 0.5 keV [124]. It is therefore not surprising that EBSD is a very surface sensitive analysis, and does not include information of subjacent grains. According to this distinct surface sensitivity, a thorough preparation of the sample surface is a major issue to obtain good data quality. Initial attempts have shown that mechanical grinding and polishing will provide a smooth surface, but will also induce signficant grain growth in nanocrystalline Fe, with grain sizes measured by EBSD in the range of 10. . . 100 μm, see Fig. 3.23(b). It was therefore necessary to subject the mechanically pre-polished samples to ion milling, similar to the sample-preparation procedure for TEM. The surface has been treated by Argon ions (1. . . 5 keV energy) at an angle of approximately 10° from the surface plane, while the sample was rotated at 2 rpm to obtain a homogeneous abrasion of material. It should be noted that different to TEM samples the ion milling was not intended to create a thin area for electron transmission, but was used to remove the top layer of the surface after mechanical treatment.

Figs. 3.23(a) and 3.23(b) show an electron image of the sample surface after mechanical polishing and

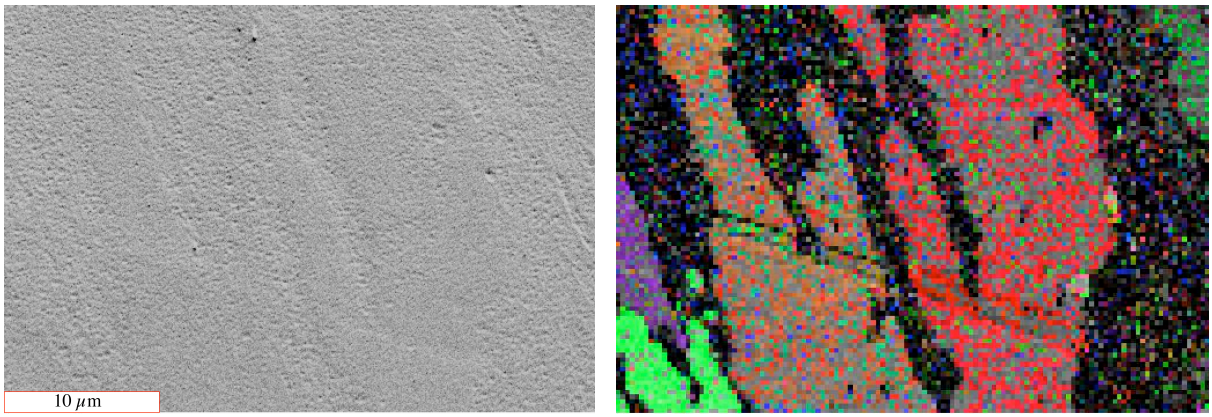

(a) (b)

Figure 3.23: a) Secondary-electron image of the scanned sample surface after ion milling, b) solution of the EBSD pattern recorded on the area of the left-hand-side image.

ion milling, and the corresponding EBSD image (overlay of the pattern-quality signal and the orientation solution), respectively. It can be seen that even after ion treatment large grains with irregular shape are still present. A thorough inspection of Fig. 3.23(a) shows that the large grains can already been observed from the surface roughness of the electron image, where a high roughness coincides with the black area of the EBSD image in Fig. 3.23(b), and a smooth surface in the electron image is found at the position of the large grains. The reason for the black areas in the right-hand image is the large field of view of the EBSD scan, for which the spatial resolution is ~500 nm. For grains smaller than this size EBSD will not be able to assign a unique orientation, and therefore the indexing software leaves the region black. The finding of areas of different roughness, which correlates directly with the examined crystallite structure may suggest that either ion milling is anisotropic, where certain crystallographic orientations are more resistant to abrasion, or that the grains resulting from mechanical polishing are much larger than the removed layer. Since the dimensions of the remaining large grains appears to be larger than the removed layer thickness, the second possibility seems more likely. However, an extended ion treatment, which could possibly remove the enormous grains completely, may cause a degradation of the crystal lattice and an amorphous atomic structure near the surface. The EBSD analyses within this study have therefore been performed in the eroded areas after ion treatment, i.e. in the dark areas of Fig. 3.23(b).

The reason for the formation of large grains during mechanical polishing of the studied samples was not in detail investigated; however it seems possible that large mechanical stresses or locally high temperatures could have initiated significant growth of the grains. A conclusive explanation requires however further research.

Chapter 4

Grain-Growth Kinetics in Nanocrystalline Materials — A Case Study on nanostructured Iron: Experimental Results

The experimental tools and analysis methods to examine the evolution of nanostructured specimens have been introduced in the previous chapter. It will be the content of this part to present in detail the experimental results from *in-situ* XRD, DSC and electron microscopy of the coarsening kinetics and the microstructural stability of nanocrystalline Fe.

The procedure and basic results of sample preparation for the investigated nanocrystalline Fe will be briefly addressed in a short preceding section.

4.1 Synthesis of Nanocrystalline Iron

4.1.1 Overview

Within the last decades a number of different synthesis routes — either top-down or bottom-up techniques — have been developed to create nano-sized individual particles or bulk-like polycrystals of nanocrystalline structure [1]. Bottom-up approaches, like for example inert-gas condensation, vapor-phase reactions, micro-emulsions or spray pyrolysis, are usually involved to prepare small individual particles. If the properties of bulk samples are however in the focus of the analysis, it is necessary to compact the particles to an larger aggregate. This post-process requires in principle high hydrostatic pressure (and usually also elevated temperatures), which makes it for nanocrystalline materials that are being in a highly unstable thermodynamic state to an unsuitable approach. It is also often observed that even after strong compaction the density of the material will be less than the one of bulk material, i.e. the specimens are not fully dense. Since pores may act like defects, which prevent grain-boundary migration, the lower density may adversely affect experiments on grain growth.

Another bottom-up technique is the rapid solidification of a molten sample, which yields however in contrast to the before mentioned processes amorphous or polycrystalline bulk material instead of

single particles. Although rapid solidification can allow to prepare alloyed samples of theoretically immiscible components, it is likely that the required temperature gradient during rapid cool-down results in anisotropic grain shape and crystallite orientations that are affected by the temperature gradient. Those features of rapid solidification, and also the fact that the achievable grain size is mostly larger than the microstructures envisaged for the present study, argue against this technique.

The common feature of most top-down techniques on the way to nanocrystalline materials is the application of severe mechanical deformation. The plastic deformation involves the creation of excessive dislocation densities and a possible rearrangement of the dislocation excess into new (sub-)grain boundaries during recovery and/or recrystallization, which will finally lead to a refinement of the initial grain structure. A typical process for a top-down approach is the cold working of a solid material, for example by torsional deformation or mechanical attrition (e.g. ball milling) [125, 126].

Assessing the advantages and disadvantages of the various synthesis routes for the preparation of nanostructured bulk-like Fe samples shows that mechanical attrition via ball milling should provide the best tradeoff in terms of sample quality and operational effort. Ball milling was therefore selected to prepare the nanocrystalline Fe specimens for the present study. Although the final result of a ball-milling process will be powder-like particles, which have been found for α-Fe to range typically between $50 \ldots 500$ μm in diameter, the dimension of the particle is still $3 \ldots 4$ orders of magnitude larger than the average crystallite size of the microstructure. The obvious large difference between particle and grain size allows therefore to investigate the growth of nano-scaled grains in a bulk environment.

At a first glance, ball milling appears to be a rather simple process, however a closer view on the involved crystal-lattice mechanisms shows that the refinement of the microstructure can be rather complex. Since the evolution of the dislocation-excess density will occupy a major part of the discussion (see Chapter 5), only a brief summary of the main steps of the nanostructure formation will be outlined in the following [34, 126, 127]:

(*i*) During a ball–particle collision, kinetic energy is transferred to the powder particle. A major fraction of the energy is converted into heat (for example via friction or elastic deformations), whereas only a minor fraction is stored due to plastic deformation. Since, the deformation process of a crystalline material is usually connected to the creation and the migration of dislocations, this process introduces an appreciable excess-dislocations density in the lattice.

(*ii*) Thereby, the free energy of the specimen is increased, which could relax again, if the dislocations are organized via dislocation recovery in networks or tangles of dislocations, which will define a uniform substructure of newly created interfaces. A prerequisite for recovery is of course that the dislocations do have a sufficient mobility to migrate over a certain spatial distance. At the end of the process the microstructure contains a high density of new low-angle grain boundaries, which are inducing a refinement of the initial grain size.

(*iii*) If the mobility of dislocations is too low for recovery, a self-organization of the dislocation excess cannot occur. In this case it might be found that a domain of lower dislocation density ("nucleus") starts to grow into the dislocation-cluttered volume and is thereby erasing the residual dislocations (this process is also known as "recrystallization"). The final microstructure depends then strongly on the available excess-energy density and the distribution of recrystallizing nuclei.

4.1.2 Sample Preparation: Experimental Procedure

The specimens for the present study on the coarsening kinetics of nano-structured Fe have been prepared via ball milling in a "Spex 8000M". All parts of the equipment (milling vail and balls), which are in direct contact with the sample, consist of hardened stainless steel to minimize abrasion. The vail is equipped with a sealed lid to provide a hermetic containment and an airtight sealing of the specimens during the milling procedure. Fig. 4.1 illustrates a schematic of the milling vail that is loaded with powder material and milling balls.

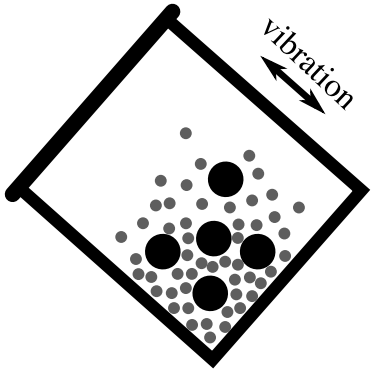

Figure 4.1: Grain refinement of nanocrystalline Fe by ball milling. The mechanical movement (vibration) of the milling vail is converted into kinetic energy of the milling balls (large black spheres) inside the vail, which will transfer their energy to the powder particles (small grey spheres) by ball-particle collisions. The collisions are creating a plastic deformation of the lattice, which is associated with the generation of excess dislocations. The subsequent reorganization of the dislocation excess into dislocation arrays allows the relaxation of the sample to a lower configuration energy and creates a refined microstructure.

Prior to the milling sequence, the vail was loaded inside a glovebox under Argon atmosphere with ~5 g of highly-pure Fe raw powder (ChemPur product ID 009205, 99.99+% metallic purity, initial particle size 5 . . . 30 μm) and a set of stainless steel balls with 4× ∅10 mm (~4.0 g) and 4× ∅5 mm (~0.5 g). The ball-to-powder mass ratio was therefore approximately 3.6 for all runs of the Spex mill. The evaluation of a test series on the influence of the milling time showed that after 15 h the maximum refinement of the microstructure is achieved. Extended milling times are not providing a further reduction of the grain size (however, at extended milling time the risk of contamination increases). Based on this finding, the running time of all milling processes to prepare nanocrystalline Fe have been set to 15 h, where the final grain size reached a value of $\langle L \rangle_{\mathrm{vol}} = 21$ nm (analyzed by XRD). Similar results on the final state of ball-milled Fe are reported by Moelle and Fecht [128], Bonetti *et al.* [129] and Börner and Eckert [130]. The soft character of highly pure bcc materials involves that the specimens agglomerate to larger clumps of 50 . . . 500 μm in size. Fig. 4.2 includes a SEM image, showing the typical morphology of the final powder particles. After completion of the sample-preparation process, the specimens have been stored inside a glovebox to avoid oxygen contact.

The samples for the present study have been prepared in two batches, which will be denoted in the following as "X1" and "X2".

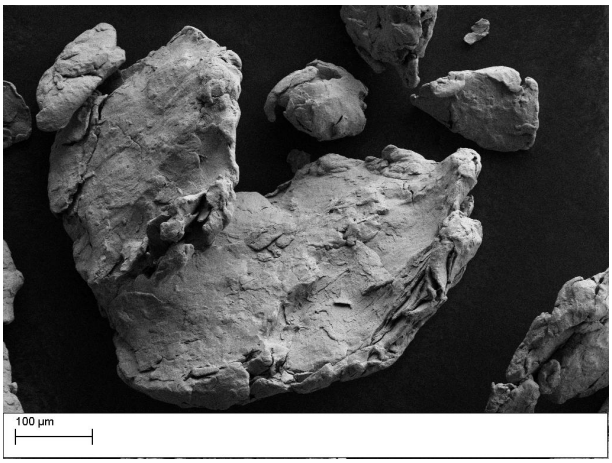

Figure 4.2: SEM image of as-prepared nanocrystalline Fe after 15 h of ball milling.

The as-prepared state of the nanocrystalline Fe was examined by XRD. The diffraction pattern of a representative sample is shown in Fig. 4.3. From the diffraction data it can be noticed that within the measured range $2\theta = 48° \ldots 130°$ no signal is found in addition to the four expected peaks of bcc Fe. This observation indicates that the specimens are indeed of single-phase type, i.e. there are no undesired phases present (for example due to oxidation) — at least not above the volume-sensitive detection limit of XRD. The WA analysis of the as-prepared diffraction data yields for the microstructure average grain-size values of $\langle L \rangle_{\text{vol}} = 21$ nm and $\langle L \rangle_{\text{area}} = 18$ nm, and a mean microstrain level $\left\langle \varepsilon^2 \right\rangle^{1/2} = 0.35\%$.[1]

With respect to the process of mechanical attrition, ball-milled samples are frequently suspected to contain critical amounts of impurities due to abrasion from the milling vail and steel balls. Since impurities can have a serious impact on grain-growth kinetics (*cf.* Section 2.6) a thorough analysis of contamination — particularly from the low-level alloying elements of the stainless-steel equipment, i.e. Carbon (C), Silicon (Si) and Chromium (Cr) — is necessary. The impurity concentrations in the powder specimens have been analyzed by atomic absorption spectroscopy (AAS) for Chromium and photometry for Silicon. The concentration of Carbon was measured in a CHN analyzer. Table 4.1 summarizes the measured impurity concentrations for both batches X1 and X2.

The compulsion of solutes to grain-boundary segregation depends basically on the difference between the excess energy that is related to the accommodation of a solute atom either in the bulk or the interface (for details please refer to Section 2.6). Following Eq. (2.59), the enthalpy of mixing ΔH_{mix} (in the bulk or the interface) is given by the sum of the respective chemical and elastic energies ΔH_{chem} and ΔH_{el}. Due to the disordered structure of grain boundaries it appears reasonable to assume that the elastic term in the interface should be significantly lower than in the bulk. For the sake of convenience it might therefore be assumed that $\Delta H_{\text{el}}^{\text{GB}} \approx 0$, whereas in the bulk the elastic energy will be positive due to tensile or compressive strain, i.e. $\Delta H_{\text{el}}^{\text{bulk}} \geqslant 0$. The enthalpy of segregation is then determined by $\Delta H_{\text{seg}} \approx \left(\Delta H_{\text{chem}}^{\text{bulk}} + \Delta H_{\text{el}}^{\text{bulk}}\right) - \Delta H_{\text{chem}}^{\text{GB}}$. The chemical excess enthalpies of the analyzed elements C, Si and

[1] As noted in Section 3.1.4.2, the microstrain will be evaluated for all analyses at $L = 5$ nm.

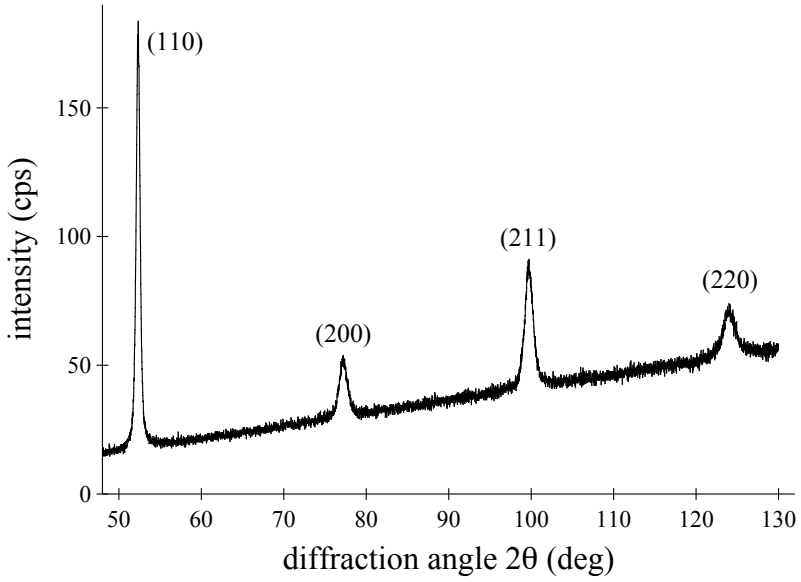

Figure 4.3: XRD pattern of nanocrystalline Fe powder in the as-prepared state after 15 h of milling. The Warren-Averbach analysis of the diffraction pattern yields an average column length $\langle L \rangle_{\mathrm{vol}} = 21$ nm and $\langle L \rangle_{\mathrm{area}} = 18$ nm, and an atomic-level microstrain $\left\langle \varepsilon^2 \right\rangle^{1/2} = 0.35\%$. XRD indicates further that beside the four diffraction peaks, which are related to the bcc structure of Fe, no additional signals are present. This proves the single-phase characteristic of the investigated specimens.

Cr are included in Table 4.2 for bulk and grain-boundary accommodation, respectively. Table 4.2 includes further the atomic radii of the particular solute elements, which can be used to assess qualitatively (from a comparison with the atomic radius of Fe) the extent of the bulk elastic strain enthalpy $\Delta H_{\mathrm{el}}^{\mathrm{bulk}}$. Table 4.2 reveals that Chromium is not expected to have an appreciable tendency for segregation in α-Fe, since both, the elastic and the chemical enthalpy is small. Thus, only Silicon and Carbon remain as candidates

Table 4.1: This table summarizes the chemical analyses for the impurity concentrations within the two investigated sample series X1 and X2. The right column of the table includes in addition the respective activation enthalpies for impurity diffusion in α-Fe. The chemical analyses have been performed by "Mikroanalytisches Laboratorium Kolbe", Mülheim a. d. Ruhr.

	X1 [at.%]	X2 [at.%]	Q^{sol} [kJ/mol]	Ref.
C	0.04	0.07	60. . . 80	[131, 132]
Si	0.14	0.10	230	[132]
Cr	0.06	0.03	250	[26]

Table 4.2: Chemical excess enthalpies for lattice and grain-boundary accommodation of impurity atoms in α-Fe [69]. The table includes additionally the atomic radii of the analyzed species C, Si and Cr in comparison to the atomic radius of Fe, which allows to estimate the magnitude of the elastic strain enthalpy for lattice accommodation of the impurity atoms.

	$\Delta H_{\text{chem}}^{\text{GB}}$ [kJ/mol]	$\Delta H_{\text{chem}}^{\text{bulk}}$ [kJ/mol]	r_{atom}
Si	−75	−18	1.1 Å $(\Delta H_{\text{el}} > 0)$
Cr	−6	−1	1.4 Å $(\Delta H_{\text{el}} \approx 0)$
C	+16	+40	0.7 Å $(\Delta H_{\text{el}} > 0)$
Fe	—	—	1.4 Å

for solute segregation and a thereby induced solute drag on grain-boundary migration.

It has been discussed in Section 2.6 that efficient solute drag prerequisites that the diffusivity of the solutes should be on the order of the grain-boundary velocity, i.e. the activation enthalpies for grain-boundary migration (approximately 175 . . . 250 kJ/mol in the examined temperature range, *cf.* Section 2.2) and for solute diffusion (see Table 4.1) should be similar. This constraint imposes the consequence that at moderate annealing temperatures Carbon is unlikely to exert substantial solute drag in α-Fe. It is therefore only Silicon, which may initiate solute drag in α-Fe. However, an estimation of the grain-boundary-area coverage with Si impurity atoms reveals that for a mean grain size of 20 nm and assuming complete segregation of the Si to the grain boundaries, only ~1% of the total grain-boundary area is occupied by Silicon. Thus, the surface concentration of Si remains negligible, even if all Si atoms are accumulated at the grain boundaries. The concentration might even be less, if the solubility of Si in α-Fe is considered (~10 at.% [133]), which makes a substantial drag effect of Si impurities unlikely .

In summary it might therefore be concluded that solute drag due to impurity atoms from the ball-milling process is not expected to influence significantly the experimental investigation of grain growth in nanocrystalline Fe.

4.1.3 Post-Preparational Treatment of Nanocrystalline Fe

Beside an impeded grain-boundary kinetics due to trace contaminations, the oxidation of the particle surface and oxygen diffusion along grain boundaries can disturb the intrinsic growth kinetics equally. Depending on the amount of dissolved oxygen, two different situation may occur. While at low oxygen concentrations a Fe-O solid solution with oxygen atoms at interstitial sites of the bcc Fe lattice is formed, concentrations above the solubility limit will cause a precipitation of new Fe-O phases [10, 133]. Due to the relatively low activation enthalpy of 90 kJ/mol for oxygen diffusion in α-Fe, solute drag by oxygen atoms seems not critical in nanocrystalline Fe [10, 134] (this situation may change however for a lower driving force for boundary motion, e.g. at larger grain sizes). Inhibition of grain growth may however occur, if second-phase islands of new Fe-O phases are formed, which could act as pinning centers for

the grain boundaries (also known as Zener Pinning). However, the analyses by XRD, EBSD and electron diffraction did not indicate the existence of oxide precipitates, neither in the as-prepared state, nor after annealing.

Even though all specimens have been carefully stored in Argon atmosphere, contact with oxygen cannot be avoided, for example during the installation of the specimen inside the *in-situ* hot-stage of the XRD. Also the condition of the as-procured raw material is not under control with respect to oxygen. To minimize any possible influence of oxygen during the isothermal anneals, the samples were subjected immediately prior to the isothermal experiment to a deoxidation procedure (annealing experiment and deoxidation are performed in the same setup of the hot-stage). For deoxidation the powder samples are exposed for 80 min to a reducing Argon/Hydrogen (95/5 vol.%) atmosphere at an ambient pressure and a temperature of ~130°C.

In the presence of oxygen, Fe may form the three oxides FeO, Fe_2O_3 and Fe_3O_4, depending on the actual oxygen concentration and sample temperature [133]. However, in the interesting temperature interval of this study, the oxide FeO is thermodynamically unstable and will therefore not be relevant ($T < 560$°C) [135]. The other two iron oxides can be reduced by hydrogen (H_2) via the following two chemical reactions [135, 137],

$$3\ Fe_2O_3 + H_2 \longrightarrow 2\ Fe_3O_4 + H_2O \quad (I)$$
$$Fe_3O_4 + 4\ H_2 + 151\ kJ \longrightarrow 3\ Fe + 4\ H_2O \quad (II).$$

Inspection of the Ellingham diagrams for both the two iron oxides involved in reaction (I) and (II) and the reaction $2\ H_2 + O_2 \longrightarrow 2\,H_2O$ shows that only reaction (I) is exothermic, whereas reaction (II) will be endothermic (+151 kJ) and require therefore sufficient thermal energy [136, 137] (the temperature for which is of course limited to avoid immediate coarsening of the microstructure). It should be kept in mind that the application of hydrogen does usually cause the formation of a metal-hydride phase, which can impair the migration of the grain boundaries in the subsequent annealing experiment. Fortunately, for the actual conditions of deoxidation, hydrogen does according to the Fe-H phase diagram not dissolve in α-Fe to an appreciable amount, and an impact on the later experiment is not expected [133].

The impact of the post-preparational treatment on the microstructure was assessed by XRD. Fig. 4.4 compares the (110) peak of nanocrystalline Fe before and after the deoxidation procedure. It is evident that the thermal activation — which is definitely small at 130°C compared to the typical temperatures $T \gtrsim T_m/2$ where substantial grain growth is usually observed — suffices to cause a measurable relaxation of the microstructure, which is reflected in a distinct decrease of the peak width. This finding is not surprising, since the sample is prior to this step in its most "non-equilibrium" state (with respect to grain size and microstrain), and every elevated temperature during this stage is likely to enable a relaxation of excess energy. As will be discussed shortly, the observed changes in peak shape following from the deoxidation procedure are primarily caused by the relaxation of residual microstrain.

To avoid re-oxidation of the specimens during the experiment, the *in-situ* isothermal annealing was performed under vacuum conditions (of course, filling the hot stage with inert gas would be easier from an operational point of view, but the scattering of x-rays in the gas atmosphere deteriorates the

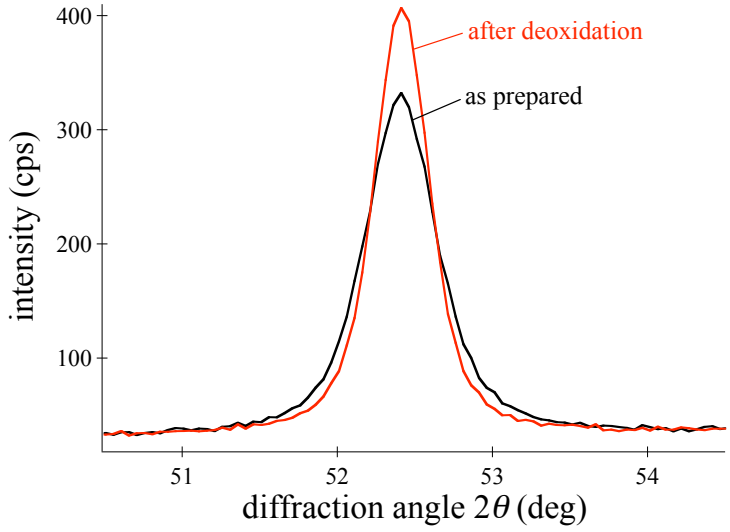

Figure 4.4: Influence of the elevated temperature conditions during the deoxidation procedure on the peak profile of the (110) reflection. As will be discussed in Section 4.3, the reduced peak width can be attributed to the recovery of excess dislocations in the as-prepared state.

quality of the diffraction signal substantially). The experiments were performed at a dynamic pressure of approximately 1×10^{-5} mbar (better vacuum conditions could not be achieved due to the necessity of x-ray-transparent polyimide (Kapton) windows and polymer sealings).

4.2 Isothermal Annealing: *In-situ* XRD

Two series of specimens from batch X1 and X2 have been analyzed by *in-situ* XRD on the microstructural evolution at isothermal temperatures between 358°C and 478°C. The parameters of the XRD scans have been selected in a way to record the (110) and the (220) diffraction peak with the required signal-to-noise quality in a scan time of ~4 min, which allowed for real-time tracking of the *in-situ* experiment. Fig. 4.5 illustrates for a sample of nanocrystalline Fe the continuous evolution of the microstructure between the quasi-initial state ($t = 2$ min) and long-term annealing ($t = 50$ h), measured by *in-situ* XRD at a sample temperature of 445°C. At a first view, the peak profile becomes continuously narrower during the annealing, as it would be expected, if the sample experiences a relaxation of microstrain or an increase of the mean grain size. Due to the broad width of the diffraction peak at small grain sizes, the K$\alpha_{1,2}$ doublet is initially concealed in one broad peak. With the ongoing relaxation of microstrain and the steady increase of the grain size, the width of the two Kα peaks reduces, and after approximately 4 h of annealing the K$\alpha_{1,2}$ doublet becomes gradually resolved.

The XRD peak profiles of the present study have been evaluated using the split-Pearson VII function of Eq. (3.53) with the shape parameters m_L and m_R and the half widths at half maximum HW_L and HW_R

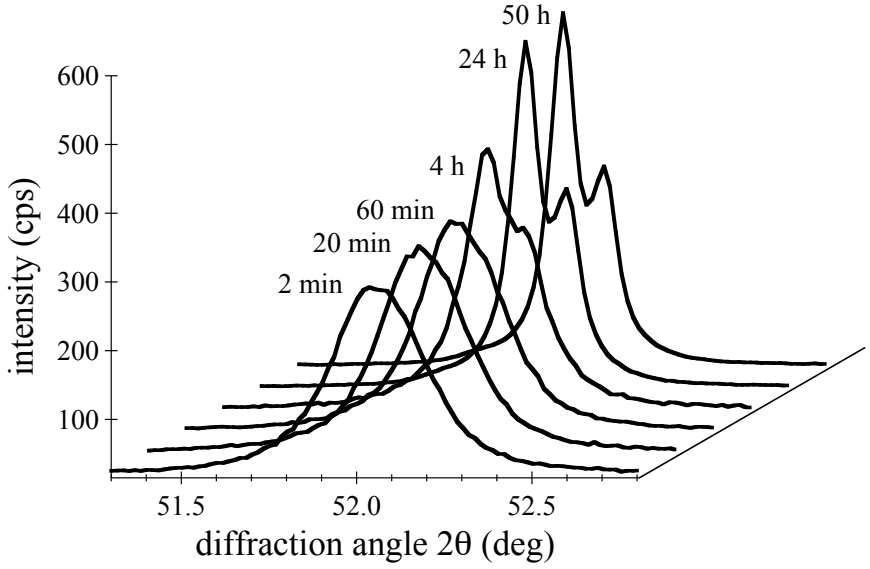

Figure 4.5: Time-resolved diffraction peak of the Kα_1 and Kα_2 (110) reflection, measured by *in-situ* XRD at a temperature of 445°C. The plot shows the continuous narrowing of the peaks that is induced by the relaxation of the nanocrystalline microstructure. (Note that the plot shows only a selection of XRD scans that have been taken during this anneal)

(note: FWHM $=$ HW$_\mathrm{L}$ + HW$_\mathrm{R}$). The FWHM and the shape parameters of the split-Pearson VII function, which were deduced from least-square analysis of the (110) diffraction profiles shown in Fig. 4.5, are plotted in Fig. 4.6 as a function of annealing time. As expected, the peak width reveals a monotonous decreases from initially 0.253° to 0.088° after 37 h. The shape parameters however reveal a peculiar characteristics: Starting from a value of ~1.5, they decrease within the first 5 h of annealing to a value just below 1.0, whereas thereafter the direction reverses and the shape parameters increase again.

Klug and Alexander argued that a size-broadened diffraction profile is typically compliant to a Cauchy function (this would be equal to a Pearson VII function with shape parameter $m = 1$), while strain boradening may yield a Gaussian-shaped intensity profile (Pearson VII function with shape parameter $m \to \infty$) [94]. A continuous decrease of the shape parameter with $m \to 1$ would therefore be reasonable, if a strained microstructure undergoes relaxation. Of course, this characteristic of the shape parameter should then also be found for higher-order (*hkl*) peak (or even stronger, according to Eq. (3.31)) — but this is actually not the case. In fact, the value of m_L and m_R stays approximately constant for the (220) peak. From this observation — but particularly from the increase of m at a later stage — it is likely that the relaxation of microstrain cannot account for the peculiar characteristics of $m_{\mathrm{L,R}}$, and a different mechanism other than the release of strain seems to be responsible.

To follow up the question on what drives the change in $m_{\mathrm{L,R}}$ it might be helpful to inspect the diffraction peak at two dedicated points: At the beginning of the anneal and when m attains the smallest value

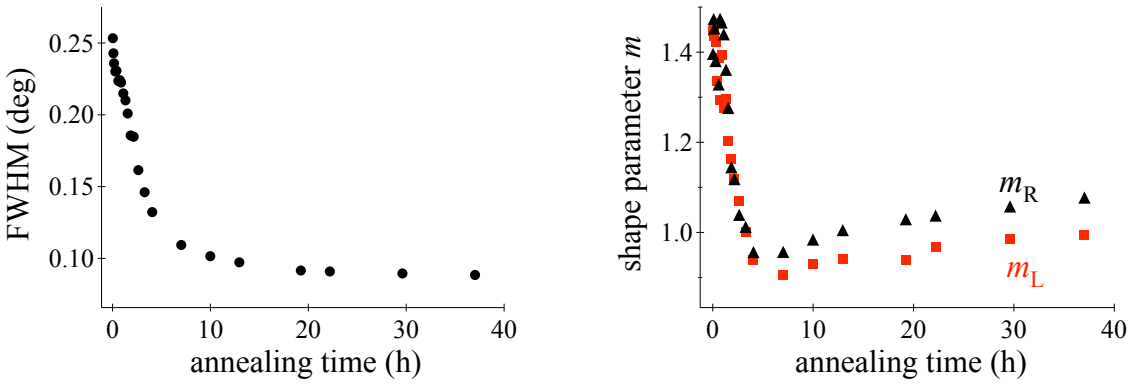

(a) (b)

Figure 4.6: a) FWHM of the XRD scans plotted in Fig. 4.5. The peak width reveals, as expected for grain growth or the relaxation of microstrain, a continuous decrease, which approaches in the long-time view an asymptotic value of 0.088°. b) Plot of the shape parameters of a split-Pearson VII function for the anneal shown in Fig. 4.5.

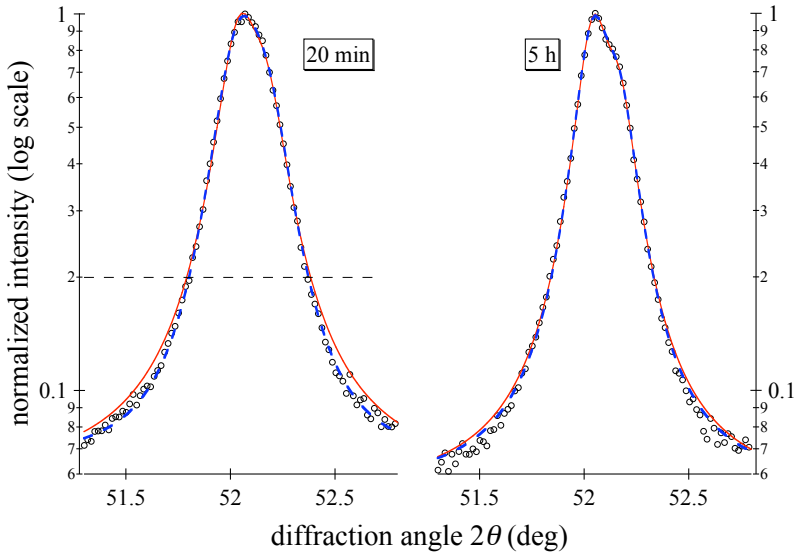

Figure 4.7: Logarithmic plot of the (110) diffraction intensity after 20 min and 5 h of the anneal at 445°C. Both measured peaks are shown with least-square fits of a Cauchy function (red solid line) and a split-Pearson VII function (blue dotted line), both functions revealing an excellent agreement in the upper part of the peaks; however, the graph shows that only the Pearson VII function yields a full compliance with both peak profiles, whereas for the Cauchy function there is a distinct deviation in the lower part of the early-stage peak (20 min).

($t \approx 5$ h). Fig. 4.7 presents the (110) diffraction peak after 20 min and 5 h of annealing (both XRD scans belong to the anneal of Fig. 4.5). In addition, the graph shows the least-square fits of a Cauchy and a split-Pearson VII function for the two diffraction peaks. Obviously, both curves, Cauchy and Pearson VII, provide a sound approximation of the two diffraction peaks, if only the part of the peak above ~20% of the maximum intensity is considered (in particular, for the data after 5 h the Cauchy function yields a satisfying fit for the complete peak). Comparing the shape of a Cauchy and Gaussian peak profile, the ratio between the peak's FWHM and the width of the peak basis is smaller in case of a Gaussian profile than for a Cauchy one. This basically shows that the shape parameters $m_{\mathrm{L,R}}$ of the Pearson VII function follows a change of peak shape, where the mentioned peak-width ratio increases within the first 5 h of annealing, and decreases afterwards again — however, this effect is rather weak.

What could be the reason for such a behavior? To find an answer to this question it is necessary to recall Section 3.1.3.1. It was discussed there that each column of unit cells will contribute to the shape of the diffraction profile independently. Since the peak width is inversely proportional to the column length (short columns, or equivalently small grains, will give broad peaks, *cf.* Eq. (3.10)), it seems that during coarsening of the microstructure some grains will not grow equally well as other grains and remain therefore small in size. The result will be that the measured diffraction profile is the superposition of a broader peak related to the "inhibited" grains, and a narrower peak due to the growing grains. Similar observations of a composite peak have been reported for example on abnormal growth in nanocrystalline Palladium (Pd) [138], which would advise that the microstructure of the nanocrystalline Fe undergoes an inhomogeneous evolution during annealing.

However, if the abnormal evolution of the microstructure is responsible for the observed continuous change of the (110) peak-shape parameter, the same should apply to higher-order peaks, too. This discrepancy — m is actually constant for the (220) peak — seems to be provoked by the significantly lower signal-to-noise ratio of the (220) peak (see for example Fig. 4.3). Such subtle changes in the tail of the peak (particularly, if the volume fraction of abnormal grains is moderate) are already difficult to detect for the (110) peak, and it seems very likely that they get lost in the increasing intensity background at higher diffraction angles.

4.2.1 Measuring the True Temperature

Since the temperature that is measured during the *in-situ* anneals does not represent the actual temperature of the specimen, the sample itself will be used as a "thermometer".[2] The true annealing temperature can then be determined by evaluating the temperature-sensitive lattice constant [139],

$$a(T) = \frac{d_{\mathrm{hkl}}(T)}{\sqrt{h^2 + k^2 + l^2}}, \tag{4.1}$$

if $d_{\mathrm{hkl}}(T)$ is the spacing of (hkl) lattice planes (for other crystal structures than cubic unit cells, the

[2] During the experiment the temperature is recorded via a thermocouple at a contact-free position (the thermocouple experiences only the thermal radiation of the heater, since the experiment is performed under vacuum). The temperature data is used as a reference input for the control loop of the heater unit to maintain isothermal conditions. With respect to this, a constant temperature reading of the thermocouple is indicative for a constant temperature of the specimen.

denominator of Eq. (4.1) will be different). Since the relationship between the temperature-dependent diffraction angle 2θ and the lattice spacing d_{hkl} is uniquely defined by the Bragg equation (*cf.* Eq. (3.1)), the lattice constant can be equated as,

$$a(T) = \frac{\lambda}{2 \cdot \sin\theta} \cdot \sqrt{h^2 + k^2 + l^2}. \tag{4.2}$$

Eq. (4.2) demonstrates that it is in principle enough to know the position of only one single diffraction peak, which however involves the uncertainty that the position of the diffraction peak may also has shifted due to the displacement of the specimen, for example by thermal expansion of the sample or the sample holder. A precise alignment of the sample within the goniometer is therefore needed, if only one peak is used to calculate $a(T)$. To avoid the complicated experimental procedure of alignment, the analysis of the lattice parameter will be based in the following on Cohen's method, where the lattice constant is determined from the peak positions of two or more peaks [94,140]. For cubic lattice structures the true lattice parameter a_0 is then obtained according to,

$$a(\theta_{\mathrm{hkl}}) = a_0 - \left[a_0 \cdot \frac{y}{R} \cdot \frac{\cos^2\theta_{\mathrm{hkl}}}{\sin\theta_{\mathrm{hkl}}} \right], \tag{4.3}$$

where $a(\theta_{\mathrm{hkl}})$ is the as-measured lattice parameter of the (*hkl*) peaks according to Eq. (4.2), y denotes the vertical displacement of the sample, and R is the radius of the goniometer. To determine a_0, the calculated lattice parameters $a(\theta_{\mathrm{hkl}})$ are plotted as a function of $\left(\cos^2\theta_{\mathrm{hkl}} / \sin\theta_{\mathrm{hkl}}\right)$. The absolute term of a linear regression yields then the corrected lattice parameter a_0. For the samples of nanocrystalline Fe the (110) and (220) peak were used in this evaluation.

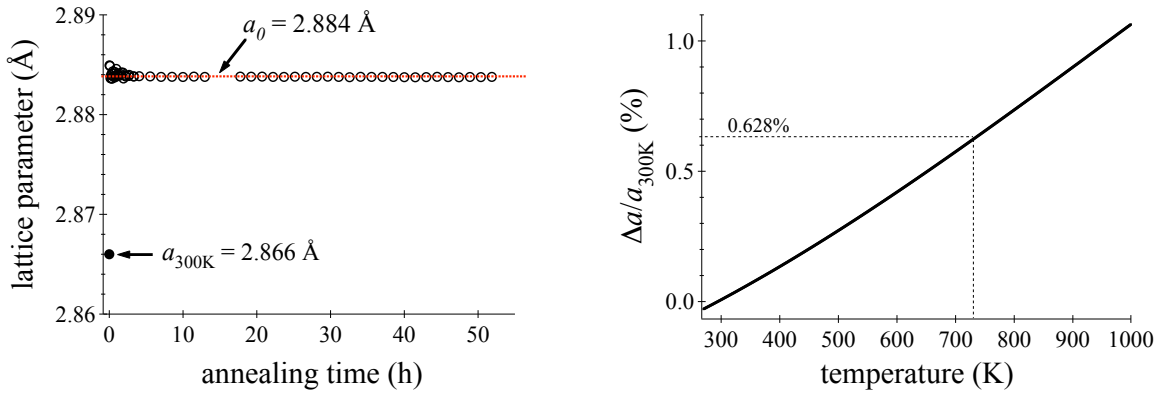

(a) (b)

Figure 4.8: a) Time-dependent lattice parameter as calculated according to Eq. (4.3) for the *in-situ* anneal of Fig. 4.5. The analysis yielded a value of $a_0 = 2.884$ Å. b) 3rd order polynomial approximation of the temperature-dependent thermal expansion coefficient $\alpha_{\mathrm{Fe}}(T)$ [83]. The lattice parameter $a_0 = 2.884$ Å (which equals $\Delta a/a_{300\ \mathrm{K}} = 0.628\%$) yields accordingly a temperature of 718 K (445°C).

Fig. 4.8(a) shows the corrected lattice parameter a_0 as a function of annealing time for the 445°C anneal of Fig. 4.5. The data points prove that the selected temperature for the isothermal anneal is almost instantaneously reached, and has an excellent long-time stability.

Fig. 4.8(b) shows the non-linear thermal expansion of α-Fe as a function of temperature [83], which was used for all samples to convert a_0 into the actual temperature of the experiment. For the lattice constant $a_0 = 2.884$ Å of Fig. 4.8(a) a corresponding temperature of 445°C is found.

4.2.2 Thermally-Induced Grain Growth

The continuous decline of FWHM in Fig. 4.6 confirms that during annealing the microstructure is subjected to a persistent process of evolution via grain growth and strain relaxation. To assess the extent and the kinetics of grain growth, the area-weighted average grain size $\langle L \rangle_{\text{area}}$ is illustrated as a function of annealing time in Figs. 4.9 and 4.10 for batch X1 and X2, respectively, where for the second batch the annealing time has been extended up to 150 h for the lowest temperatures investigated.

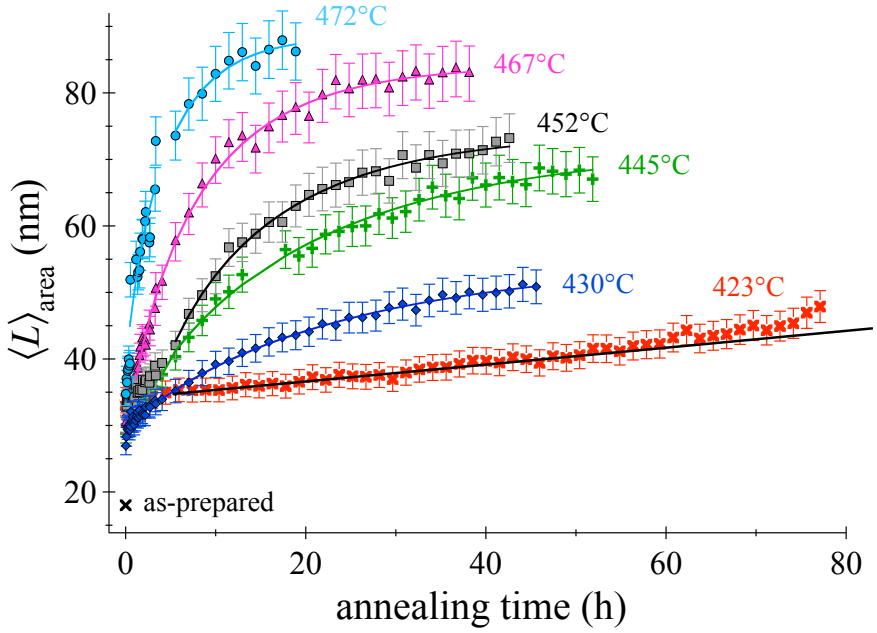

Figure 4.9: Plot of the area-weighted average grain size $\langle L \rangle_{\text{area}}$ as a function of annealing time for different isothermal experiments of batch X1. The solid lines (except for the straight line to the anneal at 423°C) represent least-square fits of Eq. (4.4) in range II.

The isothermal curves reveal for all annealing temperatures a significant jump of $\langle L \rangle_{\text{area}}$ from initially 18 nm (as-prepared state) to approximately 27. . . 35 nm within the remarkably short time of 5. . . 10 min, whereas immediately thereafter the growth rate drops to 0.1 nm/h or even less for the lowest temperatures (423°C and 358°C in Fig. 4.9 and Fig. 4.10, respectively). It should be noted that the 18 nm relate to the

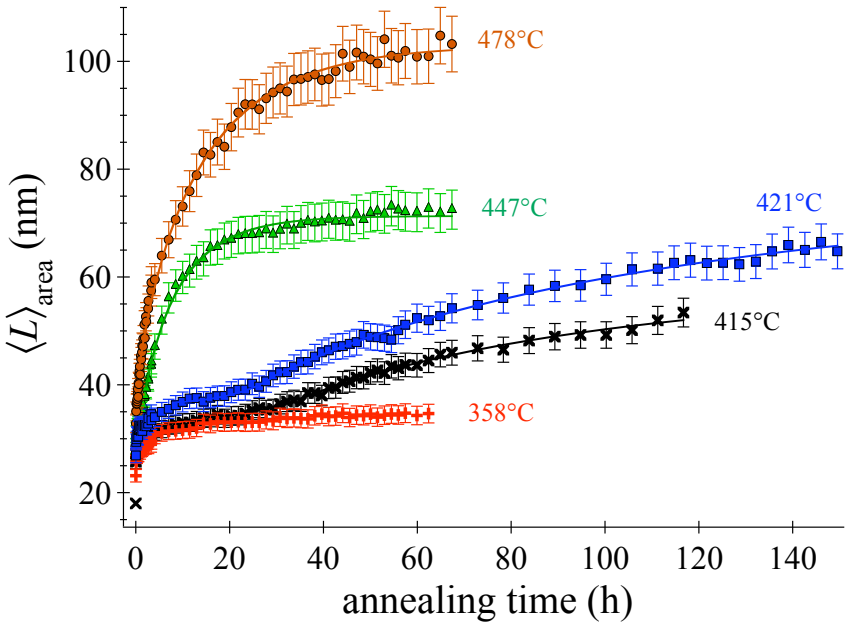

Figure 4.10: Plot of the area-weighted average grain size $\langle L \rangle_{\text{area}}$ as a function of annealing time for different isothermal experiments of batch X2. The solid lines represent least-square fits of Eq. (4.4) in range II.

as-prepared state, whereas the actual annealing experiment starts with the sample after the deoxidation procedure. The effect of this pre-treatment was found to increase the mean grain size by approximately 2 nm. However, since the initial data point is not used in the further analysis of isothermal growth, the graph refers to the as-prepared state in order to illustrate the full scale of growth of the specimens.

A detailed inspection of the isothermal growth curves reveals that the coarsening of the nanocrystalline Fe is subdivided into four distinct stages — a characteristic, which is most evident for the lowest annealing temperatures (see Fig. 4.10), but a magnified view on anneals at higher temperatures unveils the same behavior there, too. The four subsequent stages that can be observed during the evolution of the microstructure can be outlined as follows:

1. *Initial rapid growth* of the grain size at a very high growth rate. This is observed for all temperatures investigated, where the final grain size and the rate of the fast growth are apparently independent of the actual temperature.
2. *The growth kinetics abates* and proceeds at a remarkably low growth rate (orders of magnitude slower than during the initial burst). The kinetics and the duration of this evolution period depends significantly on the actual temperature. Particularly at the highest temperatures measured the duration t_{I} of this evolution step approaches zero ($t_{\text{I}} \to 0$). Different to that, the curve at 423°C of batch X1 features an obviously shallow increase during which $\langle L \rangle_{\text{area}}$ evolves quasi-linearly for a time up to 55 h (the solid straight line overlayed to 423°C in Fig. 4.9 shall be a guide to the eye for this characteristic). Also for the three lowest temperatures in Fig. 4.10 there is an extended regime

after the initial burst in which a low growth kinetics can be easily observed. The duration of this regime is approximately 25. . . 30 h at temperatures between 421°C and 415°C, whereas at 358°C the condition of a distinctly low kinetics continues for at least 60 h.
(This regime of quasi-linear growth of $\langle L \rangle_{\text{area}}$ will be denoted in the following as "range I")

3. *Transitional state and inflection point*. Inspection of the isothermal data at 423°C shows that the deviation of the growth kinetics from a linear relationship occurs after 55 h, at which point the growth rate gradually increases and an upward curvature of the growth kinetics is observed. This feature is also found at the lowest temperatures of batch X2, where the increase of the growth rate occurs after approximately 25. . . 30 h. For the higher temperatures such an inflection point in $\langle L \rangle_{\text{area}}$ is difficult to observe, since the time interval t_{I} beforehand is short and the curves are thereby too much squeezed to resolve this transition.

4. *Long-term growth kinetics*. It is the common feature of all isothermal curves in Figs. 4.9 and 4.10 that beyond the inflection point the growth rate resembles a power-law characteristic with a progressively decreasing slope. It is also found that the grain size asymptotically approaches a temperature-dependent upper limit ("stagnation of grain growth").
(The nomenclature of this regime of $\langle L \rangle_{\text{area}}$ will be in the following "range II")

Without anticipating the comprehensive discussion in Chapter 5, it is already at this point clear that the observations made on the microstructural evolution of nanocrystalline Fe are undoubtedly of curious nature, since an increase of the growth rate is not in line with basically all grain-growth models that are based on curvature-induced driving forces and uniform boundary properties. To unravel this intricate problem on the growth kinetics of nanocrystalline Fe, it is fortunate that the WA analysis provides beside $\langle L \rangle_{\text{area}}$ the independent quantity $\langle L \rangle_{\text{vol}}$ (*cf.* Section 3.1.4.2). A review of Eqs. (3.22) and (3.23) indicates that both averages must have a different sensitivity on the size and the number of large grains. Due to this different response of $\langle L \rangle_{\text{area}}$ and $\langle L \rangle_{\text{vol}}$ on the shape of the GDF it is possible to track (at least qualitatively) the evolution of the GDF, which may contribute to disclose the underlying coarsening mechanisms of nanocrystalline Fe.

Figs. 4.11 and 4.12 show $\langle L \rangle_{\text{vol}}$ as calculated from the WA analysis for batch X1 and X2, respectively. A thorough inspection reveals that the same four stages, which have been identified for $\langle L \rangle_{\text{area}}$ before, apply analogously to $\langle L \rangle_{\text{vol}}$: There is an initial rapid growth of $\langle L \rangle_{\text{vol}}$ from 21 nm in the as-prepared state to approximately 30. . . 40 nm within a very short time of 5. . . 10 min, which is then followed by the transition of the microstructure through a regime of lower and quasi-linear growth kinetics (this however is only noticeable for the lowest temperatures measured). At more elevated temperatures, the duration of quasi-linear growth becomes short (similar to t_{I} for $\langle L \rangle_{\text{area}}$) and the transition to the subsequent power-law growth is blurred.

In all isothermal anneals it was found that the duration of the low-kinetics period is much shorter for $\langle L \rangle_{\text{vol}}$ than it is the case for range I of $\langle L \rangle_{\text{area}}$. This fact can be clearly seen in Fig. 4.13, which shows $\langle L \rangle_{\text{vol}}$ and $\langle L \rangle_{\text{area}}$ of the isothermal anneal at 452°C (from batch X2). While the inflection point of $\langle L \rangle_{\text{area}}$ is reached after ∼6 h, this transition to a higher growth rate is found for $\langle L \rangle_{\text{vol}}$ already after ∼2 h.

The correct approach for a quantitative analysis of the isothermal anneals on nanocrystalline Fe is not *a priori* clear, since it must be assumed that the involved processes do not agree with established grain-

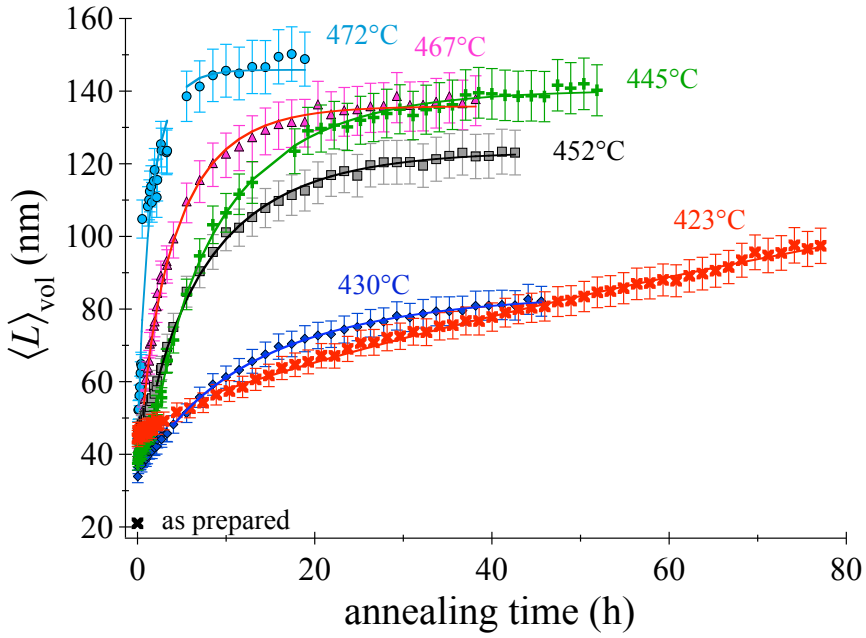

Figure 4.11: Plot of the volume-weighted average grain size $\langle L \rangle_{\mathrm{vol}}$ as a function of annealing time for different isothermal experiments of batch X1. The solid lines represent least-square fits of Eq. (4.4) in the power-law regime.

growth models. This basically excludes the mostly used models for grain growth from being applied here, which can be seen from the fact that standard parabolic growth laws will fail to reproduce the measured isothermal kinetics. Due to a currently lacking "integral" growth law that covers all of the before defined four features of coarsening, it is reasonable to divide the grain-size curves into two independent parts, one for the quasi-linear growth of range I and one for parabolic-like growth in range II. To account for the long-term stagnation of $\langle L \rangle_{\mathrm{area}}$ and $\langle L \rangle_{\mathrm{vol}}$ an adequate fit function is required for range II. Although the underlying processes that are responsible for the measured characteristics of the growth kinetics are not yet clear, it is reasonable to use an established parametric function to reproduce the behavior in the power-law regime. An appropriate function that is likely to cover the power-law growth in range II adequately, has been proposed by Michels *et al.* [141],

$$\langle L \rangle (t) = \left[2 \cdot \langle L \rangle_{\mathrm{max}}^2 - 2 \cdot \left(\langle L \rangle_{\mathrm{max}}^2 - \langle L \rangle_0^2 \cdot \exp \left\{ \frac{-8 \cdot A \cdot (t - t_0)}{\langle L \rangle_{\mathrm{max}}^2} \right\} \right) \right]^{1/2}, \tag{4.4}$$

and was originally developed to be used for growth stagnation resulting from solute drag. The free parameters $\langle L \rangle_{\mathrm{max}}$, $\langle L \rangle_0$ and A of Eq. (4.4) are the maximum grain size at stagnation, the initial grain size at time t_0 and the temperature-sensitive rate constant, respectively. The least-square fits of Eq. (4.4) on $\langle L \rangle_{\mathrm{area}}$ and $\langle L \rangle_{\mathrm{vol}}$ are shown in Figs. 4.9 – 4.12 as solid lines overlayed to the experimental data. The excellent agreement of Eq. (4.4) with the measured grain-size data can be seen in detail in Fig. 4.13.

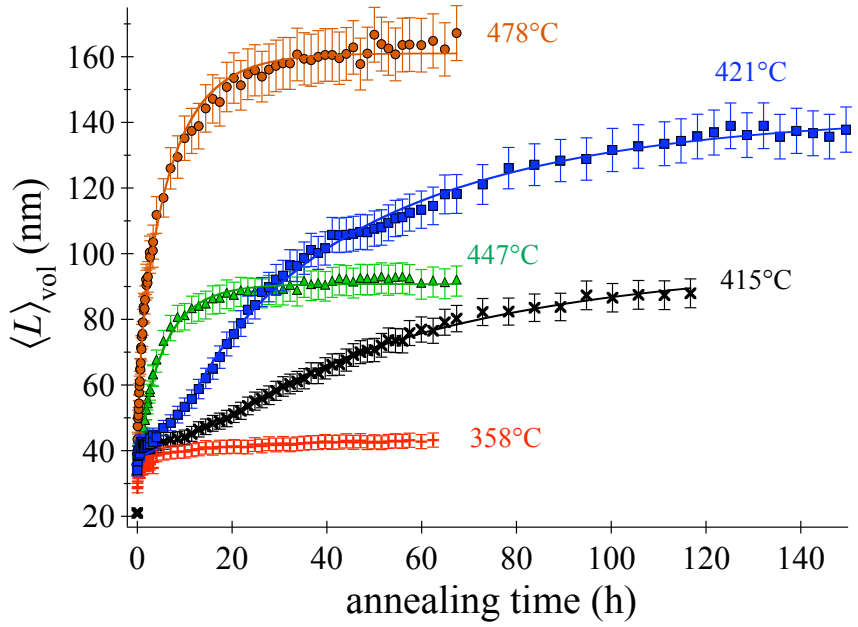

Figure 4.12: Plot of the volume-weighted average grain size $\langle L \rangle_{\mathrm{vol}}$ as a function of annealing time for different isothermal experiments of batch X2. The solid lines represent least-square fits of Eq. (4.4) in the power-law regime.

Comparing Eqs. (4.4) and (2.20) shows that $A(T)$ in Eq. (4.4) represents the temperature-dependent rate constant for grain growth, which allows to write $A(T)$ as,

$$A(T) = \frac{A_0}{T} \cdot \exp\left\{-\frac{Q^{\mathrm{II}}}{k_{\mathrm{B}}T}\right\}, \tag{4.5}$$

where Q^{II} is the activation enthalpy of the rate-controlling process for grain growth in range II.[3] A plot of the Arrhenius-type analysis of $\ln A(T)$ as a function of $1/T$, used to determine the activation enthalpies of the growth kinetics for $\langle L \rangle_{\mathrm{area}}$ and $\langle L \rangle_{\mathrm{vol}}$ in range II, is illustrated in Fig. 4.14.[4] The graph includes the data of both sample series, batch X1 (solid symbols) and X2 (open symbols). The activation enthalpies $Q^{\mathrm{II}}_{\mathrm{area}} = 220 \pm 28$ kJ/mol and $Q^{\mathrm{II}}_{\mathrm{vol}} = 210 \pm 27$ kJ/mol have been deduced from least-square fits of a straight line to the data points of $\langle L \rangle_{\mathrm{area}}$ and $\langle L \rangle_{\mathrm{vol}}$.

[3] Range II is used here as a synonym for the power-law regime of both quantities, $\langle L \rangle_{\mathrm{area}}$ and $\langle L \rangle_{\mathrm{vol}}$.

[4] Note: In contrast to the definition of the activation enthalpy according to Eq. (4.5), the analyses in Figs. 4.14 and 4.15 make use of the simplified relation,

$$A(T) = A_0 \cdot \exp\left\{-\frac{Q^{\mathrm{II}}}{k_{\mathrm{B}}T}\right\}, \tag{4.6}$$

which is justified as long as the measured temperatures lie within a narrow range. This condition can be considered to be fulfilled for the present isothermal anneals, since the data points do not systematically deviate from a linear characteristic in the plots of Fig. 4.14 and 4.15.

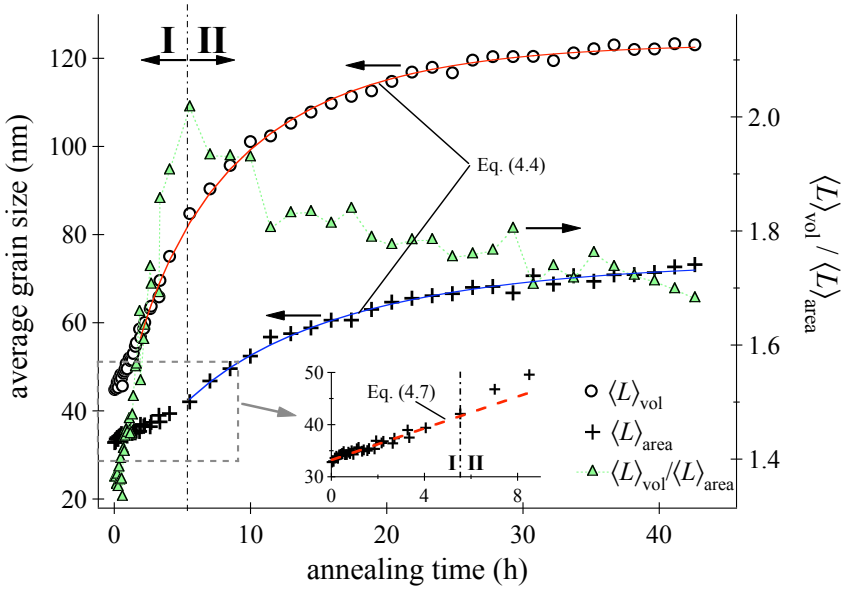

Figure 4.13: Plot of the grain size $\langle L\rangle_{area}$ and $\langle L\rangle_{vol}$ as a function of annealing time for an isothermal experiment at 452°C. The graph and the inset (showing $\langle L\rangle_{area}$ in range I) clearly show the difference between the quasi-linear range I and the power-law-like range II of the coarsening process; the transition of $\langle L\rangle_{area}$ from range I into range II (obvious by an inflection point of the curvature) is indicated by the vertical line at $t \approx 5\ldots6$ h. The solid lines in the graph are the least-square fits of Eq. (4.4) to the area and volume-weighted average grain size, respectively. The graph shows additionally the ratio $\langle L\rangle_{vol}$ / $\langle L\rangle_{area}$, which is used as an indicator for normal or abnormal grain growth. It can be clearly seen that the ratio undergoes a significant increase during range I, to return to a smaller value during grain growth in range II. It can be observed that the maximum value of $\langle L\rangle_{vol}$ / $\langle L\rangle_{area}$ obviously coincides with the inflection point of $\langle L\rangle_{area}$.

The fits of Eq. (4.4) on $\langle L\rangle_{area}$ and $\langle L\rangle_{vol}$ in range II (see Figs. 4.9-4.12) are obviously in excellent agreement with the experimental data. However, the parametric function of Eq. (4.4) has been selected mainly because of its numerical compliance with the measured data, but it is likely that the physics behind Eq. (4.4) does not agree with the underlying processes of grain growth in nanocrystalline Fe. Thus, it is expedient to cross-check the activation enthalpies found in Fig. 4.14. For this purpose the data of $\langle L\rangle_{area}$ and $\langle L\rangle_{vol}$ was fitted by a simple linear equation that solely covers the initial part of range II (i.e. the time period of the power-law curve before the growth rate begins to stagnate). The Arrhenius analysis of the slope yields then for $\langle L\rangle_{area}$ an activation enthalpy of 240 ± 30 kJ/mol and for $\langle L\rangle_{vol}$ an activation enthalpy of 225 ± 22 kJ/mol. The good agreement between the activation enthalpies found by using the rate parameter $A(T)$ of Eq. (4.4) and the simple slope of the reference analysis supports both the reliable performance of Eq. (4.4) in range II and the possibility of a meaningful interpretation of $A(T)$ for the analysis of growth kinetics.

Inspection of the isothermal anneals shows that in the regime prior to the inflection point of the curvature (i.e. in range I, see Fig. 4.13) both quantities, $\langle L\rangle_{area}$ and $\langle L\rangle_{vol}$, exhibit a quasi-linear time dependence. To

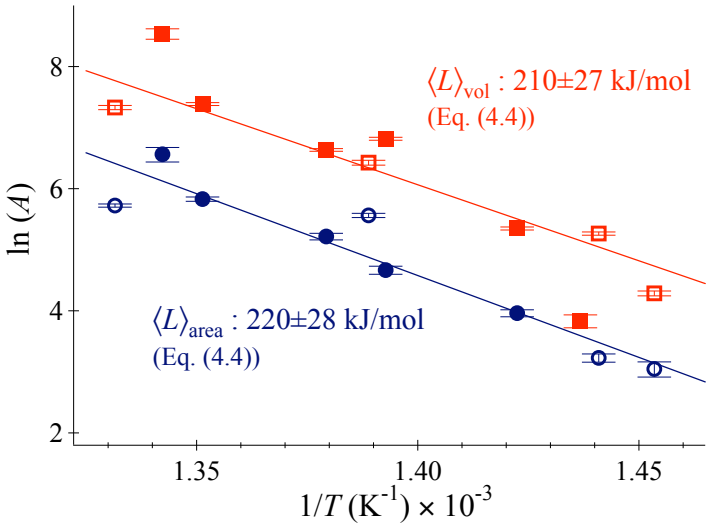

Figure 4.14: Arrhenius plot of $\ln A$ versus $1/T$ to evaluate the activation enthalpy for the growth kinetics of $\langle L\rangle_{\text{area}}$ and $\langle L\rangle_{\text{vol}}$ in range II. Open symbols represent data points related to batch X2, solid symbols show data points of batch X1. The analysis of the activation enthalpy makes use of the relationship of Eq. (4.6).

enable also for this stage of evolution a quantitative analysis of the rate-controlling mechanism of grain growth, the following linear function,

$$\langle L\rangle(t) = m_{\text{I}} \cdot (t - t_i) + \langle L\rangle(t_i), \tag{4.7}$$

has been used to assess the growth rate in the respective interval. In Eq. (4.7) the parameter t_i specifies the annealing time when the initial rapid growth of the grain size is completed and the kinetics has shifted into the much slower and quasi-linear range I. As will come out shortly, the evaluation of range I is much more complicated than the fits of Eq. (4.4) on range II, since the duration of quasi-linear growth can become significantly squeezed at elevated temperatures.[5]

The analysis of the temperature-dependent linear slope m_{I} is included for both quantities, $\langle L\rangle_{\text{area}}$ and $\langle L\rangle_{\text{vol}}$, in the Arrhenius plot of Fig. 4.15. Data points taken from sample series X1 and X2 are indicated in the graph by solid and open symbols, respectively. The intricacy of accurate least-square fits of Eq. (4.7) is reflected by a stronger scattering of the m_{I} data points in Fig. 4.15. To reduce the impact of this numerical uncertainty in the fitting procedure for the evaluation of the activation enthalpies, the most deviating data points have been identified and were not considered in the linear regression of the Arrhenius analysis. The deduced activation enthalpies for $\langle L\rangle_{\text{area}}$ and $\langle L\rangle_{\text{vol}}$ in range I are shown in the graph of Fig. 4.15.

Table 4.3 summarizes the activation enthalpies found for $\langle L\rangle_{\text{area}}$ and $\langle L\rangle_{\text{vol}}$ in range I and II, respectively. At a first glance it is remarkable that within the numerical uncertainty all four activation enthalpies

[5]Here, range I is used as a synonym for the regime of quasi-linear kinetics prior to the inflection point of both, $\langle L\rangle_{\text{area}}$ and $\langle L\rangle_{\text{vol}}$.

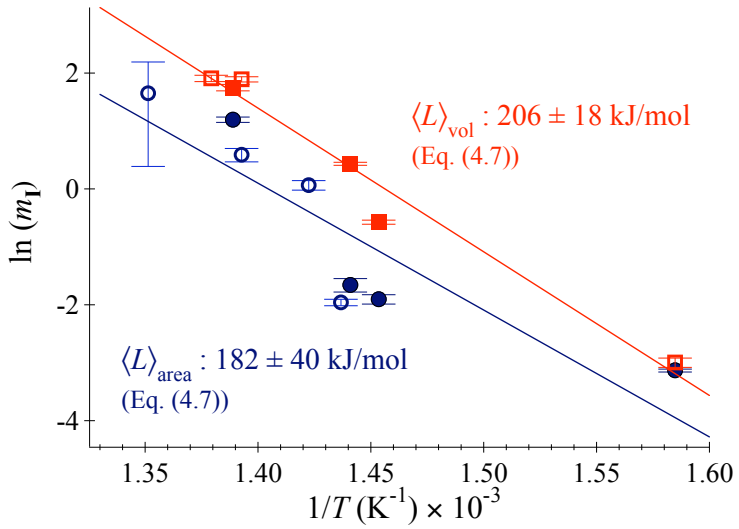

Figure 4.15: Evaluation of the activation enthalpies in the quasi-linear growth regime of range I. The graph shows the Arrhenius plot of $\ln m_I$ as a function of $1/T$, which yields an activation enthalpy of 182 ± 40 kJ/mol and 206 ± 18 kJ/mol for $\langle L \rangle_{area}$ and $\langle L \rangle_{vol}$, respectively. The squeezing of range I at elevated temperatures induces an increased uncertainty in the data, which is reflected in a larger scattering of the data points. To allow for a reasonable evaluation of the activation enthalpy, the most deviating data points have been neglected in the Arrhenius analysis (those data points are not shown in the graph); solid and open symbols represent data points related to batch X1 and X2, respectively.

are in principle identical, which suggests that there is basically no change of the rate-controlling process during annealing — although, the increasing growth rate at the inflection point of $\langle L \rangle_{area}$ and $\langle L \rangle_{vol}$ would misleadingly imply such a conclusion.

Table 4.3: Summary of the activation enthalpies calculated for the kinetics of $\langle L \rangle_{area}$ and $\langle L \rangle_{vol}$ in the quasi-linear range I and the power-law range II. The activation enthalpies were deduced from the grain-size data of the isothermal annealing experiments conducted on batch X1 and X2 of the nanocrystalline Fe samples under investigation (see Figs. 4.9 – 4.12).

	$\langle L \rangle_{area}$	$\langle L \rangle_{vol}$
range I	182 ± 40 kJ/mol	206 ± 18 kJ/mol
range II	220 ± 28 kJ/mol	210 ± 27 kJ/mol

4.2.3 Evolution of the Grain-Size Distribution

Although $\langle L\rangle_{\mathrm{area}}$ and $\langle L\rangle_{\mathrm{vol}}$ reveal the same four-stage characteristic, the transition between the different regimes is found to occur at quite different times and the instantaneous slopes $\mathrm{d}\langle L\rangle_{\mathrm{vol}}/\mathrm{d}t$ and $\mathrm{d}\langle L\rangle_{\mathrm{area}}/\mathrm{d}t$ are clearly different — especially during range I (see for example Fig. 4.13). However, since $\langle L\rangle_{\mathrm{vol}}$ and $\langle L\rangle_{\mathrm{area}}$ are weighted averages of the same GDF, a change in the ratio $\langle L\rangle_{\mathrm{vol}}$ / $\langle L\rangle_{\mathrm{area}}$ would be indicative for a non-self-similar GDF. If a lognormal function like Eq. (3.12) provides a sound description of the GDF, as it was shown in Fig. 3.7 for an annealed sample of batch X1, the width of a lognormal function can be calculated according to Eqs. (3.20) and (3.21) (and taking Eqs. (3.26) and (3.27) into account) by,

$$\sigma_{\mathrm{LN}} = \exp\left\{\frac{1}{2}\cdot\ln\left(\frac{8}{9}\cdot\frac{\langle L\rangle_{\mathrm{vol}}}{\langle L\rangle_{\mathrm{area}}}\right)\right\}. \tag{4.8}$$

Obviously, in this particular case the distribution width is directly determined by the ratio $\langle L\rangle_{\mathrm{vol}}$ / $\langle L\rangle_{\mathrm{area}}$, which shows that any measured change of $\langle L\rangle_{\mathrm{vol}}$ / $\langle L\rangle_{\mathrm{area}}$ is immediately related to a broadening or narrowing of the GDF.

Fig. 4.13 shows exemplarily the grain-size ratio $\langle L\rangle_{\mathrm{vol}}$ / $\langle L\rangle_{\mathrm{area}}$ of the 452°C anneal as a function of time. From this example — which is, as will be shown shortly, representative for all isothermal experiments on nanocrystalline Fe — it is evident that the GDF undergoes a sequential broadening and narrowing during the anneal. This observation suggests that a self-similar evolution of the GDF — and hence, a homogeneous evolution of the microstructure — is apparently not distinctive for nanocrystalline Fe.

Inspection of Fig. 4.13 reveals that the evolution of the grain-size ratio can be described by three distinct features, which are:

1. a fast increase of $\langle L\rangle_{\mathrm{vol}}$ / $\langle L\rangle_{\mathrm{area}}$ before the peak maximum (in parallel to the slow kinetics of $\langle L\rangle_{\mathrm{area}}$ in range I), i.e. a fast broadening of the grain-size distribution before the maximum width of the GDF is reached,
2. a slower asymptotic decline of the grain-size ratio beyond the peak maximum (i.e. in range II of $\langle L\rangle_{\mathrm{area}}$), and
3. the remarkable fact that the peak maximum of $\langle L\rangle_{\mathrm{vol}}$ / $\langle L\rangle_{\mathrm{area}}$ coincides with the inflection point of $\langle L\rangle_{\mathrm{area}}$ (visualized by the vertical dashed line in Fig. 4.13).

Figs. 4.16 and 4.17 illustrate the respective ratios $\langle L\rangle_{\mathrm{vol}}$ / $\langle L\rangle_{\mathrm{area}}$ for the isothermal anneals of batch X1 and X2. It can be observed that the fast increase of the ratio — which must be driven by a fast growth of $\langle L\rangle_{\mathrm{vol}}$, see Fig. 4.13 — has a distinct temperature dependence that should be comparable to the temperature-dependent slope of $\langle L\rangle_{\mathrm{vol}}$ in range I, because

$$\frac{\mathrm{d}}{\mathrm{d}t}\left(\frac{\langle L\rangle_{\mathrm{vol}}}{\langle L\rangle_{\mathrm{area}}}\right) = \frac{1}{\langle L\rangle_{\mathrm{area}}^2}\left(\langle L\rangle_{\mathrm{area}}\cdot\frac{\mathrm{d}\langle L\rangle_{\mathrm{vol}}}{\mathrm{d}t} - \langle L\rangle_{\mathrm{vol}}\cdot\underbrace{\frac{\mathrm{d}\langle L\rangle_{\mathrm{area}}}{\mathrm{d}t}}_{\ll\frac{\mathrm{d}\langle L\rangle_{\mathrm{vol}}}{\mathrm{d}t}}\right) \approx \underbrace{\frac{1}{\langle L\rangle_{\mathrm{area}}}}_{\approx\text{ const.}}\cdot\frac{\mathrm{d}\langle L\rangle_{\mathrm{vol}}}{\mathrm{d}t}. \tag{4.9}$$

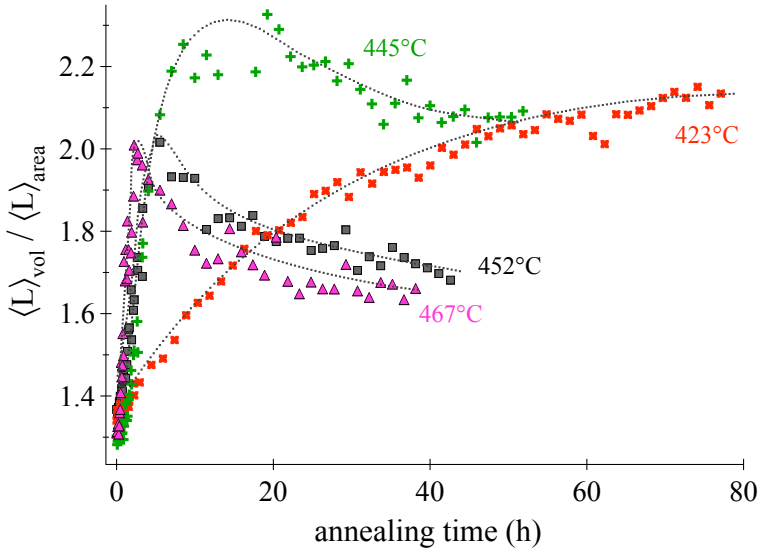

Figure 4.16: Plot of the grain-size ratio $\langle L \rangle_{\text{vol}} / \langle L \rangle_{\text{area}}$ of batch X1 as a function of annealing time. The dotted lines are splines, which shall help to visualize the time dependence of the data points.

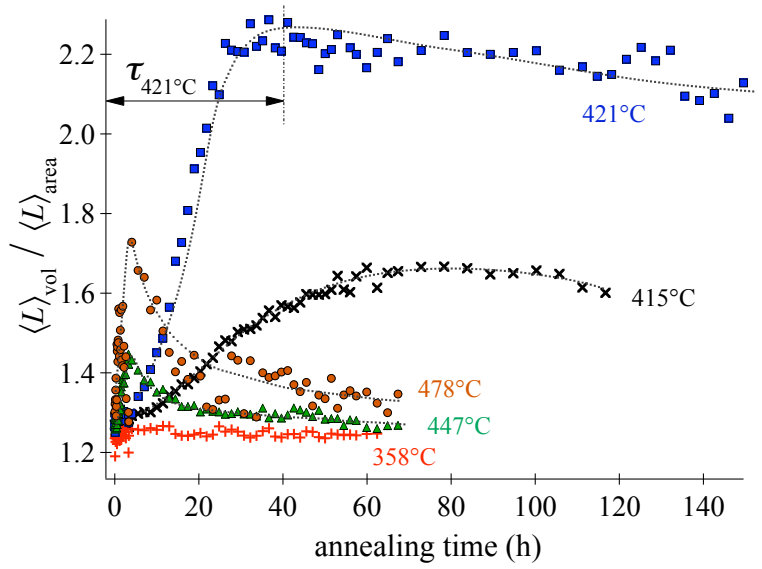

Figure 4.17: Plot of the grain-size ratio $\langle L \rangle_{\text{vol}} / \langle L \rangle_{\text{area}}$ of batch X2 as a function of annealing time. The dotted lines are splines, which shall help to visualize the time dependence of the data points. The isothermal data at 421°C defines additionally the characteristic time τ, which is the duration of the anneal before the peak maximum of the grain-size ratio is reached.

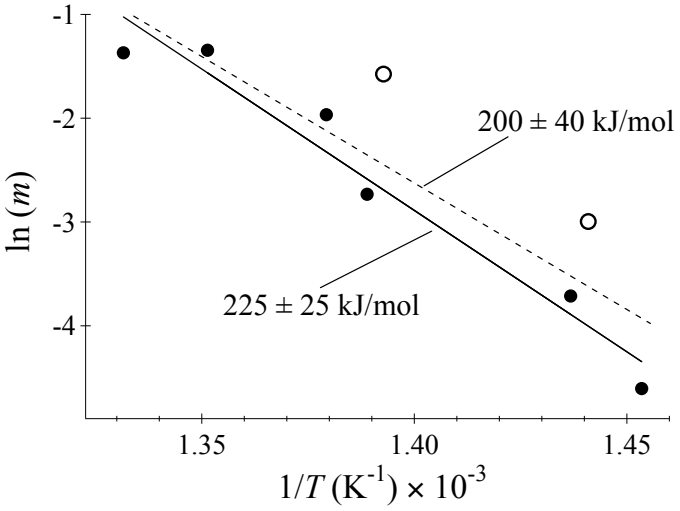

Figure 4.18: Plot of $\ln(m)$ as a function of the inverse annealing temperature to determine the activation enthalpy of the initial increase of $\langle L\rangle_{\mathrm{vol}}$ / $\langle L\rangle_{\mathrm{area}}$ during range I. Considering the scattering of the data points, the Arrhenius analysis is performed firstly with all data points in the graph, which yielded an activation enthalpy of 200 kJ/mol, and secondly for a subset of the data points, where the most deviating data points at 421°C and 445°C (shown by open symbols) were disregarded. For the second analysis the activation enthalpy was calculated as 225 kJ/mol.

To test the conclusion of Eq. (4.9) that the rapid increase of $\langle L\rangle_{\mathrm{vol}}$ / $\langle L\rangle_{\mathrm{area}}$ in range I is provoked by the kinetics of $\langle L\rangle_{\mathrm{vol}}$, the slope in range I of the grain-size ratios of Figs. 4.16 and 4.17 was fitted by a linear function and evaluated in the Arrhenius analysis of Fig. 4.18. From this analysis a characteristic activation enthalpy of 200 . . . 225 kJ/mol is found, which is obviously very similar to the activation enthalpy of $\langle L\rangle_{\mathrm{vol}}$ in range I (see Table 4.3). This similarity in activation enthalpy evidently supports the supposed correlation between $\langle L\rangle_{\mathrm{vol}}$ and the increase of the grain-size ratio — and thus, the broadening of the GDF.

The data in Figs. 4.16 and 4.17 does not only reveal a temperature dependence of the initial slope of $\langle L\rangle_{\mathrm{vol}}$ / $\langle L\rangle_{\mathrm{area}}$, it also unveils that the position of the peak maximum with respect to annealing time has some inverse proportionality to the temperature. If τ indicates the time at which the peak of $\langle L\rangle_{\mathrm{vol}}$ / $\langle L\rangle_{\mathrm{area}}$ is reached (see Fig. 4.17), it can be stated that a fast increase of the grain-size ratio is related to a short τ, whereas a slower increase of $\langle L\rangle_{\mathrm{vol}}$ / $\langle L\rangle_{\mathrm{area}}$ yields larger values of τ. Although the interpretation of the thermal characteristic of τ in terms of an activation enthalpy is unfounded, an Arrhenius-type analysis can be used for a qualitative comparison, for example with the activation enthalpies calculated in Fig. 4.18. The Arrhenius plot of the characteristic time τ is shown in Fig. 4.19, from which an "activation enthalpy" of 320 ± 30 kJ/mol is deduced. This value is about 50% larger than the activation enthalpies found in Fig. 4.18 for the fast increase of the grain-size ration, which suggests that the fast broadening of the GDF (driven by $\langle L\rangle_{\mathrm{vol}}$) and the occurrence of a peak maximum are provoked by different mechanisms.

The mechanism, which induces the long-time decline of $\langle L\rangle_{\mathrm{vol}}$ / $\langle L\rangle_{\mathrm{area}}$ is the significantly faster growth

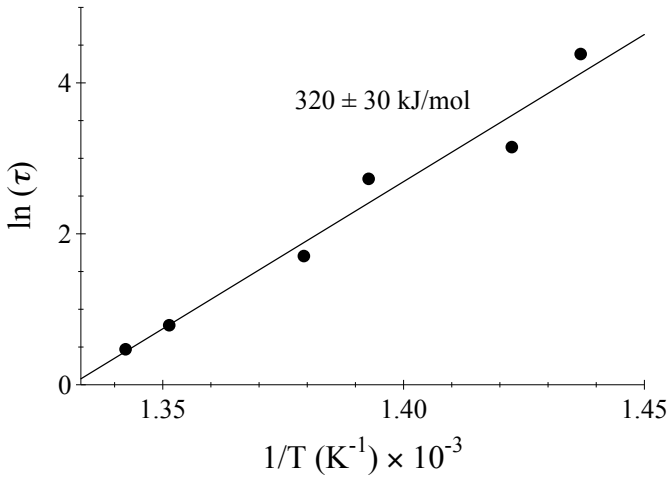

Figure 4.19: Analysis of the temperature-dependent peak position $\tau(T)$ in Figs. 4.16 and 4.17. The analysis allows to deduce a quantitative parameter that is comparable to the activation enthalpy of the initial increase of the grain-size ratio.

of $\langle L \rangle_{\text{area}}$ than $\langle L \rangle_{\text{vol}}$ in range II (starting with the inflection point of $\langle L \rangle_{\text{area}}$), which also explains why the peak of the grain-size ratio in Fig. 4.13 occurs in parallel to the inflection point of $\langle L \rangle_{\text{area}}$.[6] This follows from the following consideration: The peak of the grain-size ratio occurs, if the left-hand side of Eq. (4.9) becomes zero, i.e. the criterion for the peak to occur is defined by the slope of $\langle L \rangle_{\text{area}}$ as,

$$\frac{\mathrm{d}\langle L \rangle_{\text{area}}}{\mathrm{d}t} = \frac{\langle L \rangle_{\text{area}}}{\langle L \rangle_{\text{vol}}} \cdot \frac{\mathrm{d}\langle L \rangle_{\text{vol}}}{\mathrm{d}t}, \tag{4.10}$$

which means for the 452°C anneal that the slope of $\langle L \rangle_{\text{area}}$ must be aproximately half the one of $\langle L \rangle_{\text{vol}}$, since $\langle L \rangle_{\text{area}} / \langle L \rangle_{\text{vol}} \approx 0.5$ at the transition between range I and range II (see Fig. 4.13: $\langle L \rangle_{\text{area}} \approx 40$ nm, $\langle L \rangle_{\text{vol}} \approx 80$ nm). This criterion for the kinetics of $\langle L \rangle_{\text{area}}$ is obviously consistent with the experimental observations in Fig. 4.13. It might therefore be stated that the evolution of the grain-size ratio — and therefore also the evolution of the GDF — is controlled by $\langle L \rangle_{\text{area}}$ for annealing times $t > \tau$.

4.2.4 Relaxation of Microstrain

Particularly for nanostructured materials that are prepared by severe cold working, the investigation of microstrain — in the as-prepared state, but also the relaxation mechanisms of microstrain at elevated temperatures — is indispensable and can contribute important information to a comprehensive picture on the mechanisms underlying the microstructural coarsening. For the samples of the present study, microstrain originates mainly either from excess-dislocation densities (as a consequence of sample prepa-

[6] At lower annealing temperatures the peak of $\langle L \rangle_{\text{vol}} / \langle L \rangle_{\text{area}}$ becomes blurred and appears as an "extended" plateau, the end of which is determined by the inflection point of $\langle L \rangle_{\text{area}}$.

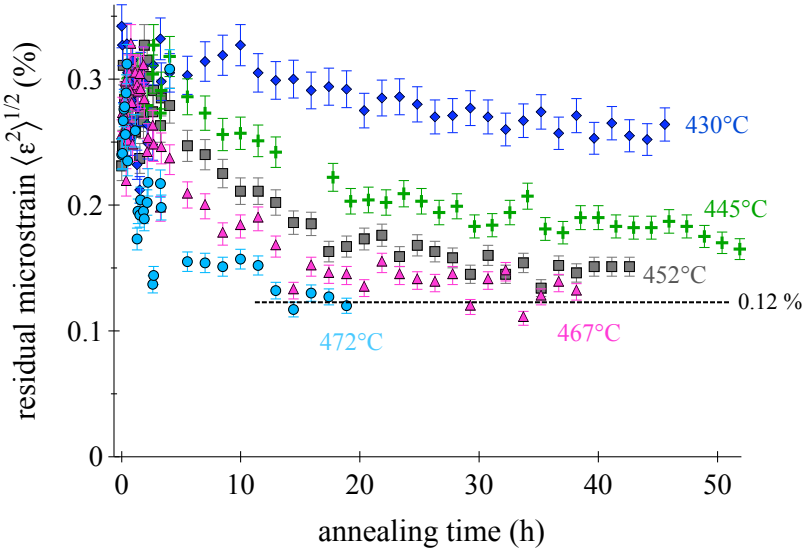

Figure 4.20: The graph shows for the isothermal anneals on batch X1 the continuous relaxation of microstrain as a function of annealing time. It can be observed that even at the highest temperatures the residual strain does not fall below a persistent level of $\left\langle \varepsilon^2 \right\rangle^{1/2} \approx 0.12\%$, even after annealing durations of up to 50 h.

ration by mechanical attrition) or from the constraint of polycrystalline contiguity, see Section 3.1.4. As it will turn out shortly, it is a key question for this study which process — either dislocation recovery or recrystallization — is responsible for the relaxation of the excess-dislocation density in the material, since depending on that, the microstructure of the material can have quite different characteristics. It is therefore a major goal of microstrain analysis (in combination with the DSC experiments in Section 4.3) to assess how the dislocation-induced microstrain is annihilated.

For the isothermal anneals on samples of batch X1 the residual microstrain is shown in Fig. 4.20 as a function of annealing time (the microstrain data of batch X2 is qualitatively similar and is therefore not included here). The curves in Fig. 4.20 reveal a monotonous and temperature-dependent decrease of the residual microstrain: Starting from $\left\langle \varepsilon^2 \right\rangle^{1/2} \approx 0.3\%$ right after the deoxidation treatment (Section 4.1.3), the microstrain relaxes and approaches asymptotically a persistent steady-state value of about 0.12% for the most extensive annealing times. The long-term-remaining residual microstrain is indicated in Fig. 4.20 by the horizontal dashed line.

The persistent residual strain even after significant annealing might be understood, if the two contributions to microstrain, i.e. the existence of a large number of dislocations and the topological contiguity of the polycrystal are considered separately. While the first contribution may decrease quite rapidly by recovery or recrystallization, the latter one depends basically on the actual size $\langle L \rangle$ of the grains, see Section 3.1.4. According to Eq. (3.22) the two averages $\langle L \rangle$ and $\langle L \rangle_{\text{area}}$ are by definition identical and thus, microstrain caused by topology should be expected to scale inversely proportional with the area-weighted mean grain size [142, 143],

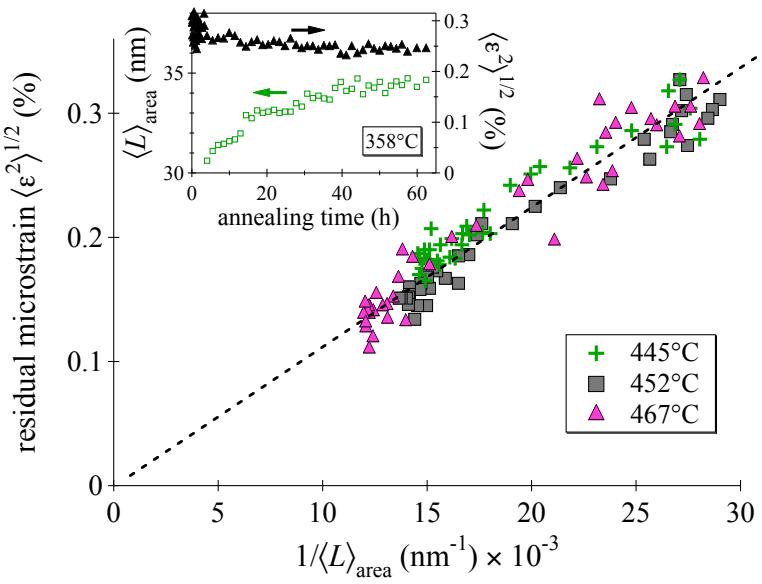

Figure 4.21: Analysis of contiguity-induced microstrain. The graph shows the residual microstrain of Fig. 4.11 as a function of the inverse grain size $\langle L\rangle_{\text{area}}^{-1}$ (for better clarity, only the data sets of 445, 452 and 467°C are plotted). The linear characteristic of the data points supports contiguity-induced microstrain to be the major strain source after the initial period of annealing ($\langle L\rangle_{\text{area}} \gtrsim 35$ nm). The inset presents the time-resolved size and microstrain data of the 358°C experiment, which indicates for an annealing time as long as 60 h neither a noticeable increase of $\langle L\rangle_{\text{area}}$, nor a substantial relaxation of strain. As the thermal activation at 358°C was found by calorimetric analyses to be sufficient for the annihilation of dislocations, strain relaxation requires apparently the distict coarsening of the microstructure.

$$\left\langle \varepsilon^2 \right\rangle^{1/2}(t,T) \propto \frac{1}{\langle L\rangle_{\text{area}}(t,T)}. \tag{4.11}$$

To test the relationship of Eq. (4.11) for the investigated specimens, Fig. 4.21 shows the microstrain data for the anneals at 445, 452 and 467°C, plotted as a function of the respective inverse grain-size data of Fig. 4.9. Two important features can be recognized from the graph: First, the plot of $\left\langle \varepsilon^2 \right\rangle^{1/2}$ as a function of $1/\langle L\rangle_{\text{area}}$ yields indeed for grain sizes $\langle L\rangle_{\text{area}} \gtrsim 35$ nm a linear relationship (which is actually the stage of grain growth following the initial jump, i.e. range I) and second, the linear extrapolation intersects with the origin of the graph, which indicates that in a grain-boundary-free microstructure the microstrain due to topological constraints vanishes completely. The linear characteristic of $\left\langle \varepsilon^2 \right\rangle^{1/2}$ as a function of the inverse grain size suggests that at this stage of the anneal (i.e. $\langle L\rangle_{\text{area}} \gtrsim 35$ nm) microstrain is primarily caused by the topology of the microstructure — whereas for grain sizes below (which is equivalent to the microstructure of the cold worked material at the very beginning of the anneal) the residual strain is the result of both grain contiguity and dislocations.

The inset of Fig. 4.21 shows $\left\langle \varepsilon^2 \right\rangle^{1/2}$ and $\langle L\rangle_{\text{area}}$ of the isothermal experiment at 358°C (both plotted as

a function of annealing time). Both curves demonstrate that even after annealing for 60 h the grain size and the microstrain do not reveal a notable change and level off at 35 nm and 0.25%, respectively. The considerable residual microstrain that remains even after such extended annealing seems likely to be related to the absence of any appreciable grain coarsening. This conclusion is substantiated by calorimetric analyses, which prove that the thermal activation at 358°C is sufficient for an efficient annihilation of dislocations on a much shorter time scale than the duration of the isothermal anneal (the detailed results of the calorimetric analyses are presented in Section 4.3 below). It is therefore not surprising to find a persistent level of microstrain, if grain growth interrupts or stagnates. A review of Figs. 4.9 and 4.10 reveals that exactly such a stagnation of the grain size (or at least a significant reduction of the growth rate) is found basically for all isothermal anneals on batch X1 and X2, which explains the general feature of a lower limit for strain relaxation in Fig. 4.20.

4.3 Calorimetric Analyses on Nanocrystalline Fe

Calorimetric analyses have been performed with the aim to assess the annihilation mechanism of dislocation excess and — if possible — the grain-growth kinetics and the activation enthalpy of the rate-controlling step during coarsening of the nanocrystalline Fe. The measurements have been performed according to Section 3.2 in the DSC mode at heating rates of 10, 15, 20 and 25 K/min, where for all scans the temperature interval between 50°C and 580°C has been passed through. The enthalpy signals of the individual DSC scans are plotted in Fig. 4.22 as a function of temperature, where the enthalpy data of each experiment is normalized to the actual mass of sample material (typically ~50 mg).

The four DSC traces in Fig. 4.22 show for appropriate scaling an obvious similarity, in which the shape of all four curves is designated by a distinct two-stage characteristic and a clearly defined termination of enthalpy relaxation around 580°C; the feature of a two-stage behavior is indicated in Fig. 4.22 by the labels “A” and “B”. It can further be observed that the transition between range A and B occurs for all four heating rates at approximately the same temperature of ~285°C. A comparison with literature data shows that the curves in Fig. 4.22 are qualitatively similar to results by Moelle and Fecht [128]. However, Malow and Koch reported quite different results, which also seem to have some kind of two-stage evolution in the temperature interval 50 . . . 580°C, but the strongest enthalpy release is found at approximately 660°C (at a heating rate of 40 K/min), i.e. outside the measured temperature range of Fig. 4.22 [10].

Inspection of Fig. 4.22 reveals that each of the two subsequent stages within the measured temperature range is basically determined by a broad peak, which is located for a heating rate of 25 K/min around 210°C and 440°C, respectively. However, if the enthalpy signal is defined by two subsequent (and therefore presumably independent) peaks, it appears likely that different enthalpy-releasing processes occur during the anneal and thus, it is of course needed that the enthalpy of each peak can be analyzed separately. For this reason, the two peaks “peak 1” and “peak 2” are defined, which relate to the low and the high-temperature range of Fig. 4.22, respectively. To analyze the overlapping peaks separately, the DSC curves were fitted by a superposition of two independent Gaussian functions, each related to one of the DSC peaks. A closer view on the shape of the high-temperature peak reveals that the enthalpy signal has a certain asymmetry with a faster drop of the enthalpy release on the high-temperature side

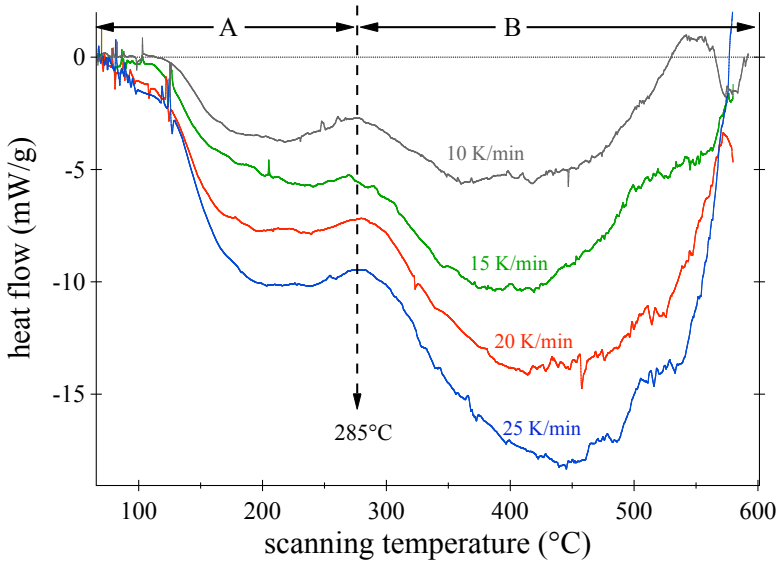

Figure 4.22: Exothermic heat flow of nanocrystalline Fe during a temperature sweep between 50°C and 580°C at heating rates of 10, 15, 20 and 25 K/min. The process of enthalpy release is designated for all heating rates by a clear two-stage characteristic, where the transition between the apparently independent low and high-temperature peak occurs at approximately 285°C.

of the peak (such a behavior is commonly observed for abnormal grain growth [121]). It is therefore not possible to fit the full high-temperature peak with a single symmetric function, and the temperature range for the fit is therefore limited to 100°C ... $T_{H_{\max}}$, where $T_{H_{\max}}$ denotes the temperature of the maximum heat flow of peak 2 (about 440°C at 25 K/min). For clear distinction from peak 2, the partial Gaussian fit of the high-temperature range is denoted by peak 2′ (see Fig. 4.23). Peak 2 can then be calculated in a final step by subtracting peak 1 from the measured DSC trace. Fig. 4.23 shows as an example the DSC analysis of the 25 K/min data according to the assumption of Gaussian peaks. The dashed line represents the superposition of the two fitted Gaussian peaks, which obviously yields a decent compliance with the experimental curve.

If the temperature axis is converted into a time axis (this must be done for each DSC experiment separately due to the different heating rates), the exothermic enthalpy release of peak 1 and peak 2 can be calculated by numerical integration of the peaks derived from the Gaussian approximates. The calculated enthalpies of the low and the high-temperature peak are included in Fig. 4.24. The enthalpy release, which is associated with the low-temperature peak is approximately the same for all four heating rates measured and takes on an average value of 125 J/mol (averaged over the four data points in Fig. 4.24). In case of the high-temperature peak, the released enthalpy appears to have an unexpected heating-rate dependence, where more enthalpy is released the faster the sample has been heated up. However, if there is a correlation between the heating rate and the amount of released enthalpy, it would be more likely to find a higher enthalpy output at lower heating rates, since the overall annealing time is longer. Due to this rationale the data point at 10 K/min in Fig. 4.24 will not be considered in the following, and the analysis is based on

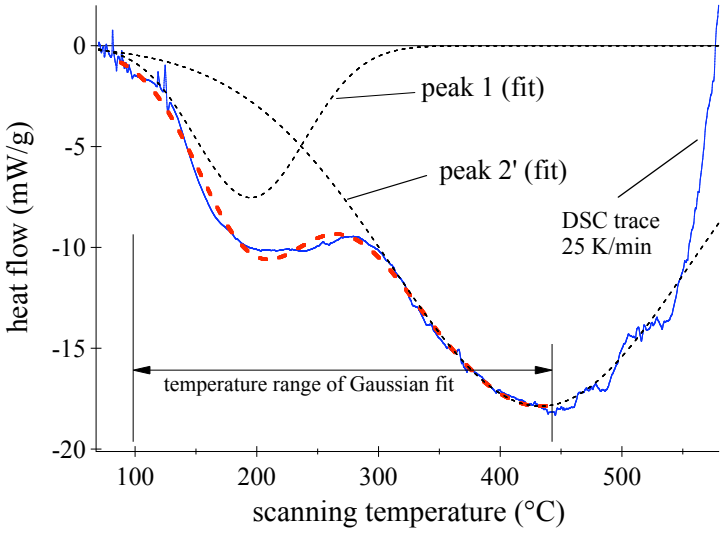

Figure 4.23: Quantitative analysis of the 25 K/min DSC scan with a superposition (dashed line) of two independent Gaussian peaks (dotted lines, peak 1 and peak 2'). According to the asymmetry of the high-temperature peak, the range for the numerical fit was set to 100 . . . 440°C for the 25 K/min curve (generally speaking, the upper end of the considered temperature interval is set to the maximum heat flow of the high-temperature peak).

the remaining three data points at 15, 20 and 25 K/min only. For those three points the average enthalpy for peak 2 yields about 600 J/mol, which is about a factor of 5 more than peak 1.

For further evaluation of the enthalpy data in Fig. 4.24 and a correlation with microstructural quantities (for example the average grain size or the residual dislocation excess), it is necessary to analyze the evolution of the microstructure during the DSC anneal by additional XRD analysis. The reference samples for XRD have been annealed in the calorimeter at a heating rate of 25 K/min to a final temperature between 200°C and 580°C. The annealing conditions for all reference samples were identical to the DSC scans in Fig. 4.22, except that the temperature was returned to ambient conditions immediately after the respective final temperature of the anneal was reached. The evaluation of the diffraction data was done according to the WA procedure, i.e. in the same way as the analysis of the isothermal anneals in Section 4.2.2 before. The mean grain size and the microstrain are shown in Fig. 4.25, plotted as a function of the respective final DSC temperature (the graph contains also for the sake of reference the grain size and microstrain data of the as-prepared (AP) state).

Fig. 4.25 reveals that both microstructural quantities, the grain size and the residual microstrain, experience a distinct temperature-dependent evolution upon annealing. However, it is also easily seen that the behavior of microstrain relaxation differs significantly from the one of grain growth. At low annealing temperatures grain growth is slow, what is expected according to the grain-boundary velocity given by Eq. (2.16) and the inherent temperature dependence of the grain-boundary mobility, and the grain size increases from $\langle L \rangle_{\text{area}} = 18$ nm in the as-prepared state (room temperature) to $\langle L \rangle_{\text{area}} = 24$ nm at 315°C.

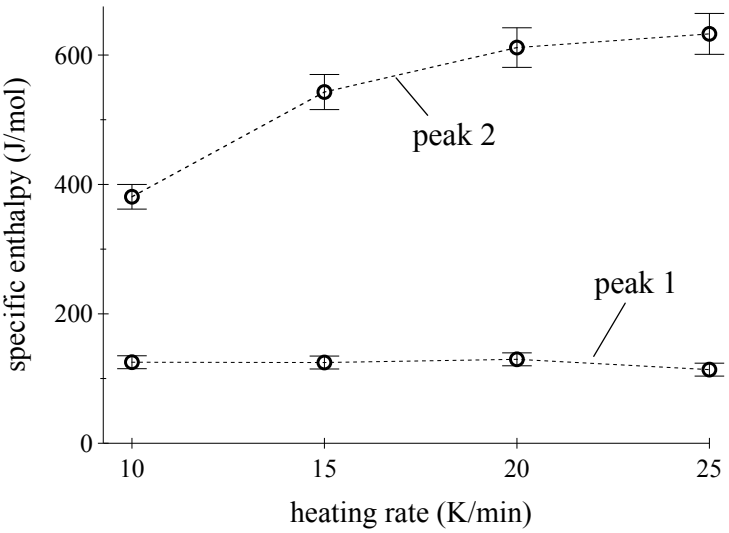

Figure 4.24: Enthalpy release associated to peak 1 and peak 2 at different heating rates. The data points have been determined by numerical integration of the Gaussian peak 1 and the calculated peak 2, defined by the difference between the measured DSC data and the numerical fit of peak 1.

At annealing conditions above 315°C the grain size increases significantly faster and reaches a value of $\langle L \rangle_{\text{area}} \approx 46$ nm for the highest temperature measured. In contrast to the kinetics of grain coarsening, the residual microstrain exhibits the fastest reduction already at annealing temperatures below ~400°C, where the residual strain relaxes quite easily from initially 0.35% to approximately 0.26%. At annealing temperatures beyond ~400°C no further decrease of residual microstrain is observed, although the grain size increases in this temperature range at the highest rate.

This obvious difference in the temperature dependence of grain-growth and microstrain-relaxtion kinetics suggests that the initial relaxation of strain is unlikely to be induced by the small increase of the grain size (i.e. via relaxation of compatibility strain). It appears more likely that the reduction of microstrain is connected to the annihilation of an excess-dislocation density. This assignment of microstrain to dislocations seems reasonable, since the as-prepared microstructure of ball-milled material is prone to the presence of excessive dislocation densities that are remaining from the grain-refinement process. This rationale, and in addition the finding that strain relaxation coincides quite well with the before defined peak 1, suggests to relate the enthalpy of 125 J/mol (Fig. 4.24, peak 1) to the annihilation of excess dislocations. Using Eq. (3.69), the enthalpy of peak 1 corresponds then to a dislocation density of $\varrho = 5.3 \times 10^{15}$ m^{-2}, where a shear modulus of $G = 82$ GPa was used, and the Burgers vector was approximated by the lattice constant of bcc Fe, i.e. $b \approx 2.886$ Å. Although this calculation is an upper-limit approximation of the dislocation density (this is, because other possible relaxation mechanisms are not considered), the result is in a reasonable agreement with dislocation densities of $\sim 3 \times 10^{15}$ m^{-2} found in Fe after sever plastic deformation [144].

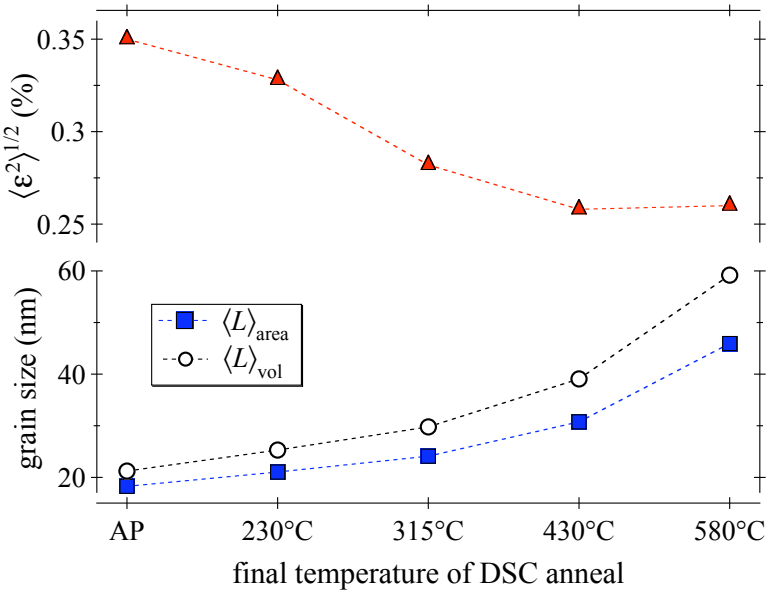

Figure 4.25: Plot of the two average grain sizes $\langle L \rangle_{\text{area}}$ and $\langle L \rangle_{\text{vol}}$ and of the residual microstrain $\left\langle \varepsilon^2 \right\rangle^{1/2}$ as a function of the end temperature of the DSC anneal. The samples have been annealed inside the DSC under identical conditions as the DSC experiments. The evaluation of the XRD scans was done according to the WA procedure.

The accuracy of the evaluated dislocation density depends of course on the uncertainty that is connected to the separation of peak 1 and peak 2 by using the Gaussian approximation. It is therefore advisable to validate the above calculated dislocation density by an independent analysis of the XRD data according to Section 3.1.4.1. The analysis of the diffraction data in the as-prepared state and after annealing to 315°C yields a dislocation density of 4.0×10^{15} m^{-2} and 1.5×10^{15} m^{-2}, respectively; the detailed analysis of those two temperatures can be seen in Fig. 3.10. The analysis shows that even after annealing to 315°C (which is approximately the tail of peak 1) the dislocation density is still at an unexpected high level. This circumstance seems to be caused by the inherent artifact of the Williamson-Hall method, that the complete strain measured by XRD (given by the slope of the δs versus s plot) is falsely ascribed to dislocations. Inspection of Fig. 4.25 suggests however that the relaxation of a dislocation-excess density is completed at ~400°C, and the remaining microstrain (0.26%) must be contributed by other reasons for lattice distortion. However, assuming that the relaxation of microstrain — from sources other than dislocations — can be neglected within the temperature range of peak 1, the difference between the calculated dislocation density at AP and 315°C should give an admissible value for the number of actually annihilated dislocations. The density of dislocations, which is removed by annealing to a temperature of 315°C is therefore equal to a value of 2.5×10^{15} m^{-2}, which is in excellent agreement with results found by Révész *et al.* and Schafler *et al.* on ball-milled and plastically deformed bulk Fe, respectively [98, 144]. However, the enthalpy that is related to a dislocation density of 2.5×10^{15} m^{-2} is only 60 J/mol, and therefore half of the enthalpy deduced from the Gaussian approximation of peak 1.

To examine the reason for the apparent discrepancy according to the two different analyses for the estimation of ϱ, the evaluation of peak 2 may contribute to solve this question. Fig. 4.25 indicates that for a major part of the temperature interval of peak 2 the residual microstrain stays at a constant level. Since grain growth and strain relaxation have been identified to be the main enthalpy-releasing processes for the present single-phase nanocrystalline samples, it is consequent to attribute peak 2 to the growth of grains.

Fig. 4.23 shows that for the Gaussian analysis peak 2 reaches far into range A, where XRD found an increase of the grain size from initially 18 nm to 23 nm at 285°C (the grain size at 285°C was calculated by linear interpolation between 230°C and 315°C). The respective enthalpy of peak 2 in the temperature interval of range A can be calculated from Fig. 4.23 as 80 J/mol, which yields according to Eq. (3.67) a grain-boundary energy $\gamma^{GB} \approx 0.5$ J/m^2 that is quite close to literature data of 0.8 J/m^2 reported by Hondros and Seah and by Malow and Koch [10,20]. Of course, the aggregate of the individual enthalpies due to grain growth (80 J/mol; peak 2 in range A) and strain relaxation (125 J/mol; peak 1 in range A) must be approximately equal to the total enthalpy of Fig. 4.22 range A, which equals ~200 J/mol (calculated by numerical integration between 100°C and 285°C).[7] Although this requirement seems to be satisfied, there are basically two aspects which question the correctness of the found enthalpy values: The calculated dislocation density of 5.3×10^{15} m^{-2} (125 J/mol) is almost 80% larger than the literature data of Refs. [98] and [144], and the grain-boundary energy of 0.5 J/m^2 is about 40% less than typical values found for nanocrystalline Fe, as given in Refs. [20] and [10]. Those observations suggest that the Gaussian functions yield an overestimation of peak 1 at the expense of peak 2.

On the other hand, the evaluation of diffraction data yielded an annihilated dislocation density of 2.5×10^{15} m^{-2}, which corresponds to an enthalpy of 60 J/mol. Consequently, for this approach the enthalpy of grain growth in range A would be equal to 140 J/mol (calculated from the difference between 200 J/mol, i.e. the total enthalpy of range A, and 60 J/mol, the dislocation enthalpy), and a corresponding grain-boundary energy $\gamma^{GB} \approx 0.8$ J/m^2 is found — a result that is obviously in excellent agreement with the literature references published by Hondros and Seah and by Malow and Koch [10,20]. This outstanding compliance of both the dislocation density and the grain-boundary energy with literature data supports the suitability of XRD to evaluate the annihilated dislocation density, and rejects at the same time the applicability of a simple Gaussian peak fit of the DSC curves.

During the full temperature scan of the DSC anneals, i.e. $T = 50°C \rightarrow 580°C$, the grain size increases approximately from 18 nm to 46 nm, which yields a grain-boundary energy of approximately 1.4 J/m^2 (corresponding to ~670 J/mol). Although this value is more than 50% larger than the grain-boundary energy calculated for range A only, it is still in agreement with the data of Fig. 2.4, where $\gamma^{GB} \approx 1.4$ J/m^2 would be representative for grain boundaries of high-angle misorientation.

The analysis of the DSC curves with respect to activation enthalpies of the involved microstructural processes yielded peculiar results, if compared to conventional solid-state diffusion processes. The analysis of the high-temperature peak returned a suspiciously low value of only 45 ± 4 kJ/mol. This is quite surprising, since Section 3.2.2.1 showed that the analysis of the activation enthalpy for the growth-

[7] Note: the temperature range of peak 1 and range A is not identical, but the area of peak 1 that is outside range A is relatively small and therefore negligible. Thus, it should be justified for this calculation to assume peak 1 and range A to cover approximately the same temperature regime.

controlling mechanism should be possible for normal grain growth. However, in case of abnormal grain growth this conclusion has to be handled with care, since then the maximum enthalpy release occurs approximately for the maximum growth rate of the volume fraction x_V of abnormal grains (*cf.* Section 3.2.2.4). The small activation enthalpy of 45 kJ/mol seems therefore to be an indication that the enthalpy release is driven by an abnormal evolution of the microstructure rather than normal curvature-induced grain growth. The deduced "activation enthalpy" would then be characteristic for the ease of the microstructure to reach the condition of the most abnormal state (which was found to occur for the fastest increase of x_V) — but it should not be confused with the intrinsic grain-boundary kinetics of abnormally growing grains.

From Fig. 4.22 it is apparent that the low-temperature peak of the DSC curves does not reveal any shift for different heating rates. This observation suggests that the related processes must be characterized by a distinctly low activation enthalpy, as it would be expected for the gliding of dislocations along slip planes. This would agree with the interpretation of peak 1 to be induced by the migration and annihilation of dislocations and the related relaxation of microstrain.

4.4 Electron Micrographs and Orientation Imaging

4.4.1 TEM Imaging

Powder samples of nanocrystalline Fe have been investigated by TEM in the as-prepared state and after annealing at 415°C for 120 h. The TEM imaging has been performed in a Phillips CM20 in collaboration with the Electron-Microscopy Group for Materials Science at Ulm University.

Fig. 4.26(a) illustrates the electron diffraction pattern of the as-prepared state, which precisely shows the Debey-Scherrer rings of the (110), (200) and (211) lattice planes. A remarkable feature of the diffraction pattern is the finding of a spot-like intensity concentration within the (110) ring, visible around the 2 and the 8 o'clock position. A similar observation is not made on the higher-order (*hkl*) reflections. Since the location of diffracted intensity is representative for the orientation of a grain, the increased intensity at the two positions of the (110) orientation indicates that the grains are not of fully random orientation, but have a preferred orientation that is reflected in a particular texture component.[8] Support for the existence of a preferred grain orientation is found in the dark field image of Fig. 4.26(b). It can be seen that a considerable fraction of the grains in the probed volume has a similar spatial orientation. Further it might be noted from the dark-field micrograph that already in the as-prepared state the individual crystallites appear to be of nearly equiaxed shape with a size ranging between 15. . . 20 nm, which is obviously on the same scale as the grain size determined by XRD. Even though both images in Fig. 4.26, the diffraction pattern and the DF image, are testifying a distinct crystalline grain structure, the non-uniform intensity within the grains (visible in the DF image of Fig. 4.26(b)) advises — similar to the DSC results — the presence of a notable number of dislocations in the as-prepared state, which are obviously remaining from mechanical processing.

[8] Since the diffraction angle in TEM is very small ($\theta < 1°$), it seems very likely that the two orientations around the 2 and the 8 o'clock position of the (110) diffraction ring belong to the same texture component.

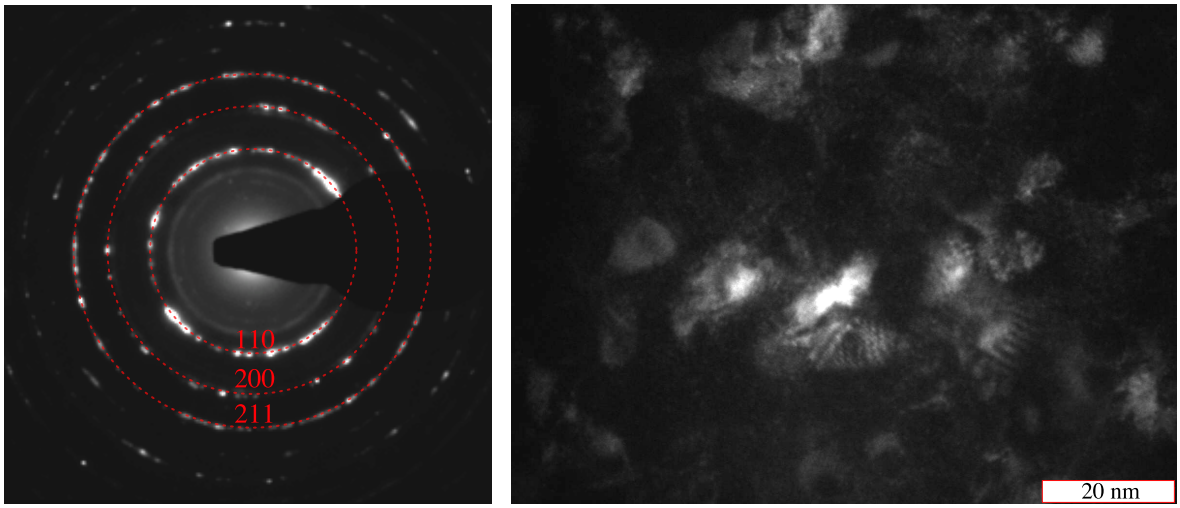

(a) (b)

Figure 4.26: a) Electron diffraction pattern of the as-prepared state of nanocrystalline Fe. The irradiated area for diffraction was approximately 400 nm × 300 nm, i.e. in total there are about 200. . . 300 grains per one $\langle D \rangle$ sample thickness contained in the probed area. The Debey-Scherrer rings are identified as the (110), (200) and (211) lattice planes of bcc Fe. b) Dark-Field image of the as-prepared state. Figure a) and b) are taken from different spots of the same specimen.

The TEM data in Fig. 4.26 suggests that a grain of the as-prepared microstructure has two options, either it will belong to the found texture component or will be part of the grain population that is deviating in orientation from the textured grains. From the angular spread of the texture component in Fig. 4.26(a) and the finite diameter of the pinhole aperture in dark-field imaging, it might be estimated that the orientations of the textured grains have a variance of less than ~20°. Although the orientation of grains and the existence of a texture component in the as-prepared state is evident from both images of Fig. 4.26, conclusions on the mean misorientation of neighboring grains (which would be needed for the evaluation of misorientation-dependent grain-boundary properties, like the specific grain-boundary energy or mobility) can be misleading since the projection of a 3-dimensional grain assembly into a 2-dimensional dark-fied image or a diffraction pattern may represent the relative orientation of the grains correctly, but it disregards the spatial arrangement of the grains.

TEM analyses of the annealed state have been performed on the 415°C sample of batch X2. Fig. 4.27 shows a series of four dark-field images of this sample. Picture (a) – (d) in Fig. 4.27 have been taken with the smallest available pinhole aperture in the back-focal plane of the TEM, where the aperture was moved in steps of $\varphi = 5°$ along the (110) diffraction ring. In all four images significant grain growth with grains in the range between 100 nm and 300 nm can be observed. Obviously, the grains are much larger than measured by XRD, where an average grain size of $\langle L \rangle_{\text{area}} \approx 60$ nm and $\langle L \rangle_{\text{vol}} \approx 80$ nm has been found (*cf.* Figs. 4.10 and 4.12). This material difference between the volume-sensitve XRD technique and the spot examination of TEM may indicate that the GDF must be significantly broadened during the anneal, and the imaged grains in the DF of Fig. 4.27 are likely to belong to the upper tail of a widespread GDF.

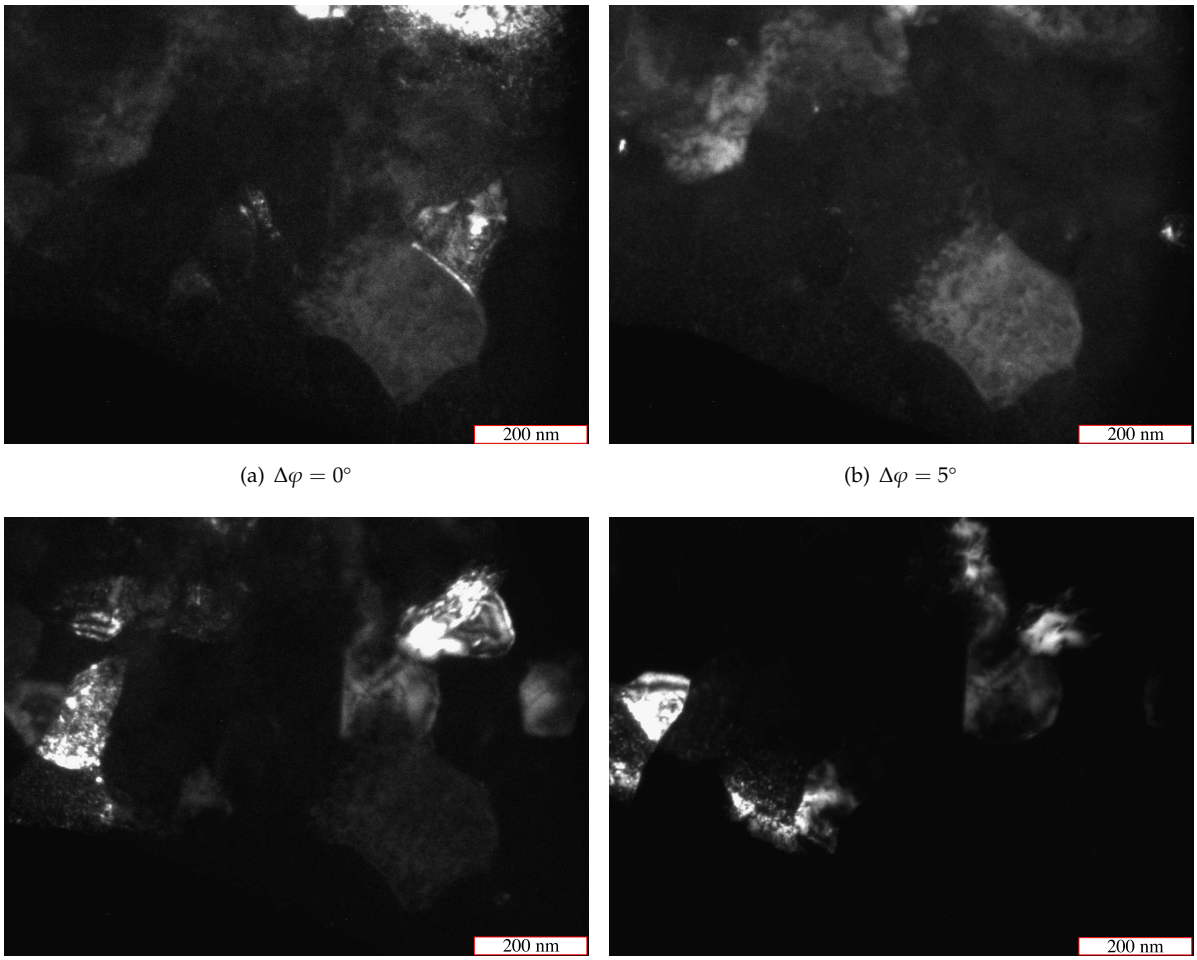

(a) $\Delta\varphi = 0°$ (b) $\Delta\varphi = 5°$

(c) $\Delta\varphi = 10°$ (d) $\Delta\varphi = 15°$

Figure 4.27: Series of DF images of nanocrytsalline Fe after annealing at 415°C for 120 h. Between each diffraction image the pinhole aperture has been moved on the (110) diffraction ring by $\Delta\varphi = 5°$. The sequential appearance and disappearance of diffracted intensity reveals that adjoining grains have a rather small misorientation of $\lesssim 10°$, i.e. those grains are preferentially separated by grain boundaries of low-angle character.

Inspection of Fig. 4.27(a) – (d) reveals in the examined field of view a successive appearance and disappearance of grains in the DF mode. According to the small step width of $\Delta\varphi = 5°$ between the four images, this sequential behavior must be characteristic for an obviously small inter-grain misorientation. Although the angular resolution of the used aperture is not known exactly, an upper limit of $5 \ldots 10°$ seems to be a reasonable estimate for the relative misorientation between the adjoining grains.

4.4.2 Orientation Imaging

Orientation Imaging Microscopy (OIM) has been performed on the final state of the 423°C sample of batch X1. This sample was selected because it constitutes the most interesting characteristic in isothermal annealing: Firstly, $\langle L \rangle_{\text{area}}$ resembles for an incredible time of 55 h a constant growth rate, which is then followed by an increase of the growth kinetics and secondly, the size distribution of the microstructure becomes continuously broader throughout the anneal — this means that the examined sample should be a paragon for a microstructure in the most non-uniform, i.e. the most abnormal configuration. OIM examination of the as-prepared microstructure was not possible due to the spatial resolution limit of the SEM/EBSD system and to the residual dislocation density, which both impaired the formation of an evaluable Kikuchi pattern.

The result of the OIM examination on the isothermal anneal at 423°C is illustrated in Fig. 4.28(b) – (i), which shows for each picture the overlay of the as-reconstructed EBSD image (reconstruction of the grain orientation has been performed with the Oxford Instruments Microanalysis Suite) and the pattern-quality image. The overlay of the pattern quality is shown for the sake of a better visualization of the grains and to mitigate the noise in the grain orientation that is due to incorrect solutions of low-quality Kikuchi patterns. For each of the eight examined spots, the normal (ND), rolling (RD) and transverse direction (TD) is shown in the left, center and right column of Fig. 4.28, respectively. For each of the three projections (ND, RD and TD), the orientation of a grain is determined by a vector $[\text{uvw}]$, which is defined to be parallel to the direction of projection, and to be parallel to the normal vector of a set of (hkl) planes. The vector [uvw] is defined by the three unique basis vectors [001], [101] and [111], which are also the corners of the pseudo-color key for the grain orientation, as illustrated in Fig. 4.28(a).

The OIM images clearly show that the magnitude and the nature of grain growth can significantly vary between different spots of the same sample. For this reason the eight OIM experiments are classified into three categories (A, B and C) of similar microstructure. For the first three spots (type A), Fig. 4.28(b) – (d), the microstructure can be described as a mixture of small ($\langle L \rangle \approx 50 \ldots 100$ nm) and large grains ($\langle L \rangle \gtrsim 500$ nm), which establish together a non-homogeneous grain assembly of bimodal grain-size characteristic. Beside the remarkable spread of the grain sizes, the microstructures of type A include grains of finger-like shape with aspect ratios of 5:1 or more.[9] Obviously, the feature of elongated grain shape is particularly inherent for the large grains, but it is not found for the small grains, which are of equiaxed shape.

In contrast to the microstructures of type A, the last two spots investigated by EBSD, Fig. 4.28(h) and (i), reveal a rather homogeneous grain-size distribution with nearly equiaxed grains in the size regime of $200 \ldots 500$ nm (type C). The feature of elongated finger-like grains is not found in type C microstructures.

An intermediate microstructure (type B) seems to be prevailing in Fig. 4.28(e) – (g), where characteristics of both types A and C are coexisting. While a few grains have finger-like shape (the aspect ratio of which appears however to be less than for type A), the general grain-size distribution seems to be homogeneous (like type C). It can further be observed that microstructures of this type do not comprise exceptionally large grains, as it was found for type A.

[9] The aspect ratio is defined as the quotient of the long-axis dimension of a grain and the perpendicular intercept length of the grain in the OIM image.

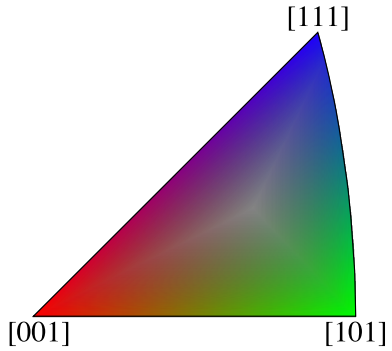

(a) Color code to identify the grain orientation.

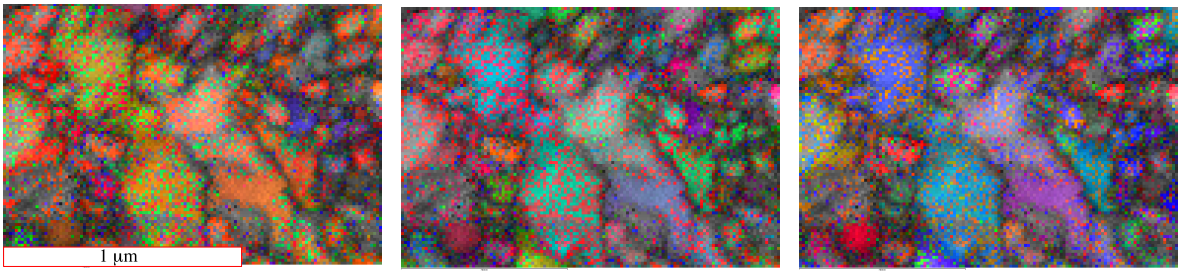

(b) Position 1, type A

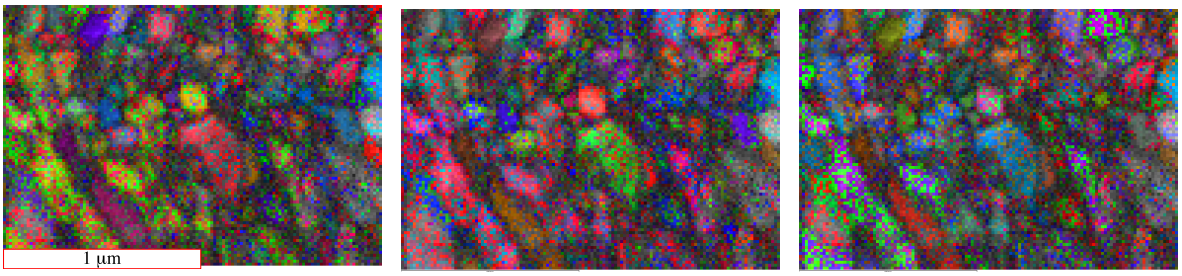

(c) Position 2, type A

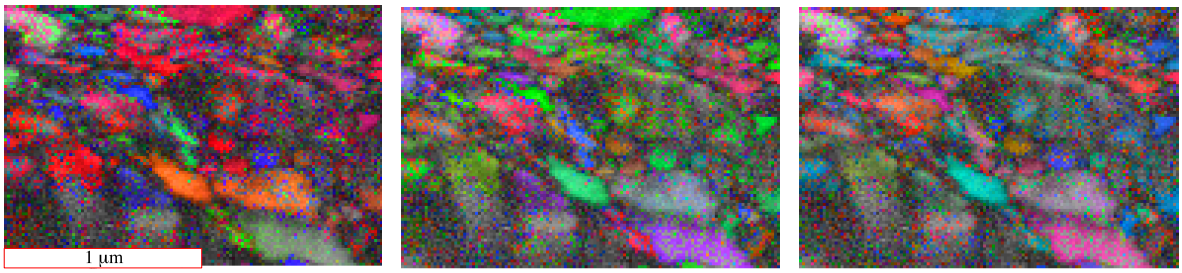

(d) Position 3, type A

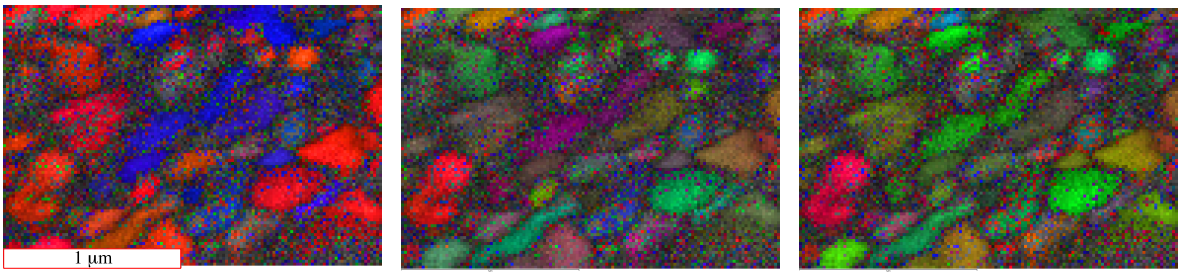

(e) Position 4, type B

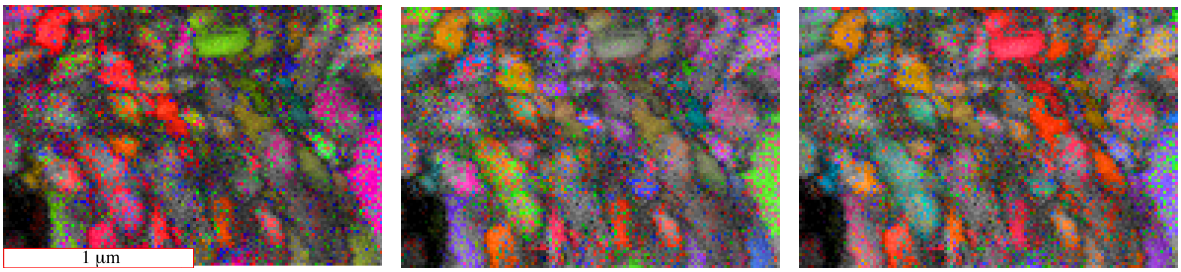

(f) Position 5, type B

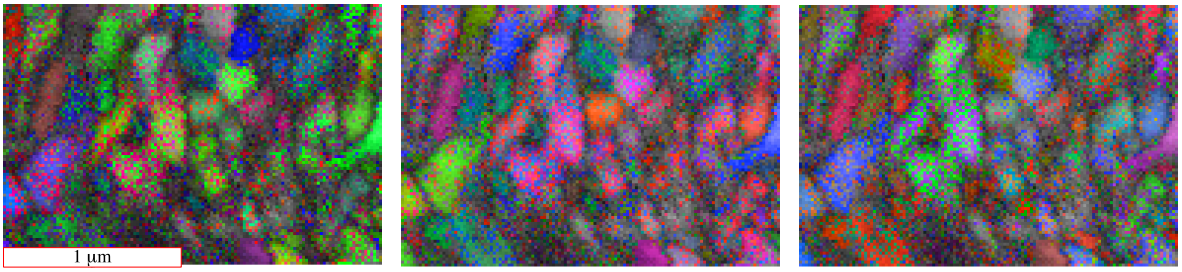

(g) Position 6, type B

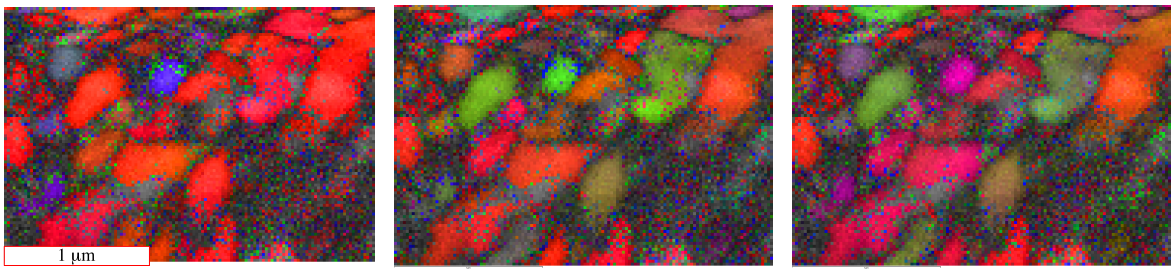

(h) Position 7, type C

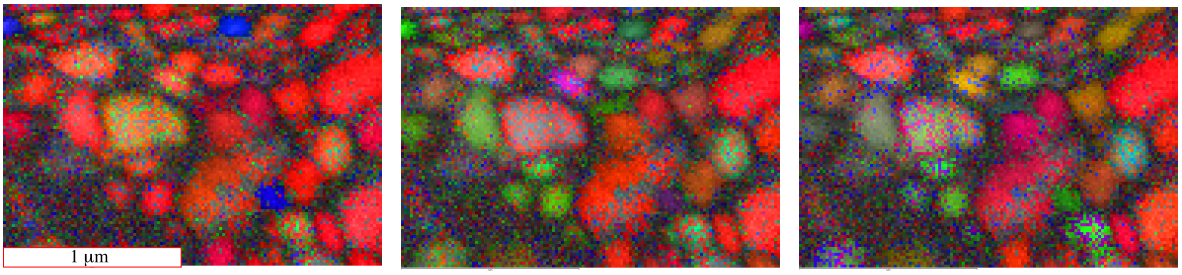

(i) Position 8, type C

Figure 4.28: OIM results of the EBSD analysis at eight different locations on the 423°C sample of batch X1.

The quite diverse microstructures of type A, B and C in Fig. 4.28(b) – (i) reveal that annealing at 423°C induces an inhomogeneous grain evolution with the extremes of strong and uniform coarsening (type C) and weaker, but anisotropic and selective growth (type A). This finding of a widespread characteristic agrees with Fig. 4.16, where for this particular anneal the strongest disparity of grain sizes — i.e. the broadest GDF — is found at the end of the annealing experiment. The inhomogeneous and anisotropic development of grain sizes is particularly obvious in type A, where the OIM images clearly suggest abnormal grain growth to be prevailing. Because of both, the microstructures of type B and C resemble a rather uniform evolution of the material and the plots of Fig. 4.16 show that for appropriate annealing conditions the width of the GDF will decrease in the long-time view, there is reason to believe that especially the type A microstructure of the 423°C sample is even after extensive annealing for 78 h in a transient evolution stage.

Of course, if the abnormal growth of grains is concluded from the observed microstructural inhomogeneity in Fig. 4.28(b) – (i), it should be investigated what could provoke such a deviation from the uniform evolution during normal grain growth. A key aspect of normal grain growth is the precondition of uniform boundary properties, which means that the actual growth kinetics is solely determined by the curvature of the grain boundary, see Section 2.3. Section 2.2 however showed that the prerequisite of uniform boundary properties will only apply, if the grain boundaries are not defined by a certain distribution of low-angle misorientations, which would immediately introduce a distribution of grain-boundary energies and mobilities. The DF image of the annealed state in Fig. 4.27 actually shows that the misorientation between facing grains (at least at the end of the anneal) is likely of low-angle

type, which would indeed contest the preconditions for normal grain growth, and favor the evolution of a misorientation-dependent growth kinetics. Since the distribution of relative misorientation plays obviously an important role in this case, the OIM images have been analyzed by inverse-pole-figure (IPF) plots. Fig 4.29 shows the orientation analysis related to the ND of the eight OIM analyses of Fig. 4.28. For the first three cases (type A) no appreciable alignment of the grains is observed (the apparent texture in Fig. 4.29(a) is induced by the presence of a few very large grains in the field of view, but is not related to a strong alignment of the much smaller matrix grains). In contrast to type A, the IPF plots of type C (Fig. 4.29(g) and (h)) present a distinct alignment of the grains, having a strong single texture. In between of the the two extremes of type A and C, the intermediate type B microstructures have a more textured grain orientation than type A, but obviously less pronounced than type C.

Comparing the microstructural characteristics in terms of grain size and grain shape of the OIM images in Fig. 4.28 with the IPF plots, a conspicuous correlation between the extent of orientational alignment and the size/shape of the grains is revealed. Qualitatively it is found that a distinct texture in the annealed state corresponds to a homogeneous size distribution with almost equiaxed large grains (type C), whereas a weak texture (or even a random orientation) involves a heterogeneous grain-size distribution with grains of finger-like shape (type A). With respect to this observation the DF TEM images of Fig. 4.27 might be assigned to type C microstructures.

If the broadening and narrowing of the GDF is considered as a transient process, the images of type C are likely to represent the final state after stagnation of growth in the long-time view, whereas type A and B still can be in an evolutionary stage where the final state of the microstructure has not been reached so far. Since the OIM investigation is made on the sample in its most "abnormal" condition (see the 423°C data in Fig. 4.16), it seems likely that the squeezing of the GDF beyond the maximum of $\langle L \rangle_{\mathrm{vol}} / \langle L \rangle_{\mathrm{area}}$ is dominated by grain configurations of type A and B.

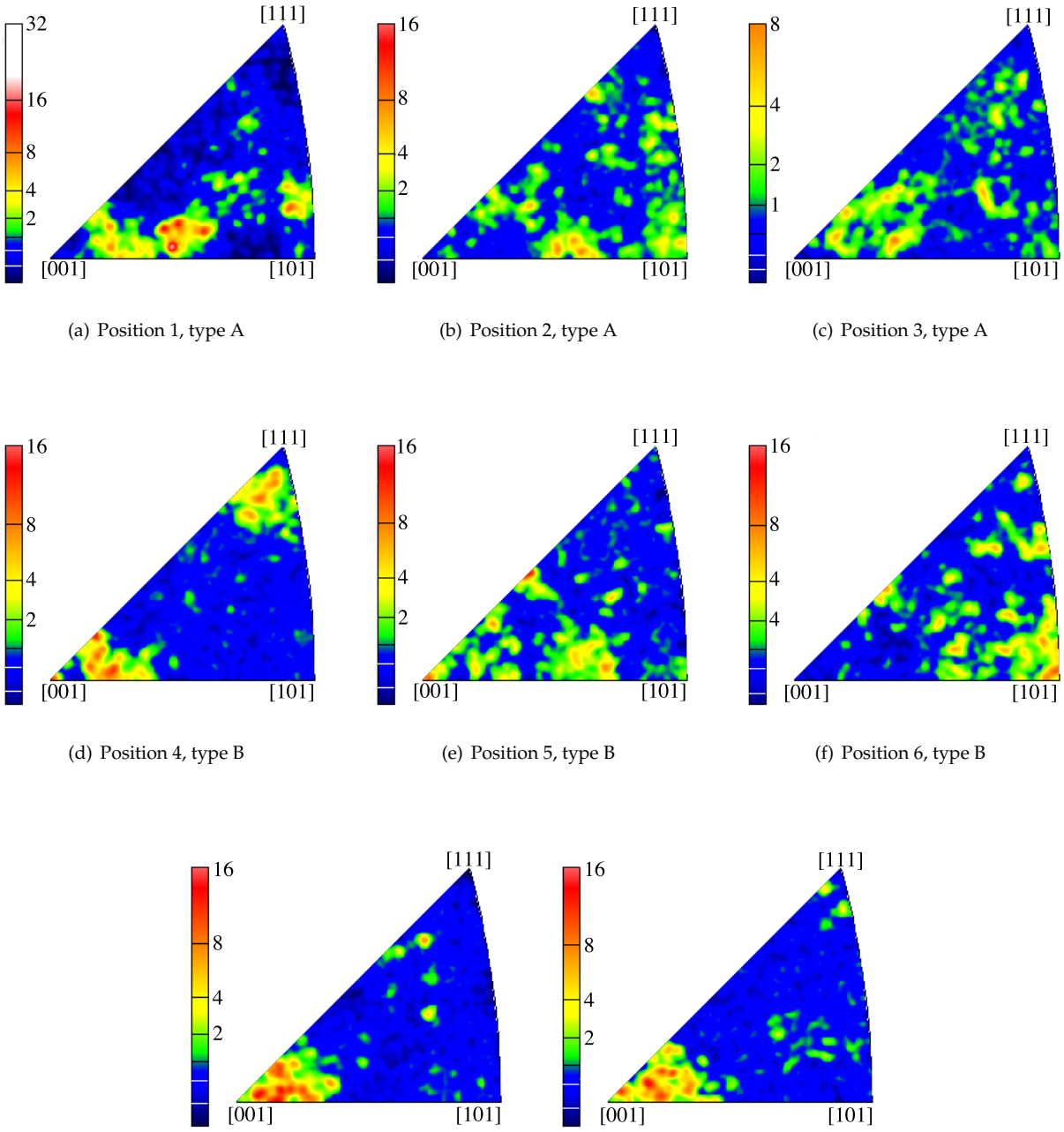

(a) Position 1, type A

(b) Position 2, type A

(c) Position 3, type A

(d) Position 4, type B

(e) Position 5, type B

(f) Position 6, type B

(g) Position 7, type C

(h) Position 8, type C

Figure 4.29: Inverse Pole Figures (IPF) for the ND projection of the OIM examinations on the 423°C anneal, shown in Figs. 4.28(b) – (i). The Inverse Pole Figures illustrate the logarithmic "pixel-orientation" frequency of the individual ND projections. Although this may increase the noise in the IPF analysis, it is the advantage that the information contained in the IPF plots does not rely on the assignment of a pixel to a particular grain.

Chapter 5

Grain-Growth Kinetics in Nanocrystalline Fe: Discussion and Conclusions

5.1 Review of Experimental Results

The experimental findings from isothermal XRD, scanning calorimetry and electron microscopy establish the foundation for the comprehensive discussion of the microstructural evolution of nanocrystalline ball-milled Fe. The following brief review summarizes the key results of the experimental investigations.

- XRD
  - The evolution of the grain size under isothermal-annealing conditions is designated by four unique characteristics: 1) a sudden increase of the grain size at the beginning of the anneal, 2) a quasi-linear growth within range I, 3) the acceleration of the growth rate at the transition between range I and range II, and 4) a long-term power-law growth with stagnation.
  - The transition of $\langle L \rangle_{\text{area}}$ between range I and range II manifests in a clear inflection point of the curvature in the grain-size/time plot.
  - The width of the GDF undergoes a non-self-similar broadening and narrowing, where the maximum width of the size distribution coincides with the inflection point of $\langle L \rangle_{\text{area}}$. The broadest state of the size distribution is reached after a time τ, which reveals a distinct temperature dependence with an "activation enthalpy" equal to 320 kJ/mol.
  - The broadening of the GDF is driven by the rapid increase of $\langle L \rangle_{\text{vol}}$ and is characterized by an activation enthalpy of 200 . . . 225 kJ/mol
  - The deduced activation enthalpies for the kinetics of $\langle L \rangle_{\text{vol}}$ and $\langle L \rangle_{\text{area}}$ are the same within the experimental uncertainty (~210 kJ/mol) and do not change during the anneal.
  - The magnitude of the shape parameters of a Pearson VII function shows for all isothermal experiments the transition through a minimum and a reversing increase at longer annealing times. The location of the shape parameters' minimum coincides with the broadest state of the GDF, i.e. occurs after a time τ.
  - In the long-time view, all isothermal anneals reveal either a clear decrease of the growth rate, or at higher annealing temperatures an asymptotic stagnation of grain growth ($m > 2$).

- ▷ Lattice strain is found to be induced by dislocations and grain topology, where the first one reveals an easy relaxation already at low temperatures, whereas the latter one relaxes proportional to the rate of grain growth.

► DSC

- ▷ All DSC curves are designated by a characteristic two-peak profile, where the low-temperature peak releases less enthalpy than the high-temperature peak.
- ▷ The transition between the two peaks is found for all heating rates at approximately 285°C.
- ▷ For all DSC runs the release of enthalpy stops almost moderate at a temperature of approximately 580°C, although only an intermediate grain size is reached at this point ($\langle L \rangle_{\text{area}} \approx 46\,\text{nm}$).
- ▷ The low-temperature peak is assigned to the fast annihilation of excess dislocations with $\Delta\varrho = 2.5 \times 10^{15}\ \text{m}^{-2}$. Above ~400°C there is no dislocation-induced microstrain remaining.
- ▷ The grain-boundary energy was estimated to be 0.8 J/m^2 and 1.4 J/m^2, depending on the analyzed range of the DSC scan.
- ▷ The high-temperature peak in DSC is designated by an activation enthalpy of 45 kJ/mol, while the low-temperature peak does not reveal any response on the heating rate. The small activation enthalpy of the high-temperature peak disagrees with normal grain growth, for which an activation enthalpy similar to the bulk or the grain-boundary self-diffusion is expected.

► TEM & OIM

- ▷ The as-prepared microstructure appears to be a hybrid of matrix grains with a preferred grain orientation and a few outsided grains with a certain misorientation from the matrix.
- ▷ The as-prepared microstructure is designated by a rather narrow grain-size distribution (this is also found by XRD), with grains of equiaxed shape. DF imaging suggests a substantial dislocation density contained in the refined grains prior to annealing.
- ▷ The microstructure can be quite diverse at an intermediate point of the anneal, ranging from equiaxed large grains in a homogeneous environment to elongated and finger-like large grains in a matrix of small grains (inhomogeneous grain-size and grain-shape distribution). The latter case witnesses anisotropic grain-boundary kinetics.
- ▷ A correlation between the annealed microstructure and the degree of texture has been identified, where a weak texture prefers a broad size distribution with finger-like grains.

5.2 Evaluation of the Experimental Results in the Context of Grain-Growth Theory

The quantitative model-based description of grain growth, i.e. the capability to predict the kinetics of grain boundaries and thereby the evolution of the microstructure, is generally based on two aspects: The unique material-dependent parameters γ^{GB} and M^{GB} that are normally used to be representative for the entire polycrystal, and a grain-size-scaled growth kinetics (*cf.* Section 2.4) in which the grain-boundary curvature remains as the only free parameter that is defining the actual growth kinetics of a grain (or more

accurately, the migration kinetics of the grain boundaries with specific curvature). For those mean-field preconditions, analytical models predict a self-similar evolution of the microstructure and an increase of the mean grain size following a parabolic time dependence (i.e. a growth exponent $m = 2$) — this mode of coarsening is usually denoted in literature as "normal" grain growth. Of course, if one of the preconditions for normal grain growth fails, for example if the kinetics of a grain boundary depends on the actual interface configuration, the growth rate of the grains will no longer be uniquely defined by the grain-size distribution, but will also be affected by the distribution function of a certain grain-boundary property (for example a misorientation distribution, or the distribution of solute drag). In this case, the prediction of the microstructural evolution is only possible, if this distribution is known exactly.

In the light of this rationale the review of the experimental data from each isothermal anneal on nanocrystalline Fe revealed two exceptional features, which are both obviously not consistent with the characteristics expected for normal grain growth:

1. There is a constant growth rate (quasi-linear growth) at the beginning of the anneal that is followed by a temporary increase of the growth kinetics (both described by a growth exponent of $m \approx 1$ and $m < 1$, respectively), and

2. the qualitative assessment of the grain-size distribution shows a consecutive broadening and narrowing of the GDF, which would not be expected, if a self-similar evolution of the GDF controls grain growth.

The finding of a non-self-similar GDF, i.e. a varying ratio between the mean size of the GDF and the largest grains (this behavior has also been observed in the diffraction raw data, which is noticeable in the respective time dependence of the Pearson VII shape parameters $m_{\mathrm{L,\,R}}$) is supported by the recorded OIM images that reveal at the broadest state of the GDF a clearly non-uniform microstructure. Obviously, the experimental findings unambiguously withdraw normal grain growth for the coarsening of nanocrystalline Fe, and refers the further discussion to the irregular growth of grains — this means that other parameters than the curvature of the grain boundary only must be involved in the actual interface kinetics of nanocrystalline Fe. If the preconditions for normal growth are not fulfilled and grain growth occurs in a non-uniform way, the mode of microstructural coarsening is mostly denoted as "abnormal" grain growth (AGG).

If AGG is taken into consideration for the nanocrystalline samples of the present study, it would be tempting to propose the impact of TL and the corresponding size-dependent rescaling of the effective mobility as the cause for failing of normal grain growth (*cf.* Section 2.5.1). A size-scaled mobility would not only account for a quasi-linear growth, if $\Gamma \ll 1$, but it would equally explain a non-self-scaling GDF, since the relative influence of TL drag depends on the grain size. At moderate temperatures this requires however that the TL mobility must have a significantly higher activation enthalpy than grain-boundary or bulk diffusion to hold for $M^{\mathrm{TL}} \ll M^{\mathrm{GB}}$, which is obviously not reflected in the activation enthalpies for $\langle L\rangle_{\mathrm{area}}$ and $\langle L\rangle_{\mathrm{vol}}$. It is rather found that the activation enthalpy of ~210 kJ/mol, which is obviously close to the one for grain-boundary self-diffusion (174 kJ/mol [26]), agrees well with activation enthalpies measured by Malow and Koch of 248 kJ/mol on nanocrystalline Fe [10] and by Vandermeer and Hu of 249 kJ/mol on coarse-grained Fe [9]. Especially the latter one, which was deduced from experiments on grains in the size range of $40 \ldots 700$ μm (which are due to their size beyond all speculation of TL drag)

indicates that the measured activation enthalpy of ~210 kJ/mol is representative for boundary-controlled kinetics, and the activation enthalpy of TL migration in α-Fe should be larger than the actually measured quantity to allow for an efficient inhibition of boundary motion.

However, beside the implausibility of the activation enthalpy, already a more fundamental point rejects TL drag. TL drag will only dominate grain-boundary migration, if the TL kinetics is slower than the intrinsic behavior of the grain boundary. Eq. (2.49) defines accordingly a transition grain size, below which TL migration can be the rate-controlling step in grain growth. If the grain size increases during coarsening of the microstructure, the influence of TL gradually abates. At the transition grain size the curvature-driven kinetics and the TL velocity will then be equal, and for further growth the intrinsic grain-boundary kinetics becomes rate controlling. Since it is always the slowest of the involved processes that will be the rate-controlling one, it is evident that at the transition where the leading mechanism changes, the overall growth kinetics will further decrease. The measured behavior of the growth kinetics is however the exact opposite, where the growth rate apparently increases after the quasi-linear regime. This shows that the transition between range I and II cannot be the result of a change of the rate-controlling step [145].

This conclusion holds also for the feasibility of QP-limited grain-boundary migration. Although the supposed grain-boundary kinetics would theoretically allow for an temporary increase of the growth rate (*cf.* Eq. (2.52)), it is the practically constant activation enthalpy of $\langle L\rangle_{\text{area}}$ and $\langle L\rangle_{\text{vol}}$ during the complete anneal, which does not lend credence to the possibility of QP drag. In summary it can therefore be concluded that neither TL motion nor QP drag are appropriate to explain the experimental results of nanocrystalline Fe and thus, a different explanation for the anomalous coarsening is needed.

The observation that within range I the ratio $\langle L\rangle_{\text{vol}}$ / $\langle L\rangle_{\text{area}}$ quickly increases shows that the initially homogeneous microstructure obviously contains particular grains — those are the grains that will drive the increase of $\langle L\rangle_{\text{vol}}$ in range I — that are able to grow at a much higher rate than the mean of the microstructure (which is approximately represented by $\langle L\rangle_{\text{area}}$), and populated easily the upper end of the GDF. The allocation of grains into two categories of clearly different growth kinetics is a paragon for AGG, where only a small fraction of abnormal grains reveals a distinct growth kinetics while the majority of grains is either disabled from coarsening or is growing on a much slower rate. It is evident that such inhomogeneous coarsening will induce — provided that AGG persists for sufficient time and spatial range — the formation of a (bimodal) two-population microstructure with an inactive matrix and the fast-growing abnormal grains, respectively. If AGG is a continuous process, the abnormal grains will gradually annihilate the matrix and the abnormal-volume fraction x_{V} increases monotonously to approach after a certain time the condition at which the microstructure becomes dominated by the abnormally-growing grains. At the end of excessive AGG the microstructure may then arrive at a state in which the entire matrix has been annihilated ($x_{\text{V}} \approx 1$) and a "new" microstructure of abnormally-grown grains only is created. In this scenario AGG would be a transient process, where a sequential broadening (due to the increasing volume fraction) and narrowing of the GDF is expected (when the abnormal grains finally annihilate the matrix) — this is apparently consistent with the experimental findings for the evolution of nanocrystalline Fe. Although a successive broadening and narrowing of the GDF would also be found if a single abnormal grain or a strong recrystallization process annihilates the initial microstructure (which may then terminate in a single crystal rather than a polycrystal), the finding of a final grain-size ratio

$\langle L \rangle_{\mathrm{vol}} / \langle L \rangle_{\mathrm{area}} > 1$ and the review of OIM and TEM images indicates that for the examined samples the final state results from a transformation of an unstable polycrystalline microstructure via AGG into a new and more stable one.

To assess whether AGG would also account for the observed three-stage grain-growth kinetics with *i*) a quasi-linear growth (range I), *ii*) the acceleration of the growth kinetics at the end of range I (together with an inflection point at the transition between range I/II), and *iii*) a stagnant power-law growth at longer annealing times (range II), a quantitative two-population model has been developed and was successfully tested on isothermal growth curves [145]. Details of the model and numerical results will be presented in Section 5.3 below.

5.3 A Phenomenological Model for Abnormal Grain Growth

Different to normal grain growth, it is usually difficult for AGG to predict the overall evolution of the microstructure, since the GDF and the growth kinetics of the associated average grain sizes are driven by anisotropic parameters that are usually not known for a particular grain boundary. Thus, the assessment of AGG kinetics on the scale of the entire sample — which is obviously the level of XRD investigations — and not only on the level of individual grains, requires to establish a suitable numerical model, which covers the basic aspects of the abnormal growth process — however, it should be recognized that such a model does not necessarily consider the physical reason for the existence of anisotropic kinetics, especially if the model is derived from empirical observations on the growth kinetics only. To investigate the obviously abnormal growth in the examined nanocrystalline Fe, an empirical two-population model has been developed and will be introduced in this paragraph.

The two populations of grains in this model are assigned to the species of matrix and abnormal grains, respectively. To treat the two species separately — in view of both, the size distribution and the number of grains — each one is represented by its own GDF, $f_{\mathrm{m}}(D)$ and $f_{\mathrm{a}}(D)$ (the indices "m" and "a" denote the affiliation to matrix and abnormal grains, respectively). Inspection of Fig. 3.7 shows that the GDF of an annealed nanocrystalline Fe sample is well approximated by the lognormal function of Eq. (3.12). It might therefore be decent to assume a lognormal distribution of grain sizes to represent $f_{\mathrm{m}}(D)$ and $f_{\mathrm{a}}(D)$ in the numerical model below — although, it is evident that AGG does in principal not allow to draw inferences from a measured GDF on the shape of the GDF at an earlier or later point in time of AGG. In spite of this possible uncertainty it might be anyway reasonable to assume a lognormal function for f_{a} and f_{m}, if the independent behavior of the matrix and the abnormal species is comparable to quasi-normal growth within the respective subpopulation, for which a lognormal function similar to the normal growth of coarse-grained Fe could be a viable approximation [8].

If the GDF for the matrix and the abnormal grains are defined in line with Eq. (3.12), the frequency will be normalized to satisfy $\int_0^\infty f_{\mathrm{m,a}}(D)\,\mathrm{d}D = 1$. However, since the model treats the microstructure as an aggregate of grains of integer number, $f_{\mathrm{m}}(D)$ and $f_{\mathrm{a}}(D)$ need to be multiplied by the number of grains N_{m} and N_{a}, which actually belong to the respective species. The overall GDF $g(D,t)$ of the entire polycrystal is then given by,

$$g(D,t) = N_{\mathrm{m}}(t) \cdot f_{\mathrm{m}}(D) + N_{\mathrm{a}}(t) \cdot f_{\mathrm{a}}(D). \tag{5.1}$$

The numerical model assumes that the size distributions f_{m} and f_{a} are virtually fixed with respect to D_0 and σ, and only the absolute number of grains $N_{\mathrm{m}}(t)$ and $N_{\mathrm{a}}(t)$ remains as a time-dependent parameter. This means that the two distributions will not move along the grain-size axis and are both by definition of self-similar nature.

During AGG the abnormal grains are growing rapidly at the expense of surrounding matrix grains. It is therefore assumed in the model that the number $N_{\mathrm{m}}(t)$ of matrix grains continuously shrinks, while the number $N_{\mathrm{a}}(t)$ of grains of the abnormal species increases. The process of AGG is therefore responsible for a continuous transfer of volume from the shrinking to the growing grain population — accordingly, the volume fraction of abnormal grains $x_{\mathrm{V}} = V_{\mathrm{a}}/V$ will steadily increase from approximately zero in the initial state to unity at the end of a transient AGG ($0 \lesssim x_{\mathrm{V}}(t) \leqslant 1$). At the same time the matrix volume reduces continuously throughout AGG and may even disappear completely at the end. Accordingly, the time-dependent volume that is occupied by each species is given by,

$$V_{\mathrm{m,a}}(t) = N_{\mathrm{m,a}}(t) \cdot \int_0^\infty \left[k \cdot D^3\right] \cdot f_{\mathrm{m,a}}(D)\,\mathrm{d}D, \tag{5.2}$$

where k is a geometrical to account for the actual shape of the grains. Since the integral in Eq. (5.2) is independent of time, the increase of V_{a} and the decrease of V_{m} is solely induced by $N_{\mathrm{a}}(t)$ and $N_{\mathrm{m}}(t)$, respectively, and thus the growth of $x_{\mathrm{V}}(t)$ is driven by the increase of the number ratio $N_{\mathrm{a}}(t)/N_{\mathrm{m}}(t)$ with time. The proposed model evaluates the overall GDF of Eq. (5.1) and calculates by numerical integration the three quantities $\langle L\rangle_{\mathrm{area}}$, $\langle L\rangle_{\mathrm{vol}}$ and x_V (using the statistical definitions of Eqs. (3.15) and (3.16), and the conversion rules of Eqs. (3.26) and (3.27) to obtain the grain-size averages in terms of L).

The viability of the proposed model will exemplarily be tested on the grain-size data of the isothermal anneal at 452°C (batch X1, see Fig. 4.13). In a first step, the parameters D_0 and σ of the two distributions f_{m} and f_{a} need to be determined. Inspection of the grain-size ratio shows that $\langle L\rangle_{\mathrm{vol}}$ / $\langle L\rangle_{\mathrm{area}}$ increases from an initial value of ~1.3 to approximately 2.0 at the most inhomogeneous state of the microstructure. On a longer time scale the grain-size ratio reduces again monotonously to a level of ~1.65 at the end of the anneal. A review of annealing experiments by H. Hu on coarse-grained Fe reveals that normal — i.e. self-similar — grain growth occurred at a value of $\langle L\rangle_{\mathrm{vol}}$ / $\langle L\rangle_{\mathrm{area}} \approx 1.25$, which is apparently the same as the initial conditions of the microstructure of the examined nanocrystalline Fe [8, 80]. This basically shows that the starting point of the isothermal anneals is likely to be homogeneous (characterized by a rather compact GDF), and does therefore not necessarily induce AGG by size-dominant grains. Thus, it seems feasible to estimate the parameters of the matrix distribution f_{m} from the isothermal data at the very beginning of the anneal, when no grains have undergone abnormal growth yet. The evaluation of the grain-size data yields then the parameters $\sigma_{\mathrm{m}} = 1.55$ and $D_{0,\mathrm{m}} = 30.5$ nm.[1]

[1] The parameters σ and D_0 of the assumed lognormal distribution can be calculated from the measured grain-size data via [88]:

$\langle L\rangle_{\mathrm{area}} = \frac{2}{3} D_0 \exp\left\{\frac{5}{2} (\ln\sigma)^2\right\}$ and $\langle L\rangle_{\mathrm{vol}} = \frac{3}{4} D_0 \exp\left\{\frac{7}{2} (\ln\sigma)^2\right\}$

The assessment of the parameters for f_a is obviously more difficult, since the microstructure is composed of both the matrix and the abnormal grains during AGG. However, if AGG is understood as a transient process, the final microstructure will contain only abnormal grains, or will at least be dominated by a substantial volume fraction of the abnormal species. Figs. 4.16 and 4.17 reveal that a fully completed transient process is rather the exception (this is indicated by a still measurable slope of $\langle L\rangle_{vol} / \langle L\rangle_{vol}$ at the end of the anneal). Although the anneal at 452°C appears not to have reached the final steady-state configuration, the slope of the curve in Fig. 4.13 is already quite shallow after 40 h. It should therefore be a reasonable estimate of minor uncertainty to deduce the parameters of the abnormal distribution f_a from the isothermal data at the end of the anneal, which yields $\sigma_a = 1.88$ and $D_{0,a} = 40.2$ nm. Fig. 5.1 shows the two normalized GDF for the matrix and the abnormal population, respectively.

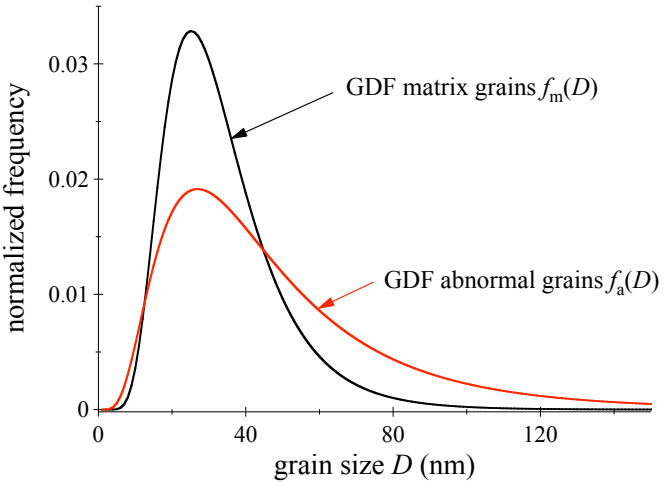

Figure 5.1: The graph shows for the isothermal anneal at 452°C the two normalized lognormal grain-size distributions f_m and f_a for the matrix and the abnormal species of grains, respectively. The superposition of the two GDF (weighted by the actual number N_m and N_a of grains) defines the overall grain-size distribution according to Eq. (5.1), which will in the following be evaluated by numerical integration.

Using numerical integration of the cumulative GDF $g(D, N_a/N_m)$ defined by Eq. (5.1), the quantities $\langle L\rangle_{area}$, $\langle L\rangle_{vol}$ and x_V can be calculated for every given ratio N_a/N_m. The numerical data of the two average grain sizes $\langle L\rangle_{area}$ and $\langle L\rangle_{vol}$ is plotted in Fig. 5.2 as a function of both the abnormal volume fraction x_V and the number ratio N_a/N_m. In addition to the numerical grain-size data, the graph of Fig. 5.2 illustrates the characteristic quantity $\langle L\rangle_{vol} / \langle L\rangle_{area}$, which acts also for the numerical model as an indicator of non-self-similar evolution of the GDF.

Indeed, it is found from the model that for a monotonous increase of N_a/N_m the same broadening and narrowing of the grain-size distribution occurs, as it was detected by XRD during isothermal annealing. The "microstructure" of the numerical model attains the state of the broadest GDF, when the volume fraction x_V reaches approximately 60%, i.e. if approximately half of the volume belongs to the growing abnormal grains. However, the position of the broadest GDF does obviously not correlate with any inflection point of $\langle L\rangle_{area}$, if plotted as a function of x_V. Since the coincidence of the peak in the

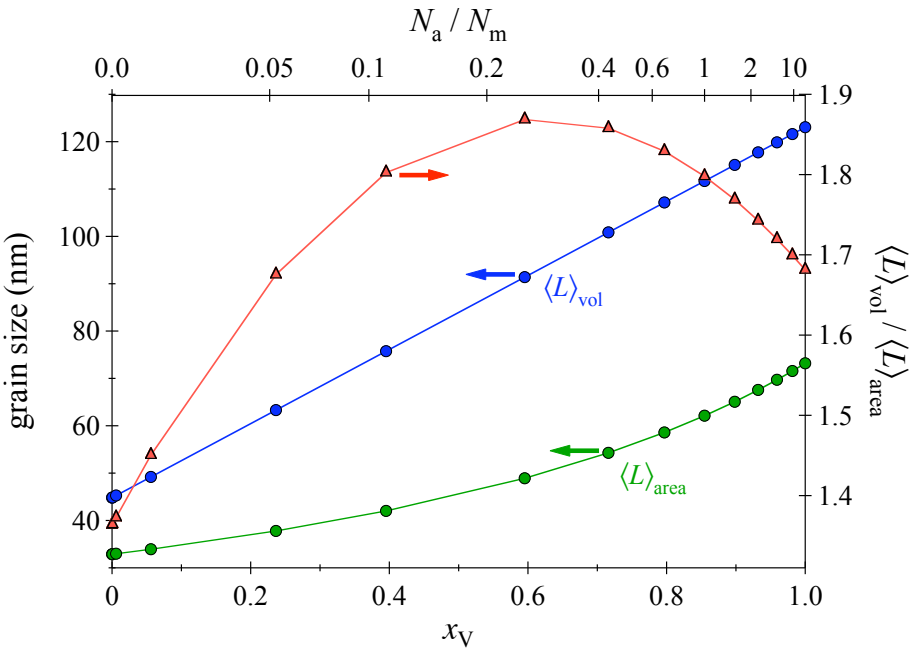

Figure 5.2: Grain-size data of $\langle L \rangle_{vol}$ and $\langle L \rangle_{area}$ and the respective ratio $\langle L \rangle_{vol}$ / $\langle L \rangle_{area}$ for abnormal grain growth, calculated by numerical integration of the bimodal GDF $g(D) = (N_a \cdot f_a + N_m \cdot f_m)$, where f_a and f_m have been defined according to the measured grain-size distribution of the 452°C anneal, see Fig. 5.1. The volume fraction of abnormal grains $x_V = V_a / V_m$ was determined according to Eq. (5.2) by the evaluation of the independent abnormal and the matrix distributions.

$\langle L \rangle_{vol}$ / $\langle L \rangle_{area}$ plot with a clearly visible inflection point of $\langle L \rangle_{area}$ is a characteristic feature of all anneals on nanocrystalline Fe, the plot in Fig. 5.2 already indicates that — provided the assumed two-population model is an adequate description of the actual microstructure — in the annealing experiment $x_V(t)$ cannot possess a linear relationship on time (what is implicitly assumed by the linear x_V-axis of the graph in Fig. 5.2). This dissimilarity of the model and the experiment implies that a comparison of both will only be possible, if they are plotted on the same time axis — i.e. a correlation between x_V and the annealing time t has to be established. An adequate empirical function $x_V(t)$ can be obtained, if the apparently linear characteristic of $\langle L \rangle_{vol}\,(x_V)$ is employed (see Fig. 5.2). While the experimental grain-growth data provides the correlation between $\langle L \rangle_{vol}$ and t, the numerical grain size of the model relates $\langle L \rangle_{vol}$ and x_V. A direct comparison of both curves will therefore provide the sought correlation $x_V(t)$ (at least for the discrete data points of the experiment, if no numerical fit of the grain-size data is used).

A plot of the discrete correlation function $x_V(t)$ is shown in Fig. 5.3. It is found that the volume fraction of abnormal grains increases continuously from zero to unity as the number ratio N_a/N_m becomes larger (*cf.* Fig. 5.2).[2] Further it can be seen that the position $x_V \approx 0.6$ of the broadest GDF correlates with the maximum abnormal growth rate $\mathrm{d}x_V/\mathrm{d}t$. This observation is consistent with the fact that for a constant

[2] In the numerical two-population model the final value of the abnormal-volume fraction will by definition be $x_V = 1$, since the model assumes $N_a/N_m \to \infty$ in the long-time view.

migration rate of abnormal grain boundaries, the fastest growth of x_V occurs approximately when on average half of the matrix has been annihilated, since then there will be a substantial number of abnormal grains that can grow into a still significant matrix volume.[3] At this point f_a starts to control $g(D,t)$ and the centroid of the overall GDF will gradually shift to larger grain sizes (the moment when the control over $g(D,t)$ changes from f_m to f_a indicates the most bimodal state of the system, before the matrix population becomes finally annihilated by AGG and $g(D,t)$ approaches f_a), which means that also $\langle L\rangle_{area}$ will then experience the fastest increase that reflects in the appearance of an inflection point in the $\langle L\rangle_{area}(t)$ data.

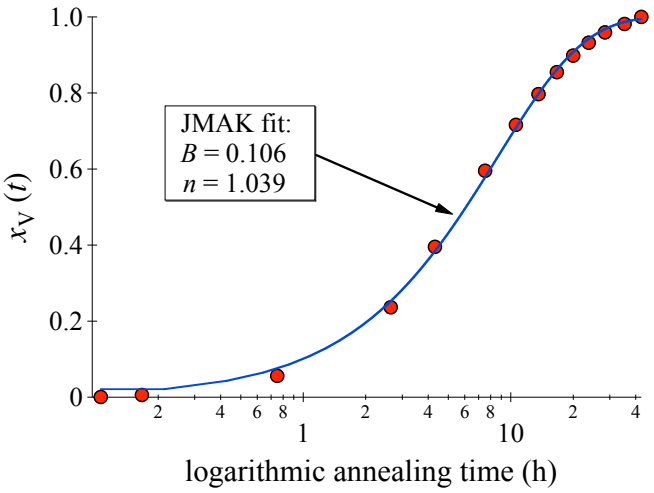

Figure 5.3: The graph shows for the data in Fig. 5.2 the temporal evolution of the abnormal volume fraction as a function of annealing time. The apparent similarity of the sigmoidal data with the JMAK model motivated for a fit of $x_V(t)$ with Eq. (5.3). The JMAK parameters of the least-square fit are included in the box.

The evaluated sigmoidal characteristic of $x_V(t)$ during AGG reveals a striking similarity to another process with comparable kinetics: The recrystallization (ReX) of a material with high dislocation density. This similarity is the reason why in literature AGG is occasionally called "secondary recrystallization" (SRX) [146]. Although the two processes are fundamentally different with respect to their formation and driving forces, the result of a fast growing volume fraction — either as large recrystallized grains, or as fast-grown abnormal grains — is fairly similar.

A frequently used description of recrystallization kinetics (including both the nucleation and growth of recrystallizing domains) was proposed by Johnson and Mehl, Avrami and Kolmogorov, and is known as the "JMAK" model [146]. For the kinetics of the volume fraction of recrystallized material, the JMAK model predicts the following relationship of sigmoidal shape [146],

$$x_{V,\mathrm{ReX}}(t,T) = 1 - \exp\{-B \cdot t^n\}, \tag{5.3}$$

[3] Prior to this point the number of abnormal grains will be small, while afterwards only a few matrix grains are remaining — both constraints will result in a lower volume increase $\mathrm{d}x_V/\mathrm{d}t$ of the abnormal grains.

where the parameters n and $B(T)$ denote a time exponent and a temperature-dependent rate constant, respectively. The solid line in Fig. 5.3 represents a least-squre fit of Eq. (5.3) to the empirical $x_V(t)$ data, yielding $n = 1.039$ and $B = 0.106$.

Obviously, the JMAK approach for recrystallization shows a strong agreement with the data of the AGG model. It should therefore be clarified whether the observed inhomogeneous evolution of nanocrystalline Fe is a fingerprint of ReX, or if the compliance is a misleading artifact that is generated by the degrees of freedom related to the two independent parameters in Eq. (5.3).

If ReX is controlled by both the constant nucleation of new grains and the isotropic growth of the nuclei, the standard JMAK model predicts a time exponent $n = 4$, which would obviously not agree with the value of $n \approx 1.0$ found in Fig. 5.3. In some recent modifications of the JMAK model however, a quickly declining nucleation rate was assumed (this assumption is of course in better agreement with AGG than an on-going nucleation of additional recrystallizing grains), which yielded a parameter n that is equal to the dimension of the growth process — i.e. $n = 1$, if recrystallization is extremely anisotropic and occurs only in one spatial direction [146]. This would obviously agree with the observation of anisotropic finger-like grains in AGG. Since OIM revealed quite different growth modi in nanocrystalline Fe, where beside finger-like structures also equiaxed grains have been observed, the determined value of n would be likely found between $n = 1$ (finger-like) and $n = 3$ (equiaxed) — depending on the actual fraction of anisotropic versus isotropic growth.

To assess the likeliness of ReX it should be considered that this process depends basically on both the ability of nucleation and the migration rate of the nuclei boundaries. Since the nucleation of recrystallizing domains is a statistical event, it is difficult to assess this process quantitatively. Thus, the assessment of ReX focuses on the boundary migration of the nuclei walls. The driving force for the migration of a nucleus boundary is the excess enthalpy G_D, which is connected to the presence of a excess-dislocation density ϱ around the nucleus. During ReX the nucleus will grow due to the enthalpy release of dislocation annihilation, whereas at the same time the excess energy of the nucleus surface $\gamma^{ReX} \cdot A^{ReX}$ increase (γ^{ReX} specifies in analogy to the grain-boundary energy the specific energy of the interface between the recrystallized and the unrecrystallized volume, and A^{ReX} is the surface of the nucleus). The two effects are basically opposing, where the first one provides the condition for the nucleus to grow, whereas the latter one intends to shrink the surface of the nucleus, similar to the principles of grain growth.

For a quantitative evaluation of the growth of a recrystallizing nucleus it might be helpful to adapt the perception of AGG as illustrated in Fig. 3.20: A grain or a nucleus of low dislocation density (and therefore lower excess enthalpy than the surrounding volume) is growing into the bordering area that still contains the initial dislocation density [146]. Since the surface-to-volume ration of a grain scales inversely with the grain size, particularly small grains need a considerable excess energy G_D around them to compensate the increasing surface excess and thus, to enable ReX.

Assuming that a spherical nucleus grows from a size D_0 to a size $D_0 + dD$, the grain-boundary enthalpy increases according to,

$$dG^{GB} \approx 2\pi \cdot D_0 \cdot dD \cdot \gamma^{ReX}. \tag{5.4}$$

At the same time the growing grain expelled the dislocations in the recrystallized area, which corresponds to a release of excess enthalpy of,

$$\mathrm{d}G^{\mathrm{ReX}} \approx -\frac{\pi}{2} \cdot D_0^2 \cdot \mathrm{d}D \cdot G_{\mathrm{D}}. \tag{5.5}$$

The criterion to allow for recrystallization is then given by $\mathrm{d}G^{\mathrm{GB}} + \mathrm{d}G^{\mathrm{ReX}} < 0$, which defines for a material with an excess enthalpy G_{D} a critical grain size D_{X} for a nucleus of [147],

$$D_{\mathrm{X}} \approx \frac{4 \cdot \gamma^{\mathrm{ReX}}}{G_{\mathrm{D}}}. \tag{5.6}$$

Eq. (5.6) can be tested if for γ^{ReX} a typical value for α-Fe of $0.8\,\mathrm{J/m^2}$ is assumed and the dislocation enthalpy is estimated from the low-temperature DSC peak as 60 J/mol (recall, this peak has been assigned to the relaxation of microstrain due to annihilation of residual dislocations). Taking those two parameters into account, Eq. (5.6) yields for the critical grain size a value of $D_{\mathrm{X}} \approx 380$ nm, which is obviously larger than any grain sizes reached throughout the annealing experiments on nanocrystalline Fe. This implies that ReX is unlikely to occur for the presumed conditions.

TEM investigations of the as-prepared state show that the samples already formed a well-defined polycrystalline microstructure right after sample preparation. This involves however that a recrystallizing grain does not only annihilate dislocations, but would also assimilate the surrounding grains (matrix grains). In this grain-assimiliation process, the before existing grain boundaries between matrix grains would of course also be removed, which provides an additional release of enthalpy. The enthalpy of grain-boundary excess (due to matrix grain boundaries), which is released when the recrystallizing grain grows from D_0 to $D_0 + \mathrm{d}D$ can be estimated for spherical grains by,

$$\mathrm{d}G^{\mathrm{m}} \approx -\frac{3}{2} \cdot \gamma^{\mathrm{m}} \cdot \frac{\pi \cdot D_0^2 \cdot \mathrm{d}D}{\langle d \rangle}, \tag{5.7}$$

where γ^{m} is the grain-boundary energy of matrix-matrix interfaces, and $\langle d \rangle$ denotes the mean size of the matrix grains (i.e. $\langle d \rangle^{-1}$ is proportional to the volume density of matrix grain boundaries). With this additional enthalpy term the criterion for ReX extends to $\mathrm{d}G^{\mathrm{GB}} + \mathrm{d}G^{\mathrm{ReX}} + \mathrm{d}G^{\mathrm{m}} < 0$, and the critical nucleus size is now,

$$D_{\mathrm{X}} \approx \frac{4 \cdot \gamma^{\mathrm{ReX}}}{G_{\mathrm{D}} + 3 \cdot \gamma^{\mathrm{m}} / \langle d \rangle}. \tag{5.8}$$

Experiments on ReX revealed that growing nuclei are usually sharing high-angle boundaries with their neighbors, which allow for a high recrystallization kinetics [146]. It is should therefore be reasonable to use for the nucleus boundaries typical high-angle values like $\gamma^{\mathrm{ReX}} \approx 0.8\,\mathrm{J/m^2}$ (as for Eq. (5.6) before). Since the grain-boundary energy of low-angle boundaries is strongly dependent on the actual misorientation and therefore not easily known, it is assumed that γ^{m} is about 50% of a high-angle boundary, i.e. $\gamma^{\mathrm{m}} \approx 0.4\,\mathrm{J/m^2}$ (the reason to assume low-angle boundaries for the matrix bases on the recovery of the deformed state,

as will be discussed shortly). If the average size of the matrix is assumed as the value of $\langle L \rangle_{\text{area}}$ in the as-prepared state (~20 nm), the critical nucleus size reduces to only 46 nm. As the as-prepared GDF is rather narrow (see Fig. 5.8), there is only little reason to expect a notable number of grains to meet the critical nucleus size, i.e. ReX is not expected to play a major role.

Beside this thermodynamic consideration, there are already two other "empirical" aspects, which do not lend credence to ReX. First, the annihilated dislocation density of $\varrho \approx 2.5 \times 10^{15}$ m^{-2} allows at a mean grain size of 20 nm only one dislocation per grain and second, DSC revealed that dislocation annihilation occurs easily to an extensive degree at temperatures $T \lesssim 400$°C, which erases the driving force for ReX on the long-time view. Although it might be possible to find ReX during the fast growth of the grain size at the very early stage of annealing, ReX cannot be the reason for the sustained AGG that is observed in nanocrystalline Fe. This conclusion involves that the apparent similarity between $x_V(t)$ in Fig. 5.3 and the JMAK model is obviously a misleading observation.

With the correlation function $x_V(t)$ of Fig. 5.3, the numerical results presented in Fig. 5.2 can now be plotted on the same time axis as the experimental data. The graph of Fig. 5.4 shows the direct comparison of the numerical model and the isothermal anneal (note that the correlation between x_V and t has been derived from $\langle L \rangle_{\text{vol}}$, the agreement between model and experiment has therefore to be evaluated on

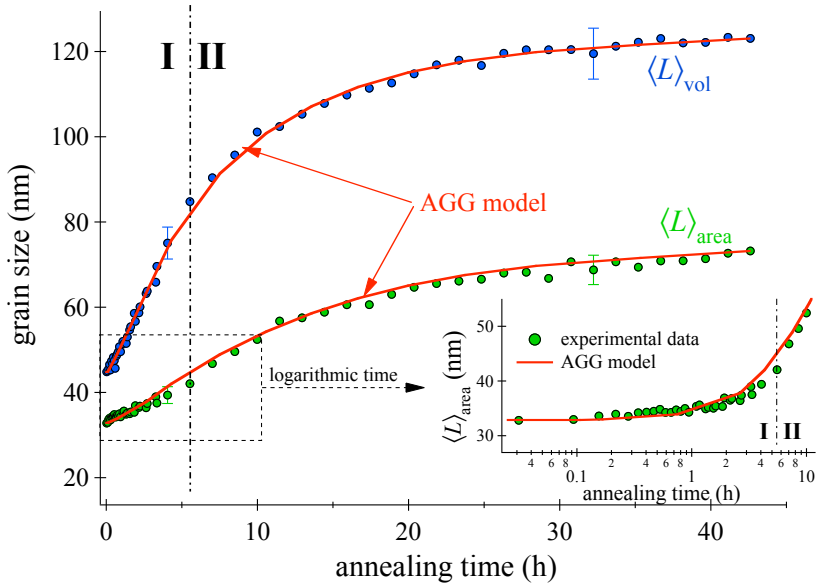

Figure 5.4: Comparison of the experimental data and the numerical grain sizes of Fig. 5.2 that were calculated from the numerical two-population model. For the conversion between the x_V axis of Fig. 5.2 and the actual annealing time, the correlation $x_V(t)$ of Fig. 5.3 is used. The inset shows for the first 10 h the comparison of numerical and measured data for $\langle L \rangle_{\text{area}}$ on an enlarged logarithmic time axis. Both plots in the graph reveal for the complete experiment an excellent agreement between the numerical data of the model and the isothermal anneal.

$\langle L\rangle_{\mathrm{area}}$). For the sake of a better inspection, the inset of Fig. 5.4 presents in detail the evolution of $\langle L\rangle_{\mathrm{area}}$ within the first 10 h of annealing. Inspection of the measured and the calculated values of $\langle L\rangle_{\mathrm{area}}$ reveals over the full annealing time an excellent agreement, which is reflected in:

1.) A quasi-linear growth of $\langle L\rangle_{\mathrm{area}}$ within range I (see inset of Fig. 5.4).

2.) The increase of the growth kinetics at the end of range I.

3.) The transition of an inflection point at the border between range I and II.

4.) A power-law growth with $m > 2$ until coarsening stagnates.

It is the essence of this analysis to show that the suggested numerical model can explain basically all "curious" features that were found to be characteristic for the isothermal coarsening of nanocrystalline Fe in terms of an inhomogeneous AGG and the associated continuous increase of the abnormal-volume fraction. It can be concluded that particularly the successive broadening and narrowing of the GDF and the apparent acceleration of the growth kinetics at the end of range I are not driven by a modified grain-boundary kinetics or a change of the rate-controling process, but are an inherent feature of a dedicated abnormal evolution of the microstructure. The model also reveals that the long-term growth is not related to a conventional curvature-driven power law, and the coarsening kinetics — particularly the asymptotic stagnation of growth — is determined by the gradual approach of $x_{\mathrm{V}}(t) \rightarrow 1$.

In view of those conclusions it is reasonable that $\langle L\rangle_{\mathrm{vol}}$ and $\langle L\rangle_{\mathrm{area}}$ reveal a dissimilar behavior on time. According to Eqs. (3.22) and (3.23) both weighted average have a different sensitivity on the size and the number of the largest grains of the GDF. From the definition of the two weighted averages it is evident that particularly $\langle L\rangle_{\mathrm{vol}}$ is likely to increase instantaneously upon a growth of x_{V}, even if x_{V} is still at a low level. The delayed response of $\langle L\rangle_{\mathrm{area}}$ on an increase of x_{V} is caused by the less pronounced sensitivity of the area-weighted average on large grains. This explains why $\langle L\rangle_{\mathrm{area}}$ does not react immediately on a minor increase of N_{a}. Only if a sufficient number of abnormal grains populates f_{a} and the centroid of the overall GDF gradually moves towards the abnormal grain population, $\langle L\rangle_{\mathrm{area}}$ will start to increase and an upward curvature in the grain-size/time plot should be found. Since the inflection point of $\langle L\rangle_{\mathrm{area}}$ coincides with the broadest state of $g(D,t)$ (beyond which the distribution width decreases again), it is obvious that the increase of the $\langle L\rangle_{\mathrm{area}}$ "growth rate" — and also the return of the GDF to a more homogeneous assembly — must be driven by the annihilation of f_{m}.

A similar case of AGG within a bimodal GDF has been analyzed by Lücke *et al.* [148] via computer simulation. Starting from two lognormal distributions f_{m} and f_{a} (x_{V} is only 0.1% in the starting configuration), the distribution of small grains (f_{m}) is completely annihilated by the artificially seeded abnormal grains. The mean grain size of the ensemble revealed the same basic characteristics as the numerical model and the experimental data have shown above: Initially, the mean grain size is determined by f_{m} and possesses a shallow slope, whereas at later times f_{a} dominates the microstructure and an upward slope in the grain-size/time plot is found (growth exponent $m < 1$). Although the initial microstructure was insignificantly different from a configuration of only having f_{m} (in which case normal grain growth was found in the simulation), the very small volume fraction x_{V} was sufficient to initiate dominant AGG [148].

The excellent agreement of the proposed phenomenological model with the experiment is an important step to understand the curious coarsening kinetics of nanocrystalline Fe. Although the AGG model

substantiates an abnormal evolution of the microstructure, it does not tell the reason for that and does not clarify the conditions, which will motivate a grain to grow either abnormally or to stay in the matrix. At this point only ReX and TL/QP drag have been been closely discussed and it was found for both that they are unlikely the responsible effect. It is therefore needed to survey other possibilities, which might trigger AGG in the examined nanocrystalline samples.

5.4 Analysis of the Root Cause for Abnormal Grain Growth in Nanocrystalline α-Fe

The empirical model in the previous section revealed that the inhomogeneous growth of the examined nanocrystalline samples is obviously driven by the dissimilar behavior of two defined species of grains: The matrix grains, which are merely static, and the abnormal grains, which are growing and gradually annihilating the matrix. As a consequence of that, the microstructure undergoes an inhomogeneous evolution, which would not be expected if normal grain growth would be the actual growth mode. Since normal grain growth is expected only, if in a sample with a stable GDF the grain-boundary properties are uniform and a size scaling of the driving force applies, it is evident that at least one of the preconditions must be violated. Since the thermodynamic driving force for boundary migration is not expected to vary significantly in the examined samples (except for the inherent curvature depedence) — that is because for the examined samples the most likely inhomogeneous impact on γ^{GB} is given either from the segregation of solute atoms to the grain interfaces and a thermodynamic lowering of the grain-boundary energy (*cf.* Section 2.6), which does not seem plausible for the decidedly low impurity concentrations, or would come from a distinct misorientation distribution of low-angle boundaries, which however would explain a grain-boundary-specific γ^{GB}, but obviously not a fully disabled growth of matrix grains — it seems likely that either the uniform-boundary criterion (with respect to the grain-boundary kinetics/mobility) or the stability of the GDF is a too strict constraint to allow a uniform coarsening of the material.

A review of literature shows that there are several possibilities, which can affect the boundary characteristic and may provoke an anisotropy in terms of grain-boundary kinetics. As will be addressed below, the induced anisotropy can be a concomitant effect to the type of sample-preparation process, or can be an inherent feature of the microstructure itself.

Anisotropy related to the synthesis of poly- or nanocrystalline materials can be:

- the presence of impurity atoms or second-phase particles, which may enable solute drag [149] or Zener pinning [150–152],
- an inhomogeneous grain-size distribution of the refined microstructure with exceptionally large grains, either in the as-prepared microstructure or after recrystallization and recovery, which will then dominate grain growth during annealing [148],
- or a residual excess enthalpy (e.g. due to dislocations), which can give rise to discontinuous recrystallization (e.g. in cold-worked materials of low dislocation mobility) [24, 146, 147].

On the other hand, there is of course also the possibility that the anisotropy is an inherent property of the

microstructure, which could relate to:

- the size-dependent rescaling of the grain-boundary mobility, if TL or QP exert a drag force on the grain boundary during migration [61,153] or,
- the misorientation dependence of the grain-boundary energy $\gamma^{\mathrm{GB}}(\theta)$ and mobility $M^{\mathrm{GB}}(\theta)$, which could be the case, if the involved grain boundaries have a misorientation within the LAB regime, see Section 2.2 [24,28,31,154–156].

Particularly the last point is likely to be a permanent property of every polycrystalline microstructure, since an arbitrary spatial assembly of individual grains must involve that there is a distribution of different grain-boundary misorientations (unless, there is a significant alignment of the grains, i.e. the microstructure is designated by a distinct texture).

5.4.1 Assessment of the Potential Candidates for Anisotropic Boundary Properties

The previous section showed that there is obviously a considerable number of possible effects that are able to create a distribution of grain-boundary kinetics within the specimen. The origin of those non-uniform properties can be quite diverse and may relate to sample processing or, independent of that, to the inherent features of the material or the microstructure. A thorough review of the experimental investigations and the chemical analysis allows already at this point to disprove the likeliness of several reasons for non-uniform boundary characteristics, which reduces the number of potential candidates.

- Inspection of TEM investigation in DF and diffraction mode, and the analysis of XRD spectra disproves the presence of both second-phase particles and exceptionally large (unstable) grains in the initial state of the nanocrystalline microstructure.
- The possibility of long-term recrystallization was examined during the assessment of the abnormal growth kinetics $x_{\mathrm{V}}(t)$. It was found that the prerequisite of a sustaining dislocation density for recrystallization is obviously not maintained by the investigated Fe samples.
- Also the likeliness of TL and QP drag has been discussed before and was discarded as not appropriate to explain the observed abnormal evolution of the microstructure.

With those rationales the survey of the responsible effect that is driving AGG can be concentrated on the remaining two candidates:

- the impurity concentration of Si (with respect to non-uniform solute drag),
- and the inherent misorientation dependence of grain-boundary properties (mainly the grain-boundary mobility $M^{\mathrm{GB}}(\theta)$ of Eq. (2.13)).

It has been discussed in Section 4.1.2 that due to the low Si concentration the average grain-boundary coverage with Si atoms can only be small, and a significant impeding effect on grain growth was not expected if the impurity atoms are homogeneously distributed. However, in the light of AGG it might be asked: What would happen, if the Si is not homogeneously distributed, but is concentrated in a few areas of excessive Si concentration. Of course, in such a case it is conceivable that two types of grain

boundaries will exist: Either solute-free interfaces, which maintain the intrinsic migration kinetics, or grain boundaries that are immobilized by solute drag. During temperature-induced coarsening, grains with solute-impeded boundaries will stay in the initial configuration (like matrix grains), whereas the unaffected grains are growing on their regular kinetics. However, for the overall low Si concentration it is rather unlikely that a major fraction of grain boundaries can be pinned, while only a small fraction of grains would remain mobile — but exactly this would be required to allow for AGG that is induced by selective growth. Instead, it seems that only a small fraction of the microstructure could be severely affected by solute drag (provided that the impurity atoms are actually concentrated at some grain boundaries), which would permit a widely normal coarsening of the microstructure and the inclusion of a few inhibited small grains.

Since also solute drag seems not plausible to be the root cause for the AGG in the specimens of nanocrystalline Fe, only the inherent misorientation dependence of the grain-boundary energy $\gamma^{\mathrm{GB}}(\Theta)$ and mobility $M^{\mathrm{GB}}(\Theta)$ is remaining out of the possible candidates to account for the inhomogeneous coarsening. A review of Section 2.2 shows that a misorientation-dependent behavior of the grain-boundary properties is a characteristic of the low-angle regime, whereas for high-angle boundaries a misorientation-independent value of $\gamma^{\mathrm{GB}}(\Theta)$ and $M^{\mathrm{GB}}(\Theta)$ should be expected. This of course states that, if AGG is indeed driven by the influence of misorientation, the microstructure of the nanocrystalline material must be dominated by low-angle boundaries (LAB). Since LAB are usually not common in coarse-grained polycrystalline materials, it will be necessary to examine the mechanisms leading to grain refinement during mechanical attrition, since the newly created boundaries during refinement are likely to be the ones that are involved in the experimentally found AGG.

5.4.2 Processes Related to the Refinement of the Microstructure

The kinetic energy in ball milling that is transferred during a ball/particle collision is largely converted into heat (e.g. by elastic deformation and friction), and only a minor fraction causes a plastic deformation of the sample. This plastic deformation of the material however involves the creation of additional lattice defects, mainly in the form of extended lattice dislocations. The generated excess density of lattice defects contributes then to the overall free energy of the system (*cf.* Eq. (2.1)) [157]. For practical purpose the excess density of point defects is presumably negligible, since already moderate temperatures are sufficient to support an efficient relaxation of the excess back to the equilibrium density [157, 158]. It should therefore be justified to concentrate on the excess-energy contribution of deformation-generated dislocations, which allows to estimate the excess-energy density stored in the strained lattice by Eq. (3.69).

Of course, the additional dislocation energy will have the same effect as the grain-boundary excess and pushes the microstructure further away from the state of thermodynamic equilibrium. While for the grain boundaries the coarsening of the microstructure reduces the free energy of the polycrystal, the relaxation of dislocation-induced excess energy occurs usually via dislocation recovery or recrystallization (ReX). However, since both processes are obviously impelled by the same excess-energy reservoir, it is likely that only one of the two processes — namely the faster one — will prevail. To elaborate whether recovery or ReX will be dominating the microstructure of the investigated nanocrystalline Fe, the prerequisites for both processes have to be evaluated in the context of the experimental findings.

5.4.2.1 Recrystallization of the As-Prepared Microstructure

Although ReX was not deemed before to be the reason for the long-term AGG, this conclusion does not necessarily hold for a possibly short transient reorganization of the as-prepared sample. The calorimetric DSC analyses (Fig. 4.22) and the evolution of microstrain in the DSC reference samples (Fig. 4.25) reveal that the reorganization of the initial state is apparently accompanied by a strong relaxation of dislocation excess at temperatures below ~400°C. Simultaneously to the annihilation of dislocations (and the decrease of microstrain), the grain size increases from initially $\langle L \rangle_{\text{area}} = 18$ nm to approximately 30 nm at the end of the low-temperature DSC peak (see Fig. 4.25). Similar to the substantial growth of the grain size within the reference analysis of DSC, it was found that basically all isothermal anneals are characterized by an equally fast increase of the grain size during the first few minutes of annealing. During this period the grain size almost "jumps" to a value of 30 . . . 35 nm, which is quite surprising, since the growth stops quite suddenly at the end of this short-lead rapid increase. The observation of rapid coarsening with an abrupt termination that is obviously accompanied by the annihilation of dislocations and the relaxation of excess energy draws the attention of course to a process like temporary ReX.

It is the current state of understanding that low-energy domains (nuclei), as for example dislocation cells or subgrains, are the starting centers for ReX [146]. The assessment of the critical nucleus size (*cf.* Eq. (5.8)) yielded that for the annihilated dislocation energy of the low-temperature DSC peak, nuclei larger than ~46 nm are unstable and support ReX. A review of the TEM images of the as-prepared state shows that only a small number of grains could meet this constraint and would therefore be suitable to grow via ReX. Starting from a homogeneous dislocation distribution, the formation of a nucleus with low excess-energy density requires the local clean-up of dislocations via recovery (e.g. by rearrangement into dislocation arrays or by annihilation), which can occur either upon dedicated annealing or already during deformation ("dynamic recovery"). This need for recovery has of course a profound consequence for the likeliness of ReX, since it entails that ReX necessitates dislocation recovery, while the reversed causal relationship is not valid and recovery can occur without ReX. This entails that ReX (or better to say the nucleation for ReX) can only emerge, if the dislocations have a sufficient mobility to create low-energy domains, but the mobility must not reach a limit at which extensive recovery occurs.

Although ReX would adequately fit to the DSC characteristics and also to the initial rapid growth during isothermal annealing, there are basically two points that raise doubt on the likeliness of ReX. First of all, on average there is only one dislocation per grain, which is unlikely to let a nucleus grow by ~60% in diameter (this is the increase of the grain size during the initial "jump" of the isothermal experiments). The handicap of this low excess-energy density G_{D} is witnessed by a comparison of the energy release due to dislocation annihilation and the assimilation of matrix grain boundaries, which shows that the latter effect is almost one order of magnitude larger than the relaxation of dislocation excess. This entails that, if the grain boundaries of the nucleus have the required mobility, it would be more likely to find discontinuous growth maintained by the matrix grain-boundary-excess density or a normal curvature-driven growth of high kinetics (due to the large curvature of the small matrix grains), rather than growth impelled by dislocations. The second point, which questions ReX is that a recovery process with slow kinetics is a prerequisite to create the required nuclei (that is in principle the reason, why ReX processes usually show an incubation time at their beginning, which is obviously not observed for the initial rapid growth upon isothermal annealing), but does not exhaust the complete dislocation density before ReX

can establish. As will be discussed in the following paragraph (Section 5.4.2.2), it seems likely for α-Fe that recovery — once activated — will annihilate the dislocation density to a great extent. In this case of course, substantial ReX would be unlikely or even impossible.

5.4.2.2 Dislocation Recovery in the As-Prepared Microstructure

The driving force for a material to undergo dislocation recovery is the excess energy that is connected to the core and the strain field of a dislocation. Since the specific strain energy, which is related to the lattice distortion in the vicinity of a dislocation is not a constant, but will decrease in an atomically disordered environment, it is straight to assume that dislocations will aim for such preferred regions of lower atomic coordination [158]. Thus, the energy contribution of a dislocation to the overall free energy of the polycrystal can be lowered via recovery, if either the dislocation moves to a pre-existing grain boundary and is subsequently annihilated by the grain-boundary excess volume, or the excess-dislocation density undergoes a local self-organization into new low-energy structures. For the latter case the dislocations rearrange in a first step into tangled networks ("cell walls"), which surround and separate defect-free domains ("cells") [122,158,159]. The cell size is thereby dependent on the actual strain during deformation (i.e. the number of available dislocations during recovery), and the cell size will be smaller the larger the strain has been during deformation. A further relaxation of excess energy occurs when the cell walls transform into well-defined low-angle boundaries. Thus, if the dislocation excess is dismantled by the creation of low-angle boundaries (LAB) within a pre-existing grain structure of common high-angle boundaries (HAB), a new substructure of interfaces with LAB properties is established.

The question whether recovery can proceed at a rate that does not allow ReX to occur depends basically on the actual mobility of the dislocations [24]. If the dislocation mobility is low, the dislocation-excess energy is retained in the microstructure and may provide the precondition for ReX. However, if the mobility of dislocations is appropriate, the dislocations will move under the influence of a driving force $\mathbf{F}_\mathrm{D}$ towards a low-energy configuration. The driving force on the dislocation can in principal be exerted by two effects, either the potential energy of the dislocation E_D reduces, if the dislocation migrates in the strain field of the dislocation density and participates in the formation of a cell wall, i.e. $\mathbf{F}_\mathrm{D} = -\nabla E_\mathrm{D}$, or the dislocation is attracted by the "image force" of an existing boundary [68,95]. Particularly the second effect is usually strong in nanocrystalline materials, since the grain size is comparable to (or even smaller than) the range of the strain field, which results in an improved attractive interaction between the dislocation and the interface.

Whether a dislocation possesses the needed mobility for migration or not depends on the actual efficiency of the involved atomic-scale processes for dislocation migration, which are the "gliding" on slip planes (in a direction perpendicular to the dislocation plane) and the "climbing" of the dislocation (parallel to the dislocation plane). While gliding along a slip plane is merely the switching of atomic bonding between adjacent lattice planes, climbing involves the long-range transport of vacancies to the climbing edge of the dislocation. This explains why gliding does usually not require large effort, and is therefore expected to have a rather small thermal activation level. The breaking of atomic bonding during dislocation glide might be compared to the melting of the material, for which the characteristic heat of fusion is approximately 15 kJ/mol in Fe, which confirms a small thermal activation for dislocation gliding. The

constraints for dislocation climb are clearly different, since here the process relies on the availability of vacancies at the edge of the dislocation. Thus, in the limiting case the kinetics of dislocation climb will be controlled by the transport of vacancies, which conveys that solid-state self-diffusion is the key parameter for the ability of dislocation climb [159].

Climbing of dislocations does usually not occur on the entire length of a dislocation at a time, since this requires the availability of a considerable non-equilibrium vacancy concentration in the immediate vicinity of the dislocation edge — obviously, this would be a thermodynamically unfavorable situation and therefore unlikely to be found. Instead, climb occurs stepwise, involving so-called "jogs", which are atomic steps of certain width along the dislocation line and thus, the ease of dislocation climb depends on the jog-formation probability, i.e. on the nucleation frequency of jogs [160].

The most common picture of dislocations is the construct of an additional lattice half-plane that is inserted into the nominal crystal lattice. Considering dislocation climb however it should be borne in mind that those unit dislocations may dissociate into partial dislocations, if the smaller Burgers vector provides a lower excess energy according to Eq. (3.68). If a dislocation dissociates, an extended stacking fault of width $d_{\mathrm{SF}} = G \cdot b^2 / (4\pi \cdot \gamma_{\mathrm{SFE}})$ is formed, where γ_{SFE} denotes the specific stacking-fault energy (G and b are the shear modulus and the Burgers vector, respectively, as defined in Eq. (3.68)) [157,161]. The formation of a stacking fault however involves that the jogs also need to dissociate over the same stacking-fault distance d_{SF} to enable efficient climb. The formation energy of a jog — and thereof inversely related the nucleation probability — is smallest for a unit dislocation and increases with a growing separation d_{SF} of the partials [4,160]. Thus, the probability for the formation of a stacking-fault jog is reduced compared to a unit-dislocation jog, and climb will be difficult in materials, which are prone to the formation of partial dislocations. Considering the impact of stacking-fault energy it should therefore be expected that materials of high SFE are more resistant to dislocation dissociation, and should therefore have a better dislocation mobility than low-SFE materials. Hence, it would be reasonable to assume that high-SFE materials have a higher tendency to create low-energy boundaries via recovery than other materials (which may retain due to restricted dislocation mobility the excess-energy density in the lattice) [157,158].

The SFE of α-Fe has been investigated in computer simulations by R. Watanabe, where a mean SFE of $\gamma_{\mathrm{SFE}}^{\mathrm{Fe}} \gtrsim 160\ \mathrm{mJ/m^2}$ was found [162]. This SFE is considerably higher than typical values for Ag, Au or Cu of 16, 32 and 45 $\mathrm{mJ/m^2}$, respectively [160], and indicates that α-Fe should exhibit the features of a high-SFE material. Extensive recovery in α-Fe is therefore more likely than ReX, and the observation of a well-defined low-angle subgrain structure would be expected [4,159,163].

The TEM investigation of the as-prepared state certifies that immediately after ball milling the microstructure is made up of well-defined grains in the size range 15 ... 20 nm, which are internally structured by residual dislocations. Upon annealing to temperatures $T \lesssim 400^{\circ}\mathrm{C}$ it was found that the remaining dislocations are annihilated expeditiously. This relaxation process upon annealing is witnessed by both the low-temperature heat flow in DSC (peak 1 in Fig. 4.23) and the accompanying rapid relaxation of microstrain (Fig. 4.25). The evaluation of the as-prepared XRD data proves further that the initial microstructure is determined by a homogeneous constitution ($\langle L \rangle_{\mathrm{vol}} / \langle L \rangle_{\mathrm{area}} \approx 1.2 \ldots 1.3$), which suggests that the formation of nanoscaled crystallites should be a generic feature of the material, and not be induced by selective or stochastic events.

The observation of a well-defined nanoscaled microstructure immediately after mechanical processing implies that the refinement of the grain size must be driven by an instantaneous "relaxation process" of excess dislocations during mechanical attrition. It is unlikely that ReX can be this *in-situ* process, since this would involve that the formed crystallites are the result of nucleation and growth, and no dislocations would remain in the recrystallized volume. The fact that α-Fe should be naturally prone to dislocation recovery promotes of course the consideration of "dynamic recovery", i.e. recovery simultaneous to the mechanical processing. The prerequisites for dynamic recovery (besides a high SFE) are apparently met by the samples of the present study, which are a high dislocation density during attrition (witnessed by the small grain size) and a highly pure material that does not cause dislocation pinning by impurity atoms [4]. The uniform grain-size distribution in the dark-field TEM image of the as-prepared state actually supports dynamic recovery to take place, since the dislocation density is approximately the same within the processed volume and thus, recovery is supposed to occur homogeneously all over the sample (yielding a homogeneous grain-size distribution). Although there is no direct data available on the actual misorientation of the newly created subgrains (the finding of a low-angle substructure would be of course a convincing evidence for recovery), the observation of a rather uniform intensity in dark-field TEM and a cumulated intensity within the (110) electron-diffraction ring indicates that the grains should have a preferred orientation (texture), from which it might be inferred that the relative misorientation between grains of this texture component must be small.

The conclusion of substantial recovery in α-Fe agrees with experiments by Michalak and Paxton on the recovery kinetics of zone-melted Fe. It was found that the activation enthalpy of the recovery process increases from initially 91 kJ/mol to 280 kJ/mol at the end of recovery [159]. This result is particularly interesting, since it shows that dislocations with simple migration mechanism (e.g. gliding) can be annihilated without significant thermal activation, whereas dislocations relying on climb to move are only mobile, if the thermal energy enables solid-state diffusion to the required extent. This is apparently reflected in an activation enthalpy that is in agreement with the one for lattice self-diffusion in α-Fe of $250 \ldots 290$ kJ/mol [25, 26, 159]. The results of the recovery experiments by Michalak and Paxton further indicate that the rate and the extend of recovery is significantly influenced by the amount of strain and temperature during deformation. While higher strain and low temperature induces considerable recovery after deformation, lower strain and higher working temperatures will result in less recovery after deformation. This evinces that dynamic recovery plays an important role during the mechanical processing of α-Fe, and affects significantly the subsequent evolution of the microstructure during annealing. Fig. 5.5 illustrates the microstructure of zone-melted Fe, processed at 20°C and 9% strain [158]. The micrograph clearly demonstrates that the dislocations have been self-organized by dynamic recovery into tangled cell walls (dark-colored regions in Fig. 5.5), which surround nearly defect-free and equiaxed domains of approximately 1 μm in dimension.

The results by Michalak and Paxton indicate that dislocations with easy migration mechanism are not likely to be found in α-Fe after ball milling. The dislocation density of $\varrho = 2.5 \times 10^{15}$ m^{-2}, which is annihilated in the temperature interval up to $300 \ldots 400$°C is therefore likely to cover the dislocations of diffusion-controlled climb, for which the temperature during ball milling was apparently too low for appreciable migration.

The two-step process of dynamic and temperature-activated dislocation recovery involves the forma-

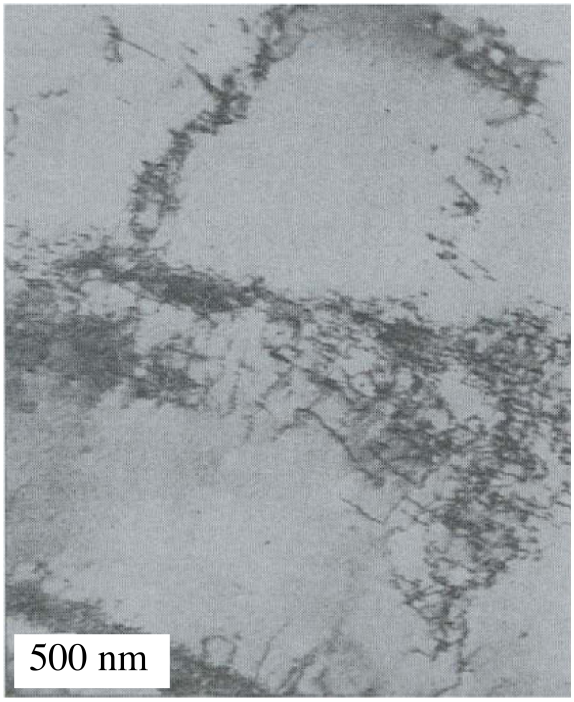

Figure 5.5: TEM micrograph of zone-melted Fe deformed to 9% strain at 20°C (from Ref. [158], p. 157). The dark areas prove the formation of dislocation tangles by dynamic recovery, which are surrounding nearly defect-free and equiaxed cells.

tion of a low-energy network (subgrain structure). The obviously small grain size of the as-prepared microstructure attests that during ball milling the dislocation density must have been significantly high to provide the condition for a dedicated refinement via dynamic recovery. However, if the dislocation density attains a level at which the original lattice orientation becomes obliterated in a state of high atomic disorder, the newly created subgrains after recovery can have a crystal orientation different from the original coarse-grained material. Of course, if during recovery new grain boundaries are created by the relaxation of cell walls, it is reasonable that they will be of a kind, which reduces the energy excess to a minimum. Since a strong misorientation dependence of the grain-boundary energy is predicted by the Read-Shockley Equation (2.6), where the energy $\gamma^{\mathrm{GB}}(\Theta)$ increases monotonously within the regime of LAB and attains its maximum at the transition to high-angle boundaries, it is consequent to expect the new grain boundaries to have low-angle character. Thus, a microstructure of low-angle subgrain boundaries (SGB), where the misorientation Θ of the SGB is described by a certain misorientation distribution $\nu(\Theta)$, is a likely result of grain refinement in α-Fe.

However, both the grain-boundary energy and the mobility are characterized by a substantial misorientation dependence in the LAB regime (see Section 2.2, Eqs. (2.6) and (2.13)), which consequently introduces anisotropic grain-boundary properties, if the subgrains are carrying a certain misorientation spread according to $\nu(\Theta)$. Especially the significant increase of $M(\Theta)$ by several orders of magnitude can obviously induce a substantial variation of SGB interface kinetics, depending on local boundary conditions. Since

dislocation recovery and the involved creation of low-angle boundaries appears to be a key feature of ball-milled nanocrystalline Fe, anisotropic interface properties seem to be the rule, rather than an exception for the studied samples [163]. This conclusion obviously confirms anisotropic grain-boundary properties to be the most-likely root cause for AGG in the examined nanocrystalline samples.

5.5 Abnormal Grain Growth Induced by Grain-Boundary Misorientation

Anisotropic interface properties will have profound consequences on the growth kinetics of a grain. If the grain-boundary energy or mobility depends on the actual misorientation across the grain interface, two grains of equal size — which would have according to standard coarsening theory the same growth kinetics — can have extremely different grain-boundary velocities. This entails that size-scaling of the kinetics fails and the evolution of the microstructure cannot be described by a standard analytical model. The growth kinetics of each grain depends then on the actual — but usually unknown — misorientation-dependent interface properties. The consequence of anisotropic interface kinetics will be the rapid migration of grain boundaries with high velocity (i.e. the fast growth of those grains), while boundaries of grains with low interface velocity have basically a disabled kinetics.

A quantitative description of the abnormal growth of a particular grain with fast boundary kinetics has been proposed by F.J. Humphreys [164]. The model assumes a matrix of grains of mean size $\langle D \rangle$ and mean misorientation $\langle \Theta \rangle$ that surrounds a particular grain of size D and misorientation Θ relative to his neighbors (the misorientation Θ should be considered as a mean value for all grain boundaries of the particular grain, although the actual misorientation across a certain interface may deviate in an untextured matrix from Θ, as the particular grain has only a single orientation). The microstructural configuration of Humphreys' model (which might be seen as a local "quasi-mean-field" model for AGG, assuming a uniform matrix and an isotropic abnormal grain) is sketched in Fig. 5.6.

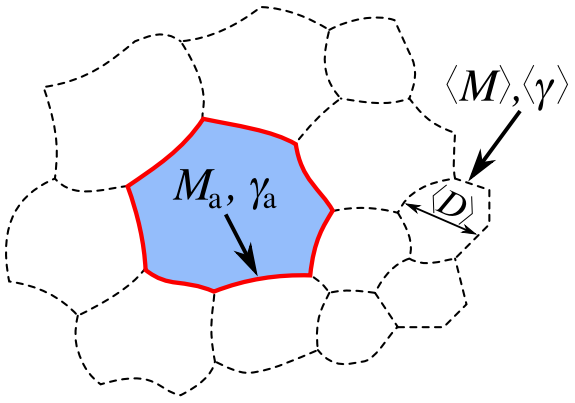

Figure 5.6: Schematic configuration of grains for Humphreys' analysis of AGG. The abnormal grain (blue colored) of size D and high-kinetics grain boundaries with $\gamma_a(\theta)$ and $M_a(\theta)$ is surrounded by matrix grains (dashed lines) of mean size $\langle D \rangle$ and interface properties defined by their mean misorientation $\langle \theta \rangle$.

The model assumes that the grain boundaries of the particular grain will migrate into the matrix and annihilate thereby the matrix-matrix grain boundries. The driving force of AGG is therefore given, similar to the calculation of the critical nucleus size for ReX, by the difference between Eq. (5.4) and Eq. (5.7),

$$-\frac{\mathrm{d}G^{\mathrm{AGG}}}{\mathrm{d}R} = 8\pi \cdot g_1 \cdot R \cdot \gamma_{\mathrm{a}} - 6\pi \cdot g_2 \cdot \langle\gamma\rangle \frac{R^2}{\langle R\rangle}. \tag{5.9}$$

In Eq. (5.9) the grain size is written as the radius $R = D/2$ of the equivalent sphere, and g_1 and g_2 denote geomtric constants on the order of unity to account for the actual grain shape. With Eq. (5.9) the growth rate of the particular grain can be equated as,

$$\frac{\mathrm{d}R}{\mathrm{d}t} \approx M_{\mathrm{a}} \cdot \left(\frac{3\langle\gamma\rangle}{2\langle R\rangle} \cdot g_2 - \frac{2\gamma_{\mathrm{a}}}{R} \cdot g_1\right). \tag{5.10}$$

Assuming mean-field properties for the particular grain, i.e. $M_{\mathrm{a}} = \langle M\rangle$ and $\gamma_a = \langle\gamma\rangle$, Eq. (5.10) merges obviously into Hillert's standard mean-field equation (2.24) (taking $g_1 = 1/2$ and $g_2 = 2/3$), which shows that the particular grain is then equal to the matrix and no abnormal growth is expected.[4] Eq. (5.10) states further that the particular grain will grow only (i.e. $\mathrm{d}R/\mathrm{d}t > 0$), if $R/\langle R\rangle > \gamma_{\mathrm{a}}/\langle\gamma\rangle$ — otherwise the particular grain is stable or even shrinks. A high interface energy γ_{a} of the abnormal grain is therefore an obstacle for the evolution of AGG [154, 155, 164].

For the experimental coarsening data, AGG has been identified by an increase of the grain-size ratio $\langle L\rangle_{\mathrm{vol}} / \langle L\rangle_{\mathrm{area}}$. In a similar way the criterion for AGG within the model can be expressed by the time dependence of the grain-size ratio $R/\langle R\rangle$ of the particular grain and the matrix, i.e.

$$\frac{\mathrm{d}}{\mathrm{d}t}\left(\frac{R}{\langle R\rangle}\right) = \frac{1}{\langle R\rangle^2} \cdot \left(\langle R\rangle \cdot \frac{\mathrm{d}R}{\mathrm{d}t} - R\frac{\mathrm{d}\langle R\rangle}{\mathrm{d}t}\right) > 0 \text{ for AGG.} \tag{5.11}$$

With the growth rate of the particular grain from Eq. (5.10) and assuming for the matrix Hillert's mean-field growth kinetics of Eq. (2.26), the criterion for AGG in Eq. (5.11) reads (with the assumed geometric factors $g_1 = 1/2$ and $g_2 = 2/3$) [164],[5]

$$M_{\mathrm{a}} \cdot \langle\gamma\rangle - \left(M_{\mathrm{a}}\gamma_a \cdot \frac{\langle R\rangle}{R}\right) - \left(\frac{\langle M\rangle \cdot \langle\gamma\rangle}{4} \cdot \frac{R}{\langle R\rangle}\right) > 0. \tag{5.12}$$

Using the normalized parameters $r = R/\langle R\rangle$, $\mu = M_{\mathrm{a}}/\langle M\rangle$ and $\epsilon = \gamma_{\mathrm{a}}/\langle\gamma\rangle$ to rewrite Eq. (5.12), the particular grain will be unstable and undergo AGG, if the following inequality is fulfilled [164],

$$4\mu r - 4\mu\epsilon - r^2 > 0. \tag{5.13}$$

[4] Note that Hillert's mean-field equation on normal grain growth and Humphrey's model for AGG are using basically the same relaxation approach of the grain-boundary-related excess-energy density.

[5] Assuming a mean-field growth law for the evolution of the matrix might be decent, if the distribution of matrix misorientation is narrow. Then, the matrix subpopulation will have quasi-uniform boundary conditions.

Instability of the microstructure in Fig. 5.6 is only possible, if the quadratic expression of Eq. (5.13) does not yield an imaginary root (for this constraint the condition $\mu > \epsilon$ must hold). The criterion to enable an instability of the particular grain is then defined by the two real roots, which satisfy the constraints of the quadratic function in Eq. (5.13). To account for the effect of misorientation on the interface energy and mobility (for both the particular grain and the matrix grains), the normalized parameters μ and ϵ are related to the misorientation-dependent definitions $M(\Theta)$ and $\gamma(\Theta)$ of Eqs. (2.6) and (2.13), respectively.

Fig. 5.7 illustrates the numerical solution of Eq. (5.13), which defines the borderline between stable and unstable growth of a particular grain. For a given mean misorientation of the matrix $\langle\Theta\rangle = 2°$, 5° and 10° (from which the grain-boundary properties $\langle M\rangle$ and $\langle\gamma\rangle$ are unambiguously defined), the graph shows the relative grain sizes r as a function of misorientation Θ (defining the values of M_a and γ_a), for which the particular grain is growing abnormally.

Fig. 5.7 shows that AGG of the particular grain is possible, if two conditions are fulfilled: $\Theta > \langle\Theta\rangle$ and the normalized size r must be above a lower limit, i.e. $r > r_{min}$. If both conditions are met, the particular grain will grow abnormally until the normalized size reaches the upper limit r_{max}, i.e. AGG is possible for a relative abnormal grain size $r_{min} < r(t) < r_{max}$. If the abnormal grain has reached r_{max} the grain still may grow, but $r(t)$ will be constant or even shrink (if $\langle R\rangle$ increases equally fast or faster than R, i.e. depending on the coarsening rate of the matrix).

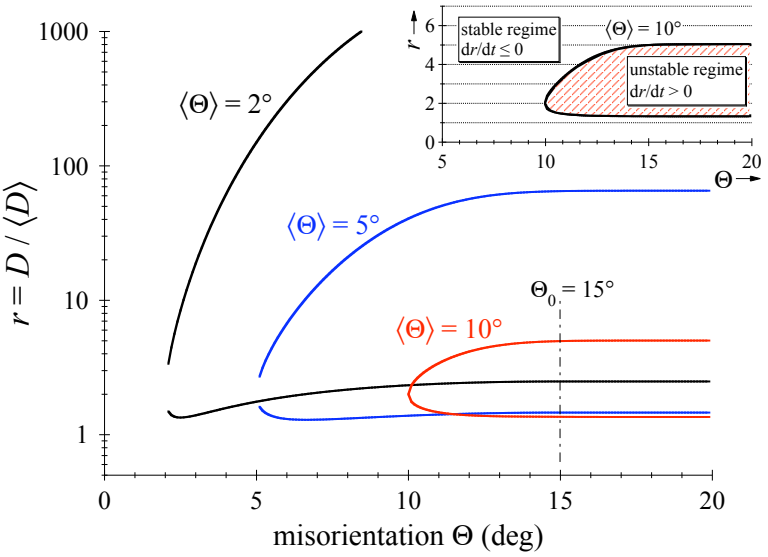

Figure 5.7: Numerical solution of Eq. (5.13) for different matrix misorientations $\langle\Theta\rangle$. The square roots are defining the borderlines with respect to the grain-size ratio r between the stable and unstable evolution of a particular grain. The actual grain-boundary energy $\gamma^{GB}(\Theta)$ and mobility $M^{GB}(\Theta)$ for the particular grain and the matrix misorientation (given from Eqs. (2.6) and (2.13)) are calculated for a LAB/HAB transition angle of $\Theta_0 = 15°$. The inset of the graph shows in detail the stable and unstable regime for an empirically reasonable mean misorientation of the matrix grains $\langle\Theta\rangle \approx 10°$, which has been estimated from the TEM data of the investigated nanocrystalline Fe samples.

Humphreys model reveals that the average misorientation $\langle\Theta\rangle$ of the matrix grains will have significant impact on both the abnormal growth kinetics according to Eq. (5.10) and the prerequisites on the relative abnormal size r to enable AGG. To be able to apply the outcome of Humphreys model to the nanocrystalline Fe specimens investigated, it is therefore important to have a sound estimate of $\langle\Theta\rangle$. In this respect TEM examination of the as-prepared microstructure revealed that there is a major fraction of grains with similar orientation (*cf.* Section 4.4.1). For this texture component the full width of the angular orientation distribution (note: not to be cofused with the misorientation distribution $\nu(\Theta)$) was estimated from DF and diffraction mode to be approximately 20°. Since in the LAB regime γ^{GB} increases with Θ, it is reasonable to assume that the actual misorientation of neighbored grains will be on average less than the maximum spread of the orientation distribution. For this reason it should be decent to assume that the matrix grains have a mean misorientation $\langle\Theta\rangle \lesssim 10°$.

Of course, if $\langle\Theta\rangle$ is approximately 10° and the condition for abnormal grains to be unstable and grow discontinuously is $\Theta > \langle\Theta\rangle$, the grain boundaries of the particular grains can be in principle of both low or high-angle type (*cf.* Fig. 5.7). To follow up the question on the type of abnormal grain boundaries it might be helpful to survey the activation enthalpies measured on isothermal annealing kinetics. The experimentally measured activation enthalpy of ~210 kJ/mol shows that in principle both interface types LAB and HAB are equally likely, since the compliance with the respective activation enthalpy for grain-boundary self-diffusion of ~175 kJ/mol (for HAB) and for lattice self-diffusion of ~250 kJ/mol (for LAB) is nearly the same. However, the activation enthalpies for LAB and HAB migration refer to "ideal" atomic-scale processes, whereas the actual activation enthalpy can be increased, if the involved atomic diffusion mechanism is somehow aggravated by an impeded diffusion. Consequently, the actual activation enthalpy may be above the one of the ideal diffusion process, but it seems unlikely in the present case that auxiliary mechanisms will reduce the required thermal activation. With this argument it appears likely that the migration of abnormal grain boundaries is controlled by grain-boundary diffusion and hence, the interfaces of the particular grains that are undergoing discontinuous growth seem to be of high-angle type.

The inset of Fig. 5.7 shows that for the empirically estimated matrix misorientation $\langle\Theta\rangle \approx 10°$ abnormal growth will be facilitated for grains larger than $r_{\mathrm{min}} \approx 1.3$, which will then grow for an interface misorientation $\Theta > \Theta_0$ to a maximum size of $r_{\mathrm{max}} \approx 5.0$ (if the particular grain shares boundaries of low-angle type, i.e. $\Theta < \Theta_0$, the maximum size would be a function of misorientation and be less than $r_{\mathrm{max}} \approx 5.0$). Of course, both the apparently moderate maximum size of abnormal grains relative to the matrix (and not a vigorous AGG as it might be found for very small values of $\langle\Theta\rangle$ where $r > 10^3$ is easily possible) and the strict termination of abnormal growth at $r = r_{\mathrm{max}}$ are in remarkable agreement with the defined GDF for the matrix and the abnormal grains of the numerical AGG model in Section 5.3. The compliance between both models is reflected in the only small offset of the abnormal distribution f_{a} from the matrix distribution f_{m} and the fixed median $D_{0,\mathrm{a}}$ of the abnormal GDF, which both fully agree with the sharp cutoff of abnormal growth at $r = r_{\mathrm{max}}$ [145]. Additionally, EBSD examination of the annealed state testifies that the maximum normalized grain size $r_{\mathrm{max}} \approx 5.0$ is a reasonable estimate for the relative grain sizes of the actual microstructure (*cf.* Fig. 4.28). Since the abnormal grains are growing at most to a size that is about five times the average size of the matrix grains, it is evident that a bimodal split-up of the GDF $g(D)$ is not expected and the superposition of both f_{m} and f_{a} will presumably result in a broadening of the overall size distribution. In fact, this is obviously the result of isothermal annealing, where a gentle

broadening of $\langle L \rangle_{\mathrm{vol}} / \langle L \rangle_{\mathrm{area}}$ is observed, but not an unrestrained growth of abnormal grains. Inspection of Fig. 5.7 reveals that a gentle broadening of the GDF (which is of course the same as a moderate value of r_{max}) requires the mean misorientation $\langle \Theta \rangle$ of the matrix to be close to the transition Θ_0 between the LAB and HAB regime. In other words, the abnormal and the matrix grains must not be too different with respect to their grain-boundary properties in order to allow for a gentle broadening of the GDF only (in other cases a much larger value of r_{max} will control AGG and a distinct bimodal evolution seems likely).

The compliance of Humphreys' model with both the empirical characteristics of inhomogeneous coarsening and the proposed numerical model for AGG provides reliable evidence that the misorientation-dependent grain-boundary mobility $M(\Theta)$ is not only an inherent feature of the investigated samples, but is to a high certainty the root cause for AGG in nanocrystalline Fe. The conclusion of AGG that is induced by anisotropic grain-boundary mobilities is also supported by computer simulations on subgrain growth reported by E.A. Holm *et al.* and by O.M. Ivasishin *et al.* [30, 155, 156], where the artificially introduced misorientation distribution of the microstructure yielded the dominant and abnormal growth of particular grains that are equipped with highly mobile interfaces.

The outcome of Humphreys' model that already a minor orientation offset of the particular grain of 2. . . 3° from the matrix — wherefore the particular grain might even be part of the same texture component as the matrix grains — is sufficient to induce substantial growth to 4 or 5 times the size of the matrix grains suggests that the misorientation offset of the abnormal grains is unlikely the limiting constraint for AGG. It seems more plausible that the size criterion $D_{\mathrm{crit}} / \langle D \rangle > 1.3$ is the key parameter for the ability of a specific grain to undergo abnormal growth [164]. Fig. 5.8 shows the approximated GDF of the as-prepared microstructure where similar to the numerical model a lognormal function has been assumed (the parameters D_0 and σ have been calculated from the average grains size $\langle L \rangle_{\mathrm{vol}} = 21$ nm and $\langle L \rangle_{\mathrm{area}} = 18$ nm measured for the as-prepared state). Although the GDF is rather compact, only a small fraction of approximately 7% of all grains contained in the polycrystal would obviously satisfy the size criterion for AGG. Since for a grain of mean size $\langle D \rangle$ (which should be according to the apparently narrow GDF in Fig. 5.8 a reasonable size estimate for the majority of grains in the as-prepared state) the average number of nearest neighbors is ~14 [41], each grain would be expected to have on average one neighbor that allows for abnormal growth.

Depending on both the spatial distribution of high-mobility grains with $r \gtrsim 1.3$ and the actual — and possibly different — grain-boundary misorientations that an abnormal grain can have with his bordering neighbors, the local conditions for each abnormal grain can be quite diverse. This anticipation is obviously reflected in the OIM images in Fig. 4.28, which reveal that the shape of an abnormal grain can vary significantly between equiaxed and finger-like. As the shape and the size of the grains in the as-prepared state is more or less homogeneous, it is conspicuous that this characteristic of non-uniform abnormal growth is concealed in obviously different growth rates of the grain boundaries, which the abnormal grain shares with his next-nearest matrix grains. Obviously, the growth rate of a particular grain according to Eq. (5.10) may deviate from Humphreys' "quasi-mean-field" consideration, if either a unique misorientation Θ is an oversimplification of the actual grain boundaries' characteristics, or the abnormal grain shares boundaries with neighbors of significantly different size, which would not allow to describe the matrix by a single mean parameter $\langle R \rangle$. The latter reason appears from the empirical data less likely, since the GDF in Fig. 5.8 is rather narrow and would not support a significant spread of grain

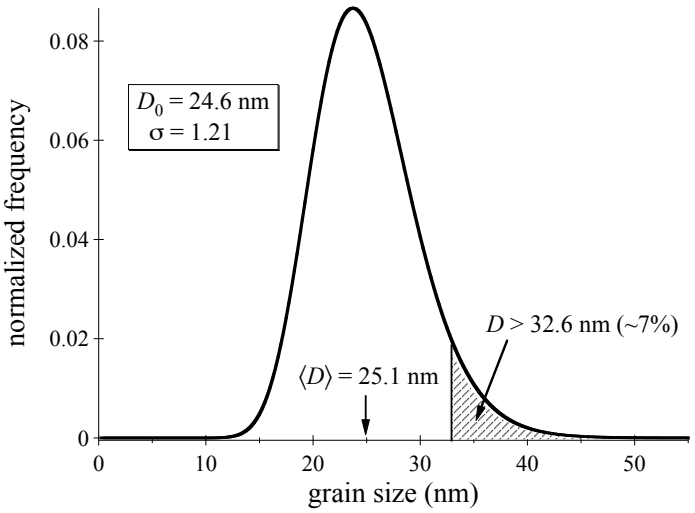

Figure 5.8: Lognormal GDF of the as-prepared state, calculated from $\langle L \rangle_{\mathrm{vol}} = 21$ nm and $\langle L \rangle_{\mathrm{area}} = 18$ nm. The shaded area indicates the grains that fulfill the size criterion $D_{\mathrm{crit}} / \langle D \rangle > 1.3$ to enable AGG.

sizes. The first possibility for spatially anisotropic growth of abnormal grains — i.e. a misorientation distribution along the perimeter of an abnormal grain — is of course a likely candidate, if the matrix grains do not have a substantial orientational alignment ("texture"), i.e. if the matrix-matrix interfaces are described by a larger width $\Delta\Theta$ of the misorientation distribution $\nu(\Theta)$. Only if the misorientation distribution $\nu(\Theta)$ is narrow, so that $\Delta\Theta \ll \Theta - \langle\Theta\rangle$, the relative misorientations of the abnormal grain with his neighbors can be quasi-isotropic and uniform spatial growth is possible — yielding homogeneous equiaxed grains. If texture is however weak, the actual misorientation across the individual grain boundaries of an abnormal grain can vary considerably, i.e. while some interfaces possess high mobility, others may not [31, 155]. Consequently, rapid abnormal growth will be possible only in some preferred directions and it is conceivable that substantial abnormal growth with respect to spatial isotropy and copiousness will not be found — the result will be selective growth and grains of finger-like shape.

Unfortunately, instantaneous information on the misorientation distribution $\nu(\Theta)$ in the as-prepared microstructure is not available. However, the examination by TEM showed that the initial grain orientation is characterized by a distinct texture component, for which an angular orientation spread of approximately 20° was found. Although it is not possible to infer from the measured orientation distribution on the misorientation distribution $\nu(\Theta)$ of the matrix, the notable spread observed by TEM may allow to speculate that also the misorientation is determined by a distribution of certain width $\Delta\Theta$ around the estimated mean value $\langle\Theta\rangle \approx 10°$. The correlation between grain alignment and the type of microstructure found during AGG is obviously reflected by the EBSD and IPF plots of the OIM analyses, *cf.* Figs. 4.28 and 4.29. For type A microstructures, for which the texture analysis did not yield a substantial alignment of the grains (i.e. $\Delta\Theta$ is large), an inhomogeneous grain assembly with finger-like shape of the abnormally-grown grains is discovered. This obviously underlines the difficulty for an abnormal grain to grow uniformly under those conditions, and the selective growth in mobility-favored directions (i.e.

grain boundaries with higher misorientation) imposes an elongated grain shape. A completely different situation is found for microstructures of type C. It can be observed, that the microstructure is very homogeneous and comprises uniformly-grown equiaxed grains (type C microstructures have the most pronounced texture). Although this appears to be the final state of a transient abnormal evolution (a notable number of matrix grains is no longer found), which does therefore not provide information on the actual misorientation conditions during the precedent phase of abnormal growth, the type C microstructure is an example for the result of a strongly textured matrix (i.e. small $\Delta\Theta$), which provides for the individual interfaces of an abnormal grain very similar misorientations.

The importance of a narrow texture component for the evolution of extensive and uniform AGG has been demonstrated by O.M. Ivasishin *et al.* in computer simulations on grain growth under anisotropic interface mobilities [156]. The simulation used a Gaussian misorientation distribution, where the width of the distribution was changed between 2° and 30°. The results indicate that for a weak texture AGG cannot evolve and the microstructures grows normally. However, for $\Delta\Theta \lesssim 10°$ grains of high mobility reveal rapid growth and reach at longer times a growth stagnation with a size that is ~6 times the size of the matrix grains. The average grain size of the overall microstructure (including the abnormal grains) reveals in parallel to the rapid growth of the largest grains (those might be identified as $\langle L\rangle_{\mathrm{vol}}$) the same temporary increase of the growth rate as $\langle L\rangle_{\mathrm{area}}$ before the kinetics passes an inflection point and stagnates during further coarsening. In the simulation, impingement of the abnormal grains has been identified as the cause for long-term stagnation — however, in principal every situation, which cancels the growth advantage of the particular grains will terminate AGG (and may allow normal curvature-driven growth to continue). Both the low-angle misorientation of large grains in the TEM investigations of the annealed state (Fig. 4.27) and the OIM images of type C microstructures would obviously agree with the explanation of impingement. The possibility of low-angle impingement would also agree with the before noted hypothesis that the particular grains could originally belong to the same texture component as the matrix grains, which means that at least a certain fraction of abnormally-growing grains would have a very similar orientation (defining low-mobility interface by impingement).

Summarizing the conclusions of the discussion so far clearly yields that with high probability the misorientation-dependent anisotropy of grain-boundary mobility is the root cause for the long-term AGG observed during isothermal annealing of nanocrystalline Fe. However, the root cause for another key feature of the coarsening kinetics has not been explained yet: The soaring increase of the grain size during the first few minutes of annealing. Since ReX, which would perfectly fit for such a rapid kinetics, has been discarded to account for the initial jump of the grain size (*cf.* Section 5.4.2.1), the reason for this feature must be driven by another effect. From the current point of view it seems most likely that the initial jump of the grain size is closely related with the before discussed mobility-driven long-term AGG. A review of Eq. (5.10) shows that grains of high mobility will grow abnormally, if they are larger than the critical size r_{min}. The fact that more than 90% of all grains do not meet this size criterion in the as-prepared state evinces that there is a substantial probability to find a high-mobility grain with $r < r_{\mathrm{min}}$. However, what will happen to a grain of high interface mobility that cannot perform rapid growth? Considering Hillert's mean-field model it is clear that all grains with $R < \langle R\rangle$ will shrink and disappear at a certain point. The same is basically predicted by the growth rate of the particular grain (*cf.* Eq. (5.10)) where $\mathrm{d}R/\mathrm{d}t < 0$, if $R/\langle R\rangle < \gamma_{\mathrm{a}}/\langle\gamma\rangle$. This shows that — similar to normal grain growth — those grains will shrink and give up atoms to their neighbors, but due to the high grain-boundary kinetics of the shrinking

grain, this process will be much more pronounced than any other growth process at this stage. With this consideration the initial increase of the grain size is induced by the same abnormal characteristic as the long-term AGG, and establishes a short preceding phase of abnormal growth — however, the "growth direction" is inverse and the particular grains dissolve. Since the curvature of the shrinking grain increases continuously until the grain is completely annihilated by his neighbors, the kinetics of shrinkage will be self-accelerating and therefore at a higher rate than the curvature-driven growth of the matrix or the abnormal growth of the particular grains. It is therefore conceivable that the shrinkage of abnormal grains will dominate the initial period of annealing. As soon as the shrinking abnormal grains are annihilated by the matrix the process stops and the further change of the microstructure is driven by "regular" AGG (it should be kept in mind that the two processes occur in parallel, i.e. long-lasting "regular" AGG will also proceed during the initial jump of the grain size).

Another aspect of the initial rapid growth is related to the enthalpy relaxation during the DSC experiments. Considering the DSC scans it is quite surprising that the release of enthalpy stops almost instantaneously at 580°C, although the grain size reached only ~46 nm. For comparison, the maximum grain size during isothermal annealing is approximately 100 nm, but at a temperature that is about 100°C below the final temperature of DSC. From this it might be concluded that the microstructure did not attain the same level of relaxation at the end of the DSC scan as it is possible by normal annealing — although, the DSC data implies that the grain-coarsening process in the temperature interval up to 580°C is apparently terminated. Beside the abrupt termination of the DSC signal, the total enthalpy of the grain-growth-related peak ("peak 2") was found to be approximately 600 J/mol, which is only about one third of the released enthalpy measured by Malow and Koch and by Moelle and Fecht of 1.8 kJ/mol and 2.0 kJ/mol, respectively [10,128].

The evaluation of the DSC experiments and comparison with the long-term AGG obviously suggests that the evolution of the nanocrystalline Fe occurs in two steps, where the DSC apparently observes the earlier one. This conclusion is supported when the "activation enthalpies" measured by DSC and isothermal annealing are compared — both indicators for the ease of the microstructure to attain the most "bimodal" configuration during AGG. In isothermal annealing this activation enthalpy is defined by the temperature-dependent time τ (defined by the point of the broadest GDF, see Figs. 4.16 and 4.17), whereas for the DSC scans the ease of AGG is documented by the temperature-dependence of the grain-growth-related DSC peak. The Arrhenius analysis of both activation enthalpies yielded for the DSC and the isothermal process a value of 45 kJ/mol and 320 kJ/mol (*cf.* Fig. 4.19), respectively. Since both parameters are characteristic for the ability of the system to perform AGG, it has to be concluded that they do not observe the same process. Thus, it appears consequent to consider DSC to record the fast initial shrinkage of abnormal grains, whereas XRD measures the slower long-term AGG.

With the above comprehensive discussion a consistent explanation of the complete mircostructural coarsening process of nanocrystalline Fe is given. Fig. 5.9 summarizes the proposed behavior of the grain assembly and correlates the characteristic features of the isothermal data with the evolution of the microstructure. The images (A) to (C) show the time period of early rapid growth, where both the small abnormal grains and the abnormal grains above the critical size limit $r_{\min}$ are involved by shrinkage and growth, respectively, but the kinetics of the shrinking grains will dominate this stage of coarsening (the long-term AGG does not affect the overall growth kinetics notably at this point, since $\mathrm{d}x_{\mathrm{V}}/\mathrm{d}t$ is

still small). Images (C) to (E) illustrate the long-term AGG, where the abnormal grains (green-colored in Fig. 5.9) gradually annihilate the matrix, $x_V(t) \rightarrow 1$.

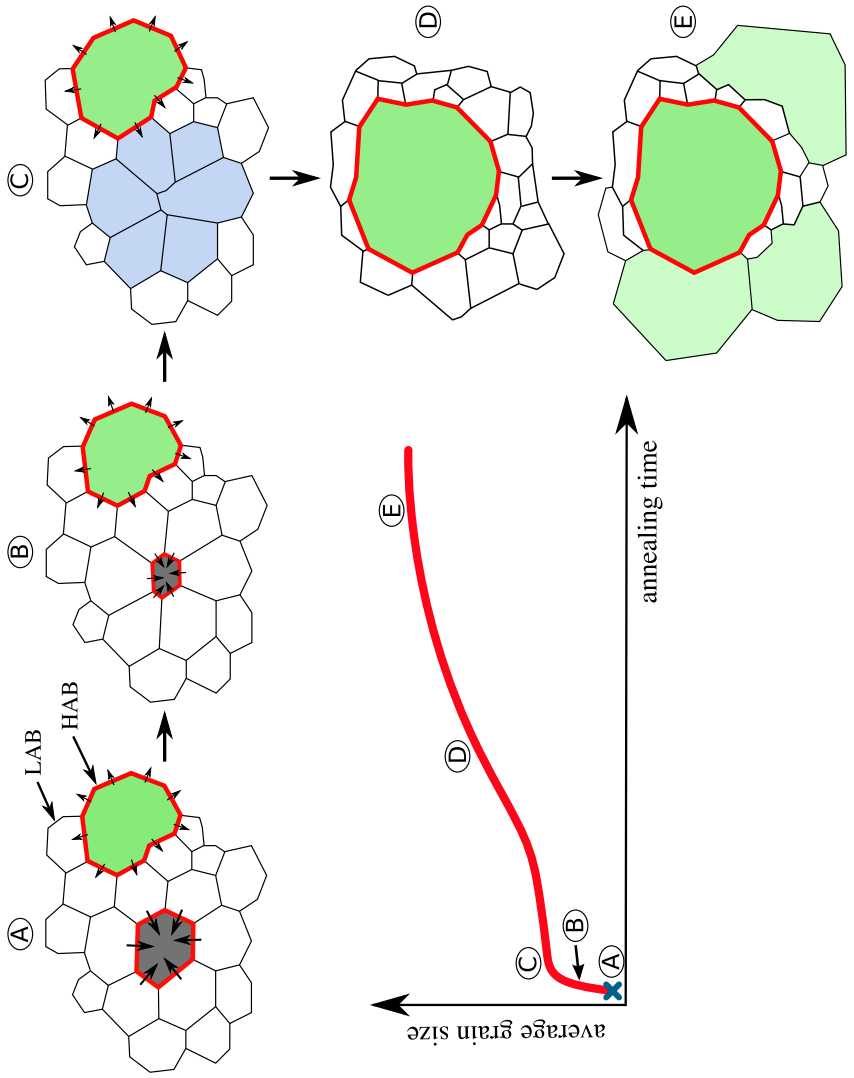

Figure 5.9: Proposed model for the evolution of the microstructure of nanocrystalline Fe, based on the comprehensive discussion of the experimental observations. Steps (A) – (C) describes the early AGG, driven by the rapid shrinkage and dissolution of unstable grains. The increase in grain size relates to the receive of volume by the matrix grains (blue-colored). Steps (C) – (E) illustrate the long-term AGG that is driven by the anisotropy of the grain-boundary mobility in low-angle interfaces (abnormal grains are shown green).

Chapter 6

Summary & Prospective Questions

The innate thermodynamic instability of nano-structured materials encouraged this experimental study to investigate the microstructural evolution of nanocrystalline bulk materials when exposed to elevated temperatures. The motivation for this thesis was derived from the subject matter: Which underlying microscopic processes and which kinetics-controlling mechanisms impel or constrain microstructural coarsening of nanocrystalline materials? The investigations have been based on three fundamental questions that were outlined in the introductory chapter of this thesis, and were guiding the investigations and the experimental approach. Within this summarizing chapter, answers to these questions are provided on the basis of experimental observations and the conclusions drawn in the discussion part.

The experimental analyses have been conducted on the model system nanocrystalline α-Fe, which allowed a comparative study with respect to results of former investigations on the coarse and nano-structured state of the material — it should be noted that it was the main disadvantage of former studies on nanocrystalline Fe not to be capable to provide conclusive explanations on the guiding questions of this study. The experimental examinations of the present exploration concentrated on *in-situ* XRD to investigate isothermal growth kinetics, calorimetric analysis in the differential scanning mode (in combination with XRD analysis) and microscopic imaging via TEM and EBSD/OIM on the as-prepared and the annealed state. The specimens under investigation were prepared in a laboratory high-energy ball mill with an average grain size of approximately 18 nm in the as-prepared state.

Isothermal Growth Kinetics

From a superficial inspection of the isothermal anneals it was appealing to find that the average grain size apparently increased in a temperature-dependent parabolic-like manner, as it would be expected for normal curvature-induced grain growth. Of course, the measured long-term growth stagnation (at grain sizes below ~100 nm) is clearly in conflict with the ideal picture of grain growth, but such an observation is not unusual (see for example Fig. 1.1), and is normally denoted in literature by growth exponents $m > 2$. The observation of impeded grain-boundary migration and the concomitant deviation from ideal parabolic growth is mostly ascribed to effects like grain-boundary dragging and pinning, for example due to impurity atoms or embedded second-phase particles. Although the preparation route of ball milling is frequently suspected to be responsible for significant impurity concentrations, the chemical analysis and the assessment of the quantified impurity species indicated that solute drag and pinning by second-phase particles cannot be of significant level in the investigated samples. Thus, from this point of view, there would be no reason to doubt the prevalence of normal growth in the examined samples —

however, the detailed inspection of the isothermal experiments revealed that the temporal evolution of the mean grain size (particularly at lower annealing temperatures) is characterized by two very exceptional features, for which it is obviously difficult to explain them by the kinetics expected for normal grain growth: Firstly, a very fast increase (or almost an instantaneous jump) of the grain size immediately after setting the temperature for isothermal conditions (a feature, which is more or less independent of the actual temperature conditions) and secondly, a regime of quasi-linear growth, which is followed by an apparent increase of the growth rate. The unique time period of a quasi-linear and an upward-curved grain-size/time relationship is defined in time by the observation of an inflection point (distinguishing the largest slope of the grain-size curve), beyond which the growth kinetics merges into the before explained stagnant power-law curve with a growth exponent $m > 2$. The unusual growth characteristic is found for both the volume and the area-weighted average grain size, $\langle L \rangle_{\mathrm{vol}}$ and $\langle L \rangle_{\mathrm{area}}$, where the first quantity is due to its statistical definition primarily sensitive to the evolution of the largest grains of the polycrystal, whereas the second one is rather a measure for the mean grain size of the overall microstructure. However, the experimentally determined values of $\langle L \rangle_{\mathrm{vol}}$ and $\langle L \rangle_{\mathrm{area}}$ perform the features of quasi-linear growth and the apparent increase of the growth kinetics on clearly different time scales, where $\langle L \rangle_{\mathrm{vol}}$ is obviously faster than $\langle L \rangle_{\mathrm{area}}$ and changes the growth mode earlier [145]. The different kinetics of the two weighted averages is reflected in a broadening of the grain-size distribution, which returns back to a narrower configuration as soon as the quasi-linear regime of $\langle L \rangle_{\mathrm{area}}$ has been passed and the growth rate of the mean grain size has reached its maximum — this is approximately equal to the inflection point of $\langle L \rangle_{\mathrm{area}}$ in the grain-size/time plot. The behavior of the grain-size distribution indicated that the evolution of the microstructure during grain growth is not of self-similar type and thus, the growth kinetics is unlikely to be of unique size-scaled characteristic — as it would be a generic feature of normal curvature-controlled growth. The isothermal anneals clearly evinced that the initial evolution of the microstructure (i.e. the period of broadening of the grain-size distribution) must be driven by the unusual growth of a few particular grains (which are the grains that are controlling $\langle L \rangle_{\mathrm{vol}}$), and the development at later times (i.e. the narrowing of the grain-size distribution) is controlled by a gradual shift of the centroid of the overall grain-size distribution to larger values, which has been shown to be driven by the gradual annihilation of the grains with low growth ability — according to statistical constraints of the average grain size, this shift encourages an increase of the overall mean grain size $\langle L \rangle_{\mathrm{area}}$.

From those observations on *in-situ* annealing, and also the finding of a very inhomogeneous grain-size distribution measured by EBSD directly on the annealed state of the material, it was concluded that in nanocrystalline Fe uniform curvature-driven grain growth cannot account for the underlying processes of microstructural evolution. The fact that TEM and XRD found the as-prepared state of the specimens to be of homogeneous nature and the initial grain-size distribution to be rather compact emphasized, that the measured inhomogeneity of the microstructure must be the result of a substantial non-uniform coarsening process, which is also driving the abnormal broadening/narrowing of the grain-size distribution.

Question 2: "*Do nanocrystalline materials fulfill the prerequisites for self-similar normal grain growth, or are they growing irregularly via abnormal grain growth? This means, is grain growth in nano-scaled microstructures predictable*?"

The experimental results of *in-situ* annealing and the EBSD micrographs revealed that in nanocrystalline Fe obviously a strong inhomogeneous coarsening exists that is clearly violating the general features of normal grain growth and involves an abnormal evolution of the grain-size distribution. From this point, the evolution of the microstructure in nanocrystalline Fe is complex and cannot be assessed by an analytical macroscopic growth law. In principle, this lack of an appropriate description prevents to determine the further evolution of the nanocrystalline microstructure by solely evaluating the configuration of the grain-size distribution, or even the analysis of the grain assembly locally — if the abnormal growth is induced by parameters that are not directly related to the grain size.

However, the comparison of the isothermal anneals and the evaluation of activation enthalpies showed that the growth characteristic is scaling with temperature, and the different isothermal curves are for appropriate scaling of very similar shape. This observation suggests that, although the coarsening is driven by abnormal grain growth, the actual evolution of the microstructure must obviously follow a defined process, if considered on a statistical macroscopic view. This basically involves that for the particular grains — which are sustaining the abnormal coarsening — the growth mechanism is likely to be quite similar, and a numerical/empirical description could be established.

Possible Change of the Rate-Controlling Mechanism

Although there are of course several possibilities which could be responsible for the recorded abnormal growth of the microstructure, the recently suggested impact of topological obstacles — viz. triple lines or quadruple points — on both the nanocrystalline growth kinetics and the accompanying redefinition of the rate-controlling mechanism was from a first review of the isothermal experiments the most tempting explanation for the observed unusual characteristics (and was also in the focus of former studies on the growth kinetics of nanocrystalline Fe). The proposed size-dependent impediment of grain-boundary migration, which is assumed by recent theories to be imposed by restraining drag due to the required migration of those 1- or 0-dimensional structures together with the grain boundaries, could have explained the unusual growth advantage of particular grains fairly well, if they are above a critical size limit, while at the same time other (smaller) grains are mainly impeded due to efficient drag — consequently, the result of this size-dependent sensitivity on structural drag could have promoted a broadening of the grain-size distribution. However, a thorough review of the activation enthalpies that were experimentally deduced from isothermal growth kinetics showed that a size-dependent rescaling of the growth kinetics due to triple-line or quadruple-point drag cannot be confirmed — basically because the abnormally-growing grains and the matrix are defined by a rather compact grain-size distribution of the initial state, i.e. size-dependent mechanism should equally affect the complete microstructure. Moreover, the constant value of the activation enthalpy suggested that the rate-controlling mechanism of microstructural coarsening does generally not change throughout the investigated time scale and grain-size regime ($D \lesssim 100$ nm). This obviously involves that, if there is an increase of the growth kinetics (what would definitely be a tempting interpretation of an upward-curved behavior in the grain-size/time plot), this could only be induced by an

increase of the driving force on the grain boundaries of the fast-growing particular grains, but obviously not by an intermediate increase of their mobility (since this would need a switchover to a faster migration process and should therefore be reflected in the measured activation energies). However, for curvature-maintained grain growth the increase of the driving force is only possible either by a significant increase of the actual grain-boundary energy γ^{GB}, or by a change of the grain configuration, where the neighbors of the growing particular grains become smaller and create thereby a larger curvature (for normal growth this would be equal to a redefinition of the cutoff grain size R_c in the mean-field growth law) — obviously, both possibilities for a higher driving force on the migrating boundaries are violating either uniform grain-boundary conditions and/or the validity of an unique grain-growth model, what would explain the abnormal evolution of the assembly. Recalling the rather narrow grain-size distribution found in electron micrographs of the as-prepared state however suggested that the idea of smaller adjoining grains cannot be substantiated to explain an increase of growth kinetics. Of course, there would be still the possibility of an increasing γ^{GB} remaining, however from the discussion of possible root causes for abnormal growth it is evident that only the misorientation dependence in the regime of low-angle boundaries could affect γ^{GB} in a substantial way, but the advantage of such grain boundaries to dominate the evolution of the microstructure is apparently weak, since this would require a very wide-spread distribution of interface misorientations — which was actually not observed in the as-prepared state. In summary the discussion revealed that abnormal grain growth is unlikely impelled by an anisotropic driving force on the grain boundaries.

Question 1: *"Can evidence be found that a process other than grain-boundary diffusion can become rate-controlling in nanocrystalline materials, i.e. is there a transition grain size below which the rate-controlling step changes and thus, a slower growth kinetics is introduced?"*

The evaluation of the isothermal growth data yielded an activation enthalpy of ~210 kJ/mol for both $\langle L \rangle_{area}$ and $\langle L \rangle_{vol}$, which is constant (within the experimental uncertainty) for the complete period of annealing. This observation indicates that for the acquired conception of abnormal nanocrystalline coarsening in α-Fe the rate-controlling mechanism is obviously not changing, i.e. a dedicated transition grain size below which a different (slower) rate process is controlling the growth kinetics, cannot be confirmed.

Furthermore, the discussion of isothermal growth kinetics revealed that the experimentally deduced activation enthalpy is close to the one for grain-boundary self-diffusion in bcc Fe, which is clearly suggesting that the migration of nanocrystalline grain boundaries occurs microscopically under the same conditions as it was found by Hu's study on the coarse-grained state. Of course, this particularly discards the possibility of triple-line or quadruple-point drag, because their specific mobility should be significantly lower than the one of intrinsic grain-boundary migration in order to be able to inhinbit grain-boundary migration substantially. In general, it can be concluded that evidence for a change of the rate-controlling step could not be confirmed from the experimental analyses on nanocrystalline Fe.

A Numerical Model for Abnormal Grain Growth

The conclusion — based on the evaluation of empirical observations — that nanocrystalline Fe is undergoing an inhomogeneous coarsening process is surprising, since it was demonstrated by H. Hu that

the same material, if present in a coarse-grained polycrystalline state, is evolving under normal-growth characteristics (*cf.* Fig. 1.1). The characteristics that are featured by Hu's data, i.e. a parabolic growth curve and a self-similar grain-size distribution for all times of the anneal, are not shown by the experimental data of this study and thus, it was only consequent to find the failure of analytical models, which were developed under the perception of uniform curvature-controlled coarsening of the microstructure, to describe the growth curves measured on nanocrystalline Fe.

The obvious failure of conventional theories to explain grain growth in the unusual case of nanocrystalline Fe entailed that no appropriate relationship was available, which would have allowed to describe the measured kinetics analytically. To provide evidence for the proposed hypothesis of abnormal grain growth (AGG), and to be able to evaluate the growth kinetics quantitatively with respect to an inhomogeneous evolution of the nanocrystalline microstructure, a numerical two-population model was defined, where the two populations have been assigned to an abnormal (i.e. fast growing) and a matrix species (with restricted growth) of grains. The quantitative results that were obtained from the numerical model permitted the conclusion that basically all "curious" features of the isothermal experiments — especially the linear/upward-curved growth kinetics and the broadening/narrowing of the grain-size distribution — are fully covered by the expeditious growth of particular abnormal grains into a matrix of grains with low-kinetics boundaries [145,165]. The excellent compliance between the model and the measured growth kinetics has of course an important consequence, since it demonstrates that the unexpected features in the isothermal grain-size/time plots and the temporary broadening of the grain-size distribution, are obviously inherent features of the very contrary behavior of the two grain species. The analysis of the numerical model proved further that the evolution of the microstructure is solely driven by the dominant growth of a few abnormal grains together with the simultaneous annihilation of grains of the impeded species. Based on this conclusion it is of course evident that the before mentioned idea of a "physically" accelerated grain-boundary velocity — for which actually no reasonable explanation could be given — would be tempting from a first view, but is a clearly misleading interpretation of the experimental data.

The numerical model confirmed that the unusual growth kinetics of the isothermal anneals is the result of the statistical nature of the measured volume and area-weighted average grain size, and was found to be controlled by the gradual increase of the abnormal-volume fraction, $x_V(t) = 0 \rightarrow 1$. The analysis of $x_V(t)$ revealed a sigmoidal time dependence — similar to the nucleation-and-growth kinetics of recrystallization, as proposed by Johnson and Mehl, Avrami and Kolmogorov. However, the discussion disproved the feasibility of recrystallization, since the available excess energy in the as-prepared state is already low due to dynamic recovery, and further relaxation of dislocation excess occurs rapidly via thermally-induced recovery, which finally erases the driving force for recrystallization completely. The easy relaxation of dislocations via recovery involves that the empirical long-term AGG cannot be driven by fast recrystallization of the microstructure. With the same argument of missing dislocation-excess energy, recrystallization has been discarded from being responsible for the initial rapid increase of the grain size that was found to be a generic feature for the early evolution of all isothermal anneals.

The excellent agreement between the numerical model and the experimental data provided evidence that the coarsening of the investigated nanocrystalline Fe is driven by the abnormal growth of particular grains and the successive annihilation of the inhibited matrix. However, the evolution of the microstructure by the growth of a few particular grains would of course be a situation, which should allow to find a bimodal

decomposition of the initially narrow grain-size distribution. But obviously, the ratio $\langle L \rangle_{vol} / \langle L \rangle_{area}$ (which was used in the model and the experiment to test the microstructure on self-similarity) did not reveal a distinct bimodal characteristic. Comparing the two grain-size distributions used by the numerical model for the matrix and the abnormal grain species respectively (both grain-size distributions were defined according to the measured isothermal grain-size data) unveiled, that the median of the abnormal grain-size distribution is only ~30% larger than the one of the matrix distribution, i.e. the abnormal grains are not expected to grow unlimited and occupy an independent range of the grain-size distribution. This size limitation involves that AGG should be a transient process, which terminates in a polycrystalline microstructure of larger abnormally-grown grains — and, in case of $x_V < 1$, a certain fraction of remaining matrix grains (depending on the initial density of abnormal "nuclei" in the microstructure). The plots of $\langle L \rangle_{vol} / \langle L \rangle_{area}$ as a function of annealing time suggested that for the examined Fe samples a complete transient evolution is not accomplished within the investigated time frame (and seems also not to be reached easily even for extended isothermal annealing duration), which means that AGG is not necessarily able to transfer the microstructure completely into a new state of before abnormally-grown grains — i.e. to annihilate the matrix completely.

The Root-Cause for Abnormal Grain Growth

A major part of this thesis has been devoted to the question on what is driving the observed inhomogeneous evolution of the material, i.e. which process or which mechanism is responsible that a grain will either belong to the growing abnormal or to the inhibited matrix population. If the velocity of a grain boundary is determined by the product of driving force and mobility, the growth advantage of the abnormal grains compared to the matrix must be related to the supremacy of at least one of the two parameters. The evaluation of various root causes, which are empirically known to have the potential to modify grain-boundary kinetics in an anisotropic way revealed that — except for only one mechanism — none of the possible candidates appears to be suitable (and likewise probable) to yield a convincing explanation of the experimental results.

The discussion showed that only the anisotropy of the grain-boundary mobility, which is induced by a misorientation distribution of low-angle boundaries, can adequately account for the conditions needed to establish a microstructure that provides the inhomogeneous properties that will drive a grain either abnormally, or will leave the grain in the impeded matrix — depending on the actual interface mobility $M(\Theta)$ [165]. Of course, Hu's conclusion of normal growth in coarse-grained Fe and the AGG observed in the nanocrystalline state led the focus to the grain-refinement process to which the studied samples of this investigation have been subjected. It was the essence of the discussion to show that the reorganization of the material during and after mechanical processing is determined by dislocation recovery, which will turn the material due to its nature into a microstructure of newly created dislocation-free cells that are surrounded by boundaries of low-angle structure. Particularly the innately high stacking-fault energy of α-Fe (which suppresses the dissociation of dislocations into partials) and the apparently low impurity concentration in the material (which excludes significant dislocation pinning) support an unimpeded dislocation mobility, which is rudimental for substantial recovery of the microstructure either during deformation (i.e. dynamically) or at the beginning of an experiment (i.e. if dislocations' migration and annihilation is improved due to higher thermal energy).

The feasibility of substantial dynamic recovery was experimentally confirmed by the observation of

a homogeneous as-prepared microstructure, which is built-up of well-defined nano-sized grains. The residual dislocation excess remaining after dynamic recovery was found by DSC to be easily annihilated in the temperature range up to ~400°C, where parallel to the clean-up of dislocations a significant relaxation of microstrain was measured by XRD (relaxation of residual microstrain after dislocation annihilation was found to rely on the coarsening of the grain structure, which confirmed this microstrain to belong to the effect of grain contiguity). The TEM dark-field imaging and electron diffraction revealed that the nano-sized grains of the as-prepared microstructure are bordered by low-angle boundaries, which were found to define an angular misorientation distribution $\nu(\Theta)$ of certain width and thus, introducing a distribution of grain-boundary mobility $M(\Theta)$ and energy $\gamma^{\mathrm{GB}}(\Theta)$ in the material. From the obvious affinity of the examined material to undergo substantial recovery during and after sample preparation it was concluded that the existence of anisotropic grain-boundary properties must be a generic and inherent feature of all nanocrystalline Fe specimens that are prepared by mechanical processing in a top-down approach.

Question 3: "*To what extent can the microstructural evolution observed in the model system ball-milled Fe be generalized to other nanocrystalline materials*?"

Abnormal grain growth in nanocrystalline materials is not unusual and has also been observed for example on Palladium or Copper. However, as there are several reason for the microstructure to deviate from normal grain growth, the physics of AGG is likely to depend on the properties of the investigated material and hence, a generic explanation is therefore difficult. Nevertheless, a numerical description like the two-population model above, which does not consider the actual cause for AGG, could be understood as a more general approach to quantify abnormal-growth kinetics, and might also be applied for root causes other than the anisotropy of grain-boundary properties due to a misorientation distribution.

A detailed and fundamental explanation — including the driving mechanisms and the constraints for a certain microstructural evolution — for both the stability and the growth kinetics of a specific nano-structured material will require a case-by-case study. It is however clear from this study that nanocrystalline materials are presumably more susceptible to abnormal grain growth than coarse-grained polycrystals of the same material.

Humphreys' Model on Abnormal Grain Growth

Although the anisotropy of grain-boundary misorientation was found from all conceivable effects to be the most likely reason for the abnormal growth of nanocrystalline Fe, a quantitative evaluation of the interface kinetics of grains that are growing by the advantage of higher misorientation-induced mobility was still not available. This deficiency was resolved by analyzing a quantitative model on misorientation-driven AGG that has been introduced by F.J. Humphreys. The model has the characteristic of a quasi-mean-field description, which considers a single abnormal grain with unique misorientation Θ and size R that is surrounded by matrix grains of mean misorientation $\langle\Theta\rangle$ and size $\langle R\rangle$ (with those two misorientation parameters the grain-boundary energy γ^{GB} and mobility M^{GB} of both grain species were uniquely defined). The model showed that AGG will be enabled, if the particular grain has a misorientation $\Theta > \langle\Theta\rangle$ and a relative size $r = R/\langle R\rangle$ with respect to the matrix grain size that is larger

than the cutoff value $r_{\min}(\langle\Theta\rangle, \Theta)$; those constraints for positive AGG involve that the abnormal grain will have both a higher grain-boundary kinetics than the surrounding grains and the particular grain will actually grow (i.e. $\mathrm{d}R/\mathrm{d}t > 0$) rather than shrink. If both conditions are fulfilled, the model predicts that the considered grain grows abnormally until the driving force on the abnormal boundaries is depleted, and the relative size approaches the upper size limit $r_{\max}$ at which the mixed microstructure of abnormal and matrix grains arrives at the broadest state of the grain-size distribution. Of course, the model includes both the anisotropy of $\gamma^{\mathrm{GB}}(\Theta)$ and $M^{\mathrm{GB}}(\Theta)$, which are both contributing to non-uniform grain-boundary kinetics. However, the numerical evaluation of Humphreys' model made clear that the increase of the grain-boundary energy at higher misorientations Θ of the abnormal grain — as defined by the Read-Shockley equation — is adverse to the evolution of AGG and thus, misorientation-induced AGG must be initiated from a distribution of grain-boundary mobilities.

For the examined nanocrystalline samples, the mean misorientation between matrix grains has been estimated from TEM analysis of the as-prepared material to be $\langle\Theta\rangle \approx 10°$. For this condition, the evaluation of Humphreys' model yielded that the abnormal grains will grow to a size $r_{\max}$ that is approximately five times the average size of the matrix. Obviously, this result is quite appealing, since it accounts for the following key characteristics of AGG in nanocrystalline Fe:

- ◇ The predicted moderate growth of the particular grains with respect to the size of the matrix agrees with the experimentally deduced parameters for the abnormal and the matrix grain-size distribution of the numerical model above. Both size distributions have been described by lognormal functions, where the center position of the abnormal distribution is only slightly shifted to larger grain sizes compared to the lognormal density of the matrix grains.

- ◇ The expectation that the abnormal grains are restricted in growth and do not significantly exceed a relative size $R/\langle R\rangle \approx 5$ is reflected by the grain-size distributions observed via EBSD micrographs of the annealed state.

- ◇ The size-limited abnormal growth is the reason for the observed moderate broadening of the grain-size distribution during AGG. In case of a larger relative size which the abnormal grains can reach, the measured grain-size distribution would be likely to show a distinct bimodal characteristic. Humphreys' model revealed that the constraining criterion for moderate AGG is the misorientation $\langle\Theta\rangle$ of the matrix grains, which has to be close to the transition between the regime of low and high-angle boundaries. Only in this case the properties of the abnormal and the matrix grain boundaries are not too different and provide a certain — but not irresistible — growth advantage to the particular grains within the microstructure. In all other cases the model predicts the ability for abnormal growth to grain sizes that are orders of magnitude larger than the size of the matrix grains (i.e. catastrophic AGG).

  Although highly misoriented abnormal grains would also account in Humphreys's model for moderate AGG (the maximum size is solely determined by $\langle\Theta\rangle$), the finding via OIM and TEM of orientation-aligned abnormal grains in the annealed state suggests that both the matrix and the abnormal grains belong to the same initial orientation texture. In this case, the discussion clarified that only the size criterion for AGG, i.e. $r > r_{\min}$, will remain as the key parameter for the release of AGG, and the result of AGG is determined by the spatial distribution of particular grains (which are ~7% of all grains in the initial configuration).

Beyond the excellent agreement of Humphreys' model with the AGG covered by the numerical model before, it is the commendable proficiency of this model to approach successfully the initial rapid and short-termed growth of the grain size at the beginning of each isothermal experiment. Looking at this unusual feature, other processes like recrystallization, which are known to create a temporarily-limited high growth kinetics, have failed to provide a reliable explanation. With respect to Humphreys' model it was proposed that the jump of the grain size at the very beginning is most likely driven by the fast shrinkage of particular grains of "abnormal mobility" (i.e. $\Theta > \langle\Theta\rangle$), which do not meet the size criterion (i.e. particular grains with $r < r_{\min}$), and are therefore not qualified to be part of the long-term AGG. The initial jump of the grains size is therefore also a kind of abnormal growth, however with a reversed sign and short duration (due to the high — and further increasing — boundary curvature of the small matrix-annihilated abnormal grains) [165].

Influence of Texture

The discussion of the experimental results and the comparison with appropriate numerical models confirmed the evolution of nanocrystalline Fe via misorientation-driven AGG. This anisotropic process was particularly observed in the EBSD/OIM images that were taken on the annealed material and revealed the coexistence of small matrix grains and much larger abnormal grains. The inspection of the micrographs however showed also that the abnormal growth of a grain can occur in very different ways, where the abnormal grains have been found to develop in a range between large equiaxed grains in an environment of rather uniform size distribution, and large finger-like grains that are located in a very inhomogeneous size distribution. Especially the latter case shows that the growth of a particular grain can be itself very anisotropic. The finding of spatially anisotropic abnormal growth is in principle directly related to the magnitude of orientational alignment of matrix grains, which can dismiss the quasi-mean-field approach in Humphreys' model, if the individual grain boundaries of a particular grain have clearly different misorientations. If the texture within the matrix is weak, a distribution of misorientations for one and the same grain is likely and hence, each grain boundary relates according to Humphreys' analysis to both a different maximum size $r_{\max}$ and abnormal growth kinetics — the result will be the evolution of anisotropic finger-like grains. For a distinct texture the various interfaces of an abnormal grain are mostly identical and uniform growth with equiaxed grains occurs. This correlation between abnormal-growth behavior and matrix texture was experimentally confirmed by the comparison of inverse-pole-figure plots and the corresponding OIM images, showing a clearly anisotropic AGG with long-streched finger-like grains in an environment of small and equiaxed matrix grains, if the matrix is not characterized by defined orientation texture.

6.1 Resumé

The microstructural instability and the involved coarsening mechanisms of nanocrystalline materials have been examined in a number of experiments and analyses on the model system α-Fe. In summary of this study it can be concluded that a generic statement on the question of how nano-structured bulk materials behave cannot be given. It was found that in the particular case of α-Fe a systematic AGG — which was found to be impelled by anisotropic grain-boundary misorientation, established by dislocation

recovery during the grain-refinement process — is controlling the evolution of the microstructure, and transfers the material via a transient process into a new assembly of abnormally-grown grains. The fact that the observed transient abnormal process terminates in a quasi-static microstructure with average grain sizes between 50 and 500 nm (depending on the actual annealing temperature) suggests that after completion of the AGG phase the established microstructure is relatively stable, and does not show the tendency of further significant coarsening under the same isothermal conditions.

The conclusions, based on the experimental findings, follow without appealing to recently proposed models of grain growth controlled by the migration of triple lines or quadruple points, and also do not confirm a switch-over of the rate-controlling mechanism for grain-boundary migration at a critical grain size. In other words, nanocrystalline coarsening in α-Fe is guided by the same rate-controlling process as it is found in coarse-grained microstructures — namely, the migration of high-angle boundaries by grain-boundary self-diffusion. In the context of the substantial probability of dislocation recovery in α-Fe it was concluded that the development of anisotropic grain-boundary properties and the related non-uniform evolution of the microstructure in a dedicated abnormal growth process, must be inherent features of nanocrystalline Fe after grain refinement by mechanical attrition. A schematic summary of the conclusions drawn on the nanocrystalline AGG in α-Fe was given in Fig. 5.9.

The experimental results, comprehensive discussions and conclusions drawn within this thesis have been published in Refs. [145, 165, 166].

6.2 Outlook — Prospective Questions

Although the comprehensive discussion was able to explain the mode and the parameters which are controlling the coarsening of nano-structured bulk Fe, the experimental results itself and also the conclusions drawn will stimulate new questions and encourage further investigations beyond this study. The following aspects are intended to give a concise outlook on interesting issues that could attract the attention in further investigations.

- The grain-boundary misorientation of the as-prepared state was estimated from the orientation distribution measured by electron diffraction — the evaluation of this point has been done within this thesis to the best of the currently available techniques and methods. As the actual misorientation of grain boundaries plays a key role for the observed AGG, a dedicated misorientation analysis of the as-prepared microstructure would be a primary candidate for prospective experiments. This includes the preparation of samples by techniques other than mechanical polishing and ion bombardment (for example via focused ion beam (FIB)), which could improve the surface quality and therefore allow better spatial resolution of crystallographic orientation.
- The formation of a low-angle subgrain network by dislocation recovery was found to be the major prerequisite for the evolution of AGG. As recovery cannot be expected in all materials to be equally likely, it would be interesting (and equally important) to investigate the coarsening characteristics of nanocrystalline materials with material-specific properties different from those of α-Fe.
- The AGG in nanocrystalline Fe was found to be a transient evolution of the material and yielded

a microstructure that might still remain within the grain-size range of nano-structured materials. Although the possibility of low-angle impingement was found to agree with major aspects of the experimental results, a thorough analysis of the reason for terminating AGG would provide valuable information and may also explain the obvious stability of the microstructure after the transient AGG is completed.

- Although the misorientation dependence of the grain-boundary mobility is the key parameter for both the actual evolution and the quantitative analysis of AGG, there is currently no reliable material-specific data about the influence of grain-boundary misorientation available and thus, an empirical function with parameters derived from experiments on aluminum had to be used. It would be expedient, if evidence could be provided by appropriate experiments that the adopted empirical description represents a sound explanation of the mobility vs. misorientation relationship, or could provide a better empirical description of the grain-boundary mobility as a function of misorientation.

Bibliography

[1] Gleiter, H. in *Physical Metallurgy*. R.W. Cahn and P. Haasen (Eds.), North-Holland (1996), Chap. 9, pp. 843.

[2] Gleiter, H. *Prog. Mater. Sci.* **33**, 223 (1989).

[3] Suryanarayana, C. and Koch, C. *Non-Equilibrium Processing of Materials*. Pergamon (1999).

[4] Humphreys, F. and Hatherly, M. *Recrystallization and Related Annealing Phenomena (Second Edition)*. Elsevier (2004), Chap. 6, pp. 169.

[5] Malow, T. and Koch, C. in *Synthesis and Processing of Nanocrystalline Powder*. D.L. Bourell (Ed.), The Minerals, Metals & Materials Society (1996), pp. 33.

[6] Burke, J. and Turnbull, D. *Prog. Metal Phys.* **3**, 220 (1952).

[7] Humphreys, F. and Hatherly, M. *Recrystallization and Related Annealing Phenomena (Second Edition)*. Elsevier (2004), Chapt. 11, pp. 333.

[8] Hu, H. *Can. Metall. Q.* **13**, 275 (1974).

[9] Vandermeer, R. and Hu, H. *Acta Metall. Mater.* **42**, 3071 (1994).

[10] Malow, T. and Koch, C. *Acta Mater.* **45**, 2177 (1997).

[11] Michels, A., Krill, C., Ehrhardt, H., Birringer, R. and Wu, D. in *Grain Growth in Polycrystalline Materials III*. H. Weiland, B.L. Adams and A.D. Rollett (Eds.), The Minerals, Metals & Materials Society (1998), Warrendale, PA.

[12] Krill, C., Helfen, L., Michels, D., Natter, H., Fitch, A., Masson, O. and Birringer, R. *Phys. Rev. Lett.* **86**, 842 (2001).

[13] Stokes, R. and Evans, D. F. *Fundamentals of Interfacial Engineering*. John Wiley & Sons (1996).

[14] Sutton, A. and Balluffi, R. *Interfaces in Crystalline Materials*. Oxford University Press (1996).

[15] Humphreys, F. and Hatherly, M. *Recrystallization and Related Annealing Phenomena (Second Edition)*. Elsevier (2004), Chapt. 4, pp. 91.

[16] Read, W. and Shockley, W. *Phys. Rev.* **78**, 275 (1950).

[17] Humphreys, F. and Hatherly, M. *Recrystallization and Related Annealing Phenomena (Second Edition)*. Elsevier (2004), Chapt. 5, pp. 121.

[18] Wolf, D. *Phil. Mag. B* **59**, 667 (1989).

[19] Wolf, D. *Phil. Mag. A* **62**, 447 (1990).

[20] Hondros, E. and Seah, M. in *Physical Metallurgy*. R.W. Cahn and P. Haasen (Eds.), North-Holland (1983), pp. 855.

[21] Sandström, R. *Acta. Metall.* **25**, 905 (1977).

[22] Haessner, F. and Hofmann, S. *Recrystallization of Metallic Materials*. Dr. Rieder-Verlag (1978).

[23] Huang, H., Humphreys, F. and Ferry, M. *Acta. Mater.* **48**, 2543 (2000).

[24] Doherty, R., Hughes, D., Humphreys, F., Jonas, J., Jensen, D. J., Kassner, M., King, W., McNelley, T., McQueen, H. and Rollett, R. *Mat. Sci. Eng. A* **238**, 219 (1997).

[25] Inoue, A., Nitta, H. and Iijima, Y. *Acta Mater.* **55**, 5910 (2007).

[26] Brandes, E. and Brook, G. (Eds.). *Smithells Metals Reference Book (7th Edition)*. Butterworth Heinemann (1992), pp. 13-12, 13-117.

[27] Winning, M., Gottstain, G. and Shvinderlman, L. *Acta Mater.* **49**, 211 (2001).

[28] Humphreys, F. *Acta Mater.* **45**, 5031 (1997).

[29] Moldovan, D., Wolf, D., Phillpot, S. and Haslam, A. *Phil. Mag. A* **82**, 1271 (2002).

[30] Holm, E., Miodownik, M. and Rollett, A.D. *Acta Mater.* **52**, 2701 (2003).

[31] Wejrzanowski, T., Spychalski, M., Pielaszek, R. and Kurzydlowski, K. *Solid State Phenom.* **129**, 145 (2007).

[32] Krill, C., Ehrhardt, H. and Birringer, R. *Z. Metallkd.* **96**, 1134 (2004).

[33] Hillert, M. *Acta Metall.* **13**, 227 (1965).

[34] Humphreys, F. and Hatherly, M. *Recrystallization and Related Annealing Phenomena (Second Edition)*. Elsevier (2004).

[35] Underwood, E. *Quantitative Stereology*. Addison-Wesley (1970).

[36] Mullins, W. *J. Appl. Phys.* **59**, 1341 (1986).

[37] Mullins, W. *Acta Mater.* **46**, 6219 (1998).

[38] Mullins, W. *J. Appl. Phys.* **27**, 900 (1956).

[39] Wu, D. *Mat. Res. Soc. Symp. Proc.* **343**, 61 (1994).

[40] Atkinson, H. *Acta Metall.* **36**, 469 (1988).

[41] Rios, P. and Glicksman, M. *Mater. Res.* **10**, 371 (2007).

[42] Hunderi, O. and Ryum, N. *J. Mater. Sci.* **15**, 1104 (1980).

[43] Kurtz, S. and Carpay, F. *J. Appl. Phys.* **51**, 5725 (1980).

[44] Feltham, P. *Acta Metall.* **5**, 97 (1957).

[45] Marthinsen, K., Hunderi, O. and Ryum, N. *Acta Mater.* **44**, 1681 (1996).

[46] Streitenberger, P. and Zöllner, D. *Scr. Mater.* **55**, 461 (2006).

[47] Nordbakke, M., Ryum, N. and Hunderi, O. *Acta Mater.* **50**, 3661 (2002).

[48] Fradkov, V. and Udler, D. *Adv. Phys.* **43**, 739 (1994).

[49] Zöllner, D. *Scr. Mater.* **54**, 1697 (2006).

[50] Jeppsson, J., Ågren, J. and Hillert, M. *Acta Mater.* **56**, 5188 (2008).

[51] Gottstein, G. and Shvindlerman, L. *Scr. Mater.* **52**, 863 (2005).

[52] Galina, A., Fradkov, V. and Shvindlerman, L. *Phys. Met. Metall.* **63**, 165 (1987).

[53] Soraes, A., Ferro, A. and Fortes, M. *Scr. Metall.* **19**, 1419 (1985).

[54] Czubayko, U., Sursaeva, V., Gottstein, G. and Shvindlerman, L. *Acta Mater.* **46**, 5863 (1998).

[55] Fortes, M. *Interface Sci.* **2**, 183 (1994).

[56] Protasova, S., Gottstein, G., Molodov, D., Sursaeva, V. and Shvindlerman, L. *Acta Mater.* **49**, 2519 (2001).

[57] Mattissen, D., Molodov, D., Shvindlerman, L. and Gottstein, G. *Acta Mater.* **53**, 2049 (2005).

[58] Upmanyu, M., Srolovitz, D., Shvindlerman, L. and Gottstein, G. *Acta Mater.* **50**, 1405 (2002).

[59] Gottstein, G., King, A. and Shvindlerman, L. *Acta Mater.* **48**, 397 (2000).

[60] Gottstein, G. and Shvindlerman, L. *Acta Mater.* **50**, 703 (2002).

[61] Novikov, V. Y. *Scr. Mater.* **52**, 857 (2005).

[62] Mora, L. B., Mohles, V., Shvindlerman, L. and Gottstein, G. *Acta Mater.* **56**, 1151 (2008).

[63] Gottstein, G. and Shvindlerman, L. *Scr. Mater.* **54**, 1065 (2006).

[64] Estrin, Y., Gottstein, G. and Shvindlerman, L. *Acta Mater.* **47**, 3541 (1999).

[65] Estrin, Y., Gottstein, G. and Shvindlerman, L. *Scr. Mater.* **41**, 385 (1999).

[66] Estrin, Y., Gottstein, G., Rabkin, E. and Shvindlerman, L. *Scr. Mater.* **43**, 141 (2000).

[67] Upmanyu, M., Smith, R. and Srolovitz, D. *Interface Sci.* **6**, 41 (1998).

[68] Hirth, J. in *Physical Metallurgy*. R.W. Cahn and P. Haasen (Eds.), North-Holland (1996), Chap. 20.

[69] de Boer, F., Boom, R., Mattens, W., Miedema, A. and Niessen, A. *Cohesion in Metals: Transition Metal Alloys*. Elsevier (1988).

[70] Krill, C.E., Erhardt, H. and Birringer, R. in *Chemistry and Physics of Nanostructures and Related Non-Equilibrium Materials*. E. Ma, B. Fultz, R. Shull, J. Morral and P. Nash (Eds.), The Minerals, Metals & Materials Society (1997), Warrendale, PA.

[71] Lücke, K. and Detert, K. *Acta Metall.* **5**, 628 (1957).

[72] Lücke, K. and Stüwe, H. *Acta Metall.* **19**, 1087 (1971).

[73] Cahn, J. *Acta Metall.* **10**, 789 (1962).

[74] Mendelev, M. and Srolovitz, D. *Acta Mater.* **49**, 589 (2001).

[75] Mendelev, M. and Srolovitz, D. *Phil. Mag. A* **81**, 2243 (2001).

[76] Gibbs, J.W., Andrews, H., Longley, W.R. and Van Name, R.G. *The Collected Works of J. Willard Gibbs*. Longmans, Green and Co. (1928).

[77] Kirchheim, R. *Acta Mater.* **50**, 413 (2002).

[78] Weissmüller, J. *Nanostruct. Mater.* **3**, 261 (1993).

[79] Krill, C.E., Ehrhardt, H. and Birringer, R. *Z. Metallkd.* **96**, 1134 (2005).

[80] Krill, C.E. *Kinetics and Thermodynamics of Grain Growth from the Nanoscale to the Conventional Size Regime*. Habilitationsschrift, Universität des Saarlandes (2002).

[81] Hubbell, J. and Seltzer, S. *Tables of X-Ray Mass Attenuation Coefficients and Mass Energy-Absorption Coefficients.* National Institute of Standards and Technology (1996).

[82] Cullity, B. *Elements of X-Ray Diffraction*. Addison-Wesley (1978).

[83] Touloukian, Y. (Ed.). *Thermophysical Properties of Matter*. IFI/Plenum, New York, (1970).

[84] Warren, B. *X-Ray Diffraction*. Dover Publicatios (1990).

[85] Bragg, W. *J. Chem. Soc.* **1** (1916).

[86] Scherrer, P. *Göttinger Nachrichten* (1918), pp. 98.

[87] Patterson, A. *Phys. Rev.* **56**, 978 (1939).

[88] Krill, C. E. and Birringer, R. *Phil. Mag. A* **77**, 621 (1998).

[89] Bertaut, E. *C.R. Acad. Sci., Paris* **228**, 187 (1949).

[90] Bertaut, E. *C.R. Acad. Sci., Paris* **228**, 492 (1949).

[91] Bertaut, E. *Acta Cryst.* **3**, 14 (1950).

[92] Smith, W. L. *J. Appl. Cryst.* **9**, 187 (1976).

[93] Stokes, A. and Wilson, A. *Proc. Phys. Soc. London* **56**, 174 (1944).

[94] Klug, H. and Alexander, L. *X-Ray Diffraction Procedures*. Wiley (1974).

[95] Hull, D. and Bacon, D. *Introduction to Dislocations (4th Edition)*. Butterworth-Heinemann (2001), Chap. 4.

[96] Williamson, G. and Hall, W. *Acta Metall.* **1**, 22 (1953).

[97] Tian, H. and Atzmon, M. *Phil. Mag. A* **79**, 1769 (1999).

[98] Révész, A., Ungár, T., Borbély, A. and Lendvai, J. *Nanostruct. Mater.* **7**, 779 (1996).

[99] Stokes, A. and Wilson, A. *Proc. Camb. Phil. Soc.* **40**, 197 (1944).

[100] Warren, B. *Acta Cryst.* **8**, 483 (1955).

[101] Warren, B. and Averbach, B. L. *J. Appl. Phys.* **21**, 595 (1950).

[102] Warren, B. and Averbach, B. *J. Appl. Phys.* **23**, 497 (1952).

[103] Delhez, R. and Mittemeijer, E. *J. Appl. Cryst.* **9**, 233 (1976).

[104] van Berkum, J., Vermeulen, A., Delhez, R., de Keijser, T. and Mittemeijer, E. *J. Appl. Cryst.* **27**, 345 (1994).

[105] Turunen, M., de Keijser, T., Delhez, R. and van der Pers, N. *J. Appl. Cryst.* **16**, 176 (1983).

[106] Jenkins, R. and Snyder, R. *Introduction to X-Ray Powder Diffraction*. John Wiley & Sons (1996).

[107] Cheary, R. and Coelho, A. *J. Appl. Cryst.* **31**, 851 (1998).

[108] Masson, O., Guinebretiere, R. and Gauger, A. *J. Appl. Cryst.* **34**, 436 (2001).

[109] Stokes, A. *Proc. Phys. Soc. London* **61**, 382 (1948).

[110] Taupin, D. *J. Appl. Cryst.* **6**, 266 (1973).

[111] Alexander, L. *J. Appl. Phys.* **21**, 126 (1950).

[112] Alexander, L. *J. Appl. Phys.* **19**, 1068 (1948).

[113] Krill, C., Haberkorn, R. and Birringer, R. in *Handbook of Nanostructured Materials and Nanotechnology*. H.S. Nalwa (Ed.), Academic Press (2000), Chap. 3.

[114] Wagner, C. and Aqua, E. *Adv. X-ray Anal.* **7**, 46 (1964).

[115] Chantler, C., Olsen, K., Dragoset, R., Chang, J., Kshore, A., Kotochigova, S. and Zucker, D. *NIST Standard Reference Database 66, X-ray Form Factor, Attenuation, and Scattering Tables*. National Institute of Standards and Technology (2001).

[116] Natter, H., Schmelzer, M., Löffler, M., Krill, C., Ficht, A. and Hempelmann, R. *J. Phys. Chem. B* **104**, 2467 (2000).

[117] Prevey, P. *Adv. X-ray Anal.* **29**, 103 (1986).

[118] Maskil, N. and Deutsch, M. *Phys. Rev. A* **38**, 3467 (1988).

[119] Richtmyer, F. and Taylor, L. *Phys. Rev.* **36**, 1044 (1930).

[120] Kissinger, H. *Anal. Chem.* **29**, 1702 (1957).

[121] Chen, L. and Speapen, F. *J. Appl. Phys.* **69**, 679 (1991).

[122] Humphreys, F. and Hatherly, M. *Recrystallization and Related Annealing Phenomena (Second Edition)*. Elsevier (2004), Chap. 2.2.3.

[123] de Graef, M. *Introduction to Conventional Transmission Electron Microscopy*. Cambridge University Press (2003).

[124] Zangwill, A. *Physics at Surfaces*. Cambridge University Press (1988).

[125] Koch, C.C. *Nanostruct. Mater.* **9**, 13 (1997).

[126] Fecht, H.-J. *Nanostruct. Mater.* **6**, 33 (1995).

[127] Fecht, H.-J. *Nanophase Materials*. Kluwer (1993).

[128] Moelle, C. and Fecht, H.-J. *Nanostruct. Mater.* **6**, 421 (1995).

[129] Bonetti, E., Bianco, L. D., Pasquini, L. and Sampaolesi, E. *Nanostruct. Mater.* **12**, 685 (1999).

[130] Börner, I. and Eckert, J. *Mater. Sci. Eng. A* **226-228**, 541 (1997).

[131] Iijima, Y. *J. Alloys Compd.* **234**, 290 (1996).

[132] LeClaire, A. and Neumann, G. *Landolt-Börnstein - III Condensed Matter, Vol. 26 (Diffusion in Solid Metals and Alloys)*. H. Mehrer (Ed.), Springer Verlag (1990).

[133] Massalski, T., Okamoto, H., Subramanian, P. and Kacprzak, L. (Eds.). *Binary Alloy Phase Diagrams (Second edition), Vol. II*. ASM International (1996).

[134] Takada, J. and Adachi, M. *J. Mater. Sci.* **21**, 2133 (1986).

[135] Hollemann, A. and Wiberg, N. *Lehrbuch der Anorganischen Chemie, 102. Auflage*. de Gruyter (2007), Chap. XXIX.

[136] Rao, Y. *Stoichiometry and Thermodynamics of Metallurgical Processes*. Cambridge University Press (1985), Chap. 9.

[137] Tiernan, M. Barnes, P. and Parkes, G. *J. Phys. Chem. B* **105**, 220 (2001).

[138] Krill, C.E., Natter, H., Helfen, L. and Schmelzer, M. Experiment HS-477 (ESRF), (1998).

[139] Tilley, R. *Crystals and Crystal Structures*. John Wiley & Sons (2006).

[140] Cohen, M. *Rev. Sci. Instr.* **6**, 68 (1934).

[141] Michels, A., Krill, C.E., Ehrhardt, H., Birringer, R. and Wu, D. *Acta Mater.* **47**, 2143 (1999).

[142] Tian, H. and Atzmon, M. *Acta Mater.* **47**, 1255 (1999).

[143] Weissmüller, J. in *Proceedings of the 22nd Risø International Symposium on Materials Science: Science of Metastable and Nanocrystalline Alloys Structure, Properties and Modelling*. (2001), pp. 155.

[144] Schafler, E., Zehetbauer, M., Borbely, A. and Ungar, T. *Mat. Sci. Eng. A* **234-236**, 445 (1997).

[145] Paul, H. and Krill, C.E. *Scr. Mater.* **65**, 5 (2011).

[146] Humphreys, F. and Hatherly, M. *Recrystallization and Related Annealing Phenomena (Second Edition)*. Elsevier (2004), Chap. 7, pp. 215.

[147] Zurob, H., Bréchet, Y. and Dunlop, J. *Acta Mater.* **54**, 3983 (2006).

[148] Lücke, K., Brandt, R. and Abbruzzese, G. *Interface Sci.* **6**, 67 (1998).

[149] Kim, S. and Park, Y. *Acta Mater.* **56**, 3739 (2008).

[150] Rios, P. *Acta Mater.* **45**, 1785 (1997).

[151] Dennis, J., Bate, P. and Humphreys, F. *Acta Mater.* **57**, 4539 (2009).

[152] Novikov, V. Y. *Interface Sci.* **6**, 77 (1998).

[153] Novikov, V. Y. *Mater. Lett.* **62**, 2067 (2008).

[154] Rollett, A.D. and Mullins, W. *Scr. Mater.* **36**, 975 (1997).

[155] Holm, E., Miodownik, M. and Healy, K. *Mater. Sci. Forum* **467-470**, 611 (2004).

[156] Ivasishin, O., Shevchenko, S. and Semiatin, S. *Scr. Mater.* **50**, 1241 (2004).

[157] Humphreys, F. and Hatherly, M. *Recrystallization and Related Annealing Phenomena (Second Edition)*. Elsevier (2004), Chap. 2, pp. 11.

[158] Hull, D. and Bacon, D. *Introduction to Dislocations (4th Edition)*. Butterworth-Heinemann (2001), Chap. 9.1.

[159] Michalak, J. and Paxton, H. *Trans. metall. Soc. AIME* **221**, 850 (1961).

[160] Hirth, J. and Lothe, J. *Theory of Dislocations (Second Edition)*. John Wiley & Sons (1982), Chap. 8.9 & 15.6.

[161] Hull, D. and Bacon, D. *Introduction to Dislocations (4th Edition)*. Butterworth-Heinemann (2001), Chap. 5.3.

[162] Watanabe, R. *Strength Fract. Complex.* **5**, 13 (2007).

[163] Smith, C. and Dillamore, I. *Met. Sci. J.* **4**, 161 (1970).

[164] Humphreys, F. *Acta Mater.* **45**, 4231 (1997).

[165] Paul, H. and Krill, C. *Acta Mater.*, to be submitted.

[166] Paul, H., Dake, J. and Krill, C. *Mat. Sci. Forum* **715-716**, 315 (2012).

Danksagung

An dieser Stelle möchte ich allen danken, die mich über den Zeitraum, in dem diese Arbeit entstanden ist, begleitet und in unterschiedlichster Weise unterstützt haben.

Besonders bedanken möchte ich mich bei meinem Doktorvater Herrn Prof. Krill, der mir die Möglichkeit gab mich in dieses Themengebiet einzubringen, und zugleich für sein persönliches Engagement und die vielen wertvollen Diskussionen, die wesentlich zum Gelingen der Arbeit beigetragen haben. Die guten Ideen und die konstruktive Kritik dieser Diskussionen waren mir stets ermutigender Ansporn und Hilfestellung.

Mein Dank gilt auch Herrn Prof. Birringer, der dankenswerter Weise die fachliche Begutachtung meiner Doktorarbeit übernommen hat. Danken möchte ich weiter Herrn Prof. Graichen und Herrn Prof. Fischer für ihr Mitwirken im Promotionskolloquium.

Ein wichtiger Meilenstein während meiner Doktorarbeit war die Mitarbeit im BMBF Projekt „Nanolux“, welches sich mit der Synthese und Untersuchung von nanoskaligen YAG:Ce auseinandersetzte. Es ist mir deshalb ein besonderes Anliegen Herrn Prof. Herr zu danken, der mir die Möglichkeit gab an diesem innovativen Thema mitzuarbeiten, und dabei interessante Aspekte des optischen Verhaltens von Nanopartikeln kennenzulernen.

Ein ganz besonderer Dank richtet sich an Herrn Dr. Wunderlich, der mir nicht nur die DSC für etliche Messungen überlassen hat, sondern mir auch mit seiner großen Erfahrung und seinem vielseitigen Wissen hilfreiche Unterstützung gab.

Für die tolle Unterstützung bei den Untersuchungen mittels Rasterelektronenmikroskopie und EBSD, sowie der dafür notwendigen Probenpräparation, möchte ich Alexander Minkow danken. Danken möchte ich auch Jürgen Ankele, der durch sein Geschick für elektronische und mechanische Geräte öfters auch schwierigere Problem gelöst hat. An dieser Stelle ist es mir auch ein Anliegen Frau Faisst für die stets tolle Unterstützung in organisatorischen Fragen zu danken.

Mein Dank richtet sich ebenfalls an Sören Selve, Dr. Johannes Biskupek, Dr. Andrey Chuvilin und Frau Prof. Kaiser von der Arbeitsgruppe Elektronenmikroskopie der Uni Ulm für die Unterstützung und Zusammenarbeit bei den TEM Untersuchungen.

Insgesamt bedanken möchte ich mich bei meinen ehemaligen Kollegen Senthil, Thomas, Rao, Kai, Matthias und Neda, Jules sowie Lionel, mit den auch fachfremde und teils „tiefsinnige“ Themen während der Kaffee- und Mittagspausen eingehend diskutiert wurden. Natürlich werden die heiteren und unvergesslichen Momente, die ich mit euch erlebt habe, mir stets in Erinnerung bleiben.

Am Ende gilt mein ganz besonderer Dank natürlich meinen Eltern und meiner Familie, die zu jeder Zeit uneingeschränkt hinter mir standen und mich immer nach besten Kräften unterstützt haben.

Curriculum Vitae

For privacy protection, the electronic issue of this thesis does not contain the Curriculum Vitae.

List of Publications

1. H. Paul, H. Kaps, T. Gleich, V. Raeesi, U. Herr and M. Zachau
"Vapour phase synthesis of nanocrystalline in-situ YAG:Ce"
Solid State Phenom. **128**, 7-12 (2007)

2. H. Kaps, M.L. Arefin, U. Herr and H. Paul
"Concentration dependent fluorescence lifetime in nanocrystalline Y2O3:Eu phosphors"
Solid State Phenom. **128**, 165-171 (2007)

3. H. Paul, D. Kessler and U. Herr
"Optical properties of nanocrystalline YAG:Ce"
Solid State Phenom. **140**, 9-16 (2008)

4. J.Z. Jiang, W. Chen, Y.H. Lu, M. Wang, L. Kroner, H. Paul, H.-J. Fecht, J. Bednarcik, K. Stahl, Z.L. Zhang, U. Wiedwald, U. Kaiser, P. Ziemann, T. Kikegawa and C.D. Wu
"Synthesis, thermal stability and properties of ZnO_2 nanoparticles"
J. Phys. Chem. C **113**, 1320-1324 (2009)

5. M. Trautvetter, U. Wiedwald, H. Paul, A. Minkow and P. Ziemann
"Thermally driven solid phase epitaxy of laser-ablated amorphous AlFe films on (0001)-oriented sapphire single crystals"
Appl. Phys. A **102**, 725-730 (2010)

6. H. Paul and C.E. Krill
"Anomalously linear grain growth in nanocrystalline Fe"
Scr. Mater. **65**, 5-8 (2011)

7. H. Paul and C.E. Krill
"Origin of abnormal grain growth in Nanocrystalline Fe prepared by ball milling"
Acta Mater. (to be submitted)

8. H. Paul, J.M. Dake and C.E. Krill
"Tales of the abnormal: Nanocrystalline Grain Growth at low temperatures"
Mat. Sci. Forum **715-716**, 315-316 (2012)